

Direct Laser Written Nano- & Micro-Optical Textures for Photovoltaics Applications

Zur Erlangung des akademischen Grades eines

DOKTOR-INGENIEURS

von der KIT-Fakultät für
Elektrotechnik und Informationstechnik
des Karlsruher Instituts für Technologie (KIT)

genehmigte

DISSERTATION

von

M.Sc., Stephan Dottermusch

geb. in: Pforzheim

Tag der mündlichen Prüfung: 06. Juni 2019

Hauptreferent: Prof. Dr. Bryce Richards

Korreferenten: Prof. Dr. Christiane Becker
Prof. Dr. Heinz Kalt

Kurzfassung

Im Gegensatz zu anderen Technologien, welche der Gewinnung von elektrischer Energie dienen, basiert die Photovoltaik nicht auf einer langen Umwandlungskette. Anstatt einen Kraftstoff zu verbrennen, die Abwärme dieses Prozesses zur Wassererwärmung zu nutzen um schließlich mit Wasserdampf eine Turbine zu betreiben, welche einen elektrischen Generator antreibt, gelingt in der Photovoltaik die Umwandlung von Lichtenergie in elektrische Energie direkt. Dieser Vorgang ermöglicht eine Dezentralisierung der elektrischen Energiegewinnung. Des Weiteren besitzt die Photovoltaik mit der Sonne eine erneuerbare Energiequelle, welche auf menschlichen Zeitskalen nicht erlischt. Zusätzlich entstehen im Betrieb keine Treibhausgase, welche den Klimawandel weiter anheizen.

Trotz der vielen Vorteile der Photovoltaik lohnt sich die Produktion von Solarzellen, als Herzstücke der elektrischen Energiegewinnung in der Photovoltaik, erst dann im großen Stil, wenn der Preis pro erzeugte kWh elektrische Energie mit dem anderer herkömmlicher Energieträger mithalten kann. Insbesondere der Wirkungsgrad einer Solarzelle hat signifikanten Einfluss auf die Kosten für die elektrische Energie. Der Wirkungsgrad hängt zum einen ab von der Effizienz, mit der einfallendes Licht in freie Ladungsträger umgewandelt werden kann, und zum anderen davon, mit welcher Effizienz die Ladungsträger extrahiert werden können. Diese Dissertation beschäftigt sich mit Oberflächenstrukturen, welche eine gesteigerte Nutzung des einfallenden Lichtes ermöglichen.

Der Vorteil von Oberflächenstrukturen, welche Grenzflächenreflektion senken und den Lichtpfad beeinflussen, ist in der Photovoltaik altbekannt. In modernen, kommerziell erhältlichen kristallinen Siliziumsolarzellen wird auf die Halbleiteroberfläche eine Struktur aufgetragen, welche zu einer deutlichen Wirkungsgradsteigerung führt. Strukturen für andere Grenzflächen und Solarzell-Technologien werden hingegen weiterhin erforscht. Insbesondere für die sogenannten Dünnschicht-Technologien gibt es derzeit keine Standardstrukturen, wobei gerade hier eine effizientere Nutzung des einfallenden Lichtes große Vorteile hätte. Die kommerziellen Dünnschicht-Technologien (basierend auf den Halbleitern amorphem Silizium, Kupfer-Indium-(Gallium)-Diselenid /-Disulfid (CIGS) und Cadmium Telluride (CdTe)) haben in den letzten Jahren Marktanteile gegenüber den etablierten kristallinen Silizium-Technologien verloren. Dieser Trend basiert auf den, trotz eines höheren Materialaufwandes, paradoxerweise geringen Kosten für kristallines Silizium. In der Forschung hingegen haben die Dünnschicht-Technologien mit neuen Materialien, wie Perowskiten und Nanokristallen, sowie neuen Anwendungsgebieten, wie der gebäudeintegrierten Photovoltaik, erneut Aufwind erfahren.

Es existiert eine große Anzahl an guten Ideen, um Dünnschicht-Solarzellen zu strukturieren. Insbesondere auf der Basis numerischer Modellrechnungen konnte das enorme Potential der verschiedenen Strukturierungsansätze aufgewiesen werden. Auch an im Labor hergestellten Strukturen konnte eine deutliche Steigerung der Absorption von einfallendem Licht nachgewiesen werden, jedoch litt in vielen Fällen (insbesondere bei der Verwendung von Ätzverfahren) die Effizienz mit der Ladungsträger extrahiert werden und somit der Wirkungsgrad der Solarzelle. Außerdem konnten, auf Grund von Grenzen bei den Herstellungsverfahren, bisher nicht alle Strukturierungsansätze umgesetzt werden. Diese Dissertation widmet sich einem vergleichsweise neuen Verfahren zur Herstellung von 3D-Freiform-Strukturen, mit der Idee die Herstellung neuartiger Nano- und Mikrostrukturen für die Photovoltaik zu ermöglichen. Des Weiteren werden Verfahren verwendet, welche keinen (oder nur einen geringen) Einfluss auf die Extrahierung der Ladungsträger haben.

Mit dem zum Einsatz kommenden Strukturierungsverfahren „Direktes Laserschreiben“ (eng. direct laser writing (DLW)) lassen sich in einem Polymer (mit Hilfe eines Submikrometer großen Grundbausteins) Nano- und Mikrostrukturen, auf einer Fläche von mehreren Quadratmillimetern, verwirklichen. Das Verfahren benötigt keine lange Vorbereitung und kommt ohne eine Maske aus. Es ist somit gut geeignet um Prototypen zur optischen Charakterisierung zu entwickeln. Es wurde untersucht, inwiefern DLW verwendet werden kann, um optisch kleine und optisch große Strukturen für die Photovoltaik zu erforschen.

Optisch kleine Strukturen, mit Größenordnungen im Bereich der Wellenlänge des Lichtes, beugen einfallendes Licht und können es so in Bauelemente der Dünnschicht-Photovoltaik einkoppeln. Einkoppeltes Licht verweilt lange in der Solarzelle und wird somit stärker absorbiert. Für die Photovoltaik interessante Wellenlängen sind typischerweise im Bereich 300 nm bis 1200 nm vorzufinden. Dieser Bereich befindet sich an der Auflösungsgrenze des DLW-Systems. Ein wichtiger Teil dieser Studie war somit die Bestimmung geeigneter Parameter für die Herstellung der Strukturen. Um den Ladungsträgertransport nicht zu beeinflussen, wurde ein neuartiges Verfahren untersucht, bei dem das lichtabsorbierende Halbleitermaterial nachträglich in die Struktur eingefügt wurde. Dieses Verfahren beruht auf der Möglichkeit die zuvor erwähnten neuen Dünnschichtmaterialien flüssig zu prozessieren. In einer ersten Demonstration wurde eine mit DLW hergestellte Polymerstruktur mit CuInSe_2 (CIS) Nanokristallen infiltriert. Die CIS Nanokristalle lagen zunächst in Lösung vor. Nach dem Auftragen verdampfte das Lösungsmittel und hinterließ eine kompakte CIS Schicht welche die Polymerstruktur umschloss.

Ein wichtiger Teil der Studie war das Bestimmen der optischen Materialeigenschaften. Im Rahmen dieser Materialuntersuchung wurde für das DLW belichtete Polymermaterial IP-Dip ein Brechungsindex von etwa 1.53 bestimmt. Es wurde außerdem festgestellt, dass IP-Dip einen höheren Brechungsindex von etwa 1.54 besitzt, wenn es mit ultraviolettem (UV) Licht belichtet wurde. Für die CIS Nanokristalle wurde ein Brechungsindex von etwa 2.0 bestimmt. Mittels dieser Parameter war es möglich die Lichteinkopplung in eine erste Teststruktur im Detail numerisch zu untersuchen. Es wurde eine sehr hohe Übereinstimmung zwischen numerischen und experimentellen Ergebnisses gefunden. In einer fertiggestellten Solarzelle, konnte außerdem nachgewiesen werden, dass die Strukturen sich nicht schädlich auf die Ladungsträger-Extraktion auswirken. Bedauerlicherweise konnte, bedingt durch den sich als sehr gering herausgestellten Brechungsindexunterschied zwischen IP-Dip und den CIS Nanokristallen, nur eine sehr geringe Erhöhung der Absorption einfallenden Lichtes (auf Basis der angestrebten Lichteinkopplung) nachgewiesen werden. Andererseits kam es zu einem unerwarteten Kapillareffekt, auf Grund dessen sich die Schichtdicke der CIS Nanokristalle im Bereich der Strukturierung erhöhte.

Optisch große Strukturen, die sich in der Größenordnung eines Vielfachen der Wellenlänge bewegen, können die Reflektion an einer Grenzschicht von einem niedrigen Brechungsindex zu einem höheren Brechungsindex (in die Solarzelle hinein) deutlich reduzieren und in die andere Richtung (aus der Solarzelle heraus) deutlich erhöhen und so Licht gefangen halten. Dies ist das Grundprinzip der oben erwähnten Mikrostrukturen auf modernen kristallinen Siliziumsolarzellen. Um die Vorteile dieses Prinzips für die Dünnschicht-Photovoltaik zu nutzen, können Strukturen an der obersten Schicht eines Solarmoduls (Glas) angebracht werden. Der Halbleiter wird so nicht beschädigt und der Ladungsträgertransport nicht beeinflusst. In der im Folgenden beschriebenen Studie wurde DLW als Verfahren zum Erstellen von Freiform-Prototypen voll ausgenutzt, indem Strukturen zunächst mittels

DLW erstellt wurden und dann mit Hilfe von Nanoprägelithografie auf verschiedene Substrate transferiert wurden.

In vorangegangenen numerischen Studien hatte sich das Aspektverhältnis von Mikrostrukturen als Schlüsselparameter für Anwendungen in der Photovoltaik herauskristallisiert. Mittels DLW konnte ein experimenteller Beweis geliefert werden und eine für die Anwendung optimierte Struktur hergestellt werden. In einer systematischen Studie wurde der Einfluss des Aspektverhältnisses von kegelförmigen Mikrostrukturen auf die Reflektivität der Grenzschicht und das Potential Licht in der Solarzelle einzuschließen, numerisch und experimentell untersucht. Mittels optischer Untersuchungen auf unterschiedlichen Substraten, konnte zunächst eine hohe Übereinstimmung zwischen numerischen und experimentellen Ergebnissen gezeigt werden. So war es möglich eine Struktur mit einem für senkrecht einfallendes Licht optimierten Aspektverhältnis von 0.73 herzustellen. Außerdem konnte eine signifikante Wirkungsgradsteigerung verschiedener Solarzellen durch die Mikrostruktur gezeigt werden.

Mit Hilfe von kristallinen Siliziumsolarzellen, wurde die Relevanz der Mikrostrukturen für eine etablierte Technologie gezeigt. Die Mikrostrukturen wurden als zusätzliche Schicht auf einer Siliziumsolarzelle mit bereits strukturierter Halbleiterschicht aufgetragen. Mittels Messungen der externen Quanteneffizienz wurde eine relative Erhöhung der Kurzschlussstromdichte um 5.4% (im Vergleich zu einer Zusatzschicht ohne Strukturierung) bei senkrechtem Lichteinfall nachgewiesen. Die etablierte Technologie der Antirefleksionsbeschichtung kommt in einem ähnlichen Vergleich auf eine relative Erhöhung von nur 3%. Bei schrägem Lichteinfall entfalten die Mikrostrukturen ihr volles Potential. In einer Berechnung der Energieausbeute unter realen Bedingungen, kamen die Mikrostrukturen auf eine relative Erhöhung von bis zu 9%, wohingegen 4% für die etablierte Antirefleksionsbeschichtung bestimmt worden waren. Zu guter Letzt wurden CIGS Solarzellen verwendet, um das Potential der Mikrostrukturen auf Dünnschicht-Solarzellen mit hohem Wirkungsgrad zu zeigen. Unter Standardbedingungen wurde eine Erhöhung des Wirkungsgrades von 20.2% auf 20.9% nachgewiesen. Des Weiteren ergab der Vergleich mit einer konventionellen MgF_2 Beschichtung eine deutlich stärker reduzierte Reflektion unter senkrechtem Einfall und eine deutlich höhere Kurzschlussstromdichte für große Einfallswinkel.

Table of Contents

Kurzfassung	xv
Table of Contents	xix
List of Abbreviations.....	xxiii
List of Symbols	xxv
Latin symbols.....	xxv
Greek symbols.....	xxvi
Summary.....	xxvii
1 General introduction.....	1
1.1 Photovoltaics.....	1
1.1.1 Solar cell materials.....	1
1.1.2 Light management in photovoltaics	3
1.1.3 Micro- and nano-texture fabrication techniques.....	5
1.2 Content of this dissertation.....	6
2 Fundamentals	9
2.1 Photovoltaics.....	9
2.1.1 Solar cell working principle	9
2.1.2 Solar cell parameters	11
2.1.3 Solar cell efficiency	12
2.2 Light - matter interaction	13
2.2.1 Basic formalisms of electrodynamics.....	13
2.2.2 Light at a planar interface	14
2.2.3 Thin-film interference	16
2.2.4 Total internal reflection and optical modes.....	17
2.2.5 Photonic crystals and diffraction	18
2.2.6 Effective medium approximation	21
2.2.7 Geometrical optics.....	22
3 Methodology	23
3.1 Direct laser writing.....	23
3.1.1 Direct laser writing fundamentals.....	23
3.1.2 Sample preparation	24
3.1.3 Texture fabrication.....	25
3.1.4 Interface detection	26
3.1.5 Tilt correction.....	27
3.1.6 Sample development	29
3.2 Characterization tools	29
3.2.1 Microscopy.....	29
3.2.2 Reflectance, transmittance & absorptance	29
3.2.3 Photogoniometry	30
3.2.4 Spectroscopic ellipsometry and prism coupling	31
3.2.5 Solar cell characteristics.....	32

3.3	Optical simulations	34
3.3.1	Finite difference time domain simulations	34
3.3.2	Ray-tracing simulations	34
3.3.3	Transfer matrix method	35
4	Nano-optics for ink infiltrated photonic crystal solar cells	37
4.1	Introduction.....	37
4.2	Working principle of the photonic crystal pattern	39
4.3	Prototype preparation.....	40
4.3.1	Direct laser writing parameters	41
4.3.2	CIS nanocrystal infiltration	44
4.4	Optical properties of IP-Dip	45
4.4.1	DLW fabrication of flat layers.....	46
4.4.2	Stitching induced diffraction	47
4.4.3	The exposure dependent refractive index of IP-Dip	48
4.4.4	The extinction coefficient of IP-Dip.....	50
4.5	Optical properties of CIS nanoparticles	51
4.5.1	CIS nanocrystal layer preparation	51
4.5.2	The complex refractive index of CIS nanocrystal layers.....	51
4.6	Numerical prototype analyzation.....	53
4.6.1	Initial calculations.....	53
4.6.2	FDTD prototype simulations	55
4.7	Experimental prototype analyzation	60
4.7.1	Feasibility of the infiltration	60
4.7.2	Quantizing the light-trapping	61
4.8	CIS nanocrystal infiltrated photonic crystal PV device	64
4.8.1	Nanocone fabrication on electrodes.....	65
4.8.2	FDTD device simulations	66
4.8.3	Device preparation and analysis	67
5	Micro-optics for the front surface of solar modules.....	69
5.1	Introduction.....	69
5.2	Working principle of the microcone texture	72
5.3	Optical simulations	73
5.3.1	Reduced interface reflectivity	74
5.3.2	Light-trapping effect.....	75
5.4	Microcone fabrication	79
5.4.1	DLW prototyping.....	79
5.4.2	Texture replication	81
5.5	Optical analysis.....	84
5.5.1	Photogoniometric analysis.....	84
5.5.2	Analyzing the reduced interface reflectivity	86
5.5.3	Analyzing the light-trapping	87
5.6	Applying the microcone textures to solar cells	90
5.6.1	Comparing the microcone textures on planar silicon solar cells.....	90
5.6.2	Microcone textures on silicon solar cells with a textured semiconductor layer	94
5.6.3	Microcone textures on CIGS thin-film solar cells	98

6 Conclusion & Outlook	101
6.1 Nano-optics for ink infiltrated photonic crystal solar cells	101
6.2 Micro-optics for the front surface of solar modules	103
Appendix Refractive index data	107
Measured data	107
Literature data	108
References	111
List of related publications	125
Acknowledgments	127

List of Abbreviations

AM	Air mass
AOI	Angle of incidence
AOR	Angle of refraction
AR	Aspect ratio
ARC	Anti-reflection coating
AZO	Aluminum-doped zinc oxide
CI(G)S	Copper indium (gallium) diselenide
CNM	Center for Nano- and Molecular Science and Technology
CW	Continuous-wave
DiLL	Dip-in laser lithography
DLW	Direct laser writing
EMA	Effective medium approximation
EQE	External quantum efficiency
EY	Energy yield
FDTD	Finite difference time domain
FF	Fill factor
FWHM	Full width half maximum
IA	Inclination angle
IQE	Internal quantum efficiency
IMT	Institute of Microstructure Technology
NA	Numerical aperture
NIR	Near infrared
NOA88	Norland optical adhesives 88
NREL	National Renewable Energy Laboratory
OA	Opening angle
OPP	One-photon polymerization
PCE	Power conversion efficiency
PDMS	Polydimethylsiloxan
PECVD	Plasma enhanced chemical vapor deposition
PhC	Photonic crystal

List of Abbreviations

PV	Photovoltaics
SEM	Scanning electron microscope
TE	Transverse electric
TIR	Total internal reflection
TM	Transverse magnetic
TMM	Transfer matrix method
TPP	Two-photon polymerization
UV	Ultra-violet
ZSW	Zentrum für Sonnenenergie- und Wasserstoff-Forschung Baden-Württemberg
1D	One-dimensional
2D	Two-dimensional
3D	Three-dimensional

List of Symbols

Latin symbols

a	Lattice constant
A	Absorptance
\mathbf{B}	Magnetic induction (field vector)
c	Speed of light
d	Diameter
\mathbf{D}	Displacement field (field vector)
\mathbf{e}	Unit vector
E	Energy
\mathbf{E}	Electrical field (field vector)
F	Volume fraction
h	Height
\hbar	Reduced Planck constant
\mathbf{H}	Magnetic field (field vector)
i	Imaginary unit
I	Electrical current
\mathbf{J}	Electrical current density
k	Wavenumber
\mathbf{k}	Wavevector
\mathbf{K}	Reciprocal lattice vector
l	Layer thickness
\mathbf{M}	Transfer matrix
n	Refractive index
\mathbf{N}	Normal vector
N	Quantity
P	Power
\mathbf{P}	Propagation matrix
r_s, r_p	Amplitude reflection coefficients for s- and p-polarization

\mathbf{r}	3D position vector
R	Reflectivity / Reflectance
\mathbf{R}	Translation vector
t	Time
t_s, t_p	Amplitude transmission coefficients for s- and p-polarization
T	Transmissivity / Transmittance
\mathbf{u}	Periodic function
V	Electrical voltage
x, y, z	Spatial coordinates

Greek symbols

β	Longitudinal propagation constant
γ	Fitting parameter
Δ	Difference
ϵ	Permittivity
θ	Polar angle
κ	Extinction coefficient
λ	Wavelength
μ	Permeability
π	Archimedes' constant
ρ	Charge density
Φ	Photon flux density
ϕ	Azimuth angle
ω	Angular frequency
∇	Nabla operator

Summary

When it comes to the generation of electrical energy using photovoltaics (PV) on a large scale, cost is key. The employment of PV devices is only practical, if the cost per generate kWh of energy is low enough to compete with rival technologies. A key cost driver is the efficiency of the PV device in converting incident light to usable electrical energy. Light absorbed in a PV device generates free charge carriers that, when extracted, make a current flow. Surface texturing has long been known to increase the absorption of light in PV devices by reducing reflection losses at interfaces and by trapping light. As long as the texturing does not interfere with the charge carrier extraction process, an increase in light absorption directly leads to a stronger current and, in consequence, to an increased power conversion efficiency (PCE).

Micron-scale textures applied to the front surface of crystalline silicon wafers are in industry standard. Textures at all other interfaces and for all other PV technologies, are subject to ongoing research. This is especially true for the so-called thin-film technologies, making use of hundreds of nanometers thick semiconductor layers. Lately, the relative market share of thin-film PV has been steadily decreasing due to a significant reduction in crystalline silicon PV costs (in spite of the larger material demand). In research, on the other hand, thin-film PV has regained importance as new materials, such as nanocrystals and perovskites, promise high PCEs at low costs and the acquisition of new markets.

There is a vast number of ideas for employing textures in thin-film PV. Numerically, various complex texture designs have been explored with intriguing results in increasing the absorption of light in PV devices. In many cases, the realization of these textures was limited by the utilized fabrication techniques. In other examples, texturing was achieved, but the charge carrier extraction efficiency was reduced. Thus, it was not possible to transfer the increase in absorption of light to an increase in PCE. In this dissertation, the versatile technique of direct laser writing (DLW) was employed, to enable the realization of complex architectures. Additionally, texturing techniques were employed that do not interfere with the charge carrier extraction.

DLW is a lithography technique making use of a building block of submicrometer dimension, to construct arbitrary nano- to micro-meter scale architectures. In contrast, conventional optical lithography techniques, employing a mask, are much more restricted in the possible designs. Therefore, DLW is a perfect tool for the rapid prototyping and testing of textures for PV applications. Two types of DLW fabricated textures were explored in the following study.

The first type of texture was a periodic nano-texture, called a photonic crystal (PhC), molding the flow of light. In the study, a polymeric PhC pattern was fabricated using DLW. An integral part of the study was determining suitable DLW parameters, since nano-textures are at the resolution limit of DLW fabrication system. In a novel process, the fabricated polymeric PhC patterns were infiltrated with PV active CuInSe₂ (CIS) nanocrystals, dispersed in a solution. After solvent evaporation, the CIS nanocrystals perfectly embedded the PhC pattern. Using spectroscopic reflectance, transmittance, and absorptance measurements, it was possible to show that the patterning directed incident light to longer paths through the layer – increasing the absorption of light. Measurements of the current-voltage characteristics of a PhC infiltrated CIS nanocrystal device showed that the efficiency in charger extraction, compared to an untextured device, did not significantly decrease.

A further important part of the study was determining the optical material properties of the polymer (IP-Dip) and those of the CIS nanocrystals. It was found that (with a value of about 1.53 for visible wavelengths) the refractive index of IP-Dip, exposed using DLW, is about 0.01 lower than that of UV exposed IP-Dip. The CIS nanocrystals were found to have a refractive index of about 2.0. The determined complex refractive indices of the two materials were used in simulations for determine suitable parameters for the PhC. Based on simulations, the small refractive index step between IP-Dip and the CIS nanocrystals was identified as the major limiting factor in the scheme.

The second type of texture was a micro-texture targeting the reduction of reflectance at the air-glass interface in a solar module and the trapped light in the PV device. The investigated texture was implemented as an additional polymeric layer at the air interface, leaving the semiconductors in the solar cells unharmed. The study made full use of DLW as a tool for rapid prototyping of novel textures, while the application of the textures to PV devices was achieved by using a soft-imprinting technique. The key investigated parameter was the texture aspect ratio. Numerical studies had already indicated the importance of this parameter for the targeted texturing scheme. DLW allowed an experimental prove. In a systematic study the influence of the aspect ratio, of a conical texture, on reducing reflectance and the trapping of incident light was investigated numerically and experimentally.

Not only could an optimum aspect ratio of 0.73, for near normal incidence light, be determined for the microcone textures, but also significant enhancement of the performance of PV devices was shown. Using crystalline silicon based PV devices, the relevance of the investigated front surface textures for an established technology was demonstrated. Based on normal incidence external quantum efficiency (EQE) measurements, it was inferred that the microcone textures led to a relative enhancement in the short circuit current of 5.4%, compared to an untextured front surface. While only about 3% had been obtained using a conventional thin-film anti-reflection coating (ARC) on glass. The observed enhancement in EQE was most significant for large angles of incidence. Consequently, an even large relative increase of up to 9% was calculated in an energy yield analysis, taking into account real world conditions – compared to about 4% that have been obtained using a conventional ARC. Lastly, the microcone textures were applied to CuInGaSe₂ (CIGS) thin-film PV devices. A technology in which textures in general, and micron-scale textures especially, are uncommon. Using the microcone textures of aspect ratio 0.73 the PCE of one of the PV devices was increased from 20.2% to 20.9%. Furthermore, the microcone textures clearly outperformed a conventional MgF₂ thin-film ARC in terms of reducing reflectance and increasing current generation – especially for large angles of incidence.

1 General introduction

1.1 Photovoltaics

Electrical energy providing light, heat, and mobility, as well as power to all kinds of electrical devices has become a key component to human life on earth. The generation of electrical power is typically achieved in a long conversion chain; for example by burning a fuel to boil water and using the steam to turn a turbine powering an electrical generator. Photovoltaics (PV) is different. In PV the electromagnetic radiation from the sun is directly used to generate electrical power. This brings various advantages. PV allows decentralization of electricity generation. And unlike fossil based fuels that are available in a limited quantity on human time scales, PV is renewable and in general cleaner, as no air pollutants are released during operation.

From the first discovery of the photovoltaic effect in 1839 by Alexandre-Edmond Becquerel [1], it has taken more than 100 years for solar cells (the PV power sources) to be commercialized by Bell Laboratories in 1954 [2]. These first PV devices had low power conversion efficiencies of about 6%. In combination with high costs they only had a single application: space. Since then the attractiveness of PV has always been linked to the oil price. While PV has had some niche applications, such as powering a calculator, and was subject to government funding (due to the advantages stated above), economically PV power plants only make sense if they can compete with other centralized electricity sources. Now this time has come. In recent years, an increasing world production has lowered the solar power price, reaching values as low as 0.0234 \$/kW [3] - rivaling that of all other sources. With PV prices still falling the rise of PV to becoming the dominant electricity source on the planet is ahead. In the light of global warming PV promises a more sustainable future.

1.1.1 Solar cell materials

The energy conversion in solar cells is based on several steps. First, incident light is absorbed, generating pairs of positive (holes) and negative (electrons) charge carriers. Secondly, these two types of charge carriers are separated and extracted on opposite ends to an external circuit. Semiconductors are utilized to absorb the incident light for the generation of charge carrier pairs. The band gap of the semiconductor, and its relation to the photon energy of the incident light, determines which part of the incident spectrum is absorbed by the solar cell. An important quantity, in this regard, is the dispersive extinction coefficient of the utilized semiconductor material: The smaller the extinction coefficient, the larger the penetration depth. Consequently, a thicker semiconductor layer is necessary for an efficient absorption of the incident light. While the absorption of light is key to the solar cell power conversion efficiency (PCE) on the optical side, the charge carrier conductivity in the solar cell is key on the electrical side. An important quantity, in this regard, is the charge carrier diffusion length, determining the mean distance the charge carriers travel before recombining. The place in which charge carrier pairs are generated should be within the diffusion length of the place in which they are extracted from the solar cell. This limits the thickness of the semiconductor layer. In semiconductor materials, appropriate for use in a solar cell, the diffusion length of the charge carriers must be long compared to penetration depth of light.

1 General introduction

With a market share above 90% the global market is currently dominated by mono-crystalline silicon (c-Si) and multi-crystalline (mc-Si) based solar cells. Silicon has many desirable properties for PV applications. It is stable, non-toxic, and abundant. Furthermore, rapid increases in material purity have been achieved due to simultaneous developments in the computing industry. To date, the highest PCE achieved in a c-Si solar cell under standard illumination conditions are 26.7% [4], very close to the theoretical limit of ~29% [5,6]. This high efficiency plus the, nowadays, extremely low cost of the abundant material silicon are the reason for the great success of silicon solar cells.

Compared to all other semiconductors used in PV, crystalline silicon possesses a long penetration depth for large parts of the incident solar spectrum. This circumstance is completely compensated for by the high purity of silicon leading to long diffusion lengths. As a consequence, crystalline silicon solar cells make use of a hundreds of micrometers thick silicon layers, accounting for as much as 50% of the production costs. Due to shorter penetration depth, as well as shorter diffusion lengths, all other solar cells technologies make use of hundreds of nanometers thick layers [7]. For comparison the most recent laboratory record efficiencies (in converting incident radiant power from the sun to usable electrical power) for various solar cell technologies are shown in **Table 1**. The data was extracted from the best research-cell efficiency chart by the National Renewable Energy Laboratory (NREL) [8]. For an estimation of the research effort, put forth to achieve this record, the year of the first listing in chart is presented as well.

Technology	Year of first record in NREL chart	Recent record efficiency
III-V (tandem)	1983	39.2%
III-V (non-tandem)	1977	29.1%
c-Si	1977	26.1%
mc-Si	1984	22.3%
a-Si	1976	14.0%
CIGS	1976	22.9%
CdTd	1976	22.1%
Organic	2001	15.6%
Perovskite	2013	24.2%
Nanocrystal	2010	16.6%

Table 1. Year of first record and current laboratory record efficiency under standard testing conditions for various solar cell types. Data extracted from the best research-cell efficiency chart (1976-present) by the National Renewable Energy Laboratory (NREL) [8].

The highest PCE are achieved with so called III-V semiconductor solar cells - composed of elements from the third and fifth main-group. Tandem solar cells, employing multiple layers of different material compositions (and band gaps) enable a more efficient use of the solar spectrum. III-V semiconductor solar cells are epitaxially grown. In a time consuming process crystal layers are deposited on a substrate in vacuum at high temperatures, leading to large costs and a reduced industrial scalability. Therefore, III-V semiconductor solar cells are less suitable for large area applications, but play an important role for applications in which efficiency is key. Examples are systems that concentrate solar light.

The most direct rivals to the crystalline silicon technologies in PV have been the materials copper indium (gallium) diselenide / disulfide ($\text{CuIn}(\text{Ga})(\text{Se}_2/\text{S}_2)$), or short CIGS, and cadmium telluride (CdTe) both targeting very similar applications. Compared to silicon solar cells these thin-film solar cells need less active materials, leading to shorter energy amortization rates and less greenhouse gas emission [9]. Disadvantages include the usage of less abundant, partially toxic materials, and shorter system life times. In general, the superior market share of crystalline silicon is asserted to a much greater research effort and related material costs - not to technological inadequacies.

The low cost of crystalline silicon wafers is a major restraint to the success of thin-film PV technologies. Lower material costs have been the major selling point for thin-film technologies of low PCE, such as, amorphous silicon (a-Si). In the current market their application is limited to systems in which the PCE is of minor importance, such as pocket calculators.

When it comes to further reducing costs and finding new applications solution processing is a key topic. While III-V semiconductor, CIGS and CdTe layer deposition conventionally involve vacuum-processing and high-temperatures, solution processing is inherently a high-throughput room-temperature technology. Various kinds of organic solar cells have been the first in this field. To date, they suffer from low efficiencies [10] and material degradation [11]. Nevertheless, they have opened the route for exploring new types of PV markets, for example flexible substrates or building integration where partial transparency is important. Emerging technologies in these areas are nanocrystals (also called quantum dots) and perovskites. Perovskites are currently the shooting star in PV technologies, with a PCE of 20.9% [12] having been achieved within less than 10 years after their first reporting in PV [13]. However, also in the case of perovskites, the key challenge is material degradation under ambient conditions [14]. Nanocrystals are chemically synthesized small inorganic colloidal particles that are dispersed in a solvent to form a solution processable ink [15]. Ligand molecules are typically necessary to dissolve the molecular precursors in a solvent. The solution is directly used to produce uniform films of the desired stoichiometry. Amongst others, solar cells have been produced from CdTe nanocrystals [16], CIGS nanocrystals [17], and emerging material systems such as AlBiS₂ nanocrystals [18]. For demonstrating the results in this dissertation, CuInSe₂ (CIS) nanocrystals are made use of, alongside conventionally produced c-Si and CIGS solar cells.

1.1.2 Light management in photovoltaics

In common to all of the above described technologies is a desire for thinner solar cells. A thinner semiconductor layer helps in the extraction of charge carriers and in reducing material costs. However, with the film thickness the absorption of light reduces as well, directly reducing the PCE. Therefore, an important research topic is decreasing optical losses in solar cells while maintaining thin layers.

The term 'light management' summarizes all the different efforts for reducing optical losses in solar cells, not only the once related to the solar cell thickness. Further optical loss mechanisms are the reflection of light at material interfaces, as well as on metallic contacts, and the so-called parasitic absorption of light without charge carrier generation occurring in all materials. Light management efforts range from the reduction interface reflectivity, over light-trapping schemes for increasing the path length of light through the solar cell, to implementing photon energy conversion processes. Light-trapping and the reduction of interface reflectivity are also called 'anti-reflection' schemes. There are many different possibilities for achieving anti-reflection [19]. One of the simplest and most commonly applied is a single layer thin-film anti-reflection coating (ARC). The interference based working principle enables the complete annihilation of interface reflectivity in a certain wavelength range.

A versatile approach for achieving anti-reflection is texturing an interface. Three types of textures are distinguished in relation to the texture dimensions and the wavelength of the incident light (compare **Figure 1**):

Nano-scale textures, with lateral features much smaller than the wavelength of the incident light, let optical interface disappear completely when the depth of the texture is significantly larger than the

wavelength (**Figure 1(A)**). These textures form a graded-index surface greatly reducing reflectivity [20]. A prominent example is the so-called moth-eye texture [21,22], named after the animal on which they were found. Further examples that make use of a graded-index surface are black silicon [23,24] and porous materials [25,26].

Meso-scale textures, with feature sizes on the order of the wavelength of light not only reduce the reflectivity, they also scatter light [27] (**Figure 1(B)**). Depending on the wavelength (and the feature size), the above mentioned textures (moth-eye and black silicon) are also attributed to this category. In general, random textures lead to diffuse scattering of light [28], while periodically arranged textures, termed ‘nanophotonics’, mold the flow of light in specific spectral regions [29]. Nanophotonics include so-called photonic crystals (PhCs) [30] and plasmonic structures [31,32]. Plasmonic structures incorporate metallic textures enabling unparalleled strong interactions with light, but also introducing new types of loss mechanisms. PhCs, on the other hand, are periodic variation of dielectric materials. Simple one-dimensional (1D) grating textures [33] have long been implemented in solar cell, while complex 3D architectures [34] showing large gains have mostly been covered theoretically. A special class of nanophotonic architectures worth mentioning are nanowires [35].

Micron-scale textures with feature sizes much larger than the wavelength of light allow a broadband (wavelength independent) manipulation of light (**Figure 1(C)**). Next to reducing interface reflectivity, micron-scale textures trap light in optically dens media [36]. Naturally, micro-scale textures have mostly been applied to micro-meter thick solar cells (c-Si and mc-Si). Especially for the case of c-Si micro-scale textures have become an industry standard, due to the possibility of achieving such a texture using a low-cost, large-area wet-etching technique [37].

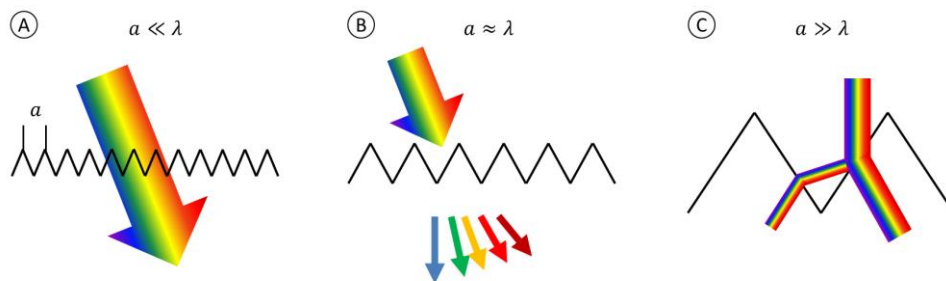


Figure 1. Illustration of the three size regimes for textures: **(A)** nano-scale, **(B)** meso-scale, and **(C)** micron-scale and their interaction with light of different wavelength (λ).

When employing textures in a solar cell avoiding additional losses is an important consideration. While almost any texture will enhance the optical performance of a solar cell, they are often invasive to the charge carrier transportation. Textures increase the surface area, introducing impurities and affecting the layer deposition process. When directly texturing the semiconductor in a solar cell often special care must be taken with layer passivation [38]. The efficient application of textures to interfaces other than a c-Si surface is subject to ongoing research.

1.1.3 Micro- and nano-texture fabrication techniques

As vast as the number of texturing schemes is the number of fabrication techniques for producing them [39,40]. Texturing techniques in PV applications are either based on removing, adding or forming material:

Techniques for removing material. The removal of material to achieve texturing in PV is most common. Rather crude mechanical methods for removing material are milling [41] (periodic textures) and sandblasting [42] (random textures). More typically, wet- and dry- etching techniques are used to obtain a precise micro- to nano- scale pattern. In wet-etching a chemical solution is used to pattern a surface. The etching is either isotropic [43], with the same etching speed in all directions, or anisotropic [44] where specific (crystal lattice) directions are preferred. While a mask is necessary to generate a pattern using isotropic etching, anisotropic etching allows maskless texture generation. Dry-etching makes use of a plasma [45] or of an ion beam [46,47] to physically and/or chemically pattern a substrate. Furthermore, it is possible to remove material to form a pattern in electrochemical processes, for example when anodizing aluminum [48].

Techniques for adding material. The addition of material to obtain a texture for PV applications is either done physically or chemically. In physical vapor deposition (PVD) materials are evaporated and deposited on a sample in vacuum. A mask is employed to deposit materials in the desired positions [49]. In the case of chemical vapor deposition the deposition is made possible by a chemical reaction. Either masks or catalyst are used to grow a pattern [50]. Further techniques of patterning by addition are ink-jet printing [51], dip-pen lithography [52], making use of self-assembly [53], or the use of pre-textured substrates [54].

Techniques for forming material. Forming in PV applications is achieved using imprinting - employing hard or soft stamps. In the case of organic solar cells imprinting has directly been used to pattern the organic semiconductor layers [55]. In case of inorganic semiconductor based solar cells resins are employed for transferring a pattern. Pressure is used to transfer the pattern from a stamp into the viscous resin. While still applying the pressure the resin is polymerized either using heat- or optical-curing. The solid resin is then either directly applied to a solar cell [56] (an additional layer enabling light management) or it is used as a mask to transfer the pattern into the solar cell semiconductor layer using the above described removal techniques [57].

In this dissertation, resins are made use of to fabricate textures that are either directly applied to the solar cell semiconductor or imprinted into an additional layer on top of the solar cell stack. In general, the polymerization of a resin is ideal for achieving texturing. The most common technique for fabricating a polymeric texture is lithography. In lithography, first a resin gets exposed in the desired pattern. During development either the exposed (positive-tone) or the unexposed (negative-tone) resin is removed. Masking lithography techniques, such as photolithography [58] and interference lithography [59], allow large-area exposure in an instance. Alternatively, direct lithography techniques are maskless and allow rapid prototyping of patterns by sequential exposure. The most common direct lithography technique is electron beam (e-beam) lithography. It is typically used to produce the masks for photolithography. An interesting alternative to e-beam lithography is laser lithography. In general, laser lithography has a lower resolution than e-beam lithography, but it does not require a vacuum, enables higher fabrication speeds, and a more precise control of the exposure does in a certain spatial region. These aspects make laser lithography a perfect candidate for the fabrication of novel architectures.

Along these lines, laser lithography, in the form of sterolithography [60], has been one of the first technologies enabling the design and fabrication of three-dimensional (3D) microarchitectures.

With 3D manufacturing the shape complexity is greatly increased and with it the number of possible schemes for texturing PV devices to enhance the utilization of incident light. The most recent step towards rapid prototyping of 3D textures has been the utilization of multi-photon processes. Multi-photon laser fabrication techniques are also called direct laser writing (DLW). Using DLW it is possible to directly fabricate programmed free-form 3D microarchitectures at high precision [61]. DLW is a highly useful tool for fabricating novel architectures on a small scale. In this dissertation, the possibilities of DLW are explored to fabricate nano- to micron-scale textures for PV applications. The DLW system (employed for this dissertation) makes use of two-photon processes occurring in the focal spot of a laser beam focused into a photoresist. Polymerization only takes place in a sub-micrometer region, called a voxel. This voxel serves as the building block to produce microscopic textures at high precision.

1.2 Content of this dissertation

In the following, the DLW fabrication of two very different types of textures and their use in PV applications is explored. On the one hand, nano-patterning is examined. DLW enables the fabrication of arbitrary PhC architectures by point exposure without the need for precise control of the photoresist layer thickness. A novel infiltration technique is introduced, making use of the new possibilities arising from solution processable PV, to pattern a CIS nanocrystal solar cell with a PhC. On the other hand, micro-patterning is used for fabricating free-form surfaces applicable as additional layers to solar cells. The use of DLW as a rapid prototyping method is demonstrated. The micro-textures are applied to silicon and CIGS based solar cells using a scalable imprinting technique.

Chapter 2 focuses on the fundamental physics needed for understanding the working principle of the employed textures and the used analyzation techniques. First, a basic description of the working principle of solar cells is presented, alongside a more detailed discussion of loss mechanisms and the resulting PCE. Secondly, the theories and mechanisms behind light-matter interaction at interfaces are explored building on the electrodynamics of light. The most important mechanisms related to PhCs are thin-film guided modes and the diffraction of light. The most important mechanisms related to the micron-scale textures are the laws of reflection and refraction at planar interfaces.

Chapter 3 discusses fabrication and analyzation tools. A large focus is placed on the utilized DLW technique and special considerations that had to be made to produce the PhC lattice with dimension close to the resolution limit of the employed system. Further fabrication techniques, such as the CIS nanocrystal layer deposition and the micro-texture imprinting, are discussed in their respective results chapter. Analyzation tools were utilized to determine optical device properties, such as reflectance and absorptance, optical material properties, such as the refractive index, and electrical device properties, such as the voltage and the current the solar cells generate. Lastly, utilized numerical tools are described that were employed to optimize the texture design and understand internal optical processes.

Chapter 4 focuses on the fabrication procedure and characterization results of the PhC patterns. First, the relating literature and working principle are reviewed in more detail. Bases on measured the material properties a detailed investigation for a square lattice on glass is performed, both numerically and experimentally. In this investigation several research questions are answered: Is a PhC lattice formed? What are the optimum lattice parameters? What is the impact of the nanocrystal infiltration on

the PhC lattice? How much performance improvement is expected in a solar cell? Lastly, the current-voltage characteristics of functional solar cells are presented. Answering the question of the impact of the PhC lattice on the solar cell performance.

Chapter 5 presents the results from the work with the fabricated micro-textures, applied as additional polymeric layers on top of solar cells. Likewise, the study is first brought into context to related literature and the working principle is explained in more detail. Unlike the DLW produced PhC patterns the microcone textures were not directly applied to semiconductor layer. They were prototyped and duplicated in a scalable imprinting process - that is explained in detail. Making use of the flexibility of DLW, the chapter investigates the impact of varying the texture aspect ratio on the light harvesting performance of solar cell in an unprecedented experimental study. Important research questions are: How do simulation results relate to experimentally obtained results? What is the impact of the aspect ratio on reducing interface reflectivity and on the light-trapping? How much of the light reflected from an untextured device is retained? How does the scattering of light at a solar cell surface relate to the light-trapping introduced by the textures? Furthermore, the performance enhancement of the textures was set into context to the state-of-the-art: Is it possible to increase the performance of modern solar cells showing little reflectance? How do the produced textures compare the conventional ARCs?

Chapter 6 summarizes the results of chapters 4 and 5 and gives an outlook on future research based on the results of this dissertation. Possibilities for further increasing the enhancement provided by the textures are discussed. Furthermore, the materials used in this dissertation are very suitable for a proof-of-concept, but not ideal for many applications. Ideas for materials in line with the target applications are outlined.

2 Fundamentals

In the following, the theoretical background is presented for understanding the results in chapters 4 and 5. Firstly, the basics of the working principle of a solar cell are explained, important solar cell parameters are introduced, and loss mechanisms are discussed. The discussion is based on textbook photovoltaics that are for example found in: (Goetzberger and Hoffmann, 2005) [62] and (Mertens, 2018) [63]. Secondly, light-matter interaction is discussed, focusing on the effect a textured interface has on the flow of light. The sections will set the basic foundation for understanding the propagation and interactions of light in dielectric media. The basic formalisms and equations of electrodynamics are included, largely based on: (Fliessbach, 2012) [64], (Klingshirn, 2005) [65] and (Saleh and Teich, 2007) [66]. The propagation of a mode confined in space is discussed based on (Adams, 1981) [67] and (Marcuse, 1991) [68]. Details on photonics crystals and how they give rise to optical phenomena such as optical band gaps and the diffraction of light are for example found in: (McGurn, 2018) [69], (Joannopoulos et al., 2008) [70] and (Angelini, 2017) [71]. More models and details for the effective medium approximation are found in: (Stenzel, 2016) [72].

2.1 Photovoltaics

2.1.1 Solar cell working principle

Solar cells are the basic power units in photovoltaics (PV). In a solar cell incident radiant energy from the sun is converted to usable electrical power. In the first step of this energy conversion process the incident radiant energy from the sun is absorbed and transferred to chemical energy by raising an electron to an excited state. Different energetic states are part of the dispersive band structure of a dielectric solid arising from the periodic discretized potential of the atoms forming the solid. Although there are large continua of possible electron energies in solids, the so called ‘bands’, some energy states are completely forbidden, the so called ‘gaps’. In semiconductors (and in isolators) the Fermi energy (E_F), the chemical potential that needs to be overcome to extract an electron, lies inside such a gap - called the band gap. The band below the band gap is called the valence band; at absolute zero it is completely filled with bound electrons. The band above the band gap is called the conduction band; an electron raised to the conduction band is no longer bound and moves through the solid. The conduction band and the valence band are separated by the band gap energy (E_G). The bands and the Fermi energy are illustrated in **Figure 2**.

To raise an electron from the valence band to the conduction band the photon energy (E_ν) must be larger than band gap energy. The photon energy is given by:

$$E_\nu = \frac{2\pi\hbar c}{\lambda}, \quad (2.1)$$

where \hbar is the reduced Planck constant, c is the speed of light, and λ is the wavelength of light. To efficiently make use of the solar spectrum semiconductors are needed, possessing a band gap of energy related to visible or to near infrared (NIR) wavelengths. When an electron is raised from the valence

band to the conduction band, a 'hole' is left behind. Similarly to electrons in the conduction band, holes move freely in the valence band.

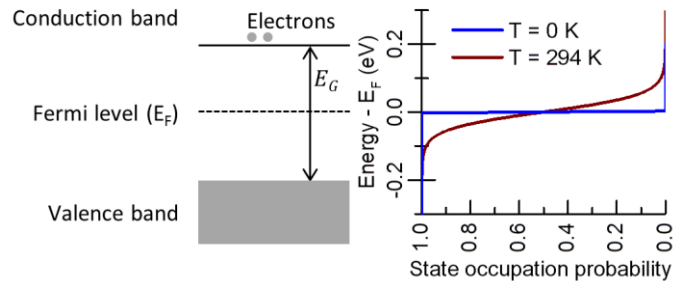


Figure 2. Illustration of the band model in a semiconductor. At absolute zero the valence band is completely filled with electrons and the conduction bands is completely empty. At room temperature, there is finite probability for electrons to occupy the conduction band.

In the second step, of the energy conversion process in a solar cell, the electrons and holes, in their respective bands, have to be spatially separated. The spatial separation is needed to prevent recombination, accumulate a voltage and enable a current to flow. As electrons and holes hold opposite charges no current flows when both are extracted in the same location. To enable the separation selective contacts are needed [73]. The material at the 'electron contact' needs to show an electron conductivity larger than the hole conductivity and, conversely, the material at 'hole contact' needs to show a larger hole conductivity. The most commonly used materials for achieving this selective conductivity are n-type and p-type semiconductors. In n-type semiconductors the Fermi energy lies close to the conduction band, leading to a filling of the conduction band with electrons (resulting in a large electron conductivity), while the concentration of holes in the valence band is low. In p-type semiconductors the Fermi energy lies close to the valence band, leading to a filling of the valence band with holes (resulting in a large hole conductivity). Intrinsic semiconductors are made n-type or p-type by means of doping. In doping electron donor or acceptor atoms are implemented into the intrinsic bulk.

A p-n junction forms when an n-type and a p-type selective contact are brought in contact. The concentration gradient driven exchange of electrons and holes leads to the formation of an internal electrical field. When the solar cell is not illuminated the diffusion currents, originating from the charge carrier concentration gradient, and the drift currents, originating from the internal electrical field, are equal (as illustrated in **Figure 3(A)**). The electrochemical potential is constant across the junction and the Fermi energies equalize. The situation changes when illuminating the p-n junction (**Figure 3(B)**). Electron-hole pairs are generated throughout the layer. To account for the equally increased concentration of charge carriers the Fermi level needs to be separated into a quasi-Fermi level for electron ($E_{F,e}$) and a quasi-Fermi level for holes ($E_{F,h}$). As a result of the large electron (hole) conductivity the extraction of electrons (holes) from the n-type (p-type) semiconductor is highly efficient. The extraction of charge carriers at either end gives rise to a slight gradient in the electrochemical potential for the two charge carriers. The gradient in the electrochemical potential is the driving force for electrons and holes across the p-n- junction. The average distance a charge carrier travels before recombining is called the diffusion length. The diffusion length is important for determining the maximum thickness of a solar cell.

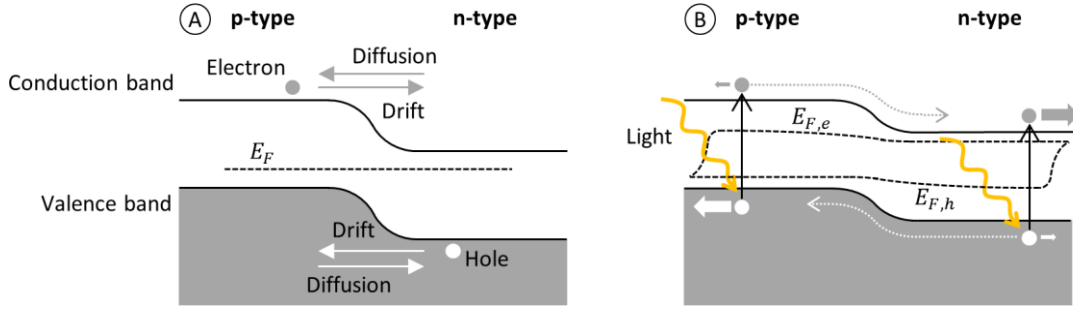


Figure 3. Illustration of a p-n junction in a solar cell in the dark (A) and under illumination (B).

2.1.2 Solar cell parameters

Solar cells are characterized by their electrical parameters. When a solar cell is illuminated, the Fermi level splits into a quasi-Fermi level for electrons and one for holes. The difference between the quasi-Fermi levels at either contact of the solar cell is equal to the outside measurable voltage multiplied with the elementary charge. The measured voltage with an infinitely high load connected to the solar cell is called the open circuit voltage (V_{OC}). The maximum load free current, on the other hand, is called the short circuit current (I_{SC}). Normalizing the I_{SC} to the solar cell area results in the short circuit current density (J_{SC}). The J_{SC} is directly related to the incident photon flux density Φ .

$$J_{SC} = e \int \Phi(\lambda)EQE(\lambda) d\lambda, \quad (2.2)$$

where e is the elementary charge and EQE is the external quantum efficiency. The EQE relates the number of incident photons to the number of electron-hole pairs collected. It depends upon the photon absorption efficiency and electrical losses in the solar cell.

The most important characteristic of a solar cell is its current (I) to voltage (V) relationship. A diode model of the solar cell allows the extraction of several solar cell parameters from the I - V characteristics. The simple one-diode model of a solar cell is shown in **Figure 4(A)**. The I - V characteristics in this model is given by

$$I = I_{SC} - I_D - \frac{V - R_S I}{R_P}, \quad (2.3)$$

where I_D is the current through the diode representing the p-n junction, R_S are series resistances and R_P are parallel resistance in the solar cell. Furthermore, the maximum extractable power from the solar cell is determined from the I - V characteristics. The power extraction is maximized when the factor $I \cdot V$ is maximized. This is called the maximum power point (MPP) and the current and voltage at this point are I_{MPP} and V_{MPP} , respectively. For simplification the fill factor (FF) was introduced relating the I_{SC} and the V_{OC} to the maximum power (P_{out}) extracted from the solar cell ($P_{out} = I_{MPP} V_{MPP} = I_{SC} V_{OC} FF$). An exemplary I - V characteristics is shown in **Figure 4(B)**. Finally, the power conversion efficiency (PCE) of a solar cell gives the ratio of extracted power to the incident radiant power (P_{in}).

$$PCE = \frac{P_{out}}{P_{in}} = \frac{I_{SC} V_{OC} FF}{P_{in}} \quad (2.4)$$

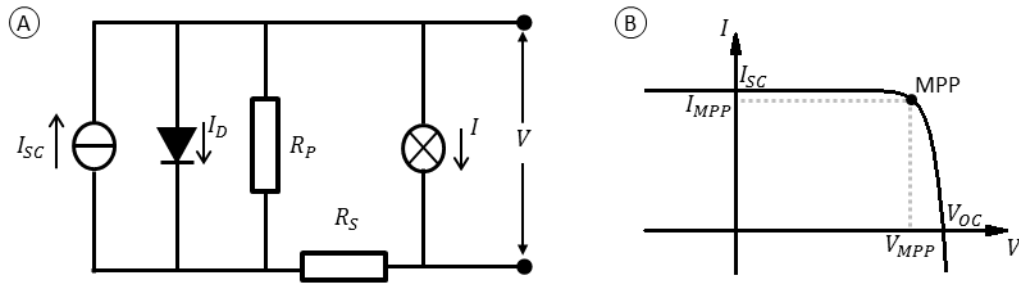


Figure 4. (A) One-diode model of a solar cell. (B) I - V -curve showing the short circuit current (I_{SC}), the open circuit voltage (V_{OC}) as well as the current (I_{MPP}) and the voltage (V_{MPP}) at the maximum power point (MPP).

2.1.3 Solar cell efficiency

The efficiency of a solar cell, depends on the efficiency of the energy conversion process and on the incident radiant power and spectrum. Under standard testing conditions a solar cell is illuminated with the so called AM1.5g spectrum (Figure 5) at 1000 W/m^2 from normal incidence. AM stands for ‘air mass’, the spectrum resembles the spectrum of the sun after having passed through 1.5 times earth’s atmosphere g stands for ‘global’ and means the light scattered by the atmosphere is taken into account. Real world illumination conditions can vary drastically from this standard condition. The energy yield (EY) of a solar module in an application is given by:

$$EY = PCE \cdot PR \cdot \bar{P}_{in}, \quad (2.5)$$

where PR is the performance ratio relating the actual achieved efficiency to the PCE, and \bar{P}_{in} is the annual average solar radiation power at the location of the solar module.

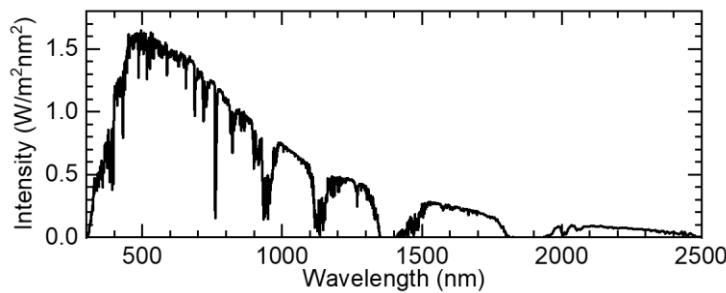


Figure 5. Air Mass 1.5 global tilt (AM1.5g) spectrum [74].

The PCE of a solar cell is determined by various loss mechanisms. Inevitable loss mechanisms in a single-junction solar cell are spectral losses, related to the wavelength and the band gap, and thermodynamic losses. Spectral losses include: photons of energy below the band gap do not raise an electron from the valence band to the conduction band, as well as the thermalization of so called ‘hot electrons’, excited by photons of energy much higher than the band gap. Thermodynamic losses include: radiative recombination, as well as a V_{OC} smaller than the band gap energy. All of these losses are part of the detailed balance limit [75], giving an upper limit for the PCE of a single junction solar cell under solar irradiation on the order of 30%. In a real solar cell further electrical and optical loss mechanisms exist. On the electrical side, ohmic and non-radiative recombination losses are distinguished, occurring

at the contacts, at material interfaces, surfaces, and material impurities. The diode model of a solar cell, described above, introduces electrical losses as series and shunt resistances. Optical losses originate from reflection at interfaces and a large penetration depth. The textures presented in chapter 4 and chapter 5 target the reduction of optical losses. For understanding the working principle of the textures we first have to take look at the propagation of light in media and at interfaces.

2.2 Light - matter interaction

2.2.1 Basic formalisms of electrodynamics

Light is an electromagnetic wave [76]. The classical laws that govern the propagation of an electromagnetic wave are known as **Maxwell's equations**. They describe the evolution of a pair of vector fields, the electrical field ($\mathbf{E}(\mathbf{r}, t)$) and the magnetic field ($\mathbf{H}(\mathbf{r}, t)$), in time (t) and space ($\mathbf{r}(x, y, z)$). On a microscopic scale these fields interact with charged particles and their induced currents. In the following formulism the Maxwell's equations represent a macroscopic averaging over the microscopic world. Bound charges and currents, as well as free charges and currents are distinguished. Bound charges and currents are included as a material property by introducing the displacement field $\mathbf{D}(\mathbf{r}, t)$ and the magnetic induction $\mathbf{B}(\mathbf{r}, t)$. The Maxwell's equations are:

$$\nabla \cdot \mathbf{D} = \rho, \quad (2.6)$$

$$\nabla \cdot \mathbf{B} = 0, \quad (2.7)$$

$$\nabla \times \mathbf{E} = -\frac{\partial \mathbf{B}}{\partial t}, \quad (2.8)$$

$$\nabla \times \mathbf{H} = \mathbf{J} + \frac{\partial \mathbf{D}}{\partial t}. \quad (2.9)$$

The free charge density (ρ) and the free current density (\mathbf{J}) are included for completeness, in the following the propagation of light in the absence of free charges and currents is discussed. Furthermore, only isotropic materials with a linear field response are discussed in detail. In this case, the constitutive relationships between the fields are:

$$\mathbf{D} = \epsilon_0 \epsilon \mathbf{E}, \quad (2.10)$$

$$\mathbf{B} = \mu_0 \mu \mathbf{H}. \quad (2.11)$$

The vacuum permittivity (ϵ_0) and the vacuum permeability (μ_0) are physical constants, while the dielectric constant (ϵ) and the relative permeability (μ) are material properties. For the materials discussed in this work it is reasonable to assume $\mu \approx 1$. Furthermore, in optics, it is common to make use of the complex refractive index (\bar{n}), instead of the dielectric constant, it is:

$$\bar{n} = \sqrt{\epsilon} = n + i\kappa. \quad (2.12)$$

Conventionally, the real part (n) of the complex refractive index is termed the refractive index, while the imaginary part (κ) is termed the extinction coefficient. The extinction coefficient leads to an attenuation

of an electromagnetic wave. In a homogenous medium this attenuation is described by the **Beer-Lambert law**

$$P = P_0 e^{-\frac{2\kappa\omega}{c}x}. \quad (2.13)$$

A wave with initial power P_0 (proportional to the square of the initial electrical field amplitude) and of angular wave frequency ω is attenuated to the power P when propagating at the speed c over a distance of x . The light is absorbed. The measurable for the absorption of radiant flux in a sample is the absorptance (A). It is: $A = 1 - P/P_0$. The penetration depth is equal to: $c/2\kappa\omega$.

Assuming an isotropic medium without free charges and free currents, and with a linear field response, Maxwell's equations simplify to **Helmholtz equations**:

$$c^2 \nabla^2 \mathbf{E} - \frac{\partial^2 \mathbf{E}}{\partial t^2} = 0, \quad (2.14)$$

$$c^2 \nabla^2 \mathbf{H} - \frac{\partial^2 \mathbf{H}}{\partial t^2} = 0, \quad (2.15)$$

where $c = 1/\sqrt{\mu_0 \mu \epsilon_0 \epsilon}$ is the speed of light in the respective medium. The simplest solutions to these Helmholtz equations is a superposition of **plane waves** of the form

$$\mathbf{E} = \mathbf{E}_0 e^{-i\omega t} e^{i\mathbf{k}r}, \quad (2.16)$$

$$\mathbf{H} = \mathbf{H}_0 e^{-i\omega t} e^{i\mathbf{k}r}, \quad (2.17)$$

where \mathbf{E}_0 and \mathbf{H}_0 are the amplitude of the respective field and \mathbf{k} is the wavevector. The angular frequency and the wavevector are related by the **dispersion relation**:

$$\omega = c_0 |\mathbf{k}| = c_0 k = c_0 k_0 n = \frac{2\pi c_0 n}{\lambda_0}, \quad (2.18)$$

where c_0 is the free space speed of light, k_0 is the free space wavenumber, and λ_0 is the free space wavelength. In the following, the free space wavelength will simply be referred to as the wavelength (λ).

The direction of the electric field in relation to the propagation direction is called the **polarization** of light. In isotropic dielectric media electromagnetic waves propagate as transverse waves with the electric field and the magnetic field oscillating perpendicular to the propagation direction ($\mathbf{k} \perp \mathbf{E} \perp \mathbf{H}$).

2.2.2 Light at a planar interface

In dielectric media only spatial variations of the refractive index influence the propagation direction of light. The simplest form of a refractive index change is a planar interface between two media of refractive index n_i and n_t . The influence of such an interface on the propagation of light is derived from Maxwell's equations. The use of boundary conditions known as the laws of Gauß and of Stokes results in the conclusion that vector components parallel (\parallel) to the interface must be continuous and vector components perpendicular (\perp) to the interface follow the material dispersion (**Figure 6(A)**). Therefore, the wavenumber (k_i) of a wave incident on the interface from medium n_i relates to the wavenumber (k_{out}) of an out-going wave by:

$$k_{i,\parallel} = k_{out,\parallel}, \quad (2.19)$$

$$k_{i,\perp} = \frac{n_{out}}{n_i} k_{out,\perp}. \quad (2.20)$$

In case of reflection (out-going medium: n_i) the absolute of the wavevector remains constant, in case of transmission (out-going medium: n_t) the absolute of the wavevector changes. Considering the angle θ_i between the interface normal and the incidence wavevector and the angle θ_{out} between the interface normal and the out-going wavevector Equation (2.20) results in **Snell's Law** :

$$n_i \sin \theta_i = n_{out} \sin \theta_{out}. \quad (2.21)$$

The reflection angle is equal to the incidence angle ($\theta_i = \theta_r$). In case of transmission, the wavefront changes direction ($\theta_i \neq \theta_t$). This is called **refraction**.

Since only vector components parallel to the interface are conserved, the polarization of light influences the reflection and transmission process. When light is incident upon an interface we define a plane spanned by the wavevector of the incident light (\mathbf{k}_i) and the interface normal. For such a wave Equation (2.16) is rewritten as a superposition of electric field components parallel (p) and perpendicular (s) to the defined plane (**Figure 6(B)**):

$$\mathbf{E} = (\mathbf{E}_p + \mathbf{E}_s)e^{i(kr - \omega t)}. \quad (2.22)$$

The **Fresnel equations** give the amplitude reflection (r) and transmission (t) coefficients, dependent on the polarization (p or s).

$$r_p = \frac{n_t \cos \theta_i - n_i \cos \theta_t}{n_t \cos \theta_i + n_i \cos \theta_t}, \quad r_s = \frac{n_i \cos \theta_i - n_t \cos \theta_t}{n_i \cos \theta_i + n_t \cos \theta_t} \quad (2.23)$$

$$t_p = \frac{2n_i \cos \theta_i}{n_t \cos \theta_i + n_i \cos \theta_t}, \quad t_s = \frac{2n_i \cos \theta_i}{n_i \cos \theta_i + n_t \cos \theta_t} \quad (2.24)$$

The two amplitude coefficients relate the amplitude of the incident wave to the amplitudes of the reflected and of the transmitted wave, respectively. In measurements not the field amplitudes, but the reflected and the transmitted power are determined. The amplitude coefficients are relate to the reflectivity (R) and the transmissivity (T) of an interface via:

$$R = |r|^2 \quad (2.25)$$

and

$$T = \frac{n_t}{n_i} |t|^2. \quad (2.26)$$

It is to be noted that it is in general not possible to measure the reflectivity and the transmissivity of an interface directly. Samples are of finite thickness and therefore include multiple interfaces. Light reflected back and forth between these interfaces influence the measurement. In the following sections the reflectance (R) and the transmittance (T) will be more important than the reflectivity and the transmissivity. The reflectance and the transmittance are the fraction of reflected and transmitted radiant flux by a layer stack, respectively.

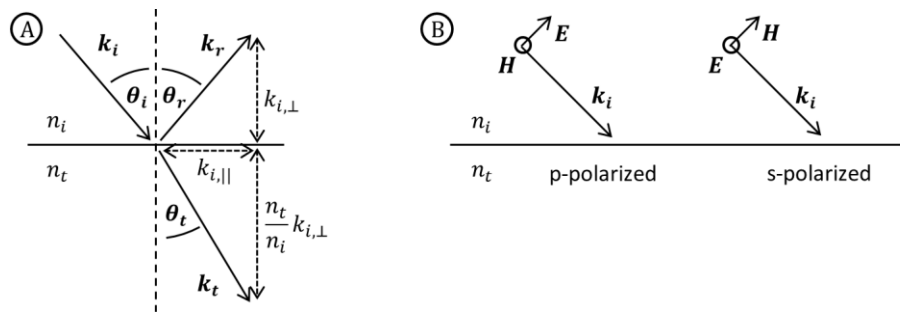


Figure 6. (A) Effect an optical interface has on the wavevector (\mathbf{k}) of light. (B) Illustration of the orientation of the electric (\mathbf{E}) and magnetic (\mathbf{H}) field vectors in case of p- and s-polarized light incident upon an interface.

2.2.3 Thin-film interference

So far, the phase of the electromagnetic wave has not been taken into account. For understanding the impact of the phase it is best to consider a superposition of two electromagnetic plane waves, of identical frequency and peak amplitude, which are shifted in phase. Therefore, at a specific point in time and at a specific spatial position their amplitudes differ. When the amplitudes of the plane waves have the same sign, constructive interference occurs and the resulting amplitude is larger than the individual amplitudes. Contrarily, when the amplitudes have opposite signs, destructive interference occurs and the resulting amplitude is lowered, or even zero.

An incident plane wave interferes with itself, when the wave is incident upon multiple interfaces in close proximity (meaning small compared to the coherence length of the wave). For example, in a dielectric film light is reflected by the front- and by the rear-surface. The film thickness determines the phase shift of the two reflected waves. By means of destructive interference the complete elimination of reflection is possible. This is the working principle of a thin-film anti-reflection coating (ARC), shown in **Figure 7**. To reduce reflection, the thin-film ARC must have a refractive index between the ambient and the bulk it is applied to. In the example in **Figure 7** a thin-film of refractive index 1.25 is applied to a bulk of refractive index 1.5 (e.g. glass) in air ($n = 1$). The thickness of the thin-film determines for which wavelength destructive interference occurs. The broadband reduction of sample reflectance is not possible using a single thin-film ARC.

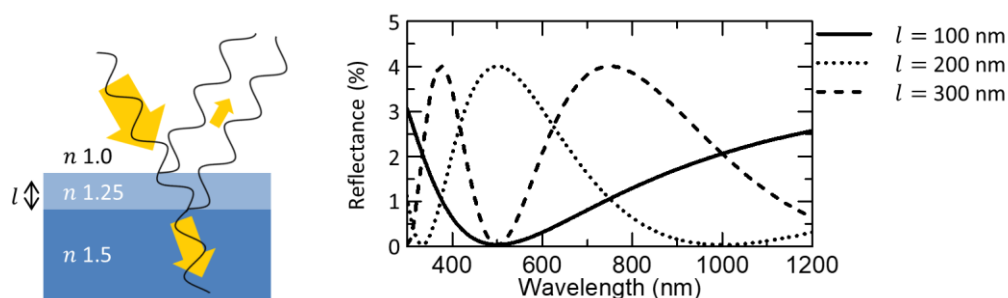


Figure 7. Illustration of a thin-film anti-reflection coating and the wavelength-dependent interface reflectance for several coating thicknesses (l).

2.2.4 Total internal reflection and optical modes

When light is incident from a medium of high refractive index (n_{hi}) onto a medium of lower refractive index (n_{low}) Snell's law (Equation (2.21)) has no solution for large incidence angles. In this case **total internal reflection** (TIR) occurs and the wave is completely reflected. The **critical angle** θ_C at which TIR sets is derived from Snell's law:

$$\frac{n_{low}}{n_{hi}} = \sin(\theta_C). \quad (2.27)$$

In a medium of high refractive index surrounded by media of lower refractive index light can be completely trapped by TIR, this configuration is called a waveguide. One of the simplest waveguides is an asymmetric slab waveguide, comprised of a film of refractive index n_F and thickness l between two semi-infinite media of lower refractive index (n_C and n_S). This kind of waveguide configuration will be of further importance in later sections. **Figure 8** illustrates a plane wave propagating in z direction in the waveguide. It is expressed as

$$\mathbf{E} = \mathbf{E}_0 e^{-i\beta z}, \quad (2.28)$$

where β is the longitudinal propagation constant, or phase constant. If θ is the angle between the wavevector and the direction of propagation it follows: $\beta = k \sin(\theta)$. Insertion into Equation (2.14) leads to

$$\frac{d^2 \mathbf{E}}{dx^2} + (k^2 - \beta^2) \mathbf{E} = 0. \quad (2.29)$$

As before, a propagating wave is described as a superposition of two polarizations. For one polarization the electrical field is transverse (TE) to the propagation direction, whereas for the other polarization the magnetic field is transverse (TM).

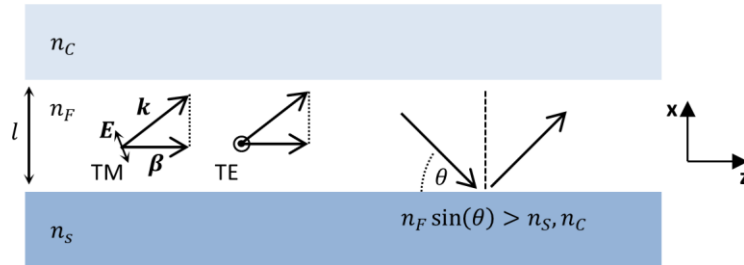


Figure 8. Illustration of an asymmetric slab waveguide.

Equation (2.29) is applied to all regions of the slab waveguide ($k_i = n_i k_0$). Solutions are found by considering the boundary conditions of continuous electric and the magnetic fields at the interfaces. Solutions for TE waves are found as eigenvalues to

$$\tan \left(l \sqrt{k_F^2 - \beta^2} \right) = \frac{\sqrt{k_F^2 - \beta^2} \left(\sqrt{\beta^2 - k_S^2} + \sqrt{\beta^2 - k_C^2} \right)}{(k_F^2 - \beta^2) - \sqrt{\beta^2 - k_S^2} \sqrt{\beta^2 - k_C^2}}. \quad (2.30)$$

For TM waves the eigenvalue equation is

$$\tan\left(l\sqrt{k_F^2 - \beta^2}\right) = \frac{n_F^2 \sqrt{k_F^2 - \beta^2} \left(n_C^2 \sqrt{\beta^2 - k_S^2} + n_S^2 \sqrt{\beta^2 - k_C^2} \right)}{n_S^2 n_C^2 (k_F^2 - \beta^2) - n_F^4 \sqrt{\beta^2 - k_S^2} \sqrt{\beta^2 - k_C^2}}. \quad (2.31)$$

Solutions to the eigenvalue equations are called modes. For each mode an effective refractive index (n_{eff}) is defined

$$n_{eff} = \frac{\beta\lambda}{2\pi} = n_F \sin(\theta). \quad (2.32)$$

Modes confined to the waveguide must fulfill $n_F \geq n_{eff} \geq n_c, n_s$.

2.2.5 Photonic crystals and diffraction

In general, any periodic spatial (\mathbf{r}) variation in the refractive index ($n(\mathbf{r})$), is termed a photonic crystal (PhC). Just like periodic atomic potentials give rise to a dispersive band structure for electrons, periodic variations in the refractive index in a solid give rise to a band structure for light. PhCs are described by the Floquet-Bloch theorem. Depending on the number of linearly independent periodic directions, a PhC is one (1D), two (2D) or three-dimensional (3D). Let us assume a 3D Bravais lattice spanned by the translation vector $\mathbf{R} = a_1 \mathbf{e}_1 + a_2 \mathbf{e}_2 + a_3 \mathbf{e}_3$ where each a_i is the lattice constant in the spatial direction \mathbf{e}_i . Modes in PhCs follow the Bloch function

$$\mathbf{E}(\mathbf{r}) = e^{i\mathbf{k}\mathbf{r}} \mathbf{u}(\mathbf{r} + \mathbf{R}) \quad (2.33)$$

where \mathbf{u} is a periodic function with the periodicity of the Bravais lattice. Eigenmodes are found numerically as solutions to Equation (2.14). The dispersion of these eigenmodes is typically visualized in a band structure folded around the first Brillouin zone; the primitive of the reciprocal lattice. The reciprocal lattice vector (\mathbf{K}) is the Fourier transform of the translation vector

$$\mathbf{K} \cdot \mathbf{R} = 2\pi i, i \in \mathbb{Z}. \quad (2.34)$$

Therefore, \mathbf{K} is also written as

$$\mathbf{K}_{mop} = m\mathbf{K}_1 + o\mathbf{K}_2 + p\mathbf{K}_3. \quad (2.35)$$

with $m, o, p \in \mathbb{Z}$ and $|\mathbf{K}_i| = 2\pi/a_i$.

PhCs give rise to several interesting phenomena. To explain these phenomena it is best to directly investigate an example structure. One of the simplest PhCs is a periodic layer stack (also termed a Bragg stack). This type of 1D PhC is illustrated in **Figure 9(A)**. Alternating layers of refractive index 1.0 and 1.5 are stacked with a lattice constant of a in z-direction. The Fourier transform is shown in **Figure 9(B)**; the primitive reciprocal vector is given by $\mathbf{K}_m = m 2\pi/a \hat{\mathbf{k}}_z$. The first Brillouin zone is in the range $-\pi/a \leq k_z < \pi/a$, with $k_z \hat{\mathbf{k}}_z = \mathbf{k}_z$ the wavevector in z-direction. The band structure of this layer stack is given in **Figure 9(C)**. The dotted and dashed lines in the graph are the light line, given by $\lambda = 2\pi n/k_z$, of a homogeneous layer of refractive index 1.0 and 1.5, respectively. Several interesting features are observable in the band structure of the layer stack lying in between the light lines. On the one hand, photonic band gaps exist; light of specific wavelengths is not allowed to propagate in the PhC. On the other hand, the dispersion is very flat in some regions - indicating the localization of light. These regions

of flat dispersion are of large interest for light guiding applications for enhancing the absorption of light [77].

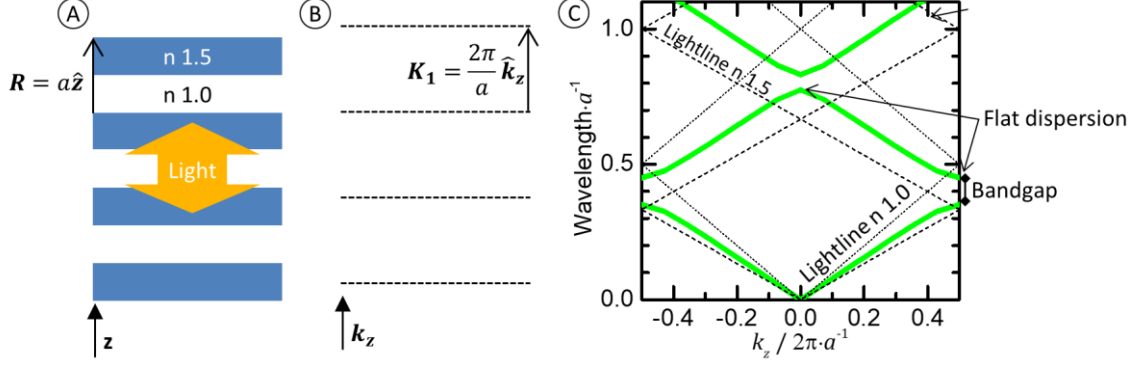


Figure 9. (A) Illustration of a 1D photonic crystal (also called Bragg stack). (B) Fourier transform on the Bragg stack in k -space. (C) Band structure of a Bragg stack.

In a homogenous medium light propagates as plane waves. In an inhomogeneous medium scattering occurs. In a periodic medium phase matching between different scattering centers takes place. This is called the Bragg condition. The Bragg condition gives rise to the scattering of waves to very specific directions, a process called diffraction. Diffraction is an interference phenomenon. To achieve phase matching the components of the incident wavevector (\mathbf{k}_{in}) and the diffracted wavevectors (\mathbf{k}'_{mop}) parallel (\parallel) to the reciprocal lattice vector must fulfill the Bragg condition:

$$\mathbf{k}'_{mop,\parallel} = \mathbf{k}_{in,\parallel} + \mathbf{K}_{mop}, \quad (2.36)$$

The components of the diffracted wavevectors longitudinal (\perp) to the reciprocal lattice vector are subject to the dispersion of light.

$$(\mathbf{k}'_{mop,\perp})^2 = \left(\frac{n_{out}}{n_{in}} \mathbf{k}_{in}\right)^2 - (\mathbf{k}'_{mop,\parallel})^2, \quad (2.37)$$

where n_{in} and n_{out} are the refractive indices of the medium light is incident from and diffracted to, respectively.

The simplest example is a classical grating, as illustrated in **Figure 10(A)**. It resembles the 1D PhC of **Figure 9(A)** rotated by 90° , with a medium of refractive index n_1 applied on top and a medium with refractive index n_2 applied to the bottom. As discussed in section 2.2.2 the transverse component of \mathbf{k}_{in} (in this case in x -direction) must be continuous across the interface. The reciprocal lattice vector is $\mathbf{K}_{m,x} = m 2\pi/a \hat{\mathbf{k}}_x$. Using θ_{in} as the incident angle of light and θ_m as the angle light is diffracted to \mathbf{k}_{in} and \mathbf{k}'_m separate into components parallel and perpendicular to the reciprocal lattice vector:

$$\mathbf{k}_{in} = n_1 2\pi/\lambda (\sin(\theta_{in}) \hat{\mathbf{k}}_x + \cos(\theta_{in}) \hat{\mathbf{k}}_z) \quad (2.38)$$

$$\mathbf{k}'_m = n_{out} 2\pi/\lambda (\sin(\theta_m) \hat{\mathbf{k}}_x + \cos(\theta_m) \hat{\mathbf{k}}_z) \quad (2.39)$$

n_{out} is either equal to n_1 or to n_2 , depending on whether light is transmitted ($0 \leq |\theta_m| < \pi/2$) or reflected ($\pi/2 < |\theta_m| \leq \pi$). Using Equation (2.36) we obtain:

$$n_1 \sin(\theta_m) - n_1 \sin(\theta_{in}) = \frac{m\lambda}{a} \quad (\text{reflection}) \quad (2.40)$$

$$n_2 \sin(\theta_m) - n_1 \sin(\theta_{in}) = \frac{m\lambda}{a} \quad (\text{transmission}) \quad (2.41)$$

This form of the Bragg condition is often called the grating equation and m is called the order of diffraction. While the transverse component of \mathbf{k}'_m follows the Bragg equation the longitudinal component is subject to the free space dispersion of the respective medium. In \mathbf{k} -space a graphical representation is possible. **Figure 10(B)** shows \mathbf{K}_m as dashed lines and the possible \mathbf{k} -vectors in the two media n_1 and n_2 are given as (semi-)circles of radius $n_k k_0$. \mathbf{k}_{in} is incident upon \mathbf{K}_0 on the $n_1 k_0$ circle. The possible \mathbf{k}'_m are shown in the graph. It is important to note, while the grating equation gives all possible directions light is refracted to, the efficiency of the refraction in a particular directions is more difficult to assess. To obtain the polarization dependent amplitude of the refracted light the Maxwell equations have to be considered. In general, efficient refraction is possible when the longitudinal component of \mathbf{k}'_m is near zero, as is for example the case for the transmitted \mathbf{k}'_1 in **Figure 10(B)**.

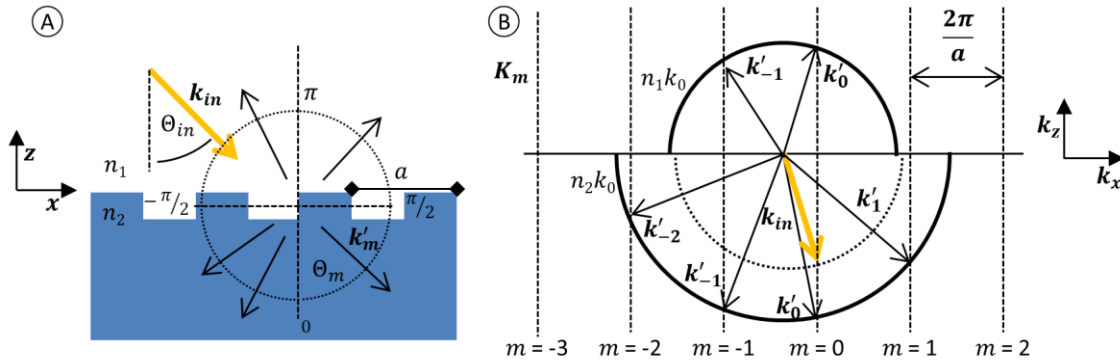


Figure 10. (A) Illustration of a grating at the interface of two media. Incident light is diffracted to various directions. (B) \mathbf{k} -space representation of the grating interface. The diffraction directions \mathbf{k}'_m are graphically determined.

In this thesis, diffraction to a layer of finite thickness, as illustrated in **Figure 11**, will be of importance. While modes in section 2.2.4 were confined to the waveguide, a grating allows coupling to the modes. The respective modes that light couples to in the film are then called quasi-guided modes. To allow coupling between incident light and a quasi-guided mode n_{eff} must be equal to $n_2 \sin \theta_m$. Equation (2.41) is rewritten to obtain the coupling condition

$$n_{eff} = \frac{m\lambda}{a} + n_1 \sin(\theta_{in}) \quad (2.42)$$

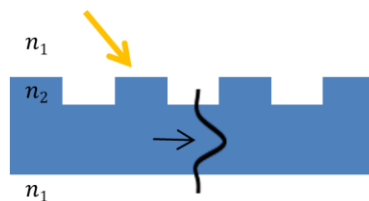


Figure 11. Illustration of incident light coupling to a thin-film mode by means of a grating texture.

2.2.6 Effective medium approximation

When light travels in a medium of varying refractive index the effective medium approximation allows a description of the light propagation as if the light were traveling through a homogenous medium. In literature, the resulting approximated refractive index is typically called the “effective” refractive index. To avoid confusion with the effective refractive index of thin-film modes, here the term “average” refractive index will be used.

A mixture of two materials on microscopic scales possess optical properties different to the properties of the individual pure materials. For spatial refractive index variations much smaller than the wavelength the material mixture is considered optically homogenous. Then an average refractive index of the mixture is determined using an effective medium approximation (EMA), describing the relationship of the average refractive index of the mixture to the refractive index of the individual materials composing the mixture.

Considering a mixture of two dielectric materials M1 and M2 of refractive indices n_1 and n_2 , respectively, the **Weiner bounds** define the limits within which the average refractive index of the composite material will lie:

$$n_{avg}^{upper} = \sqrt{Fn_1^2 + (1-F)n_2^2}, \quad (2.43)$$

$$n_{avg}^{lower} = \frac{n_1 n_2}{\sqrt{(1-F)n_1^2 + Fn_2^2}}. \quad (2.44)$$

Here, F is the volume fraction of the material M1 in the mixture. The two models are also called the parallel model and the series model, respectively. When discussing a situation where M2 is a host material with inclusions of material M1 the best suited bound depends upon the shape of the inclusion with respect to the light polarization. The upper bound, or parallel model, is particularly applicable where M1 is elongated parallel to the electrical field vector of the propagating light. The lower bound, or series model, is applicable for a situation where M1 is elongated perpendicular to the electrical field vector. Consequently, the average refractive index is polarization dependent.

When it comes to anti-reflection two types of layers, applying an EMA to reduced surface reflectivity, are distinguished. In case of a rough texture at an interface the EMA leads to a gradual refractive index change as illustrated in **Figure 12(A)**. The slow change in refractive index leads to near zero reflection at the interface. In case of a porous layer the EMA leads to a thin-film of lower refractive index (**Figure 12(B)**). When optimizing the thickness of the porous layer destructive interference is utilized to eliminate reflection in a certain wavelength range. This is the working principle of many conventional thin-film ARCs.

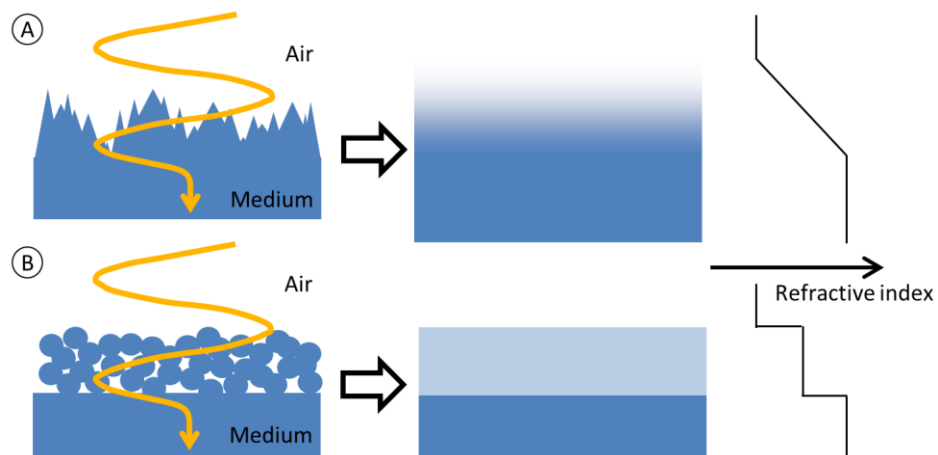


Figure 12. (A) Illustration of a gradual refractive index change at a textured surface for feature sizes much smaller than the wavelength. (B) Illustration of a porous layer of lower average refractive index at the surface of a bulk.

2.2.7 Geometrical optics

When light interacts with macroscopic objects much larger than the wavelength, several simplifying assumptions are possible. Light no longer has to be treated as a wave, instead, a ray is used that points in the direction the wave front travels. Free space rays point along straight paths. At interfaces rays are subject to refraction according to Snell's Law. The reflectivity, as well as the transmissivity are derived from Fresnel's equations. The path the ray took is completely reversible. Geometrical optics (or ray optics) are only applicable when the phase does not play a role. Therefore, interference phenomena cannot be describe.

3 Methodology

In the following, the most important methods and tools used for preparing and analyzing samples are discussed. Firstly, the direct laser writing (DLW) system used for fabricating textures is explained in detail. Next, the various characterization systems for measuring optical properties and the performance of PV devices are introduced. Finally, the simulation methods aiding the interpretation of measurement results are described.

3.1 Direct laser writing

In this work DLW was performed with a commercial tool (Photonic Professional GT, Nanoscribe). The system was equipped with a 780 nm laser with a pulse length of 100 fs at a repetition rate of 80 MHz. Different objectives and photoresist were available enabling various feature sizes. Here, the photoresist IP-Dip (Nanoscribe) and IP-S (Nanoscribe) were used together with a 63× 1.4NA (Plan-Apochromat Oil DIC, Carl Zeiss), and a 25× 0.8NA (LCI Plan-Neofluar Imm CorrDIC, Carl Zeiss) objective, respectively.

3.1.1 Direct laser writing fundamentals

Over the past two decades DLW has become an interesting tool for fabricating true 3D textures. Detailed textbook on DLW are available. This section is to a large extent based upon: (Baldacchini, 2015) [78,79].

Photoresists possess a polymerization energy threshold. At ordinary intensities it is not possible to expose a resin using light with photon energies lower than the threshold. In conventional lithography a photoresist is either not exposed, when the photon energy is too low, or it is exposed at any point along the path of the exposing beam. In consequence, conventional laser lithography only enables 2D pattern design. DLW makes use of the fact that there is not only a threshold for a one-photon polymerization (OPP) process, but also an energy threshold for two-photon polymerization (TPP) to occur. To achieve texturing a laser beam is focused into a resin with photon energies below the threshold of OPP. The laser beam will pass through the resin without causing polymerization, except in the focal point, where locally ultra-high intensities are reached. Two-photon absorption processes rely on high intensities. Such high intensities are for example achieved by use of pulsed laser and an objective of large numerical aperture (NA). The region of the focus where intensities are large enough for TPP to take place is called a voxel.

By moving the voxel through a resin 3D microarchitectures are fabricated [80]. As a result of the two-photon nature of the process the extent of the voxel is related to the square of the laser power. The ellipsoidal shape of the voxel (see **Figure 13(A)**) is derived from the Gaussian intensity profile of the used laser beam. The diameter (d_V) and the height (h_V) of the voxel are approximated with [81]

$$d_V = \frac{\lambda}{\pi \tan(\arcsin(NA/n))} \sqrt{\ln\left(\frac{4\pi^2 t P^2 \tan(\arcsin(NA/n))^4}{E_t \lambda^4}\right)}, \quad (3.1)$$

$$h_V = \frac{2\lambda}{\pi \tan(\arcsin(NA/n))^2} \sqrt{\ln\left(\frac{4\pi^2 t P^2 \tan(\arcsin(NA/n))^4}{E_t \lambda^4}\right) - 1}, \quad (3.2)$$

where P is the average power of the pulsed laser beam, t the time of exposure, n the refractive index of the material the objective is immersed into, λ is the wavelength, and E_t the TPP energy threshold. Voxel diameters of below 100 nm are possible using a laser beam of wavelength 800 nm focused through an aperture of $NA = 1.4$ [82]. Therefore, breaking the conventional resolution limit ($0.61 \lambda/NA$). Exposing a volume smaller than the resolution limit is possible due to the dependence on E_t . The resolution limit only holds for purely optical processes. DLW is a combination of an optical and a chemical process.

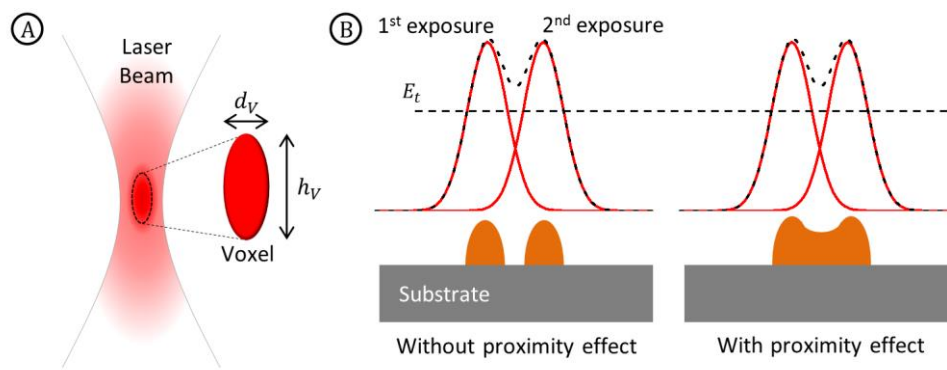


Figure 13. (A) Focused laser beam for direct laser writing. The spatial region of polymerization is termed voxel. (B) Illustration of the proximity effect. Two spatially and temporally separated exposure events will still lead to exposure of the area in between.

The chemical nature of DLW leads to a further interesting feature. While it is possible to expose single points with dimensions below the resolution limit, breaking the resolution limit has not been shown for two points exposed in direct proximity. More precisely: Two voxels of diameter d_V exposed at a distance slightly larger than d_V will still be connected by polymerized material. This is due to a memory effect in photoresists. When a region has been exposed with a dose below the polymerization threshold is again exposed some time later, taking the total dose above the energy threshold, polymerization will take place. This leads to a proximity effect [83]. Voxels exposed in close proximity will not form two separate points, but a single large feature, as illustrated in **Figure 13(B)**.

3.1.2 Sample preparation

For performing DLW substrates were first cleaned. The cleaning procedure involved wiping the substrate with isopropanol (IPA, Sigma Aldrich) using a paper towel. Drying was performed with a nitrogen gun. Before applying the desired photoresist (IP-Dip or IP-S) substrates were heated to 180°C for 20 min on a hotplate. This step was necessary since shrinkage of the photoresist during development sometimes led to lift-off from the substrate. Heating evaporates water residuals on the substrate and leads to a stronger adhesion of the photoresist. Directly after taking the substrates from the hot-plate the photoresist were applied by means of drop-casting.

3.1.3 Texture fabrication

Typical voxel diameters were on the order of 200 nm and 500 nm for IP-Dip and IP-S, respectively. The desired structures were either fabricated by single point (voxel) exposure, or by moving the focal point of the laser beam through the photoresist in lines. Both photoresists were compatible with the dip-in laser lithography (DiLL) method, where the objective was in direct contact with the resin (**Figure 14(B)**). In the Photonic Professional GT the objective was mounted facing upwards. Therefore, structures face downwards using the DiLL method. The coordinate system was rotated in comparison to the conventional setup, where exposure takes place through the substrate (**Figure 14(A)**).

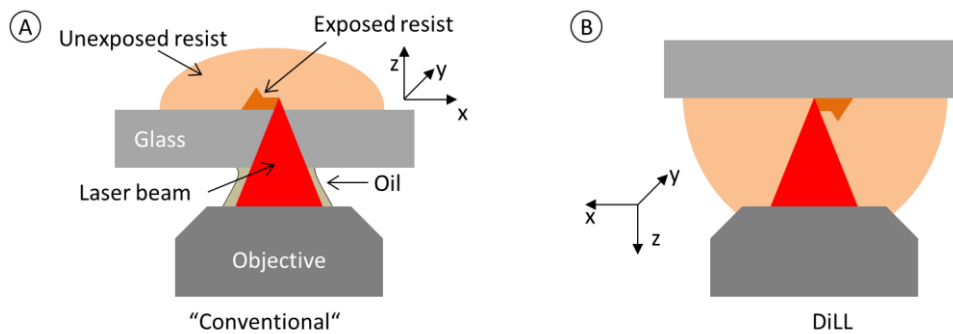


Figure 14. Illustration of the upward facing objective in relation to the sample. **(A)** In conventional DLW structures are created in an upright position. **(B)** In dip-in laser lithography (DiLL) structures are created in a downward facing position and the coordinate system is rotated by 180° around the y-axis.

The substrates, with drops of photoresist, were taped into samples holders that were then slid into the piezo controlled stage of the Photonics Professional GT. The piezo controlled stage enabled movement of the sample in all spatial directions by 300 μm . In contrast, the galvanometric mirror system (used for texture fabrication in this work) only allowed for lateral movement of the beam in the field of view (diameter: $\sim 120 \mu\text{m}$ (63 \times objective) / $\sim 250 \mu\text{m}$ (25 \times objective)). Therefore, movement in the longitudinal direction was still piezo controlled. Fabrication by means of the galvanometric mirror was 2 to 3 orders of magnitude faster than purely piezo movement based fabrication. The high lateral speed led to a layer-by-layer construction, as illustrated in **Figure 15**, being the most efficient fabrication method. The movement of the piece controlled stage and the movement of the galvanometric mirrors were not synchronized.

The most important parameters in DLW determining the quality and fabrication time of the design are the hatching and slicing distance, as well as the laser power and either the scan speed, or the exposure time.

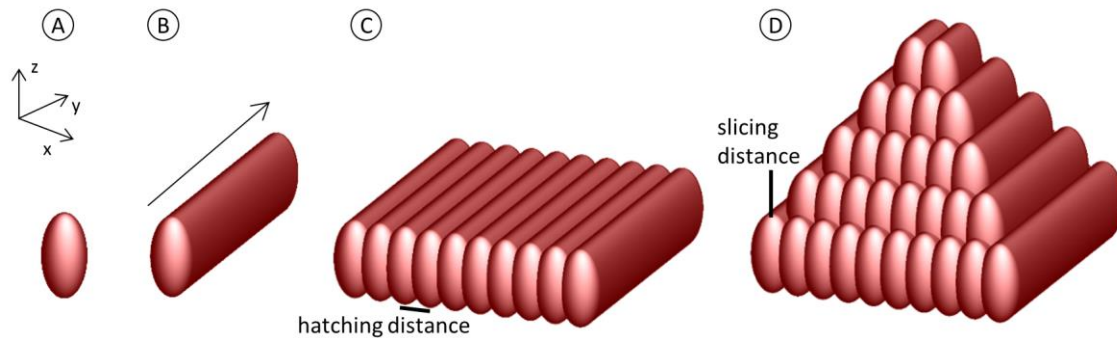


Figure 15. Illustration of the typical layer-by-layer fabrication process in DLW to form a 3D object, when using the galvanometric mirrors. The voxel **(A)** is moved to expose a line **(B)**. Several lines form a layer **(C)** and several planes the final object **(D)**.

Slicing and hatching distance. **Figure 15** illustrates how a voxel (**Figure 15(A)**) was moved in one direction to form a line (**Figure 15(B)**). Multiple lines, separated by the hatching distance, formed a layer (**Figure 15(C)**) and multiple layers, separated by the slicing distance, were stacked on top of each other to form a 3D object (**Figure 15(D)**).

Laser power. In the Photonics Professional GT software, the average laser power was defined as a percentage value. Measurements with a power meter (S121C, Thorlabs) after the objective were performed to estimate the absolute power these percentage values relate to. A power of 32 mW and 17 mW were determined to correspond to 100% for the 63× objective and the 25× objective, respectively. When absolute values are given in the following chapters they are in correspondence to these measurements.

Scan speed / exposure time. Typical lateral scan speeds of the galvanometric mirrors, for maintaining a high spatial precision, were 5 mm/s to 20 mm/s. The faster the writing speed the higher the laser power had to be for exposing the photoresist. If the laser power was chosen too high micro-explosions occurred in the photoresist. For exposing a single voxel the exposure time replaced the scan speed. In terms of total fabrication time the limiting parameter in point exposure was the time the galvanometric mirrors needed to settle in a specified position – with typically 1 ms to 3 ms the settling time of the galvanometric mirror system was up to one order of magnitude longer than the exposure time.

Stitching was necessary when an area larger than the field of view needed to be exposed. Then, the entire motorized stage was moved to a new position. This movement was less accurate than the piezo- and the galvanometric- movement. Trenches between structures occurred due to imprecise stage movement. To avoid trenches, a slight overlap between stitched textures was programmed.

3.1.4 Interface detection

Several of the structures fabricated using DLW for this dissertation had feature sizes of hundreds of nanometers, close to the resolution limit of the DLW system. Therefore, precise parameter control was necessary. One of these parameters was the positioning of the voxel with respect to the substrate surface. Variations in the z-positioning on the order of hundreds of nanometers strongly impacted whether the voxel was positioned inside the substrate (no exposure), at the substrate / photoresist

interface (voxel attached to substrate), or high above the substrate (floating in unexposed photoresist). Therefore, the z-position of the substrate surface needed to be determined with high precision.

In general, interface detection is automatically performed by the Photonic Professional GT based on interference. The “interface finder” determines the z-position of the interface based on interference fringes on a CCD camera in the confocal system of the device. However, performing the interface detection using the interface finder did not show the needed precision. After interface detection exposed voxels were attached to the substrate, but the exact position was subject to variations. Firstly, there was a high uncertainty in the determined interface position on the order of ± 200 nm. This uncertainty could be decreased to about ± 50 nm by performing the interface detection two to three times in a row. Secondly, there was a constant offset in the interface position determined by the interface finder and the true position of the substrate surface. This offset was determined by observing the focal spot of the laser beam in the confocal CCD camera (**Figure 16**). When moving the focal spot from the photoresist layer into the substrate it first dims and then becomes distorted due to the refractive index difference (**Figure 16(B)**). The focal spot is positioned at the substrate surface when it first dimes.

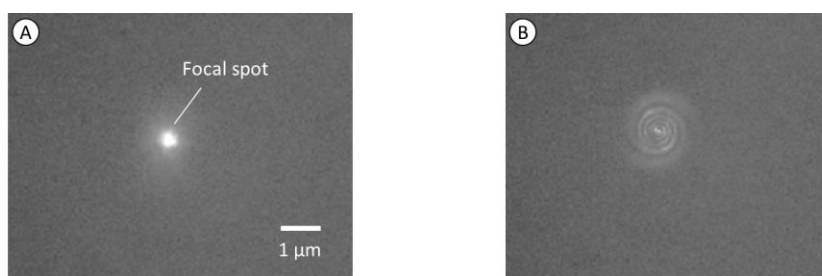


Figure 16. Focal spot as seen in the CCD camera of the Photonics Professional GT when focusing (A) into the photoresist layer and (B) into a fused silica substrate just below the interface.

It should further be noted, that the interface finder did not determine the position of the interface in the middle of the field of view. In case of the 63 \times objective and the 25 \times objective the interface position was determined about 80 μm and about 120 μm away from the center in negative x-direction (inverted z-axis), respectively. Therefore, when stitching multiple writing fields, the stage was moved in negative x-direction to avoid the detection of the interface between unexposed photoresist and already exposed textures.

3.1.5 Tilt correction

A further challenge was the tilt of the substrate with respect to the focal plane of the objective. The Photonic Professional GT was not equipped with a mechanical tilt correction. Software based tilt correction was only available for the piezo positions. The galvanometric mirrors, on the other hand, only moved the focal point in the focal plane. In case of a tilted substrate, the focal point was immersed deeper into the substrate at the one end than at the other end (illustrated in **Figure 17(A)**). In the available standard sample holders, although precisely fabricated, samples were tilted by about 200 nm to 400 nm per 100 μm . As a consequence, the height of fabricated textures varied within the field of view. This is observable in the optical image in **Figure 17(B)**, where a point exposure of several voxels was performed. When fabricating structures with several micrometer feature sizes the tilt was negligible. For the targeted PhC textures this tilt was not tolerable.

A dedicated sample holder with mechanical tilt correction was designed for this dissertation. The sample holder was composed of two plates that were spaced by three adjustable screws. When in use the two plates were held together by three very carefully tightened binding screws. A photograph of the sample holder for tilt correction is shown in **Figure 18**. For tilt adjustment samples were loaded and brought into the focal plane of the objective. The z-position of the substrate surface was detected in three positions ($\mathbf{Q}_i = [Q_{i,x}, Q_{i,y}, Q_{i,z}]$). Then a vector \mathbf{N} normal to the substrate surface was calculated

$$\mathbf{N} = \|(\mathbf{Q}_1 - \mathbf{Q}_2) \times (\mathbf{Q}_1 - \mathbf{Q}_3)\|. \quad (3.3)$$

The x- and y-positions of the spacing screws ($S_{i,x}$ and $S_{i,y}$) were known. The extrapolated z-positions ($S_{i,z}$) of the interface at the screw positions was determined from \mathbf{N} :

$$S_{i,z} = \frac{N_x S_{i,x} + N_y S_{i,y}}{N_z}. \quad (3.4)$$

The sample was exchanged for adjusting two of the screws such that: $S_{1,z} = S_{2,z} = S_{3,z}$. The spacing screws had a pitch of 350 μm . With an average lever of 120 mm the tilt could be adjusted by about 290 nm per 100 μm with a 360° turn of a screw. Manually the screws could be turned with about 30° precision – Resulting in a tilt below ± 25 nm per 100 μm .

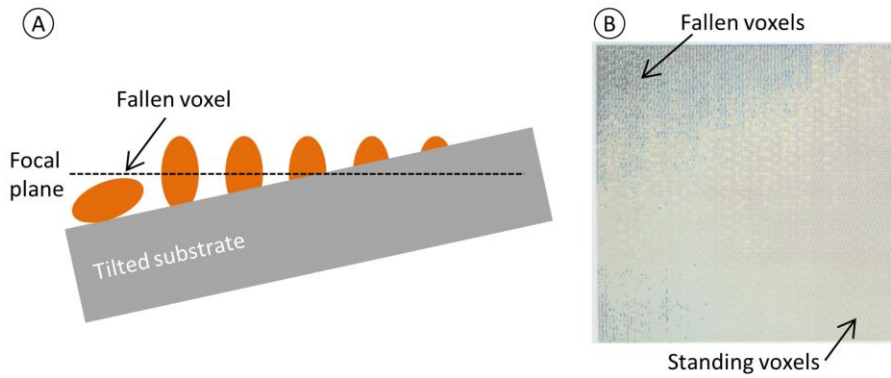


Figure 17. (A) Illustration of a substrate tilted with respect to the focal plane of the objective. In extreme cases, when performing a point exposure the exposed voxel fell over or vanished in the substrate. (B) Optical image of voxels exposed in a field of 100 μm by 100 μm without tilt correction.

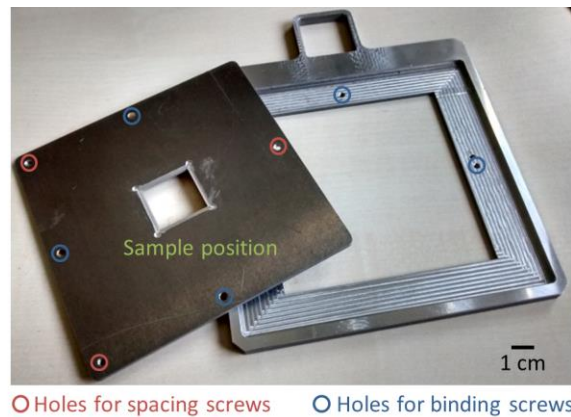


Figure 18. Sample holder for mechanical tilt correction.

3.1.6 Sample development

After DLW exposure, samples were placed upright in a bath of propylene glycol methyl ether acetate (PGMEA, Sigma Aldrich) for 15 min. Next, they were transferred to a bath of IPA for another 10 min. Finally, samples were dried, leaving only the exposed patterns on the surface. For most samples gentle drying under a stream of nitrogen was sufficient. In case strong surface tension caused a lift-off of the patterns carbon dioxide (CO₂) critical point drying was performed (Leica EM CPD300, Leica Microsystems GmbH).

3.2 Characterization tools

3.2.1 Microscopy

For a detailed analysis of their geometries, textures were imaged using optical microscopy and scanning electron microscopy (SEM). Optical microscopy was performed with a VHX-500 (Keyence Corporation), employing a VH-Z500 (Keyence Corporation) lens system with a maximum magnification of 5000×. SEM images were acquired with a Supra 55VP (Carl Zeiss). Making use of the secondary electron detector high resolution surface images were obtained.

3.2.2 Reflectance, transmittance & absorptance

Sample reflectance, transmittance, and absorptance were measured using a commercial spectrometer (Lambda 950, Perkin Elmer) equipped with a 150 mm integrating sphere. Wavelength-dependent measurements were made possible by a grating-based monochromator. In general, a spectral width of 2 nm was employed for measurements at wavelengths below 860 nm and a spectral width of 8 nm for measurements above 860 nm. At 860 nm a switch from a grating with a smaller period to a grating with a four times larger period occurred. **Figure 19** shows the integrating sphere setup. Depending upon the sample position the different optical properties were measured:

Transmittance. When placing a sample in position (a) specular transmittance (T_{spec}) was measured. Due to an aperture diffusely transmitted light did not reach the detector in the integrating sphere. Total sample transmittance (T_{total}) was measured when placing a sample in position (b). Based on the two measurements the diffuse transmittance (T_{diff}) was calculated ($T_{total} = T_{spec} + T_{diff}$).

Reflectance. The total (R_{total}) and the diffuse (R_{diff}) sample reflectance were measured in position (c). For the case of diffuse reflectance the specular reflection port had to be opened. Then, specularly reflected light exits the integrating sphere. Based on the two measurements the specular reflectance (R_{spec}) was calculated ($R_{total} = R_{spec} + R_{diff}$).

Absorptance. Sample absorptance (A) was measured by placing a sample in the middle of the integrating sphere in position (d) using an appropriate sample holder. In this setup the sum of T_{total} and R_{total} was determined directly and the absorptance was calculated according to: $A = 1 - T_{total} - R_{total}$. The sample holder was rotated to measure the absorptance for different incidence angles. It is important to note that light reflected specularly by the sample exited the integrating sphere through the entrance port for near normal incidence illumination. Therefore, $A + R_{spec}$ was measured in this case.

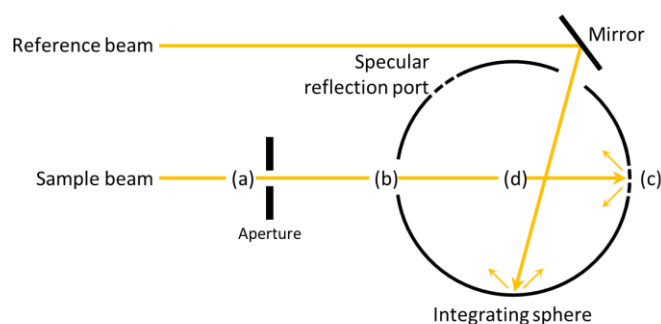


Figure 19. Sketch of the integration sphere in the Lambda 950. Showing the incident beams and positions for measuring specular (a) and total (b) transmittance, as well as reflectance (c) and absorbance (d).

The unsystematic measurement error, especially when measuring transmittance and absorbance, was in general much smaller than $\pm 0.1\%$. Many systematic errors introduced to the measurement by positioning a sample and changing the light scattering properties of the integrating sphere were compensated by the reference beam. It is to be noted that the choice of reference influenced the measurement result when investigating the reflectance. Ideally, the reference should show a similar angle-dependent reflectance to the sample under investigation. Here, a diffusive reflectance standard showing above 99.9% reflectance was employed. Furthermore, residual light reflected by the light trap introduced a systematic error on the order of $+0.5\%$ at low intensities. Statistical errors, due to noise, were reduced by choosing an appropriate integration time. Around 860 nm measurement errors larger than $\pm 1\%$ occurred, due to the grating switch and a low sensitivity of the employed detectors.

The area of interest on many samples was smaller than the cross-section of the sample beam. An aperture was employed to reduce the beam cross-section. To reduce the beam cross-section in positions (a) and (b) the aperture was placed shortly before the sample. To reduce the beam cross-section in position (d) the aperture was placed in position (b). Inherently, the sample beam was focused to position (a) and position (c) by means of curved mirrors, not shown in **Figure 19**. Thus, for reducing the beam cross-section in position (c) the aperture was placed in position (a). When employing an aperture the intensity of the sample beam was reduced and measurement noise increased. Therefore, performing longer measurements was often necessary.

3.2.3 Photogoniometry

Photogoniometry describes the angle-dependent analysis of light emitted by a sample. In this work, angle-dependent transmittance measurements were performed using a non-commercial setup, with the aid of Jan B. Preinfalk [84]. The setup is illustrated in **Figure 20**. The sample was mounted on a rotational stage and illuminated with a laser beam at a wavelength of 532 nm. Using index matching oil (Immorsol 518 F, Carl Zeiss) a large glass hemisphere was optically contacted to the glass substrate of the samples. The light, transmitted by the sample, hit the surface of the hemisphere under normal incidence and was therefore not refracted. The transmitted light was detected by a spectrometer (USB2000x, Ocean Optics). By rotating the sample around the possible polar (θ) and azimuth (ϕ) angles the angle-dependent transmittance was observed.

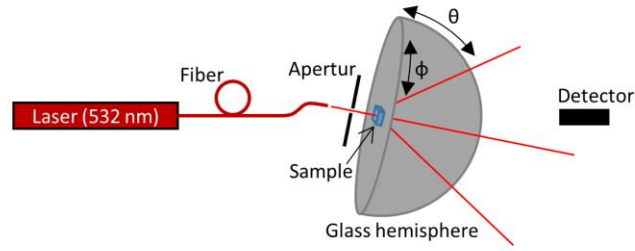


Figure 20. Illustration of a photogoniometric setup for angle-dependent transmittance measurements.

3.2.4 Spectroscopic ellipsometry and prism coupling

Material refractive indices were measured either using a commercial ellipsometer (VASE, J.A. Woollam) or a commercial prism coupler (Model 2010/M, Metricon).

Spectroscopic ellipsometry. In spectroscopic ellipsometry a monochromatic light beam was incident from free-space onto the sample under investigation. Light reflected from the sample was measured for different incident angles (θ), polarizations, and wavelengths (λ). The key parameter in spectroscopic ellipsometry was the ratio between the reflectance ($R(\theta, \lambda)$) of s- and p-polarized light (chapter 2.2.2), this value was express via $\Psi(\theta, \lambda)$ and $\Delta(\theta, \lambda)$ related to the absolute value and the phase of the ratio, respectively.

$$\frac{R_p(\theta, \lambda)}{R_s(\theta, \lambda)} = \tan(\Psi(\theta, \lambda))e^{i\Delta(\theta, \lambda)} \quad (3.5)$$

Using ellipsometry it was possible to determine the complex refractive index and thickness of layers in a thin-film layer stack. These values were obtained indirectly by comparing the experimentally determined Ψ and Δ to those determined in simulations (WVASE32, J.A. Woollam). The WVASE software determined Ψ and Δ of a given layer stack by solving the Maxwell equations for a given model of the complex refractive indices of the materials in the layer stack. Over several iterations the parameters of the employed models were optimized to match experimental results. Depending on the employed model the number of free parameters changed. When simple models such as the Cauchy model for lossless media [85] were applicable, as little as 2 free parameters (plus the layer thickness) were enough to describe the complex refractive index in a certain wavelength range. While, for many materials more complex models, such as the Tauc-Lorentz model [85], were need with a minimum of 5 free parameters. Finding a suitable model was one of the key challenge when investigating the optical properties of a new material using spectroscopic ellipsometry. Obtaining a meaningful result required homogenous layers in the area of the measurement spot and finding appropriate initial values for the free parameters, especially when their number was large.

Prism coupling. The basic principle behind the Model 2010/M prism coupler was the coupling of optical modes by variation of the angle of the incident beam. To do so, the sample was brought into contact with a prism. A laser beam was incident through the prism onto the sample and the reflected light was measured, as illustrated in **Figure 21**. As the prism refractive index is higher than the refractive index of the sample, total internal reflection (TIR) occurred for angles larger than the critical angle (**Figure 21(A)**). For a bulk sample light was coupled to the sample for incidence angles below the critical angle. When

decreasing the incidence angle a distinct drop in the measured reflectance determined the critical angle. A prerequisite for determine the refractive index of a sample was that the refractive index of the prism (n_p) was known with high precision. Using the measured critical angle (θ_c) the refractive index of a bulk sample (n_s) was determined according to:

$$n_s = n_p \sin(\theta_c). \quad (3.6)$$

In case of a thin-film sample, light coupled to modes propagating in the film (**Figure 21(B)**). When the reflectance reduced for a specific incidence angle, the effective refractive index (n_{eff}) of the mode was determined along the lines of Equation (3.6). For an asymmetric slab waveguide it was possible to make use of Equations (2.30) and (2.31) to determine the refractive index and thickness of the thin-film.

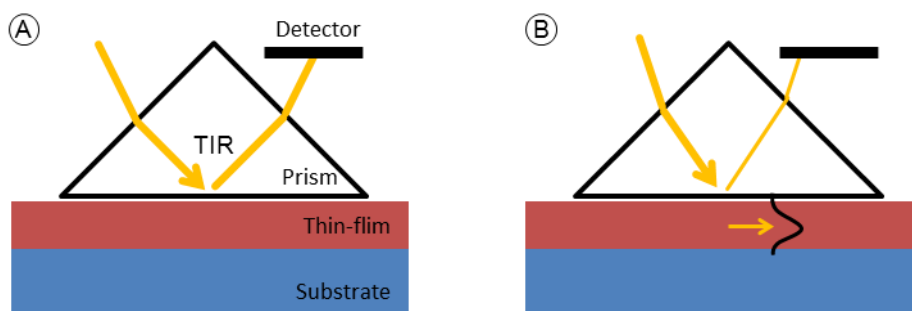


Figure 21. Illustration of the prism coupling method used by the Model 2010/M (Metricron). Depending on the incidence angle light is either **(A)** reflected due to total internal reflection (TIR) or **(B)** coupled to the sample. In case of a thin-film coupling only possible occurs to guided modes.

In the Model 2010/M the refractive index was automatically determined using the measured angle-dependent reflectance. In case of a thin-film the effective refractive index of the modes did not only dependent upon the refractive index of the layer, but also upon the layer thickness. Therefore, coupling to at least two modes was needs for determining the two unknowns. In general, this led to a need for layer thicknesses of several hundred nanometers or even several micrometers.

The used commercial prism coupler was equipped with a 637 nm continuous-wave (CW) laser diode. To determine the wavelength-dependent refractive index of a sample further laser sources were needed. For determine the refractive index at 1550 nm an external CW laser diode was used. To be able to measure the refractive index at various, freely determined wavelength in the visible range a tunable single-mode CW laser was used. This commercial tunable laser was equipped with a high power neodymium-doped yttrium aluminum garnet (Nd:YAD) laser source emitting light at a wavelength of 532 nm. The system made use of titanium-sapphire laser (SolsTis, M squared) to generate NIR light (700 nm to 1000 nm), frequency doubling (ECD-X, M squared) to generate UV-blue light (350 nm to 500 nm), and frequency mixing (EMM, M squared) to generate green-red light (525 nm to 650 nm)

3.2.5 Solar cell characteristics

The fundamental solar cell characteristics were discussed in chapter 2.1.2. In following, the measurement system used for obtaining the current-voltage (I - V) dependency and the external quantum efficiency (EQE) are discussed.

I-V measurement. The *I-V* curves of the investigated solar cells were measured using a commercial solar simulator (SUS V2.0, Oerlikon Balzers). The solar simulator made use of a halogen and of a xenon light source for generating a spectrum closely resembling the AM1.5g spectrum. The light emitted by the sources was collimated and illuminated an area of 90 cm by 90 cm. Two reference solar cells, responding to different parts of the incidence spectrum, were used to adjust the relative contribution of the two light sources and to calibrate the incident intensity at the center of the illuminated area to 1000 W/cm². A voltage sweep in 6 mV steps was performed on the illuminated solar cells and the extracted current was measured.

EQE measurement. The quantum efficiency is a wavelength-dependent characteristic of a solar cell. The EQE, relating the number of incident photons to the number of collected charge carriers, was measured using a custom build commercial system (QUE V2.0, Oerlikon Solar), illustrated in **Figure 22**. In the EQE setup light from a xenon lamp was passed through a monochromator and modulated using a chopper. The spectral bandwidth was approximately 5 nm and the chopper ran at 120 Hz. Since the signal was typically very weak lock-in amplification of the modulated signal was performed. A reference silicon solar cell of known EQE was used to determine the number of incident photons by measuring the current of the illuminated solar cell. Furthermore, a reference diode was employed in the system to account for fluctuations in the intensity. The system made measurements in a wavelength range from 320 nm to 1100 nm possible. Too little light was available for shorter wavelengths and EQE data for longer wavelengths was not available for the silicon based reference solar cell.

The EQE system was originally set up to measure solar cell with contacts on the back-side (opposite to the illuminated side). The solar cells were positioned in position (1) in **Figure 22**. For measuring solar cells with front contacts a system of mirrors and lenses was installed to guide the beam to position (2) in **Figure 22**. A rotatable stage for measuring the angle of incidence dependent EQE was placed in position (2) and an aperture was used in position (1) to reduce the beam cross-section. For large angles of incidence the solar cell reflectance, and therefore the EQE, depended upon the polarization of light according to the Fresnel Equations. In general the solar cell response to unpolarized light was of interest, but the grating-based monochromator partially polarized the light. As a consequence, a polarizer was placed in the beam path when performing measurements at large angles of incidence. To obtain the result for unpolarized light, the measured EQE of two perpendicular polarizer positions were averaged. It is to be noted that the beam intensity in position (2) was reduced by almost a factor of 10 in comparison to position (1). Therefore, a very long integration time of 5 s was used. To reduce the total measurement time the EQE was measured in 10 nm steps.

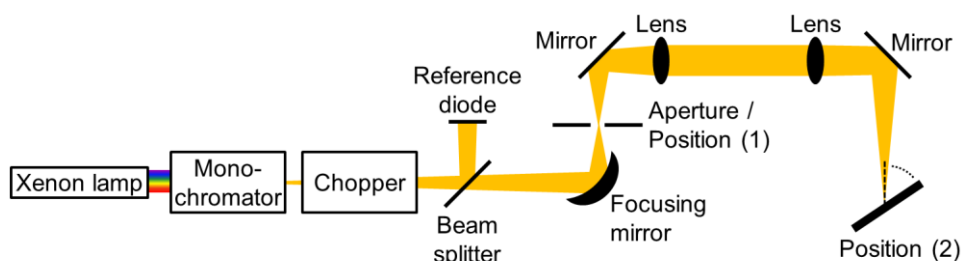


Figure 22. Illustration of the setup used to perform EQE measurements.

3.3 Optical simulations

Different methods exist for numerically simulating the interaction of light with matter. Very broadly these methods either take into account the electromagnetic wave nature of light, or use the geometrical optics approximation. In geometrical optics rays are made use of that are normal to the wave front and point in the direction of propagation. Geometrical optics is only applicable for feature sizes and layer thickness (much) larger than the wavelength. The computational power needed for electromagnetic based simulations is typically a lot higher; therefore geometrical optics are used whenever applicable.

3.3.1 Finite difference time domain simulations

In general, numerical solutions to the interaction of light with optically small textures are typically found based on solving Maxwell equations. In this work, the commercial software FDTD Solutions (Lumerical Inc., Vancouver, Canada) was used. FDTD stands for 'finite difference time domain'. In FDTD the Maxwell equations were solved in a model using a discrete grid and discrete time steps [86]. An electromagnetic wave was initialized and its temporal propagation through the model was monitored. Using the Fourier transform a frequency (wavelength) dependent solution was obtained. Especially for 3D models the spatial dimensions were limited to a few wavelengths, as the number of grid cells increased cubically. On the other hand, FDTD simulations were particularly useful for periodic textures with dimensions on the order of the wavelength. Then, periodic boundary conditions were used, where the electromagnetic wave exits the simulation on one side and simultaneously enters it again on the other side.

3.3.2 Ray-tracing simulations

Ray-tracing is a geometrical optics based simulation method, applicable to optically large systems. In this work, the commercial software LightTools (Synopsis Inc., Mountain View, U.S.A.) was used. In LightTools a source was defined, emitting rays in a certain direction. As long as the rays traveled in a homogenous medium they moved along straight lines. When encountering an interface the rays were reflected or transmitted according the Fresnel Equations (Equations (2.23) and (2.24)). Probabilistic ray splitting was used. Therefore, when encountering an interface, only one reflected or transmitted ray was traced based on the probability. The directions in which the rays traveled after encountering the interface depends upon the defined scattering properties. In case of a smooth surface the rays were refracted in a direction given by Snell's Law (Equation (2.21)). Various other optical interface properties were user-defined. For example, in Lambertian scattering an incident ray was emitted isotopically, with the same probability in all directions.

In this work, only a far field monitor was made use of to determine the reflectance from textures for PV applications. The far field monitor detects all rays leaving the simulated system. 200.000 rays are used in every simulation. Ray-tracing stopped either when a ray reached an absorbing surface, the far field detector, or when the ray power dropped below 10^{-6} of its original value. Rays lost power in the system when they traveled through an absorbing medium, or when they were partially reflected / transmitted at an interface.

3.3.3 Transfer matrix method

Within the scope of this dissertation, it was necessary to simulate the reflectance, transmittance and absorptance of a thin-film on a glass substrate. In general, it is not possible to treat optically thin-films using ray optics, due to the occurring interference phenomenon. While it is not possible to simulate millimeters thick bulk glass in FDTD. To simulate the reflectance, transmittance and absorptance in such a system an extended transfer matrix method (TMM) was used.

TMM is a well-known tool for simulating the interference of plane waves occurring in a thin-film layer stack [87,88]. TMM considers the interfaces within a layer stack and the propagation of plane waves between them. At every interface light is either reflected or transmitted to the next medium. TMM was originally only applied to coherent layers. Meaning thin compared to the coherence length (l_{coh}) of the light. Over distances longer than the coherence length (typically several wavelengths) the phase of a wave average out due to statistical variations.

Coherent layers. Based on the superpositioning of plane waves it is sufficient to consider the amplitudes of the electrical fields (E). On either side of an interface there are plane waves traveling in forward direction (+) or in backward direction (-), as illustrated in **Figure 23**. In the TMM approach, the electrical field amplitudes at the interface of a layer m to a layer n relate to each other via the transfer matrix \mathbf{M}_{nm} :

$$\begin{pmatrix} E_m^+ \\ E_m^- \end{pmatrix} = \mathbf{M}_{mn} \begin{pmatrix} E_n^+ \\ E_n^- \end{pmatrix}, \quad (3.7)$$

$$\text{with } \mathbf{M}_{nm} = \frac{1}{t_{mn}} \begin{pmatrix} 1 & r_{mn} \\ r_{mn} & 1 \end{pmatrix}, \quad (3.8)$$

where r_{mn} and t_{mn} are the amplitude reflection and transmission coefficient of the Fresnel equations (Equations (2.23) and (2.24)), respectively. Light traveling through a layer is subject to a phase change, and sometimes absorption. When light of wavelength λ travels through layer m of complex refractive index n_m and thickness l_m the propagation matrix \mathbf{D}_m relates the electrical field at one end (1) of the layer to the electrical fields on the other end (2):

$$\begin{pmatrix} E_{m1}^+ \\ E_{m1}^- \end{pmatrix} = \mathbf{P}_m \begin{pmatrix} E_{m2}^+ \\ E_{m2}^- \end{pmatrix} \quad (3.9)$$

$$\text{with } \mathbf{P}_m = \begin{pmatrix} \exp\left(-i\frac{2\pi n_m l_m}{\lambda}\right) & 0 \\ 0 & \exp\left(i\frac{2\pi n_m l_m}{\lambda}\right) \end{pmatrix}. \quad (3.10)$$

Figure 23 shows the layer stack under investigation: a thin-film (medium b) on a glass substrate (medium c) surrounded by air (medium a and medium d). Only the thin-film was a coherent layer ($l_b \ll l_{coh}$). By means of matrix multiplication the amplitude reflection and transmission coefficients of a wave incident upon the layer in forward direction (r_{ac} and t_{ac}) and in backward direction (r_{ca} and t_{ca}) were determined, respectively:

$$\begin{pmatrix} 1 \\ r_{ac} \end{pmatrix} = \mathbf{M}_{ab} \mathbf{P}_b \mathbf{M}_{bc} \begin{pmatrix} t_{ac} \\ 0 \end{pmatrix}, \quad (3.11)$$

$$\begin{pmatrix} 1 \\ r_{ca} \end{pmatrix} = \mathbf{M}_{cb} \mathbf{P}_b \mathbf{M}_{ba} \begin{pmatrix} t_{ca} \\ 0 \end{pmatrix}. \quad (3.12)$$

Using Equations (2.25) and (2.26) the reflectance (R_{ac} and R_{ca}) and transmittance (T_{ac} and T_{ca}) were calculated from the square of the amplitude reflection and transmission coefficients, respectively.

Incoherent layers. In case of incoherent layers the phase information is lost. The amplitude transfer matrix (\mathbf{M}_{nm}) at an interface of layer m to layer n must be modified to an intensity transfer matrix [89]:

$$\mathbf{M}'_{mn} = \frac{1}{T_{mn}} \begin{pmatrix} 1 & -R_{nm} \\ R_{mn} & T_{mn}T_{nm} - R_{mn}R_{nm} \end{pmatrix} \quad (3.13)$$

The reflectivity and transmissivity at the interface of two incoherent layers, such as medium c ($l_c \gg l_{coh}$) to medium d , were found using the Fresnel equations and taking the squares according to Equations (2.25) and (2.26). The coherent medium b was treated as an interface between medium a and medium c using the above calculated reflectance and transmittance. For taking absorption in incoherent layers into account the absolute square of the elements of the propagation matrix needed to be considered:

$$\mathbf{P}'_m = \begin{pmatrix} \left| \exp\left(-i\frac{2\pi n_m l_m}{\lambda}\right) \right|^2 & 0 \\ 0 & \left| \exp\left(i\frac{2\pi n_m l_m}{\lambda}\right) \right|^2 \end{pmatrix}. \quad (3.14)$$

The solution to the complete layer stack in **Figure 23** was found using the matrix multiplication:

$$\begin{pmatrix} 1 \\ R_{ad} \end{pmatrix} = \mathbf{M}'_{ac} \mathbf{P}'_c \mathbf{M}'_{cd} \begin{pmatrix} T_{ad} \\ 0 \end{pmatrix}, \quad (3.15)$$

where R_{ad} and T_{ad} are the desired reflectance and transmittance intensity of the layer stack, respectively.

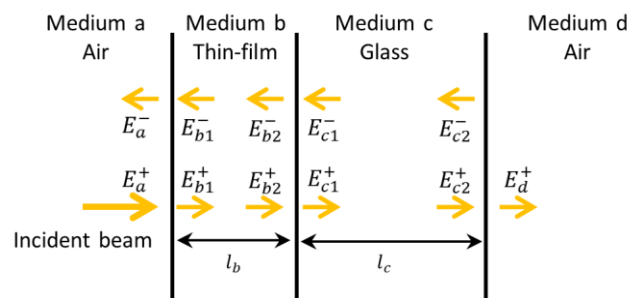


Figure 23. Schematic of a layer stack and the electrical field amplitudes as used in the transfer matrix formalism.

4 Nano-optics for ink infiltrated photonic crystal solar cells

Several of the results in the following sections have already been published.

*(Section 4.4) The results for the refractive index of IP-Dip were partially published in Opt. Lett. **43**(24) 29-32 (2019) [90]. The co-author Malte Langenhorst helped with sample preparation, mainly concerning the silanization process. The co-author Dmitry Busko helped in setting up the laser system. Ulrich Paetzold and Bryce Richards were involved in the coordination of the work and the interpretation of the results.*

*(Section 4.5) The results for the refractive index of the CIS nanocrystals were partially published in Opt. Express **25**(12), A502-A514 (2017) [91]. The nanoparticles were prepared by the co-authors from the Texas Materials Institute. The co-author Aina Quintilla performed the ellipsometry measurements and the modeling using the WVASE software.*

*(Section 4.6 & Section 4.7) The results of the numerical calculations and some of the experimental results were partially published in Opt. Express **25**(12), A502-A514 (2017) [91] as well. The nanoparticles were prepared by the co-authors from the Texas Materials Institute. The co-author Aina Quintilla helped in sample preparation. The co-authors Guillaume Gomard and Bryce Richards had large parts in developing the fabrication idea, as well as supervision of the work together with the co-author Ulrich Paetzold. The co-author Aiman Roslizar made the atomic force microscopy (AFM) image available in the publication.*

4.1 Introduction

Thin-film solar cells promise a lowering of costs in PV production, as well as novel devices and applications. Key aspects in terms of costs are vacuum-free, room-temperature processing. The long term targets are large-area production and employing solar cells on flexible substrates. Solution processable PV active materials promise to achieve these targets. Ink depositable semiconductor nanocrystals have been introduced in chapter 1. In contrast to conventional co-evaporated layers, nanocrystals are chemically synthesized at room-temperature in the desired composition [92]. In this work, CuInSe₂ (CIS) nanocrystals have been made use of. These CIS nanocrystals have, for example, been used to fabricate a solar cell directly on paper [93]. In common with many other solution processable thin-film technologies solar cells made from CIS nanocrystals suffer from a high defect density that limits the solar cell efficiency. Without high-temperature post-processing procedures, devices with a power conversion efficiency (PCE) of only about 3% have been fabricated [94]. It is to be mentioned that using post-processing, efficiencies of about 15% have been achieved [95]. In reference [94] the best performing devices (without post-processing) had a layer thickness of about 150 nm. While the absorption of light increased in thicker layers, the PCE was reduced. This is a clear indication that light-trapping textures are beneficial to these solar cells.

In the PV market dominating c-Si technology the etching of textures into the semiconductor layer is an industry standard. Anisotropic alkaline wet-etching is used to pattern the semiconductor layer into random pyramids of micron-scale dimension. These textures not only lead to a reduction in reflectance,

but also the refraction of light to oblique angles and therefore to longer path lengths through the semiconductor layer. For the CIS nanocrystal solar cells longer optical path lengths are highly desirable. On the other hand, the application of micron-scale textures to a hundred nanometers thick semiconductor layer is not feasible. Textures have to be on the order of a few hundred nanometers and, therefore, on the order of the wavelength of the incident light. As discussed in section 2.2.5 periodic textures, called photonic crystals (PhCs), on the order of the wavelength, give rise to several interesting phenomena.

PhCs in thin-film PV have been made use of for a wavelength-dependent reduction in reflectance and light-trapping [30]. Light-trapping is most commonly achieved by couple incident light to modes guided in the semiconductor layer [96]. The use of PhCs, to achieve this kind of light-trapping, has gained considerable attention over the past years, as PhCs have the potential to overcome the Lambertian limit [97] (the benchmark, when it comes to light-trapping) in a certain wavelength range [98,99]. The guided mode light-trapping mechanism is in general well understood [100,101]. Nevertheless, a clear design and optimization procedure is still subject to ongoing research. As a result of the sheer number of possible designs a vast number of numerical studies is found in literature for various different material systems [102-105].

Different texturing techniques have been proposed to produce PhCs for thin-film solar cells. In case of inorganic solar cells, especially for silicon based solar cells [106], typically isotropic etching methods, employing a mask, have been made use of [46]. Furthermore, textured semiconductor layers have been fabricated by means of bottom-up techniques 'growing' a patterned [49,107,108], as well as layer deposited on pre-textured substrate [54,109] – the substrates were often textured using nanoimprinting techniques [110,111]. The latter have also been directly applied directly to the semiconductor layer of organic solar cells [112]. While an increase in light absorption could be shown for nearly all fabricated textures [113,114], an increase in solar cell efficiency did not necessarily set in due to the disruptive nature of the texturing on charge carrier recombination. This resulted in a need for adequate passivation [115]. Nevertheless, PhCs have successfully been applied to various thin-film PV devices, such as organic solar cells [116,117], a-Si solar cells [118], mc-Si solar cells [119], thin c-Si solar cells [120,121], group-III nitride-based solar cells [122], as well as perovskite solar cells [123].

Especially when employing etching methods texturing has led to a significant increase in the non-radiative recombination of charge carriers. In the following, an infiltration method, uniquely applicable to ink depositable PV materials, is presented as a novel approach to fabricating a PhC patterned PV device. In this infiltration approach a polymeric template was used to deploy the PhC pattern. The nanocrystal ink solution with the PV semiconductor materials was deposited on this template. After the solvent dried the nanocrystals embed the PhC pattern. Thus, no additional passivation step was necessary.

Daser writing (DLW) was made use of to fabricate the polymeric template. The goal of the work was the development a process that enables the rapid prototyping of different PhC pattern designs. The above described CIS nanocrystals were used as the PV semiconductor material to demonstrate the infiltration concept. In the following, a detailed analysis was performed of the light-trapping in prototype samples consisting of a PhC patterned CIS nanocrystal layers on glass substrates. This analysis was supported by FDTD (chapter 3.3.1) simulations. The refractive indices of the polymeric template material and of the CIS nanocrystal layer were measured and implemented in FDTD simulations. For the prototypes a very good match was achieved between the numerically calculated absorptance and the experimentally

measured absorptance in the layer. Finally, a functional CIS nanocrystal infiltrated PhC patterned PV device was fabricated proving that the process is non-disruptive to the device efficiency.

4.2 Working principle of the photonic crystal pattern

PhCs diffract light. When a PhC is applied to a thin-film, this diffracted light couples to waveguide modes, which are then called quasi-guided modes, under certain circumstances. This principle was already outlined in section 2.2.5 for a 1D pattern, in the following 2D PhC patterns are investigated. When light couples to a quasi-guided mode it takes a longer path through the thin-film and is in consequence absorbed more efficiently. While PhCs have often been implemented as surface textures, in this work the complete semiconductor layer was patterned to achieve coupling to quasi-guided modes. In general, a thick patterned layer leads to stronger diffraction than a thin surface texture. Furthermore, an average refractive index (n_{avg}) arises from the material mix (section 2.2.6). This has the additional advantage of lowering the refractive index step from the typical glass cover into the semiconductor layer of a solar cell, reducing reflection related losses for all wavelengths.

A thorough and detailed understanding of the light-trapping in the used material system was targeted. A simplified layer stack was investigated to enable the identification quasi-guided modes, reduce other effects such as thin-film interference, and clearly link increase absorptance to the diffraction of light. The following detailed discussion will, to a large extent, revolve around this prototype layer stack (illustrated in **Figure 24**). The prototype layer stack consisted of a PhC patterned layer of thickness l on a fused silica substrate ($n_{sub} \approx 1.46$).

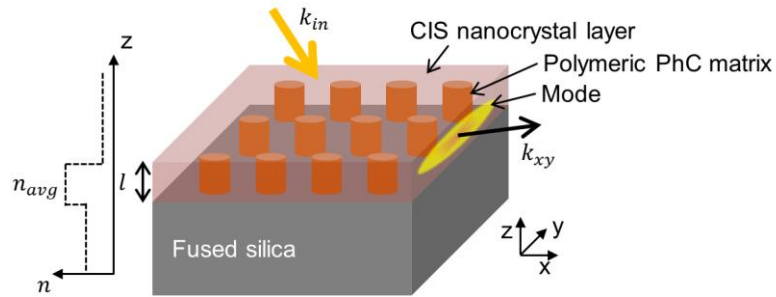


Figure 24. Illustration of a 2D PhC patterned CIS nanocrystal layer on a thick substrate.

The effectiveness of the coupling scheme depends on the wavelengths for which coupling between the ambient and (quasi-)guided modes is possible. In the following the coupling condition is determined along the same lines of section 2.2.5, but in this case for a 2D PhC pattern. Diffracted light must fulfill the Bragg condition (Equation (2.36)). The PhC matrix illustrated in **Figure 24** expands in x- and y-direction. It is possible to define an in-plane wavevector \mathbf{k}_{xy} for propagation modes:

$$\mathbf{k}_{xy}^2 = \mathbf{k}_x^2 + \mathbf{k}_y^2. \quad (4.1)$$

The reciprocal lattice vector (\mathbf{K}) is then given by

$$\mathbf{K} = \pm \sqrt{K_x^2 + K_y^2} \hat{\mathbf{k}}_{xy}, \quad (4.2)$$

Where K_x and K_y are the absolute of the reciprocal lattice vector in x- and y-direction, respectively. The in-plane component of incidence wavevector (\mathbf{k}_{in}) is:

$$\mathbf{k}_{in,\parallel} = \pm \frac{2\pi}{\lambda} \sin(\theta_{in}) \hat{\mathbf{k}}_{xy}, \quad (4.3)$$

where θ_{in} is the angle between the incidence wavevector and the surface normal. The in-plane component of diffracted light wavevectors (\mathbf{k}') in the patterned layer are:

$$\mathbf{k}'_{\parallel} = \pm n_{avg} \frac{2\pi}{\lambda} \sin(\theta_{m,p}) \hat{\mathbf{k}}_{xy}, \quad (4.4)$$

where $\theta_{m,p}$ is the angle between the wavevector of diffraction order (m, p) and the surface normal. Consequently, the Bragg condition for light diffracted to the textured layer is:

$$n_{avg} \frac{2\pi}{\lambda} \sin(\theta_{m,p}) = \left| \sqrt{K_x^2 + K_y^2} + \frac{2\pi}{\lambda} \sin(\theta) \right|, \quad (4.5)$$

To achieve coupling the mode effective refractive index ($n_{eff} = k_{xy}\lambda/2\pi$) must be equal to $n_{avg} \sin(\theta_{m,p})$. Using $K_{xy} = \pm \sqrt{K_x^2 + K_y^2}$ the coupling condition is:

$$n_{eff} = \left| \frac{\lambda}{2\pi} K_{xy} + \sin(\theta_{in}) \right|. \quad (4.6)$$

The coupling scheme is more effective for a larger number of (quasi-)guided modes (N). The number of guided modes depends upon the average refractive index of the PhC patterned layer and is given by [67]:

$$N_{TE} = \left\{ \frac{4l}{\lambda} \sqrt{n_{avg}^2 - n_{sub}^2} - \frac{1}{\pi} \tan^{-1} \left(\sqrt{\frac{n_{sub}^2 - 1}{n_{avg}^2 - n_{sub}^2}} \right) \right\}_{int}, \quad (4.7)$$

$$N_{TM} = \left\{ \frac{4l}{\lambda} \sqrt{n_{avg}^2 - n_{sub}^2} - \frac{1}{\pi} \tan^{-1} \left(\left(\frac{n_{avg}}{n_1} \right)^2 \sqrt{\frac{n_{sub}^2 - 1}{n_{avg}^2 - n_{sub}^2}} \right) \right\}_{int}, \quad (4.8)$$

for transvers electric (TE) and transvers magnetic (TM) modes that do not leak to the substrate, respectively. The larger the average refractive index, the more modes exists for diffracted light to couple to.

As described in chapter 2.2.5 it is complicated to determine the coupling efficiency between different diffraction orders and quasi-guided modes. In general: Thick patterns and a large refractive index contrast give rise to strong diffraction and broader spectral features [124]. In this work, the coupling efficiency was not determined analytically. FDTD simulations were performed to quantify the light-trapping introduced by PhC patterns in the CIS nanocrystal layer. To perform FDTD simulations, as well as the calculations above (determining the coupling wavelength and number of guided modes), the refractive indices of polymeric PhC matrix and the CIS nanocrystals had to be determined.

4.3 Prototype preparation

For the targeted investigation of the interaction of light with the designed PhCs, as well as for showing the feasibility of the infiltration scheme, textures were prepared on fused silica substrates. The PhC

matrices for infiltration were fabricated using the Photonic Professional GT (section 3.1) employing the Photoresist IP-D (Nanoscribe GmbH). For exposing the photoresist the 63× objective was used that enables the exposure of small voxel with dimensions on the order of 250 nm (lateral) by 600 nm (vertical). The desired PhC lattices were fabricated by exposing one point after the other on the surface of the fused silica substrate (**Figure 25**). For faster fabrication, the galvanometric mirrors were used to move the laser beam to the desired positions. The exposure of one voxel on the surface led to the creation of the upper half of an ellipsoid of diameter (d) and height (h), in the following called a nanocone. Several of these nanocones formed the PhC matrix. The nanocone diameter was best controlled by varying the exposure dose via the exposure time or the laser power. The nanocone height was best controlled by positioning (Δz) the focal point higher or lower with respect to the substrate surface.

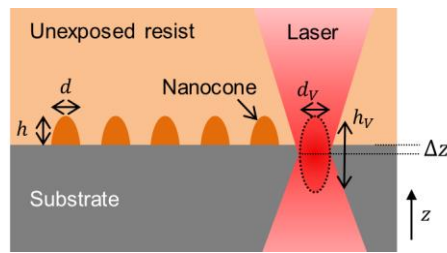


Figure 25. Illustration of the fabrication process for the PhC matrix. A voxel of diameter (d_v) and height (h_v) was utilized to produce ellipsoidal nanocones of height (h) and diameter (d). h was controlled by positioning the focal point higher or lower (Δz) with respect to the substrate surface.

4.3.1 Direct laser writing parameters

The most important parameter that determined the size the voxel was the exposure dose – related to the exposure time (t) and the laser power (P). The combinations of t and P , which allow the exposure of IP-Dip without causing micro-explosions is called the ‘writing window’. The maximum available laser power after the objective was 32 mW (see section 3.1.3). The exposure time had to be as short as possible to decrease the total fabrication time. To roughly outline the writing window:

Lower P limit: For $P < 3$ mW no exposure was possible for $t < 100$ ms.

Lower t limit: For $t < 0.015$ ms no exposure was possible for $P < 32$ mW.

Upper limit: For $t > 1$ ms micro-explosions occurred when using $P = 32$ mW.

The dimensions of the voxel are determined by Equations (3.1) and (3.2). Within these equations we find the factor $t \cdot P^2$. The factor implies that P has a stronger influence on the voxel dimensions due the non-linear nature of the polymerization. Furthermore, similar voxel dimensions are achieved by simultaneously varying P and t keeping $t \cdot P^2$ constant. Therefore, for fabricating nanocones of different dimensions it was chosen to keep t constant and only vary P . For increasing the fabrication speed a short exposure time of 0.15 ms was employed, one order of magnitude higher than the lower t limit.

To determine the voxel dimensions for different laser powers the ‘ascending voxel method’ [125] was performed. In this test, the focal spot position in relation to the substrate surface was slowly increased, until the fabricated voxels fall over and could be viewed from the side (similar to **Figure 17**). The

diameter and height of voxels were measured in SEM images (**Figure 26(A)**) with an accuracy of about ± 20 nm. **Figure 26(B)** shows the measured voxel dimensions as a function of the laser power. For example, at 13 mW the voxel had a diameter and a height of about 350 nm and 1150 nm, respectively. The voxel diameter only increased gradually for laser powers higher than 13 mW. For lower laser powers the voxel dimensions varied quite drastically. Therefore, slight variations in the laser power had a strong effect. Furthermore, the small height of the voxel at lower laser powers led to a stronger influence of variations in the position of the substrate surface (see section 3.1.4 and section 3.1.5).

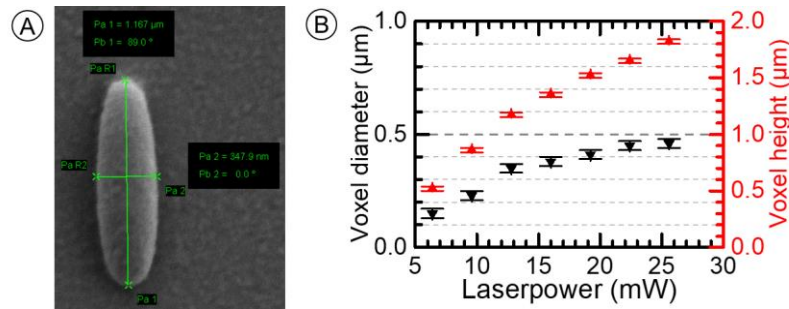


Figure 26. (A) Top view SEM image of a voxel exposed with a laser power of 13 mW. The voxel was exposed just above the substrate. It tipped over and could be viewed from the side. (B) Voxel dimensions at different laser powers for a constant exposure time of 0.15 ms measured using SEM images.

Knowing the voxel dimensions, nanocones of the desired height and diameter could be fabricated. The nanocone height was controlled by exposing the voxel at a specific position in relation to the substrate. As illustrated in **Figure 25**, Δz describes the difference in z-position of the substrate interface and the middle of the voxel. The height of the nanocone was approximated with $h = h_V/2 + \Delta z$. Since the voxel resembled an ellipsoid the tip was slightly slimmer than the waist. Therefore, when exposing the voxel deeper inside the substrate the nanocone diameter shrunk. The dependence of the nanocone diameter on Δz for a laser power of 13 mW is given in **Figure 27(B)**.

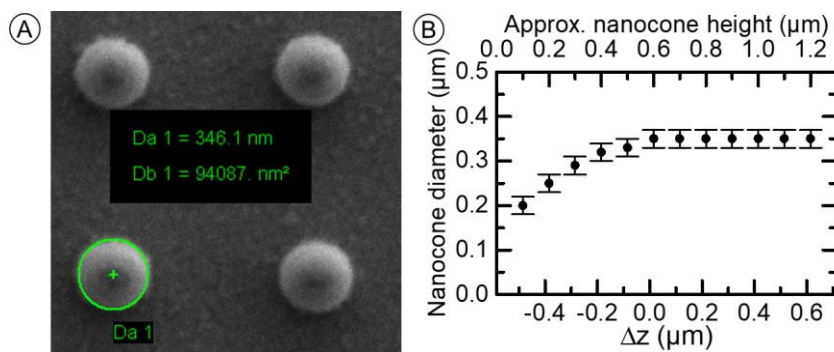


Figure 27. (A) Top view SEM images of nanocones exposed at a laser power of 13 mW, with an exposure time of 0.15 ms, and with $\Delta z = 0$. (B) Nanocone diameter in dependence of Δz , measured using SEM images.

Next to the dimensions of the individual nanocone the spacing distance was an important parameter for the prepared PhC lattices. The minimum spacing distance (a) for completely separated nanocones was limited by two proximity effects. The first kind, was a chemical proximity effect already introduced in section 3.1.1. The exposure of two voxels at close distance led to an exposure of the area between them. This chemical proximity effect typically set in when the nanocone spacing distance became

smaller than about 1.4 times the nanocone diameter. While the nanocones of diameter 350 nm in **Figure 28(A)** were completely separated for $a = 550$ nm fine exposed lines were visible between the nanocones for $a = 500$ nm in **Figure 28(B)**. The second kind of proximity effect was a physical effect important for nanocones of large aspect ratio ($h > 2d$). These high aspect ratio nanocones had a tendency to lean to one side, comparable to the Leaning Tower of Pisa. After development, when surface tensions led to high physical forces between closely spaced nanocones, a tilting of nanocones towards each other was observed as shown in the SEM image in **Figure 29**. As a consequence, nanocones of a high aspect ratio needed to be spaced further apart to obtain fully separated texture.

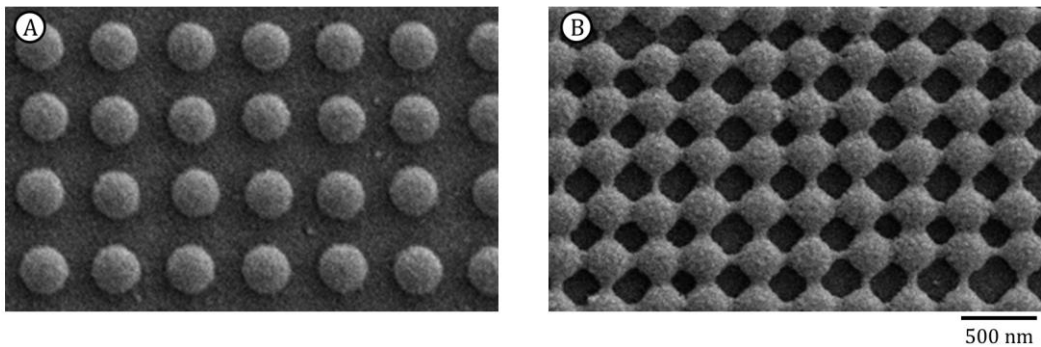


Figure 28. Top view SEM images of nanocones of approximately 350 nm diameter in a square lattice of lattice constant (A) 550 nm and (B) 500 nm. In (B) the chemical proximity effect is observable.

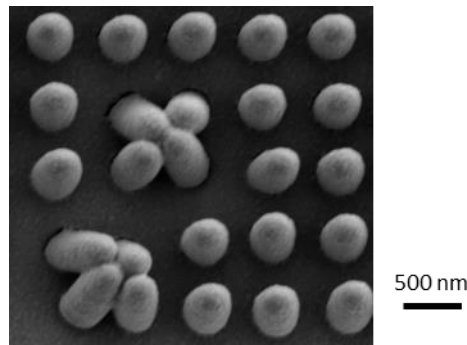


Figure 29. Top view SEM image of nanocones of about 350 nm diameter and about 1000 nm height in a square lattice of 550 nm spacing. Some of the nanocone tilted towards each other due to a physical proximity effect.

Besides the laser power, the exposure time, and Δz several other parameters also had to be considered for obtaining the desired PhCs:

Field of view. The field of view of the 63 \times objective using the galvanometric mirrors was specified with a diameter of 120 μm . Far away from the center of this field of view the beam was incident at large angles. The Petzval field curvature led to imprecisions in the position of the focal point. As exact positioning was key for the PhCs the fabrication area was limited to 80 μm by 80 μm .

Galvo settling time. After accelerating to a new position the galvanometric mirrors needed time to settle down. This parameter was the most critical in terms of the total writing time. A galvo settling time of 1.5 ms, below the default value of 3 ms, was used.

Piezo stage position. During exposure using the galvanometric mirrors the x- and y-positions of the piezo controlled stage were not changed. By default, they were set to zero in the piezo coordinate system. Due to the rotation of the coordinate system when using the DiLL method (see section 3.1.3), the x-drive was at full extend in this default position. In the fully extend state it was more sensitive to external vibrations. A swaying in the position of the focal spot was observed. **Figure 30** shows an SEM of a PhC that was programmed as a square lattice, the swaying is clearly visible. By manually setting the x-drive to the least extended position this problem could be resolved.

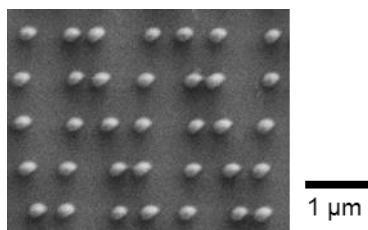


Figure 30. Top view SEM image of nanocones programmed in a square lattice. A square lattice is not obtained due to a swaying of the piezo controlling the x-drive.

Stage velocity. For accurate stitching of multiple fields not only the fabrication in negative x-direction was important (see section 3.1.4), but also a slow movement of the stage. Compared to the galvo- and the piezo-positioning the motorized stage positioning was very inaccurate. A slow movement on the order of 10 μm/s enhanced the positioning.

4.3.2 CIS nanocrystal infiltration

Produced nanocone PhC matrices were infiltrated with CIS nanocrystals using doctor blading. This thin-film fabrication technique is based on spreading an ink at constant velocity to form a homogenous wet film. The ink solvent is left to dry, leaving behind the solid content - in this case the CIS nanocrystals. The fused silica substrates on which the nanocones were produced had a dimension of 25 mm by 25 mm. For achieving a uniform CIS nanocrystal film in the textured area three fused silica slides were placed next to each other, as illustrated in **Figure 31**. The slide in the middle had the nanocone texture. On the first slide a drop (20 μl) of CIS nanocrystal ink (solvent: toluene) was placed. The blade was set to a height of 200 μm above the substrate surface. The drop was swept across the fused silica slides at a speed of 60 mm/s. The solid content was the most important parameter determining the CIS nanocrystal layer thickness. At a concentration of 100 mg/ml about 300 nm thick layers were achieved. To obtain thinner layers the concentration was decreased. To achieve thicker layer several consecutive coatings were used.

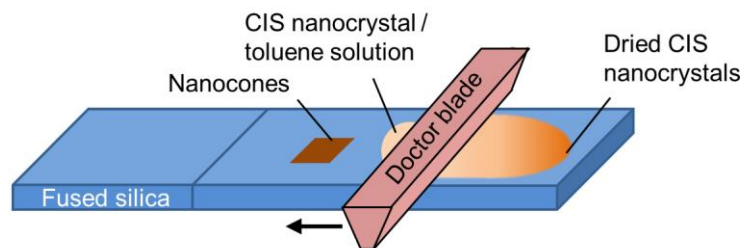


Figure 31. Illustration of the doctor blading setup used to infiltrate the PhC nanocone matrix with CIS nanocrystals.

4.4 Optical properties of IP-Dip

This chapter will discuss the results on measuring the optical properties, namely the real part (n) and the imaginary part (k) of the refractive index, of the used photoresist IP-Dip. The photoresist IP-Dip was used for fabricating patterns that were directly applied in PV devices. Precise knowledge of the optical properties of the material were therefore of importance.

While some data on the refractive index of IP-Dip became available in the time of this work [126], this data was based on measurements of UV exposed layers. Conventional UV exposure of photoresist is a one-photon polymerization (OPP) process, while DLW is two-photon polymerization (TPP) process. As the two processes are inherently different the research question to answer was whether the refractive index of produced layers would also differ. On the one hand, the refractive index depends upon degree of cross-linking, and therefore upon the dose in OPP [127] and upon the DLW parameters in TPP [128]. On the other hand, the degree of cross-linking, and with it the refractive index, goes into saturation for a large enough exposure dose. Some indication that saturation points differ for OPP and TPP exposure of IP-Dip came from Oakdale *et al.* [129]. They investigated the mechanical strength of DLW fabricated structures. While the mechanical strength varied with the DLW parameters, post-exposure with UV light after sample development did not have an effect. Only when applying additional photo-initializers for radical generation, a strong increase in the mechanical strength was possible using post-exposure treatment. Oakdale *et al.* [129] came to the conclusion that the DLW process locally consumes all photo-initializer molecules.

In this work, the application of a prism coupling method (section 3.2.4) to determine the refractive index of IP-Dip allowed a very unique comparison between the refractive index of OPP and TPP layers. While, other methods for determining the refractive index have only been suitable for one layer type. Spectroscopic ellipsometry, for example, has been used for determining the refractive index of OPP layers [130], as the needed large and flat areas could easily be fabricated - a difficult task in TPP. The refractive index of TPP photoresist, on the other hand, has been determined by means of interference in TPP fabricating geometrical structures [128] - a concept not easily transferable to OPP. The question, whether the refractive index of OPP and TPP IP-Dip layers varies was seen to have particular importance for large DLW fabricated structures. In case of large textures often only a shell has been TPP exposed and the interior has been OPP exposed after development to save writing time [61,131]. As this method combines OPP and TPP exposed IP-Dip in a single structure a difference in the refractive index will lead to an internal optical interface.

In the following, the techniques are described for fabricating samples for a direct comparison of the refractive index of OPP and TPP IP-Dip layers using the 2010/M (see section 3.2.4) prism coupler and the results are discussed.

4.4.1 DLW fabrication of flat layers

Flat layers, with an extend slightly larger than the employed laser spot (typically 1 mm^2), were needed for measurement using the 2010/M. The mode coupling method was employed, since it was in general more precise and producing layers thick enough for determining the critical angle of a bulk would have taken a lot of time using DLW. The layers should be thick enough to support at least two modes, but not too thick for the modes become indistinguishable. Reasonable layer thicknesses for IP-Dip on SiO_2 based substrates were $2 \text{ }\mu\text{m}$ to $20 \text{ }\mu\text{m}$.

The Nanoscribe Photonic GT (section 3.1), employing the $63\times$ objective, was used for DLW fabrication of IP-Dip layers on fused silica substrates. The exposure sequence used to form a flat layer within the field of view is illustrated in **Figure 32(A)**. Several planes were exposed on top of each other using a slicing distance of 300 nm to form about $3 \text{ }\mu\text{m}$ thick layers. For achieving homogenous layers several considerations had to be made: Firstly, the first plane was exposed more than the height of one voxel below the substrate surface, for a more homogenous dose throughout the layer. Secondly, a comparably small hatching distance of 125 nm was chosen to minimize surface roughness and variations of the dose within the layer. Thirdly, every exposed plane had an offset in both lateral directions of half the hatching distance (62.5 nm). This again improved the homogeneity of exposure and led to a slanted edge. The slanted edge had the additional benefit of allowing smoother stitching to produce the needed minimum area of 1 mm^2 . Blocks of $100 \text{ }\mu\text{m}$ by $100 \text{ }\mu\text{m}$ were exposed within the field of view (see SEM image in **Figure 32(B)**) and several of these blocks stitched to a large planar layer. Fourthly, to further improve the stitching an overlap of the fabricated blocks of 500 nm was used. The SEM images in **Figure 33** show the importance of this overlap. Too little overlap caused the block to rip apart during development (**Figure 33(A)**). Finally, a tilt of the substrate would have caused significant differences in the layer thickness, therefore the dedicated sample holder for tilt-correction (see section 3.1.5) was used.

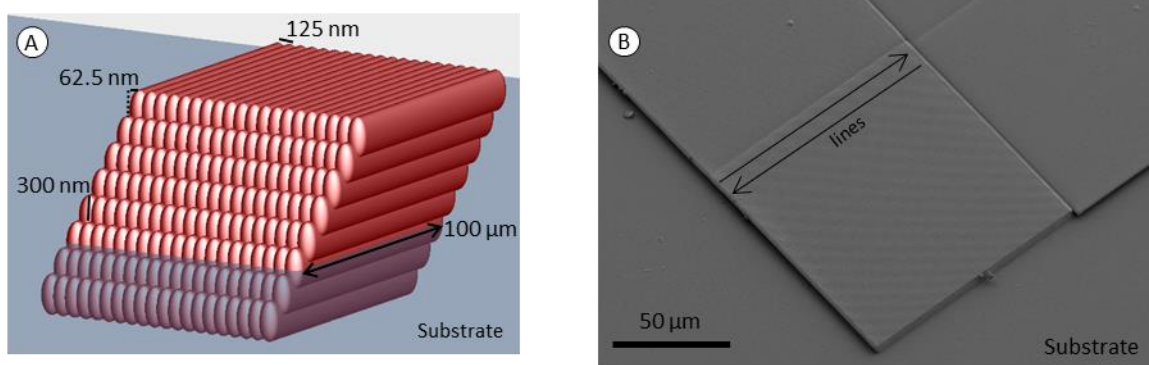


Figure 32. (A) Illustration of the exposure sequence used for the fabrication of one block of the flat IP-Dip layer. (B) SEM image (30° tilted view) of the edge of a fabricated flat layer. It is possible to distinguish the fabricated blocks at the stitched edges.

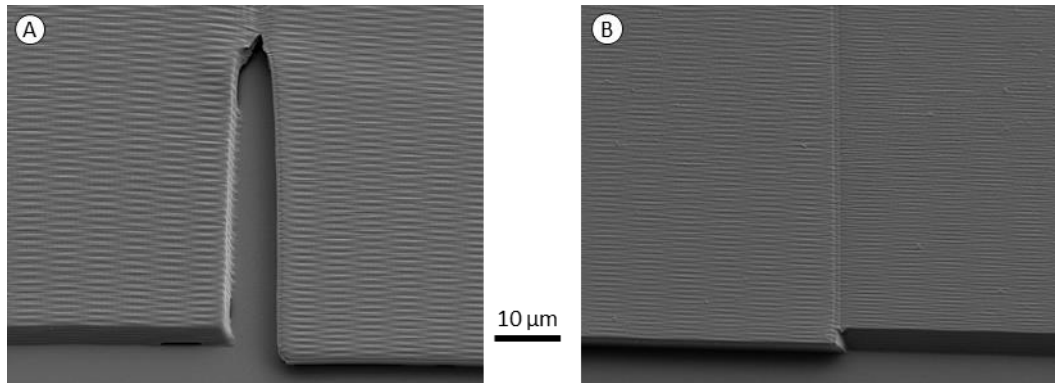


Figure 33. SEM images (30° tilted view) showing fabricated planar layers of IP-Dip. **(A)** Insufficient stitching lead to a tearing apart of fabricated blocks during development. **(B)** Stitched fields hold together when programming a larger overlap.

4.4.2 Stitching induced diffraction

The importance of proper stitching to achieve layers for refractive index measurements using the prism coupling method is to be noted again at this point. Especially in the case of low laser power trenches were likely between the fabricated blocks, as apparent in **Figure 33(A)**. A larger overlap between two blocks was needed to avoid this. The critical influence of the stitching became obvious when measuring the refractive index of a layer with inadequate stitching using the 2010/M. **Figure 34(A)** shows the detector signal of a layer with proper stitching (e.g. SEM image in **Figure 34(B)**) and the detector sample for a layer with improper stitching (e.g. SEM image in **Figure 33(A)**), at a wavelength of 637 nm. The dips in the detector signal arose from the coupling of light to guided modes in the IP-Dip layer. In **Figure 34(A)** all detected modes (indicated with a blue star) were consistent with a layer of $n = 1.540$ and thickness of $3.2 \mu\text{m}$. For the mode pattern in **Figure 34(B)**, no consistent refractive index and thickness were determined. No model of a flat layer could explain all of these modes. On the other hand, when only considering the modes marked with a blue star a consistent result was obtained ($n = 1.539$, closely matching the result of **Figure 34(A)**). The yellow triangles mark additional modes. Their origin was unclear at first. Nanostructuring of the layer due to the DLW process, as well as step variations in the layer thickness, was discussed. Finally, diffraction due to the periodic stitching came into focus.

There are just as many modes marked with a yellow triangle in **Figure 34(B)**, as there are modes marked with a blue star. The additional modes seem to be shifted versions of the original modes. As discussed in chapter 2.2.5 periodic textures diffract light and leading to specific shifts in the transmission angle at an interface. Equation (2.42) gives the effective refractive index of the modes incident diffracted light couples to. For the small shift observed in **Figure 34(B)** very large periodicities were needed. The stitching of layers resulted in a $100 \mu\text{m}$ period. **Figure 35(A)** relates the incidence angle to the mode effective refractive index (n_{eff}) according to Equation (2.42) for $m = -1, 0$, and 1 , using $n_1 = 1.9642$ (refractive index of the prism at 637 nm) and $a = 100 \mu\text{m}$. **Figure 35(B)** shows the same data as **Figure 34(B)**. For every dip indicated with a star there is a dip indicated with a triangle related to the same effective refractive index. Therefore, what seemed to be additional modes were actually the same modes. Coupling was possible under different angles of incidence due to diffraction arising from the stitching periodicity.

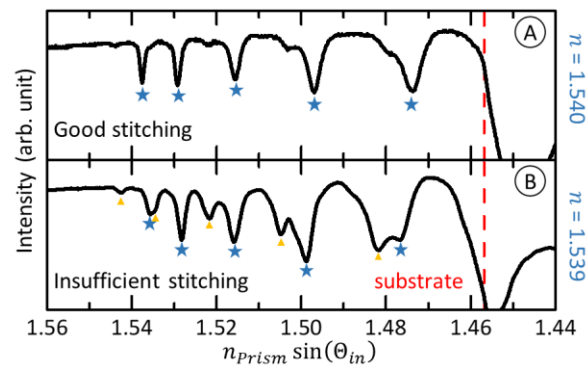


Figure 34. Detector signals for different incidence angles (θ_{in}) measured with the Model 2010/M at a wavelength of 637 nm using a prism of refractive index $n_{prism} = 1.9642$. Except for the stitching overlap all DLW parameters were kept constant. **(A)** A sample with decent stitching of the DLW produced blocks. From the identified modes mark with a blue star a film refractive index of 1.540 was calculated. **(B)** A sample with clear gaps between the blocks. From the identified modes mark with a blue star a consistent refractive index of 1.539 was calculated. Additional modes are marked with a yellow triangle.

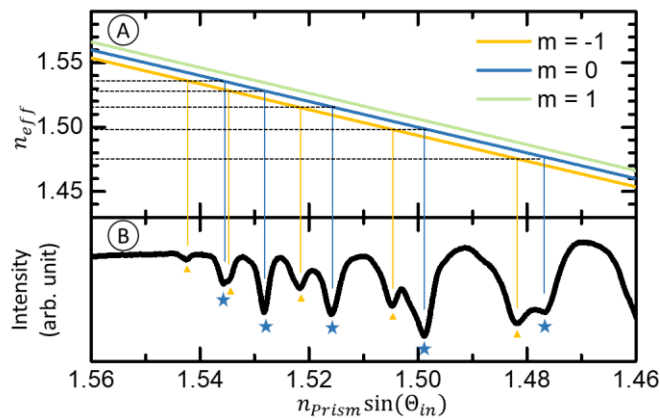


Figure 35. **(A)** Relation between the incidence angle and the effective refractive index according to Equation (2.32) for $a = 100 \mu\text{m}$. **(B)** The measured reflectance pattern already shown in **Figure 34(B)**. The detected dips in the reflectance spectrum are related to the same mode by diffraction.

4.4.3 The exposure dependent refractive index of IP-Dip

For measuring the refractive index of TPP IP-Dip layers (using the Model 2010/M) DLW fabricated layers were prepared as described above. OPP layers were prepared by sandwiching a drop of IP-Dip between two glass slides. For anti-adhesion, one of the glass slides was silanized by first treating it with an oxygen plasma at 100 W for 2 min to obtain hydroxyl groups on the surface and then placing it in a desiccator, together with 200 μl of perfluorooctyl-trichlorosilane (PFOTS, Sigma Aldrich), pumped to 200 mbar for 30 min. The PFOTS forms a monolayer on the surface, reducing the surface energy and leading to hydrophobicity. Thin IP-Dip layers were achieved by the pure force of gravity acting on the glass slide on top of the sandwich described above. The IP-Dip layers were exposed through the glass slide in an exposure chamber (Irradiation Chamber BSL-01, Opsytec Dr. Gröbel) using 405 nm LEDs at an intensity of 75 mW/cm^2 . After curing the silanized glass slide was taken off by applying a small force. The OPP IP-Dip layers had thicknesses on the order of 5 μm to 25 μm , strongly varying with the volume of the used

IP-Dip drop and the resting time before exposure. The exact thickness was not important for the refractive index measurements.

As stated earlier, the refractive index of a polymer is related to the degree of cross-linking. The degree of cross-linking is to a large extent governed by the exposure dose. In OPP, the exposure dose could easily be controlled by varying the exposure time. Saturation in the cross-linking was reached for exposure doses $>100 \text{ J/cm}^2$. In TPP, with the hatching and slicing distance fixed, the dose in the exposed layers depended upon the scan speed and the laser power. To minimize fabrication time a constant scan speed of 25 mm/s was used. The laser power was varied. For the parameters described above, the fabrication of layers without micro-explosions was possible in the laser power range $\sim 12 \text{ mW}$ to $\sim 17 \text{ mW}$. For lower laser powers the fabrication of flat IP-Dip layers was not possible. For higher laser powers micro-explosions occurred in the layer. **Figure 36(A)** shows the measured refractive index for the different fabricated layers measured with the 2010/M at a wavelength of 637 nm .

In-line with expectations, a larger dose led to a larger refractive index. In TPP, laser powers beyond 17 mW were also used for layer creation to show the further increase in refractive index. These are marked with empty circles. Due to the micro-explosions these results should be treated with caution. When exposing a TPP fabricated layer with UV light no change in the refractive index was observed. This perfectly matched the local consumption of photoinitiator postulated by Oakdale *et al.* [129]. Therefore, developed layers of TPP IP-Dip had a lower refractive index than a fully cured (dose: $>100 \text{ J/cm}^2$) OPP layers even with post-treatment. Finally, the wavelength dependence of the refractive index was investigated. A TPP layer exposed with a laser power of 14 mW , was compared to a fully cured (dose: 120 J/cm^2) OPP layer. It was possible to fit the measured data to the Cauchy model for lossless media

$$n(\lambda) = \gamma_1 + \frac{\gamma_2}{\lambda^2} + \frac{\gamma_3}{\lambda^4} \quad (4.9)$$

where γ_1 , γ_2 , and γ_3 are constants and λ is the wavelength. The fitting parameters γ_1 , γ_2 , and γ_3 for the TPP and OPP layer are given in **Table 2**.

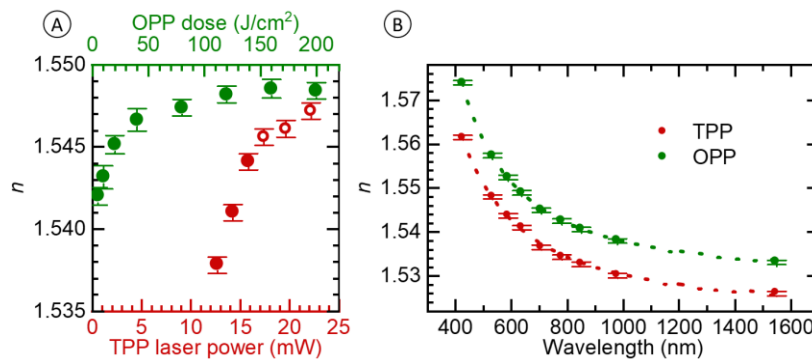


Figure 36. (A) Dose dependent refractive index (n) of TPP and OPP IP-Dip layers measured at a wavelength of 637 nm . (B) Dispersive refractive index of a TPP IP-Dip layer fabricated with a laser power of 14 mW and an OPP IP-Dip layer exposed with 120 J/cm^2 . Adapted with permission from [90], © OSA.

	γ_1	$\gamma_2 (\mu\text{m}^2)$	$\gamma_3 (\mu\text{m}^4)$
TPP (14 mW)	1.53012	0.00732	0.0001158
OPP (120 J/cm²)	1.52266	0.00733	-0.0000482

Table 2. Cauchy coefficients obtained by fitting Equation (4.9) to the dispersive refractive index in **Figure 36(B)**.

4.4.4 The extinction coefficient of IP-Dip

The extinction coefficient (κ) was determined from absorbance measurements using the spectrometer Lambda 950 (see section 2.2.4). Due to the large spot size of the system an area of more than $\sim 10 \text{ mm}^2$ was needed for measurements. Therefore, the DLW fabrication of layers thick enough for accurate measurements would have taken an intolerable amount of time. Only OPP was used to fabricate layers for absorbance measurements. As described above, layers were fabricated by sandwiching a drop of IP-Dip between two fused silica slides. To obtain layers of defined thickness polyvinyl chloride (PVC) foil (Minitron Elektronik GmbH) of thickness $l = 75 \text{ }\mu\text{m}$ was used as a spacer.

Taking into account the front surface transmissivity at normal incidence according to the Fresnel equations (Equations (2.23) and (2.24)) and the Beer-Lambert law (Equation ((2.13))) κ was approximated from the measured absorbance (A) via:

$$A \approx \frac{4n_{FS}}{(1+n_{FS})^2} \exp\left(\frac{-4l\pi\kappa_{IP-DIP}}{\lambda}\right), \quad (4.10)$$

where n_{FS} is the refractive index of the fused silica substrate (values are found the Appendix). The absorbance was measured in the wavelength range from 300 nm to 1700 nm. **Figure 37** shows the calculated κ_{IP-DIP} in dependence of the exposure dose (D). In case of an unexposed layer a large absorption peak was visible at 428 nm with a full width half maximum (FWHM) of 62 nm related to the photoinitiator of IP-Dip. During exposure this absorption peak decreased, while absorbance in the wavelength range 500 nm to 700 nm increased. In the measurement range, beyond 700 nm significant absorption only occurred in the water bands at $\sim 1200 \text{ nm}$, $\sim 1400 \text{ nm}$, and $\sim 1700 \text{ nm}$.

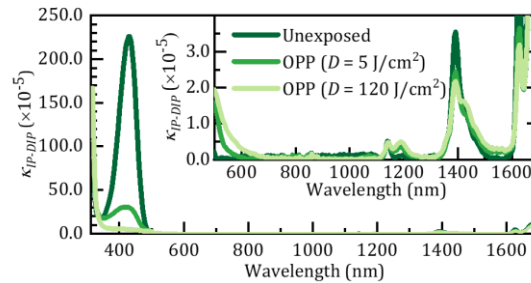


Figure 37. Extinction coefficient (κ) of IP-Dip for different exposure dose (D) calculated from absorbance measurements on $75 \text{ }\mu\text{m}$ thick layers exposed with 405 nm LEDs. Adapted with permission from [90], © 2019 OSA.

4.5 Optical properties of CIS nanoparticles

The CIS nanocrystals used in this work were prepared by the Korgel group in the Department of Chemical Engineering part of the Texas Materials Institute (TMI) at the University of Texas at Austin (UTA). They were produced by arrested precipitation using diphenylphosphine selenide reactant. Details on the synthesis are found in Supporting Information to the work of Panthani *et al.* [92]. At a reaction temperature of 240°C nanocrystals of $8.6 \pm 1.9 \mu\text{m}$ were formed. The nanocrystals are capped with oleylamine ligands and were dissolved in toluene in a 100 mg/ml solution.

4.5.1 CIS nanocrystal layer preparation

For measuring the optical properties of the CIS nanoparticle films Aina Quintilla prepared layers of thickness 80 nm, 100 nm, 170 nm and 400 nm on microscope slides of 26 mm by 75 mm dimensions using the doctor blading method described above (section 4.3.2). **Figure 38** shows the prepared layers of varying thickness. The layer thicknesses were determined by scratching the surface and scanning the scratch with a DektakXT surface profiler (Bruker Corporation, Billerica, U.S.A.).

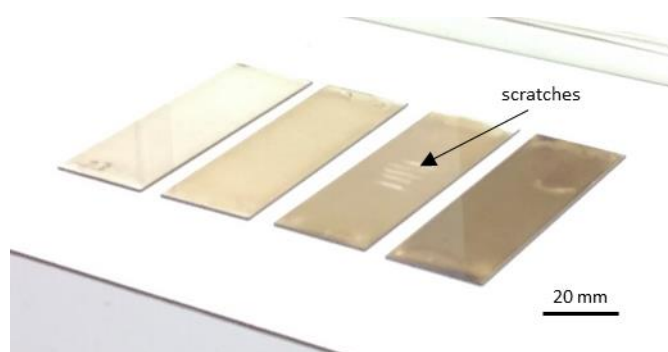


Figure 38. CIS nanocrystal layers of thickness 80 nm, 100 nm, 170 nm and 400 nm deposited on microscope slides using doctor blading.

4.5.2 The complex refractive index of CIS nanocrystal layers

The CIS film were investigated by Aina Quintilla using spectroscopic ellipsometry (chapter 3.2.4). Based on the three band transitions report in bulk CIS [132] three Tauc-Lorentz oscillators [133] were used to model the ellipsometry data in the WVASE software. Additionally, an effective medium approximation was used to model a rough surface of the CIS films. Due the large number of free parameters different initial values led to different results. To determine the best fit measurements of the reflectance and the transmittance of the samples were conducted using a UV/Vis spectrometer (chapter 3.2.2) by the author. The measurement results were compared to simulation results on the reflectance and transmittance using the transfer matrix method (TMM) approach (chapter 3.3.3) and employing the complex refractive index ($n_{CIS} + i\kappa_{CIS}$) of the CIS nanocrystal layers determined using different initial values in the spectroscopic ellipsometry model. By means of this comparison the best parameters suiting the ellipsometry model could be determined. The final parameters and model fit to the obtained spectroscopic ellipsometry data with a low mean square error (MSE) of 2.1. The determined wavelength-dependent n_{CIS} and κ_{CIS} are plotted in **Figure 39**. The values are given in the Appendix.

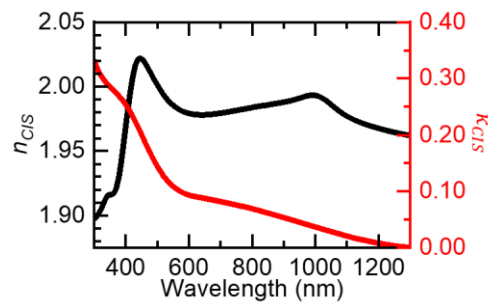


Figure 39. The real part (n_{CIS}) and the imaginary part (κ_{CIS}) of the refractive index determined for CIS nanocrystal films using spectroscopic ellipsometry. Adapted with permission from [91], © 2017 OSA.

Figure 40(A) shows the reflectance, transmittance, and absorptance of one of the sample used for determine the complex refractive index (400 nm layer thickness). The simulation data was calculated using TMM. A good match to the experimentally obtained data was achieved. **Figure 40(B)** shows the same data for a 225 nm thick film fabricated at a later point in time. A slight mismatch was observed, indicating that there might be fluctuations in the amount of solvent left in the layer, or degradation of the material. Nevertheless, the obtained n_{CIS} and κ_{CIS} data were highly usable for performing the FDTD simulations described in the following section. In general, the PhC based light-trapping scheme should target wavelengths in the range 600 nm to 1200 nm were the penetration depth of light is large.

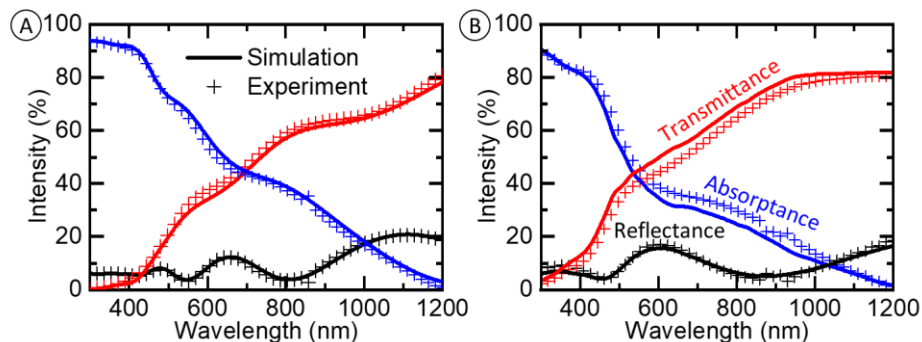


Figure 40. Experimental and simulation data of the reflectance, transmittance and absorptance of CIS nanocrystal films on glass slides. **(A)** 400 nm thick CIS film used for determining the refractive index. **(B)** 225 nm thick CIS film from a different batch. **(A)** was adapted with permission from [91], © 2017 OSA.

4.6 Numerical prototype analyzation

Numerical simulations were performed for a detailed understanding of the coupling mechanisms between incident light and optical modes guided in the thin CIS nanocrystal layers. Furthermore, simulations were used to determine optimum nanocone dimensions and determining the general effectiveness of the scheme. While Equation (4.6) gives the coupling condition, the strength of the coupling needed be analyzed using numerical simulations. FDTD (chapter 3.3.1) simulations were employed. A limiting factor was that calculating large patterns was not feasible with current desktop computers. Therefore, the following in-depth analysis was limited to a square lattice of lattice constant a , allowing the use of a small unit cell with periodic boundary conditions.

4.6.1 Initial calculations

Using the determined complex refractive indices it was possible to analyze the mode coupling in PhC patterned CIS nanocrystal layers. The equations in section 4.2 determine the number of quasi-guided modes, as well as the wavelength of incident light that couples to these modes.

Coupling condition. The wavelength of incidence light coupling to guided modes is given by the general coupling condition (Equation (4.6)). The absolute of the reciprocal lattice vector (K_{xy}) of the square lattice under investigation is given by:

$$K_{xy} = \frac{2\pi}{a} \sqrt{m^2 + p^2}, \quad (4.11)$$

where m and p are integers. The diffraction order is given by: (m,p) . Insertion into Equation (4.6) leads to:

$$n_{eff} = \left| \frac{\lambda}{a} \sqrt{m^2 + p^2} \pm \sin(\theta_{in}) \right|, \quad (4.12)$$

where θ_{in} is the incidence angle and n_{eff} the effective refractive index of a guided mode.

In the prototype setup, with the PhC patterned CIS nanocrystal layer (refractive index: $n_{CIS} < 2.0$) on top of a fused silica substrate (refractive index: $n_{sub} \approx 1.45$) the effective refractive index of guided modes followed the condition: $n_{CIS} \geq n_{eff} > n_{sub}$. Allowing a narrowing of the wavelength range in which the coupling condition was fulfilled for a given combination of a and θ_{in} . For example, in the normal incidence case ($\theta_{in} = 0$) the first diffraction order (1,0) allowed coupling to guided modes in the range $2 \geq \lambda/a > 1.45$. The “ \pm ” in Equation (4.12) led to two possible solutions for every diffraction order for larger angles of incident. For 30° incidence angle the first diffraction order allowed coupling in the range $(1,0)^+$: $1.5 \geq \lambda/a > 0.95$ and $(1,0)^-$: $2.5 \geq \lambda/a > 1.95$. **Figure 41**, shows the results for the first three diffraction orders and all the possible incidence angles. The first diffraction order, where the strongest coupling was expect should allow coupling to wavelengths at the lower absorption limit of the CIS nanocrystals around 1000 nm. It was therefore predicted that $500 \text{ nm} > a > 750 \text{ nm}$ is an interesting range.

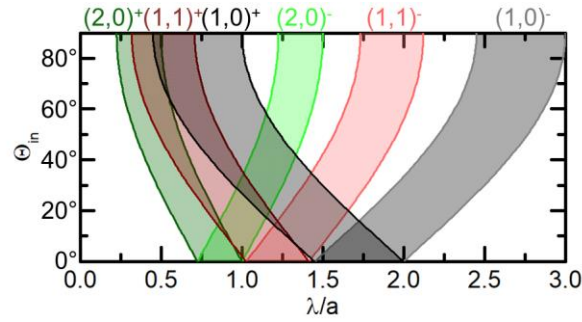


Figure 41. Solutions to the coupling condition (Equation (4.12)) for modes in the range $2 \geq n_{eff} \geq 1.45$.

Average refractive index. For determining n_{eff} of guided modes in a layer of given thickness first the average refractive index (n_{avg}) of the PhC patterned CIS nanocrystal layers needed to be calculated. The average refractive index was determined using an effective medium approximation EMA (section 2.2.6). While exact expressions for average refractive index have been determined for a 1D grating [134], it is likely that an analytical solution for the average refractive index of a 2D grating does not exist. Good results have been achieved using volumetric averaging [135] and polynomial fitting [136]. For symmetry reasons a simple weighted average has been used for normal incidence light [137]:

$$n_{avg}(\lambda) = F n_{IP-DIP}(\lambda) + (1 - F) n_{CIS}(\lambda), \quad (4.13)$$

where F is the volume fraction of IP-Dip (refractive index: n_{IP-DIP}) in the PhC patterned CIS nanocrystal (refractive index: n_{CIS}) layer. **Figure 42** shows how the weighted average relates to the Weiner bounds (section 2.2.6), using $n_{IP-DIP} = 1.54$ and $n_{CIS} = 2.0$. For simplicity the weighted average was used to determine the average refractive index in the following. It is to be noted that for TE modes the electrical field oscillates in the waveguide plane and thus perpendicular to the texturing. Therefore, the average refractive index in case of TE modes might be closer to the lower Weiner bound.

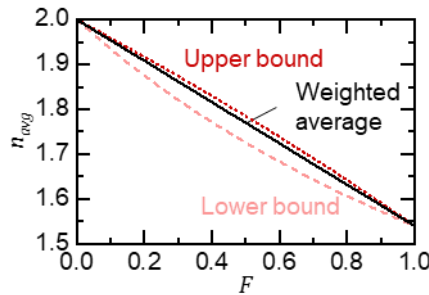


Figure 42. IP-Dip volume fraction (F) dependent average refractive index layer of the PhC patterned CIS nanocrystal layer.

The volume fraction F of the PhC matrix was determined by the dimensions of the DLW fabricated nanocones. The nanocones were approximated, as half-ellipsoids. The volume of one nanocone (V_{NC}) was estimated with:

$$V_{NC} \approx \frac{\pi}{6} h d^2, \quad (4.14)$$

where h and d are the nanocone height and waist diameter, respectively. The total volume within one unit cell (V_{UC}) of the square lattice patterned CIS nanocrystal layer, of layer thickness l , was $V_{UC} = a^2 l$. For non-overlapping nanocones ($(d < a) \equiv (F < \pi/6)$), smaller than the layer thickness, it was:

$$F = \frac{V_{NC}}{V_{UC}} = \frac{\pi h d^2}{6 l a^2}. \quad (4.15)$$

In simulations, $h = l$ was used for further simplification. Using the feasible nanocone diameters of about 200 nm to 500 nm (see **Figure 26**), F up to 50% was possible in the target lattice constant range ($500 \text{ nm} < a < 750 \text{ nm}$). Considering that even larger F would have greatly reduced the amount of active material, the possible nanocone diameters perfectly fit the enhancement scheme.

Number of guided modes. The number of TE and TM guided modes was calculated according to Equations (4.7) and (4.8), respectively. The result for $F = 20\%$ ($n_{avg} = 1.9$) is shown in **Figure 43**. In the important range for light-trapping around 1000 nm only one mode of each polarization was present for layer thicknesses in the range 100 nm to about 300 nm. For layer thicknesses up to about 500 nm there are two modes of each polarization. These small numbers of modes will be highly beneficial in the following analysis for very precisely relating an increase in absorptance to a specific mode. On the other hand, the small number of modes, arising from the small refractive index of the CIS nanocrystals, will limit the light-trapping potential of the PhC scheme in a device.

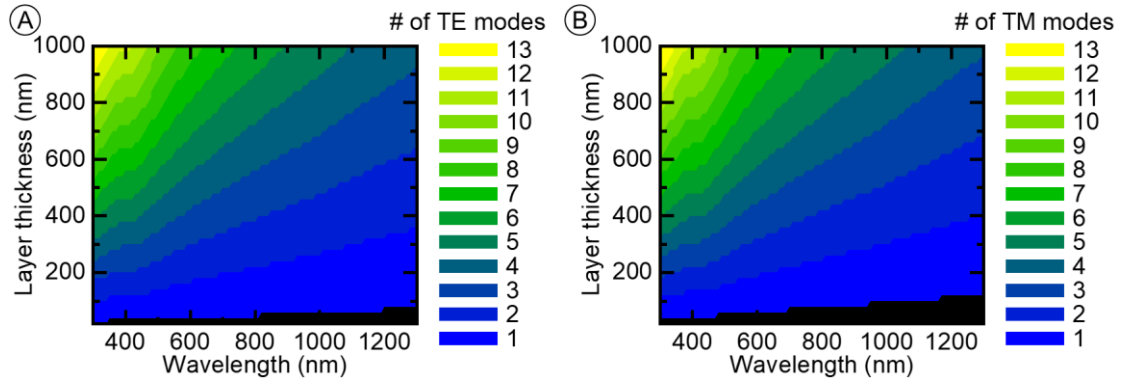


Figure 43. Number of guided (A) TE and (B) TM modes in a PhC textured layer of CIS nanocrystals in an IP-Dip matrix for $F = 20\%$, on fused silica substrate.

4.6.2 FDTD prototype simulations

The parameters defining the investigated square lattice patterned CIS layers were the layer thickness l , the lattice constant a , and the volume fraction F . The number of guided modes was most critically effected by l . The most important parameter governing the coupling condition in a film of given thickness was a . F had some effect on the number guided modes, since a higher F reduced n_{avg} . Moreover, F effected the coupling strength. FDTD simulations were performed to investigate the interplay of these parameters more precisely and find optimum parameters for increasing the absorptance of light in the layer.

Simulation setup. The commercial software FDTD solutions (section 3.3.1) was used for performing the FDTD simulations. The simulation environment is illustrated in **Figure 44(A)**. A fused silica substrate was defined, with a CIS nanocrystal layer on top. The CIS nanocrystal layer was textured into a square lattice

by the IP-Dip nanocones. As mentioned above, the nanocones were defined as half-ellipsoids exactly as high as the CIS nanocrystal layer. The PhC textured CIS nanocrystal layer was illuminated from a source in the fused silica generating plane waves in the wavelength range 300 nm to 1300 nm. In x - and y -direction the simulation region had periodic boundary conditions and was scaled to exactly one unit cell of the square lattice. In z -direction the simulation region ended with a perfectly matched layer (PML) of 24 layers, absorbing all incident light. A 10 nm mesh was used, and the auto shut-off was set to 10^{-5} . The measured complex refractive indices (chapters 4.4 and 4.5) of the materials were implemented. In the program FDTD solutions material data was interpolated by a polynomial. For the CIS nanocrystals a polynomial with 12 coefficients was used.

To obtain a planar reference for a CIS nanocrystal layer without the PhC matrix a 2D simulation setup was used (**Figure 44(B)**). In the 2D simulation the number of grid cells was greatly reduced, drastically decreasing the simulation time. To calculate the increase in absorptance induced by the PhC texturing two different planar references were possible: Either a CIS nanocrystal layer of identical thickness to the PhC textured layer, or a thinner layer of identical CIS nanocrystal volume. Both are fair comparisons. The thickness limitation of the CIS nanocrystal layer due to charge carrier transport favored a comparison to a layer of identical thickness. Economic considerations might have favored a comparison to a layer of identical CIS volume. Here, the higher benchmark of planar CIS nanocrystal layers of identical thickness were used for determining the efficiency of the PhC scheme.

The absorptance in the CIS nanocrystal layer could have been determined using a volume monitor, but determining the absorptance in every grid cell, generates large amounts of data, drastically increasing simulation time and the needed computer space. Instead, the absorptance (A) in the CIS nanocrystal layer was determined from monitoring the reflectance (R) and the transmittance (T) of light above and below the CIS nanocrystal layer (compare **Figure 44(B)**), respectively, and using $A = 1 - R - T$. As a consequence, the absorption of light in IP-Dip was not considered, since distinguishing between light absorbed in IP-Dip and in the CIS nanocrystals would not have been possible. As a restriction in FDTD solutions, only materials of constant n had $\kappa = 0$ (0th order polynomial), therefore, $n_{IP-DIP} = 1.54$ was used as a close approximation to the refractive index of IP-Dip around a wavelength of 1000 nm. Along the same lines, $n_{FS} = 1.45$ was implemented for the fused silica substrate.

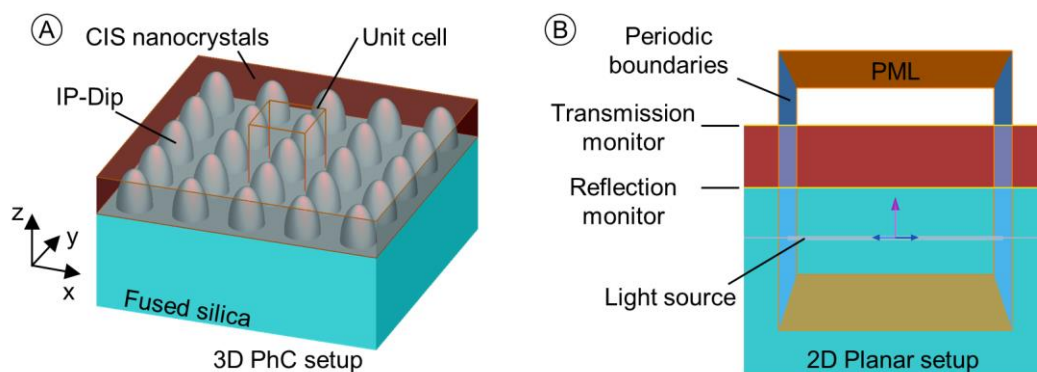


Figure 44. Illustration of the simulation setups in Lumerical FDTD solutions. **(A)** 3D simulation setup for simulating the CIS nanocrystal infiltrated nanocone matrix. **(B)** 2D simulation setup to obtain a planar reference.

Mode coupling. First, the impact of a and F on the coupling strength was investigated qualitatively. To do so a CIS nanocrystal layer of constant thickness under normal incidence illumination was simulated in

FDTD solutions. A layer of 250 nm thickness was chosen, only allowing the propagation of the 0th order TE mode in the long wavelength range (600 nm to 1300 nm). The top graphs in **Figure 45** show graphical solutions to the coupling condition according to Equation (4.12), relating the mode effective refractive index to the reciprocal lattice vector. The average refractive index of the layer, as a function of F , was calculated according to Equation (4.13). The average refractive index was used to calculate the effective refractive index of the 0th order TE mode in the 250 nm thick layer according to Equation (2.30), valid for an asymmetric slab waveguide. Furthermore, the reciprocal lattice vector is plotted in the graphs according to Equation (4.11), for different diffraction orders (m,l). The coupling condition (Equation (4.12)) was met where the mode effective refractive index and the reciprocal lattice vector intersect. These intersections related to peaks in absorptance in FDTD simulations, shown in the bottom graphs of **Figure 45**. This relation was highlighted with the guides to the eye in **Figure 45(A)**. In **Figure 45(A)** $F = 20\%$ and $a = 600$ nm were used. Two peaks were clearly visible related to the (1,0) and the (1,1) diffraction orders. The coupling strength of higher diffraction orders did not seem to be strong enough to introduce significant light-trapping. In general, even the strongest coupling to the (1,0) diffraction order barely led to a doubling in absorptance. The reason is the small refractive index difference between the IP-Dip texture and the CIS nanocrystals.

The impact of F and a on the coupling strength is shown in **Figure 45(B)** and **(C)**, respectively. While a larger F led to higher peaks in absorptance, it also drastically reduced the absorptance in the short wavelength range. This reduction in short wavelength absorptance originated from the overall low extinction coefficient of the CIS nanocrystals at all wavelength. Even light of wavelength 300 nm was partially transmitted through a 250 nm thick layer. As the CIS nanocrystal volume reduced with an increasing F an even larger amount of light was transmitted. Looking at variations in a in **Figure 45** the large possible shift of the coupling condition becomes obvious. With an increasing a the peaks in absorptance became higher and narrower, likely due to an increasing Q-factor of the modes.

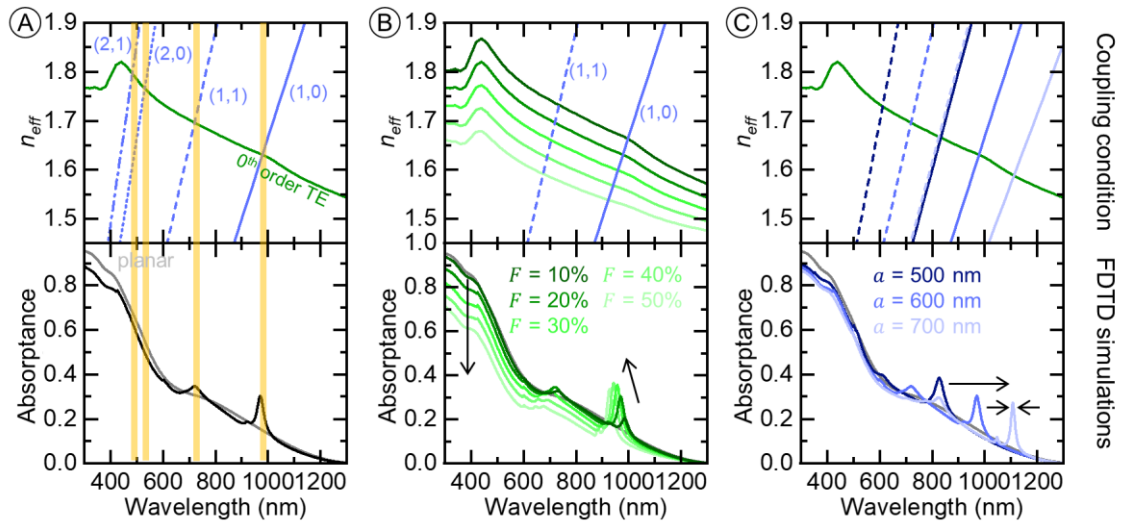


Figure 45. Simulation results for a 250 nm thick PhC textured CIS nanocrystal layer on fused silica. The top graphs show the effective refractive index (n_{eff}) of the 0th order TE mode (green) calculated according to Equation (2.30) using different volume fractions (F), as well as the reciprocal lattice vector (blue) for different lattice constants (a). The bottom graphs show the absorptance in the layer determined from FDTD simulations. **(A)** Relation (yellow guides to the eye) between the coupling condition and peaks in absorptance in FDTD simulations for $F = 20\%$ and $a = 600$ nm. **(B)** Impact of F on the overall absorptance and on the peaks in absorptance, for $a = 600$ nm. **(C)** Impact of a on the absorption peaks, for $F = 20\%$.

Parameter optimization. The parameters a and F influenced the position and amplitude of peaks in absorptance, and a large F decreased the absorptance in the short wavelength range. The important question was therefore, what were the optimum parameters for a given layer thickness. CIS nanocrystal PV devices have shown non-zero internal quantum yield in the wavelength range 400 nm to 1300 nm [94]. In a first step, the average absorptance (\bar{A}) in this wavelength range was calculated

$$\bar{A} = \frac{1}{900nm} \int_{400nm}^{1300nm} A(\lambda) d\lambda. \quad (4.16)$$

In a solar cell the utilization of the solar spectrum is important. The generated current is related to the external quantum efficiency according to Equation (2.5). Here, external quantum efficiency data was not available, thus calculating the generated current was not possible. Instead it was possible to calculate the average absorptance weighted by the photon flux (\bar{A}_Φ) as a good approximation of the potential performance:

$$\bar{A}_\Phi = \frac{\int_{400nm}^{1300nm} \Phi(\lambda) A(\lambda) d\lambda}{\int_{400nm}^{1300nm} \Phi(\lambda) d\lambda}, \quad (4.17)$$

where Φ is the incident photon flux. The AM1.5g spectrum (section 2.1.3) was used for the incident photon flux. For the case of a 250 nm thick CIS nanocrystal layer the small peaks in absorptance, due to mode coupling, did not compensate the loss in the short wavelength range for any combination of a and F . A planar layer showed the highest (weighted) average absorptance. Stronger absorption of UV light in the CIS nanocrystal layer, as well as more modes were essential for the effectiveness of the coupling scheme. In a layer of 500 nm thickness both was true.

Figure 43(A) indicates that at least two TE modes propagate in a CIS nanocrystal layer of 500 nm thickness around a wavelength of 1000 nm. The calculated n_{eff} of the first three orders TE modes in a 500 nm thick CIS nanocrystal layer with $F = 20\%$ are shown in top graph **Figure 46(A)**. For a graphical solution to the coupling condition, the first three diffraction orders for $a = 650$ nm are shown as well. High peaks in absorptance were observed in FDTD simulations where the 0th and the 1st order TE modes intersect with the (1,0) diffraction order. Since overall a much stronger attenuation of light was achieved in this thicker layer, the decrease in absorptance in the short wavelength range with increasing F was less pronounced. The average absorptance and the weighted average absorptance of a planar layer of 500 nm thickness were 0.41 and 0.45, respectively. For certain combinations of F and a higher values were achieved with a PhC textured layer. For the average absorptance (**Figure 46(B)**) the highest values were reached for a in the range 600 nm to 700 nm and F in the range 15% to 25%, peaking at $a = 650$ nm and $F = 20\%$. The weighted average absorptance (**Figure 46(C)**), on the other hand, showed a distinct dip at $a = 650$ nm. This resulted from an overlap (see **Figure 46(A)**) of the peaks in absorptance with the reduced photon flux in the AM1.5g spectrum around 950 nm and 1050 nm, arising from the absorption of light by water in the atmosphere.

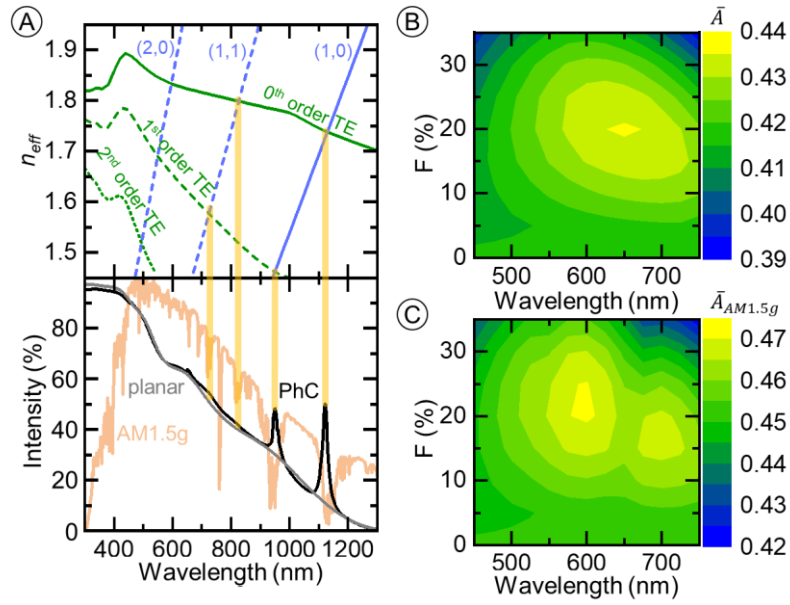


Figure 46. (A) Simulation results for a 500 nm thick PhC textured CIS nanocrystal layer on fused silica. The top graphs show the effective refractive index (n_{eff}) of the TE modes (green), using $F = 20\%$, and the reciprocal lattice vector (blue) for $a = 650$ nm. The bottom graph shows the absorptance determined from FDTD simulations, for a planar layer (gray) and a PhC textured layer (black), as well as the normalized AM1.5g spectrum. The average absorptance (B) and the AM1.5g weighted average absorptance (C) for PhC textured CIS nanocrystal layers of 500 nm thickness on fused silica.

Incidence angle and polarization. Finally, simulations with non-normal incidence light were performed. While normal incidence light only coupled to TE modes, TM modes became important for any other angle of incidence. In Lumerical non-normal incidence simulations could either be performed using Bloch-boundary conditions that ensure a periodicity in phase, or using the Broadband Fixed Angle Source Technique (BFAST). Using Bloch-boundary conditions the incident-angle was subject to dispersion. Only one wavelength could be simulated at a specific incidence angel at a time. BFAST used a new formulism that became available during the time of this dissertation [138]. It allowed the simulation of multiple wavelengths at a given incidence angle in a single run. For large angles of incidence ($>60^\circ$) BFAST was less stable than applying Block-boundary conditions.

Investigating a layer of 250 nm thickness it was possible to track the coupling to the single TE and TM mode that were present. **Figure 47** shows the FDTD simulated absorptance in a 250 nm thick CIS nanocrystal layer with $F = 20\%$ and $a = 600$ nm. For incident p-polarized light the angle-dependent (**Figure 47(A)**) positions of peaks in absorptance were related to the coupling condition (Equation (4.12)) and followed the trend already illustrated in **Figure 41**. As the symmetry was broken the single peak present at normal incidence degenerated to two possible solutions to the coupling condition. On the other hand, when changing the polarization (**Figure 47(B)**) of the incident light to s-polarization it was possible to switch between coupling to the TE and the TM mode.

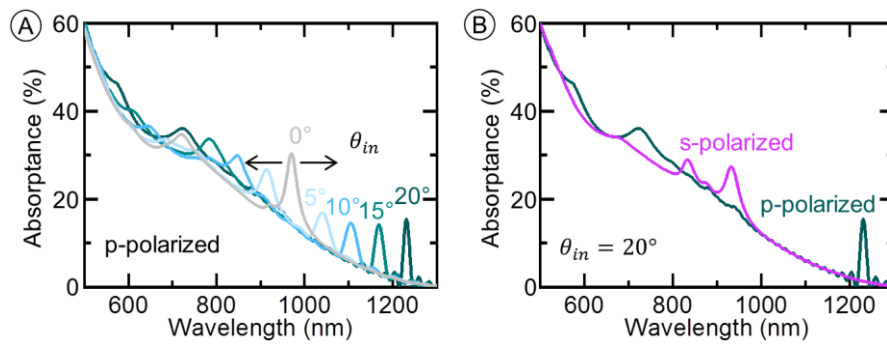


Figure 47. (A) Angle of incident (θ_{in}) dependent and (B) polarization dependent absorbance in 250 nm thick CIS nanocrystal layer textured into a PhC of $a = 600$ nm and $F = 20\%$.

4.7 Experimental prototype analyzation

4.7.1 Feasibility of the infiltration

For an investigation of the feasibility of the infiltration process the first produced samples with nanocone textures (on an area of 1.8 mm by 1.8 mm) were produced during ongoing parameter optimization. From a later point of view the nanocones on these first samples were rather small. An exposure time of 0.12 ms, a laser power of 12 mW, and $\Delta z = -100$ nm led to nanocones about 220 nm in diameter and about 300 nm in height. Even though the nanocones had a diameter below 300 nm a lattice constant of 650 nm was used to avoid proximity effects (the swaying in the x-position (see section 4.3.1) had not been resolved yet). As a consequence, F was about only about 6%. Furthermore, as the images in **Figure 48** show, tilt correct was not available for these first samples. The importance of tilt correcting became eminent when viewing the optical image in **Figure 48(A)**, where stitched fields of nanocones are displayed. The variations in nanocone height was clearly visible as brighter (smaller nanocones) and darker (larger nanocones) regions. The SEM images in **Figure 48(B)** and **(C)** show the nanocones in darker and brighter regions, respectively.

The fabricated nanocone lattices were infiltrated using doctor blading as described above (section 4.3.2). The thickness of the CIS nanocrystal layer was varied from about 150 nm (50 mg/ml) to about 300 nm (100 mg/ml) to overserve the embedding of the nanocones under different circumstances. A photograph of one of the produced samples is shown in **Figure 49(A)**. The small square in the middle of the sample is the area textured with the nanocones. The SEM image in **Figure 49(B)** shows the nanocones in a CIS nanocrystal layer thinner than the nanocone height. On all samples the nanocones stayed unaffected by the infiltration process. As intended, the CIS nanocrystal infiltrated the nanocones, without causing damage. The SEM image in **Figure 49(B)** shows a thicker CIS nanocrystal layer. The sample was broken apart for a view on the cross-section. A dense CIS nanocrystal layer was observed, perfectly embedding the nanocones.

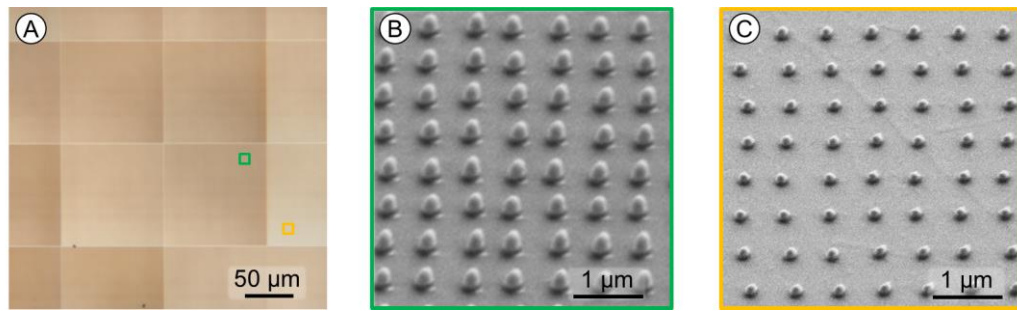


Figure 48. Impressions from the first fabricated PhC lattices before infiltration with CIS nanocrystals. **(A)** Optical microscope image of a stitched fields of nanocones. Brighter regions indicated small nanocones, darker regions indicate larger nanocones. **(B)** 30° tilted view SEM image of comparably large nanocones in a dark region. **(C)** 30° tilted view SEM image of smaller nanocones in a bright region.

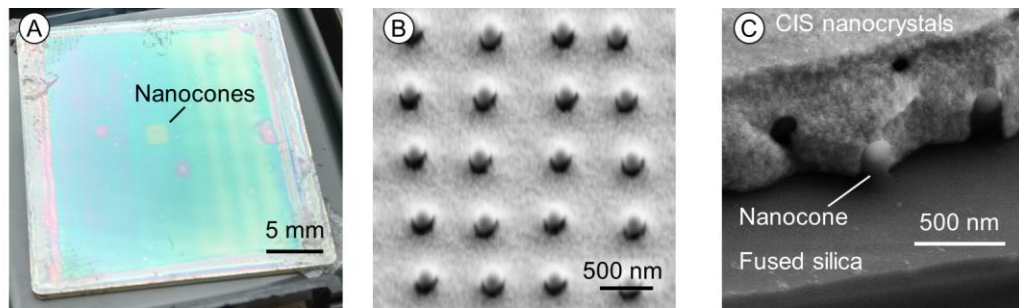


Figure 49. Impressions from the first fabricated PhC lattices after infiltration with CIS nanocrystals. **(A)** Photograph of a fused silica substrate with the nanocones textured area in the middle and a CIS nanocrystal coating. **(B)** 30° tilted view SEM image of the nanocones breaking through a thin layer of CIS nanocrystals. **(C)** 45° tilted view SEM image of the cross-section of the CIS nanocrystal layer. Individual nanocones are observed in a compact layer.

4.7.2 Quantizing the light-trapping

Using the Lambda 950 UV/Vis spectrometer (section 3.2.2) transmittance, reflectance and absorbance measurements were performed.

Normal incidence – small nanocones. First, the samples described above were investigated. Due to small sample area a pinhole was used to reduce the spot size of the measurement beam. From the obtained reflectance (R) spectra the layer thickness in the area of the texturing and in the neighboring untextured area was determined. The measured reflectance was compared to the reflectance calculated using the transfer-matrix method (TMM) (chapter 3.3.3). **Figure 50(A)** shows the measured reflectance spectrum and the best TMM fit of sample in **Figure 49(A)**. According to these calculations the CIS nanocrystal layer in the nanocone PhC textured area was a bit thicker than the CIS nanocrystal layer in the surrounding untextured area. It seemed that a kind of capillary effect, in the area with the nanocone matrix, led to thicker CIS nanocrystal layers. This effect was observed in all produced samples. These slightly thicker layers in the PhC patterned area led to an increase in the absorbance of light throughout the whole spectrum compared to the surrounding planar layer. To obtain the normal incidence absorbance (A) in the sample the transmittance (T) was measured and $A = 1 - R - T$ was used. **Figure 50(B)** shows the measured absorbance, as well as the coupling condition induced by the nanocone pattern. Due to the

slightly thicker layer the nanocone textured area showed increase absorptance in the complete spectrum. Additionally, the PhC nanocone textured area showed a slight peak in absorptance, exactly where the coupling condition was fulfilled for the 0th order TE mode and the 1st diffraction order. Given the small F and the imperfections in the fabricated nanocone lattice this was a great first result. An additional promising result was that the reduction in absorptance in the short wavelength, indicated in simulations, was not observed as strongly.

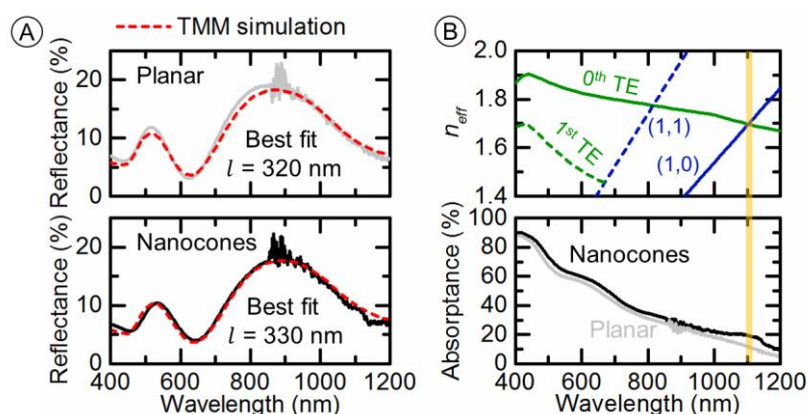


Figure 50. (A) Measured reflectance of the sample shown in **Figure 49(A)**, in the area with the nanocones (bottom) and in a planar area in close proximity to the nanocones (top). (B) Absorptance calculated from reflectance and transmittance measurements (bottom), and the coupling condition of the produced PhC layer with $l = 330$ nm, $a = 650$ nm, and $F = 6\%$.

Normal incidence – large nanocones. Distinct peaks in absorptance were observed in samples that were produced after the optimization of the DLW parameters. Compared to the samples described above the nanocone textured area was increased to 1.8 mm by 5 mm (taking into account the elongated UV/Vis measurement spot), the nanocone diameter was increased to 350 nm (exposure time: 0.16 ms, laser power: 13 mW), a correction of the substrate tilt was performed, and the swaying of the x-position could be eliminated. To close in on the optimum found for the average absorptance in FDTD simulations a lattice spacing of 650 nm was used ($F \approx 15\%$), as well as $\Delta z = 0$ nm leading to nanocones about 500 nm high and allowing for thicker layers. **Figure 51(A)** shows a top view SEM image of the nanocones before infiltration with CIS nanocrystals.

A CIS nanocrystal layer thickness of about 500 nm was targeted - equivalent to the nanocone height and thick enough for at least two TE modes around a wavelength of 1000 nm. To obtain such thick layers on the basis of a 100 mg/ml solution two consecutive coating were necessary. The SEM image in **Figure 51(B)** obtained after the infiltration process shows that also the larger nanocone were neatly embedded in the CIS nanocrystal layer – they were only visible as bumps at the surface.

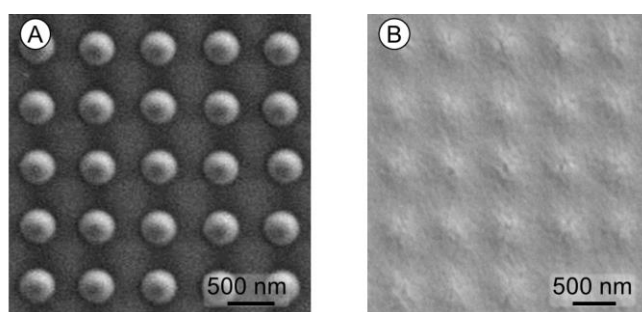


Figure 51. (A) Top view SEM image of large nanocones before infiltration with CIS nanocrystals. (B) Top view SEM image of large nanocone in a CIS nanocrystal layer.

As before, reflectance measurements were used to determine the layer thickness. The top graph in **Figure 52(A)** shows the reflectance in the planar region of a sample. Here, TMM fitting indicated a layer thickness of $l = 410$ nm. In the bottom graph the reflectance from the nanocone textured area on the same sample is shown. The best fit was achieved for a layer thickness of 600 nm (assuming $F = 15\%$). The larger nanocones led to an even stronger capillary effect, drastically increasing the film thickness in comparison to the surrounding area. Interestingly, the TMM calculations did not fit the measured reflectance for wavelengths above 900 nm. This indicated that the simple average refractive index approximation is inapplicable in this range. Additionally, this led to a slight mismatch between the calculated coupling condition and the observed peaks in absorptance, both plotted in **Figure 52(B)**. Nevertheless, the measured peaks in absorptance clearly show the possibility of mode coupling and that the corresponding coupling condition could at least be estimated. The most distinct peaks in absorptance corresponded to the coupling between the (1,0) diffraction order to the 0th and the 1st TE mode, as well as the (1,1) diffraction order and the 2nd TE mode. Indistinct peaks in absorptance were visible for coupling between the (1,1) diffraction order to the 0th and the 1st TE mode.

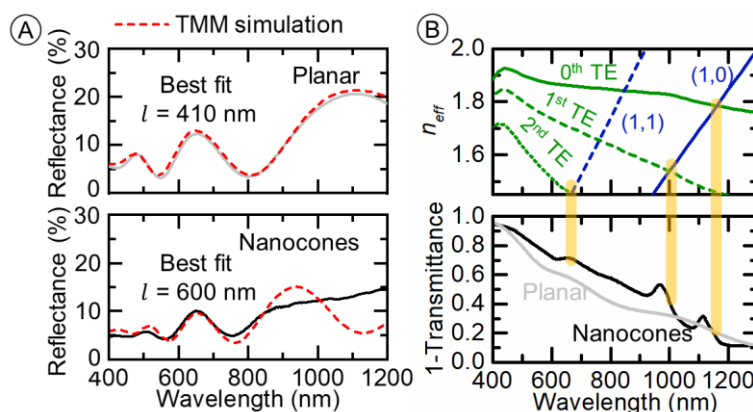


Figure 52. Optical measurements of a sample showing distinct peaks in absorptance. (A) Measured reflectance spectra, in the area with the nanocones (bottom) and in a planar area in close proximity to the nanocones (top). (B) Absorptance spectrum calculated from reflectance and transmittance measurements (bottom), and the coupling condition of the produced PhC layer with $l = 600$ nm, $a = 650$ nm, and $F = 15\%$ (top).

Angle of incidence and polarization. Using the center mount for the integrating sphere of the UV/Vis spectrometer it was possible to measure the angle-dependent absorptance of the sample. As discussed in the previous section the wavelength under which coupling to a quasi-guided mode was possible

changed with the angle of incidence. Additionally, the coupling was depended upon the polarization of the incident beam. A wire grid polarizer (Thorlabs, WP25M-UB) was used to observe this behavior. The polarizer was placed in the beam path in front of the integrating sphere. **Figure 53(A)** shows the measured absorptance for an incidence angles of 0° , 10° , and 15° for p-polarized light. As expected for the PhC lattice the position of the peaks in absorptance changed with the incidence angle. **Figure 53(B)** shows the measured absorptance spectrum when illuminating the sample with an incidence angle of 15° . The polarizer was rotated in 30° steps to observe the polarization dependent mode coupling.

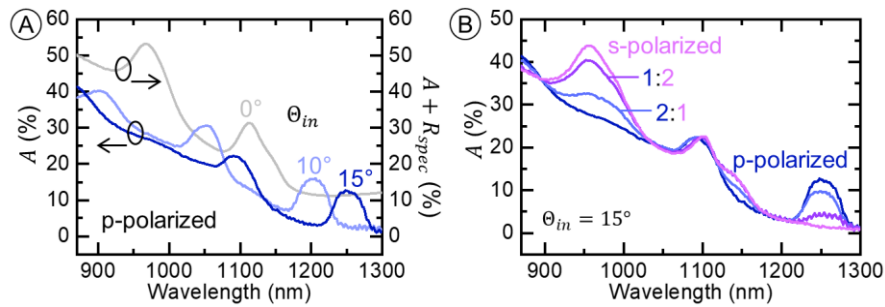


Figure 53. Measured angle of incident (θ_{in}) dependent **(A)** and polarization dependent **(B)** absorptance (A) of a PhC patterned CIS nanocrystal layer. In the normal incidence case the specular reflectance (R_{spec}) was measured as well.

4.8 CIS nanocrystal infiltrated photonic crystal PV device

CIS nanocrystal devices have been produced in two different architectures [94]. In the most common design a glass substrate has been coated by thermal evaporation with a metal layer, typically gold. The CIS nanocrystal ink has been deposited on the metal layer, using spray coating or spin coating. A CdS buffer layer has been deposited using a chemical surface deposition technique [139]. Finally, a transparent front electrode, typically indium tin oxide (ITO) and ZnO, has been evaporated on top. This setup is illustrated in **Figure 54(A)**, also showing how the nanocone could be incorporated. In the inverted setup in **Figure 54(B)** the transparent electrode has been evaporated first onto the glass substrate. The CIS nanocrystal layer, the CdS buffer layer and the metal contact have been deposited on top. To be able to apply the nanocones in both setups the fabrication of nanocones on ITO and on gold was investigated. Simulations were performed for both setups and finally solar cells were produced.

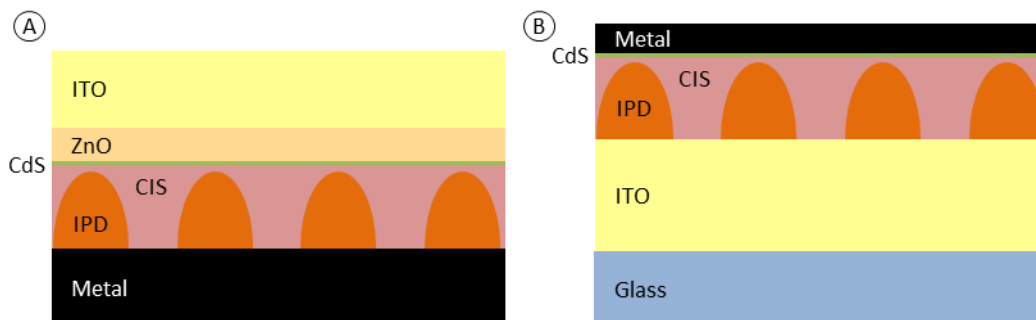


Figure 54. Illustration of possible setups for PhC pattern CIS nanocrystal devices. **(A)** Conventional setup with the metal contact deposited first. **(B)** Inverse setup with the transparent electrode deposited first.

4.8.1 Nanocone fabrication on electrodes

Nanocones were fabricated on ITO and on gold using DLW. The first thing to note is that the reflection of the laser beam by the substrate, especially in the case of gold, led to interference fringes. The voxel lost its typical ellipsoidal shape, due to local minima and maxima in intensity. When produced on the electrodes the nanocones resembled snowmen instead of ellipsoids.

Nanocones on ITO. To fabricate nanocones on ITO, commercial ITO coated glass substrates (Sigma-Aldrich) were used. The layer thickness of ITO on these commercial slides was about 150 nm. In general, the dose dependent nanocone dimensions on ITO were very similar to the nanocone dimensions on fused silica. The increased reflectance from the substrate only played a minor role. Nevertheless, the snowman shape could clearly be observed. **Figure 55** shows SEM images of nanocones on ITO produced with an exposure time of 0.18 ms and a laser power of 13 mW in a square lattice of lattice constant 650 nm. The nanocones were exposed at $\Delta z = -400$ nm, -200 nm, and 0 nm. At $\Delta z = 200$ nm there was only one interference maxima above the substrate, the nanocone resembles a sphere. For $\Delta z = -200$ nm there were two maxima and one minima, producing a burger shape. For $\Delta z = 0$ nm a classical snowman shape appeared.

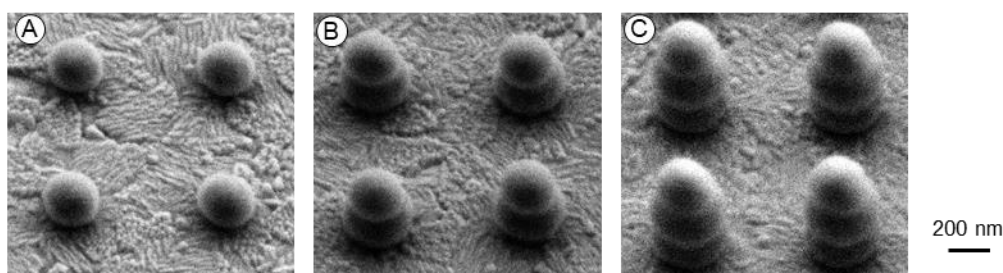


Figure 55. 30° tilted SEM images of nanocone exposed on ITO with an exposure time of 0.18 ms and a laser power of 13 mW. The focal spot was positioned (A) 400 nm, (B) 200 nm, and (C) 0 nm below the substrate.

Nanocones on gold. For the fabrication of nanocones on gold, a 5 nm adhesion layer of Cr was deposited on a cleaned glass slide followed by a 80 nm layer of gold. The layers were deposited via sputtering in vacuum (308R Coating System, Cressington). The gold layers led to strong reflectance of the laser beam. As a consequence, laser powers much lower than in the case of a fused silica substrate already led to the fabrication of a nanocone. Furthermore, the interference fringes were so pronounced that parts of the exposed voxel completely detached from the substrate. **Figure 56** shows nanocones that were produced in a burger shape, with a top and a bottom half. While, in some case the two halves stayed together after development, in many others they detached from each other. The tops could be found all over the sample. Consequently, nanocones on gold had to be fabrication far enough below the surface to only lead to one interference maxima above the surface. Good results were achieved with a laser power of 6 mW, an exposure time of 0.18 ms and $\Delta z = -400$ nm.

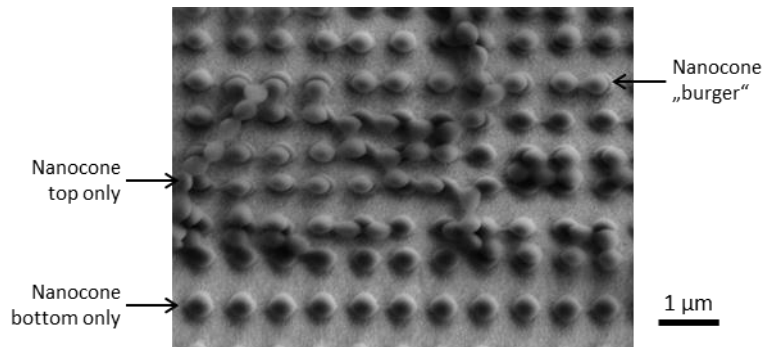


Figure 56. Top view SEM image of nanocones fabricated on a gold surface with the focal spot positioned on the substrate surface.

4.8.2 FDTD device simulations

The device setups illustrated in **Figure 54** were simulated using FDTD simulations. Literature values were used for the refractive indices of the difference layers, the values are given in the Appendix. The refractive indices of ITO ($n_{ITO}(1000 \text{ nm}) \approx 2$) and ZnO ($n_{ZnO}(1000 \text{ nm}) \approx 1.7$) were extremely close to that of the PhC textured CIS nanocrystal layer. Therefore, a strict confinement of a mode to the CIS nanocrystal layer was not possible. Nevertheless, as all layers were thin-films, a mode propagating in ITO and ZnO left a lot of energy in the CIS nanocrystal layer. Especially, in the case of the conventional design in **Figure 54(A)** there were several modes confined to the thin-film layer stack. In FDTD simulations, fixed layer thickness were used (CIS nanocrystals: 300 nm, CdS: 5 nm, ZnO: 40 nm, and ITO: 300 nm). It is to be noted that the thickness of the individual layers highly influenced the number of modes, as well as the absorptance in the CIS nanocrystal layer. Here, the investigation of the general feasibility was important and a rough determination of suitable parameters. In line with the study presented above, a square lattice of nanocones was investigated. The lattice constant (a) and the volume fraction (F) of IP-Dip in the CIS nanocrystal layer were varied. Again, identical values were used for the texture height and the layer thickness.

For determining optimum parameters the weighted averages absorptance was calculated according to Equation (4.14). As before, the absorptance was obtained by monitoring the transmittance and reflectance of power before and after the CIS nanocrystal layer. The result for the inverted design (compare **Figure 54(B)**) is shown in **Figure 57(A)**. No combination of a and F performed better than the planar setup. This was due to the leaking of modes to the glass substrate. Only very few mode were confined to the thin-film layer stack limiting the efficiency of the coupling scheme. The result for the conventional setup (compare **Figure 54(A)**) is shown in **Figure 57(B)**. Enhancing the weighted average absorptance beyond that of a planar layer was possible for ($a > 550 \text{ nm}$). An optimum was observed for $a \approx 650 \text{ nm}$. The absorptance spectrum at this optimum is shown and compared to the absorptance spectrum of a planar layer of identical thickness in **Figure 57(C)**. The wavy form of the two spectra originated from interference fringes. The peaks in the spectrum of the PhC patterned layer around 870 nm, 950 nm, and 1060 nm, on the other hand, arise from the coupling of incident light to quasi-guided modes.

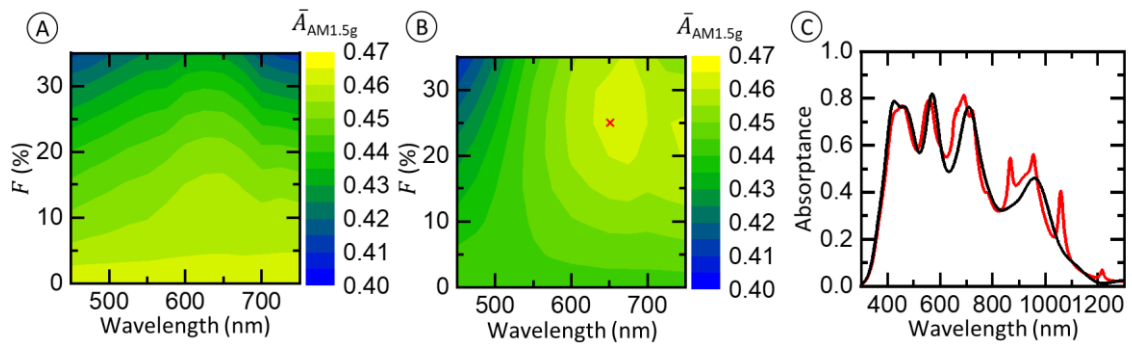


Figure 57. Simulated weighted absorbance in a 300 nm thick PhC patterned CIS nanocrystal layer in the inverted (A) and in the conventional device setup (B). (C) Wavelength-dependent absorbance in the planar conventional setup and with a PhC pattern of $a = 650$ nm and $F = 25\%$.

4.8.3 Device preparation and analysis

The final CIS infiltrated PhC device discussed in the following was fabricated in direct collaboration with Wen Liu from the Korgel group at the TMI. The nanocone patterned gold layer was prepared at KIT. As described above, a gold layer was deposited on glass by Aina Quintilla. During sputtering a mask was applied to deposit the gold in a certain pattern – necessary for contacting the device. An area of 10.5 mm by 6 mm on the gold was textured with IP-Dip nanocones by the author. An image of the nanocone pattern on the gold layer is shown in **Figure 58(A)**. The nanocones were arranged in a square lattice of 650 nm lattice constant. A laser power of 6 mW, an exposure time of 0.18 ms and $\Delta z = -400$ nm were used to produce nanocones about 300 nm in diameter and about 200 nm in height. The sample was shipped to UTA, where Wen Liu deposited an about 300 nm thick CIS nanocrystal layer by means of spray-coating. Wen Liu then deposited a CdS layer, a ZnO layer, and an ITO layer of about 5 nm, 40 nm and 300 nm, respectively. The top contact ITO and ZnO layer were deposited using a mask to obtain eight stripes (compare **Figure 58(B)**). In this way, eight electrically separated solar cells were formed on the same sample in regions where the gold layer and the top contact layer overlap. Two of these solar cells (N1 and N2) were patterned with the nanocones.

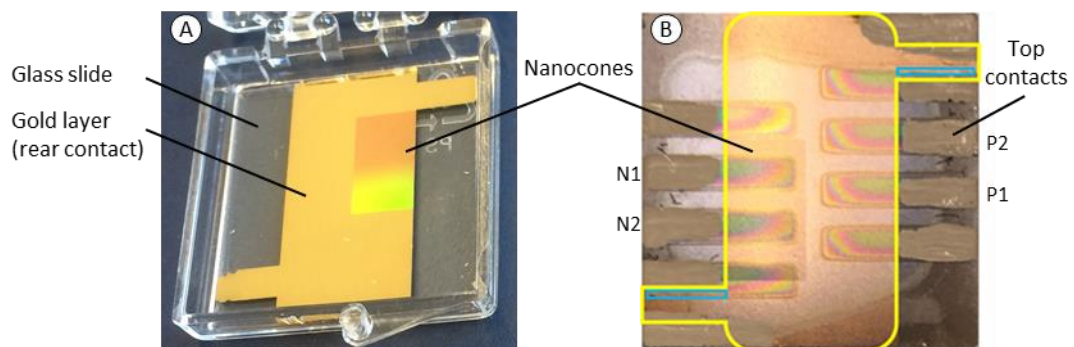


Figure 58. Images of the fabricated CIS infiltrated PhC PV device on a 25 mm by 25 mm glass slide. (A) Glass slide with a patterned gold layer partially textured with nanocones by the author. (B) Final device produced by Wen Liu at CNM.

Wen Liu also performed EQE and current-voltage (I - V) measurements at the TMI. The obtained measurement results of the solar cells are partially shown in **Figure 59**. Consistently, the EQE (**Figure**

59(A) of the nanocones patterned solar cells (N1 and N2) was considerably higher than the EQE of the solar cells without the nanocone texture (P1 and P2) on the opposite side of the glass slide. This was attributed to the aforementioned, capillary effect. In the area of the nanocones the CIS nanocrystal layer was slightly thicker than in the area without the nanocones. More light was absorbed. Distinct peaks in absorptance, comparable to **Figure 57(C)**, were not visible.

In general, due to thickness limitations resulting from the limited charge carrier diffusion length in the CIS nanocrystals an increase in EQE, due to an increased absorptance, does not necessarily lead to an increased solar cell power conversion efficiency (PCE). Therefore, I - V measurements (**Figure 59(B)**) of the solar cells were important to study the impact on the PCE. The PCE of the PhC patterned (N1 and N2) solar cells was higher than that of the unpatterned solar cells (P1 and P2). But while the short circuit current density (J_{SC}) strongly increased, the open circuit voltage (V_{OC}) and the fill factor (FF) were slightly reduced. In total the PCE of the nanocone patterned solar cells was, with an average of 1.8%, slightly higher than the PCE (average 1.5%) of the unpatterned solar cells. Thus, proving the possibility of fabricating an ink infiltrated PhC lattice solar cell. To enable significant enhancement of the PCE with the scheme various improvements are necessary.

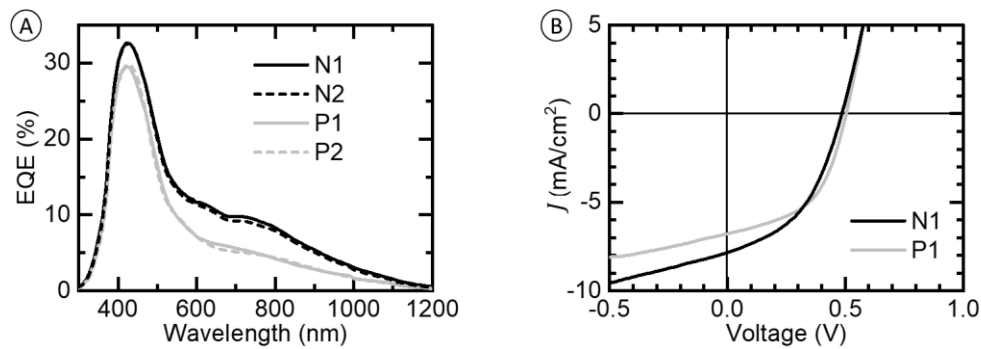


Figure 59. (A) EQE and (B) I - V measurements of the devices shown in **Figure 58(B)**.

5 Micro-optics for the front surface of solar modules

Several of the results for the DLW fabricated microcones presented in the following chapter were published in: Prog. Photovolt Res. Appl. (2019) [140]. The idea for the fabrication of the microcones was developed with the co-author Ulrich Paetzold. The co-author Raphael Schmager aided in performing simulations using LightTools. In particular the simulations for analyzing scattering angles in section 5.5.1 were performed by Raphael Schmager. The co-authors Stefan Paetel and Oliver Kiowski provided the used CIGS based solar cells. The co-author Kaining Ding provided the used planar silicon solar cell. And the co-authors Efthymios Klampafitis and Bryce Richards supervised and coordinated of the project and provided significant intellectual input. The code for calculating the energy yield in section 5.6.2 was developed by Jonathan Lehr, Malte Langenhorst and Raphael Schmager [141].

5.1 Introduction

Nanophotonic textures are particularly useful when it comes to anti-reflection and molding the flow of light in a certain spectral band [19]. With respect to the length scale of the incidence light, feature sizes have to be small in lateral direction and large in longitudinal direction. Therefore, the aspect ratio (AR), the relationship between the base width and the height of a texture element, has to be large. For broadband anti-reflection of the relevant spectrum for PV applications (~300 nm to ~1200 nm) ARs above one are needed [142]. These high ARs give rise to difficulties in fabrication, as well as a large increase in surface area - inducing the need for excellent surface passivation. When it comes to broadband enhancement in photovoltaics, micron-scale textures have certain advantages. The effectiveness of micron-scale textures is, for the most part, not dependent upon the wavelength. Furthermore, micron-scale textures do not only lead to broadband anti-reflection, but also to a broadband redirection of light [143,144].

For c-Si, micron-scale textures have become an industry standard. c-Si wafers are etched in an alkaline bath. Anisotropic wet-etching along the (100) crystal plane leads to a random pyramid texture. The angle between the facets of the pyramids and their base ideally is 54.7° , given by the crystalline planes. In real fabricated textures this inclination angle is a bit smaller [145] and lies in the range 49° to 53° . The AR is therefore below 0.7 ($< \tan(54.7^\circ)/2$). The surface area increases by a factor smaller than 1.86 ($< 1/\cos(54.7^\circ)$). Already this relatively small increase in surface area has been a challenge due an increase in surface recombination, as well as the formation of additional dangling-bonds [146]. Nowadays, techniques are available to overcome this passivation problem [147]. For the technology of black silicon, on the other hand, making use of sub-wavelength surface textures, passivation still poses a big challenge [148]. In general, the anisotropic wet-etching of c-Si is a very elegant large-area approach for achieving a micron-scale texture that greatly increases the power conversion efficiency (PCE) of a solar cell. Achieving a similar texturing in other technologies is of high interest.

Already for the case of mc-Si the technology transfer poses a challenge. Due to variations in the crystal planes wet-etching of a mc-Si does not achieve similar gains to wet-etching of a c-Si wafer [149]. To

fabricate micron-scale textures on mc-Si mostly isotropic etching has been employed making use of masks [58,150]. Other techniques that have been explored include laser ablation [151] and mechanical processes [41]. All other PV technologies, apart from crystalline silicon, rely on sub-micrometer semiconductor layer thicknesses. Therefore, the direct application of micro-scale textures on the semiconductor layer surface has not been possible.

In a solar module thicker layers are present. For practical applications, any solar module will need micro-to millimeter thick encapsulation layers to protect it against environmental conditions. The typical setup of a solar module with an encapsulant, providing optical coupling between the protective front glass and the underlying solar cells, is illustrated in **Figure 60**. Micron-scale textures have been employed on the front surface of these protective layers to bring the benefits of reduced reflectance and light-trapping with a marginal increase in surface area to thin-film PV. The front surface of these protective layers is conventionally, but not exclusively, an air/glass interface. A texture at the front surface of the encapsulation layers of a PV device is non-invasive to the solar cell semiconductor layer enabling optical gains without electrical losses. In this way, they are not only beneficial to thin-film PV, but complement the already textured semiconductor layer in c-Si based PV device.

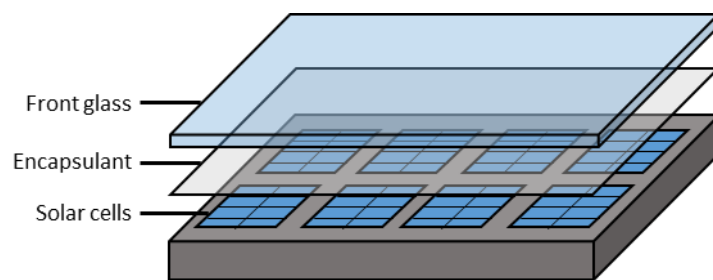


Figure 60. Illustration of the typical setup of a solar module. Several solar cells are protected by a front glass and an encapsulant layer that provides optical coupling.

In many modern solar modules, thin-film anti-reflection coatings (ARCs) [152], based on the destructive interference of light, are used at the air/glass interface for reducing reflection losses in certain wavelength range. Micro-scale textures have the additional benefits that they enable broadband anti-reflection, as well as light-trapping. Large-area micron-scale textures have, to the most part, been realized in polymeric materials. Polymeric materials have the advantage that it is easy to texture them using various techniques - such as lithography and imprinting [153,154]. Apart from polymeric materials solution processing [155] has been used to fabricate micron-scale textures on the front surface of PV devices. Micron-scale front surface textures, non-invasive to the semiconductor layer, have been applied to c-Si solar cells [156,157], a-Si solar cells [158], organic solar cells [56,159-164], CIGS based solar cells [165], perovskite solar cells [166,167], and perovskite-silicon tandem solar cells [168]. In all cases a clear improvement compared to planar layers could be shown. Additionally, various texture geometries have been investigated numerically indicating the AR as a key parameter for optimizing textures for PV applications [169-171].

Texture geometries occurring in nature have been exploited for achieving improvements in PV [172]. The nano-scale moth-eye texture is the most common example for a natural texture that has been transferred to PV [22]. The optical properties of micron-scale textures, on the other hand, are utilized by many petals and leaves [173]. **Figure 61** shows an SEM image, taken by Raphael Schmager, of conical textures found on a viola petal. Conical textures found on plants have multiple functionalities beneficial

in PV applications. Natural occurring conical textures reduce surface reflectivity, focus light [174] and have anti-soling properties [175]. The textures found on rose petals [56] and on the viola flower petal [157] have been replicated onto solar cells to show the broadband enhancement they bring. The geometrical features that influence the anti-reflection properties of textures found on plants are the AR, the peak-to-peak distance, the tip radius and the array arrangement [176]. For a sufficiently small tip radius the AR is the most important parameter defining the anti-reflection properties. Ray-tracing based simulations of conical textures found their optical properties robust against perturbations of all other geometrical features [169].

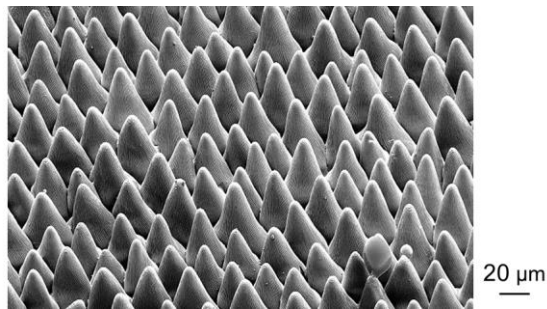


Figure 61. Scanning electron microscope (SEM) image of conical micron-scale textures found on the petal of the viola flower.

Building on the successful preliminary work with bio-replicated conical textures for PV, the study in this chapter aimed at the artificial fabrication of conical textures optimized for different PV applications. For this, a detailed understanding of the optical interaction between the textured front surface layer and the underlying solar cell was targeted. In-line with previous results the study focused on the AR, as the key parameter influencing the anti-reflection properties. Thus, microcone textures of different AR were prepared using DLW. An important consideration was achieving very little flat areas within the texture. Therefore, the conical elements have to be closely spaced and need a sharp tip. Perfect cones with right circular straight side walls were chosen. They were arranged in a hexagonal lattice and overlapped each other, such that always three cones touch in one point. This design is illustrated in **Figure 62**. In DLW, a lattice constant of 25 μm was chosen to achieve the applicability of ray optics. Thus, interference effects are excluded for all relevant wavelengths.

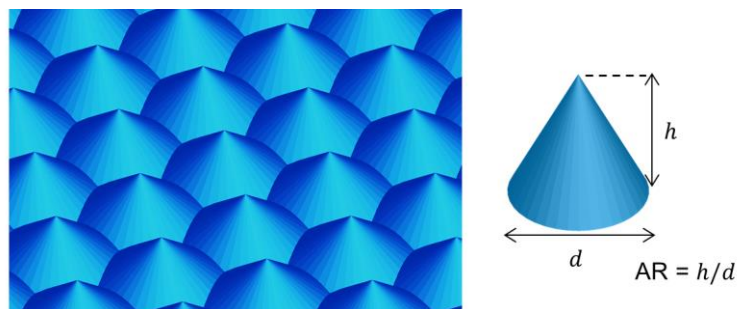


Figure 62. Illustration of the targeted microcone texture and illustration of a single conical element defining the AR.

For the targeted analysis, the DLW fabricated microcone textures were directly replicated into a photoresist coating on unencapsulated solar cells. In these prototypes the several micrometer thick photoresist layer in between the front surface texture and the solar cells represents the encapsulation

and the cover glass of a solar module. On a final note, the AR in a periodic texture is often defined as the ratio between the maximum height difference within the texture and the periodicity of the lattice. The advantage of this definition is that it is applicable to any periodic texture. For the conical textures discussed in the following a definition of the AR by the ratio between the base diameter and cone height is more convenient. It allows a direct relationship between the AR and the inclination angle of the cone walls. The importance of the inclination angle of the cone walls will be discussed in the next section.

5.2 Working principle of the microcone texture

Micron-scale textures for the front surface of solar modules enhance the light collection in the underlying solar cell via two mechanisms.

Reduced interface reflectivity. Light incident upon a dielectric interface is either transmitted or reflected. Typically 4% of the light incident upon the cover glass of a solar module is reflected due to the refractive index step. For microcones of sufficiently high AR this reflected light will impinge upon another cone and has a second (or even third) ‘change’ for transmission through the front surface.

Light-trapping. Ideally light transmitted through the front surface of a PV device is absorbed by the solar cell, generating a current. In a real device some of the light is not utilized. Apart from parasitic absorption light is also reflected. Possible sources of reflection are interfaces in the device, the contacts on semiconductor surface, or weak absorption inside the solar cell. The microcone textures at the front surface trap this light. The mechanism behind the trapping is a change in the angle of incidence. Not all the light reflected by the solar cell hits the microcones under the same angle as the incident light. To some extent the angles are randomized, total internal reflection occurs.

Both processes, the reduced interface reflectivity and the light-trapping effect, are illustrated in **Figure 63** [140]. Based on the light-trapping effect micron-scale textures for the front surface of PV devices have the highest potential when it comes to solar cells showing a large reflectance, such as organic solar cells. Explaining the large number of publications in this field cited in the precious section (5.1). Nevertheless, the enhancement in light collection introduced by the micron-scale textures (especially the reduced interface reflectivity) is beneficial for all PV technologies.

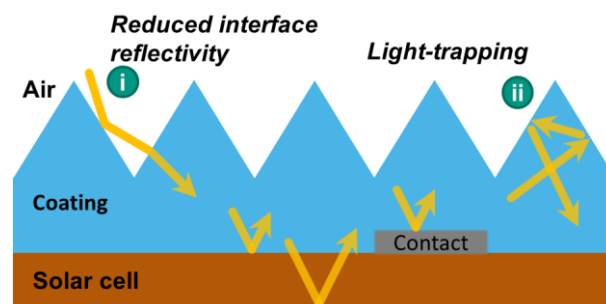


Figure 63. Illustration of the working principle of micron-scale textures for the front surface of solar module. Adapted with permission from [140], © 2019 Wiley.

An additional optical effect that should be considered is the refraction of light to oblique angles. As illustrated in **Figure 63**, near normal incident light hits the cone surface at an oblique angle. Therefore, refraction takes place. The dominant angle of refraction (AOR) is given Snell's law (Equation (2.21)) depending on the incidence angle. The AOR depends upon the inclination angle (IA) of the cone walls. The IA and the opening angle (OA) of the microcones are directly linked to the AR as illustrated in **Figure 64**. For normal incidence light it is:

$$\tan\left(\frac{OA}{2}\right) = (2AR)^{-1}, \quad (5.1)$$

$$IA = \pi - OA, \quad (5.2)$$

$$\sin(AOR) = n_c \sin(IA), \quad (5.3)$$

where n_c is the refractive index of the coating layer. Due to the refraction the path length of light through the front surface coating is increased. This increase in path length has positive and negative effects. Undesirably, more light is absorbed in the coating layer. In addition, an increase in reflectance of light at the solar cell interface is possible when light is incident from oblique angles. Positive effects are that not only the path length through the coating layer increased, but also the path length through the solar cell.

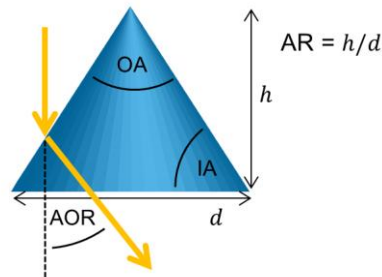


Figure 64. Illustration showing the different parameters for characterizing the microcone textures. The aspect ratio (AR), the opening angle (OA), and the inclination angle (IA). Normal incident light is primarily transmitted to the angle of refraction (AOR).

5.3 Optical simulations

Optical simulations of the microcone textures were performed using the commercial ray-tracing software, LightTools (section 3.3.2). These simulations targeted a better understanding of the interaction of light with the microcone texture, by investigating the reduced interface reflectivity and the light-trapping effect separately. Furthermore, simulations were compared to experimental results to assess the optical performance of the prepared microcone textures.

In the ray-tracing simulations, a non-absorbing layer of constant refractive index 1.56 was defined. The refractive index was chosen according to the refractive index of the employed coating layer (for further details see section 5.4.2). Conical textures were added to the front surface of the layer, using a predefined 3D texture available in LightTools. The reflectivity of the back surface representing a substrate of infinite thickness, were adapted for different scenarios. A source was defined illuminating

one unit cell of the periodic texture. Reflected rays, escaping from the simulated device, were collected by a far field monitor. The setup is illustrated in **Figure 65**. Next to structural parameters the system reflectance depends upon the polar angle (θ) and the azimuth angle (ϕ) of the incident light. Furthermore, the light-trapping effect also depends upon the thickness (l) of the coating layer [143]. Since a constant refractive index was used the simulation results are in general wavelength independent.

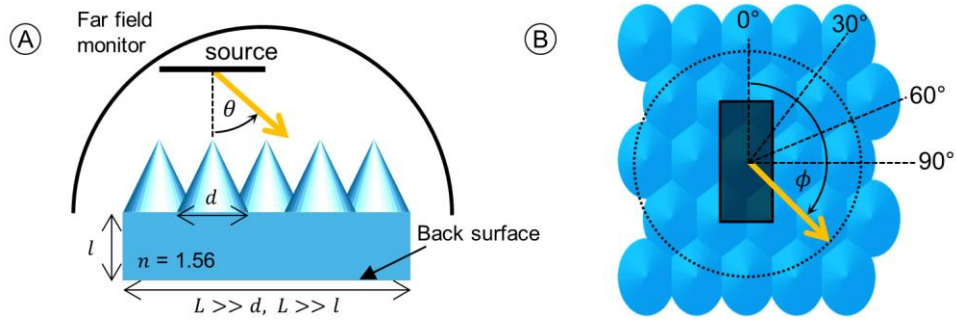


Figure 65. Illustration of the simulation setup for analyzing the incident angle-dependent reflectance of the microcone textures. **(A)** Cross-sectional view showing the polar angle θ . The coating layer was made large enough for no rays to reach the edge. The reflectivity of the back surface was freely adapted to simulate different substrates. **(B)** Top view showing the azimuth angle ϕ . One unit cell was illuminated.

5.3.1 Reduced interface reflectivity

The reduced interface reflectivity was analyzed by defining the back surface as a perfect absorber. When no light is reflected by the back surface the light-trapping effect does not take place. Only rays reflected at the front interface reach the far field detector. **Figure 66(A)** shows results for the normal incidence case. The reflectance in the planar case (AR 0) is easily calculated using the Fresnel equations (Equation (2.23) and Equation (2.24)). It is $\left(\frac{1.56-1}{1.56+1}\right)^2 = 0.0479$. Starting from AR > 0.3 the reflectance steeply drops to below 1% at AR 0.5 and reaches values below 0.1% for AR > 0.9. The importance of AR 0.5 is directly related to the IA of the microcone walls. At AR 0.5 the IA is 45°. Therefore, an incident beam will be redirected in a direction perpendicular to the microcone texture and will certainly impinge upon at least one further microcone.

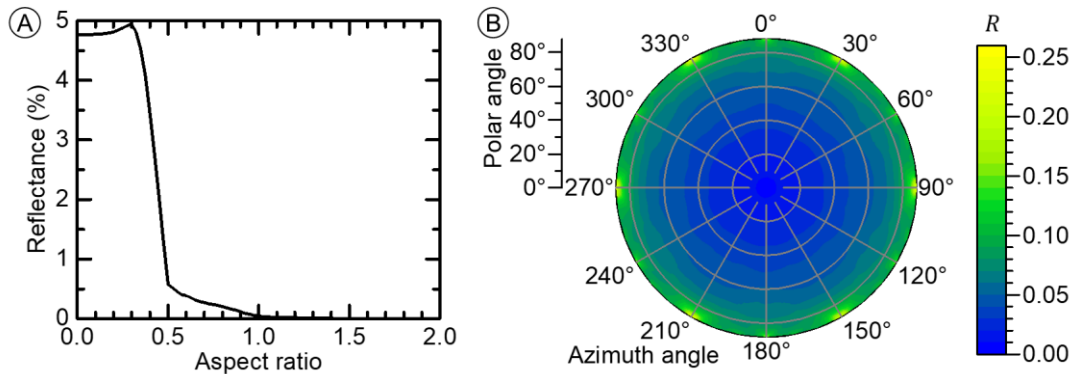


Figure 66. **(A)** Front surface reflectance of the microcone texture for normal incidence illumination. **(B)** Incidence angle-dependent reflectance (R) for a microcone textures of AR 0.5.

The incidence angle-dependent front surface reflectance was analyzed by rotating the illumination angle of the source in simulations by the polar angle θ and the azimuth angle ϕ as illustrated in **Figure 65**. **Figure 66(B)** shows the result for a microcone texture of AR 0.5. With increasing polar angle the microcone texture surface reflectance slowly increased. But, for all incidence angles the reflectance was much smaller than in the case of a planar layer showing Fresnel-type reflection. Even in the case of polar angles close to 90° , reflectance did not surpass 25%. Furthermore, the symmetry of the hexagonal lattice of the microcone texture is clearly visible in **Figure 66(B)**. With regard to the azimuth angle there is a 60° rotational symmetry and within these 60° there is an additional mirror symmetry. It is therefore sufficient to only investigate the azimuth angle from 0° to 30° .

The polar angle is the most important illumination parameter to consider. For showing the relationship between AR and the polar angle averaging over azimuth angles from 0° to 30° obtained in 5° steps was performed. **Figure 67(A)** shows the averaged reflectance. For larger polar angles larger ARs were needed for achieving low reflectance. Front surface reflectance below 1% was maintained for $AR > 1.4$ up to a polar angle of about 60° , while microcone textures of AR 0.5 already showed 5% reflectance at this incidence angle. **Figure 67(B)** shows the variation with the azimuth angle. The variation in reflectance (ΔR) at a given polar angle and AR is defined as the maximum reflectance minus the minimum reflectance obtained in simulations for different azimuth angles:

$$\Delta R(\phi) = \max_{\phi} R(AR, \theta, \phi) - \min_{\phi} R(AR, \theta, \phi). \quad (5.4)$$

The graph shows that the azimuth angle has very little impact for polar angles $< 75^\circ$. The azimuth angles only impacts the front surface reflectance for very large polar angles. For $AR > 0.7$ the azimuth angle has no significant impact even at for large polar angles.

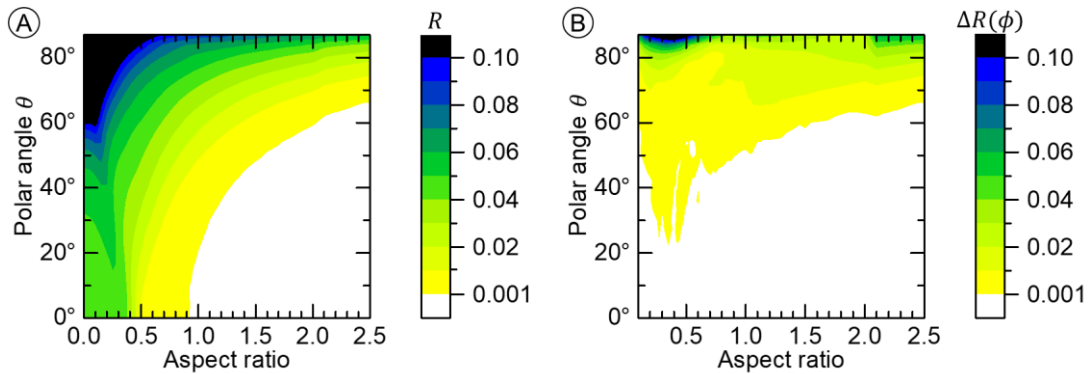


Figure 67. Simulations on the incidence angle-dependent front surface reflectance. **(A)** Polar angle (θ) and AR dependent reflectance (R) averaged over the azimuth angle (ϕ). **(B)** Variation in reflectance (ΔR) caused by different azimuth angles.

5.3.2 Light-trapping effect

For analyzing the light-trapping effect several considerations had to be made: The efficiency of the light-trapping effect is highly dependent upon the interplay between the incidence illumination and the reflectance of the underlying solar cell. In the following the two extreme cases for the solar cell of perfect specular reflection and Lambertian reflection are examined. There are three trapping mechanisms for light reflected by the solar cell and impinging upon the microcone texture from the

under-side: (I) TIR, (II) Fresnel-type reflection, and (III) light escaping through one cone and reenter the system through another (see **Figure 68(A)**). In some cases several of these mechanisms work together to trap light in the PV device. Whether a specific ray is trapped in simulations is highly dependent upon the position and angle at which light reaches the under-side of the texture.

Assuming **perfect specular reflection** of light by the solar cell there is a clear relationship between the AR, the incidence angle of light and the angle reflected light hits the under-side of the microcone texture. Light incident upon the front surface gets refracted by the microcones to specific angles (**Figure 64**). When specularly reflected by the substrate it will maintain the angle it was refracted to. Therefore, the AOR is the angle under which light will hit the under-side of the microcone texture. The position at which this occurs is also determined by the thickness (l) of the coating layer. **Figure 68(A)** and **(B)** show two exemplary cases in a 2D system for a texture of AR 0.5. In this specific case, when a beam reflected by the solar cell hits the same facet to the one on which it entered the coating layer it is trapped. When a beam hits the facet opposite to the one on which it entered it escapes. The impact the thickness has on these light paths is clearly visible.

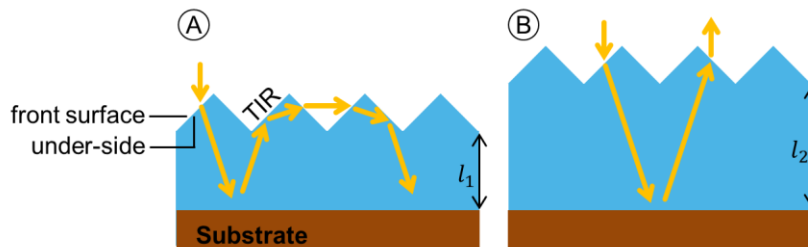


Figure 68. Illustration of the light-trapping effect for AR 0.5 in a 2D system. **(A)** Normal incident light on the front surface reaching the same facet from the under-side. **(B)** Normal incident light on the front surface reaching the opposite facet from the under-side.

The optimum AR (in terms of optics) of the microcone texture for a PV application depends upon the reflectance of the solar cell and the illumination environment. To investigate the incidence angle dependence of the light-trapping effect a back surface showing 20% specular reflectivity (**Figure 69(A)**) was implemented in simulations. The coating layer thickness l was varied by the distance Δl according to

$$\Delta l = \frac{a}{2 \tan(\text{AOR})} \quad (5.5)$$

where a is the lattice constant of the texture. In the range l to $l + \Delta l$ an incident beam is swept over one lattice period on the under-side of the texture. **Figure 69(B)** shows the total amount of light reaching the far field detector for the case of normal incidence illumination. This total reflectance (R) is the sum of light reflected at the front surface (R_0) and light escaping from the coating layer. The black curve shows the mean total reflected light averaged over all l . As expected from simulation results on the reduced interface reflectivity (**Figure 66(A)**), reflectance steeply decreases in the range AR 0.3 to AR 0.5. For AR > 0.5 reflectance is reduced by more than 10%. About 4% to 5% of the decrease is attributed to the reduced interface reflectivity. The rest is a result the light-trapping effect. The red area in **Figure 69(B)** shows the range of values achieved for different l . Especially in the range AR 0.3 to AR 0.7 the variation with l is high. Very low total reflectance is possible for AR 0.5, but only for very specific l . Around AR 0.85 there is a much more stable minimum.

When investigating the non-normal incidence case the polar and the azimuth angle have to be taken into account. Just like in the case of the increased front surface transmission the azimuth angle was found to only play a minor role for the light-trapping effect. **Figure 69(C)** shows the simulation result for different ARs and polar angles averaged over the investigated azimuth angles and layer thicknesses l . For small polar angles the minimum around AR 0.85 is visible. For larger polar angles higher ARs are more beneficial. The total reflectance is dominated by the strongly reduced interface reflectivity of higher AR microcone textures. Along the lines of Equation (5.4) **Figure 69(E)** and **(F)** show the variation with the thickness and the azimuth angle, respectively. Interestingly, **Figure 69(E)** shows that the thickness only plays a role around AR 0.5 for near-normal incidence. In any other case the variation in total reflectance was less than 1%. **Figure 69(F)** shows a very similar result to **Figure 67(B)**; the azimuth angle is only important for very large polar angles.

While the total reflectance is the most important parameter in the scheme, a quantification of the light-trapping effect was also targeted. In the case of perfect light-trapping, no light that entered the coating layer escapes. Therefore, a parameter for the effectiveness of the light-trapping is the ratio between the light escaping from the coating layer and the light that entered the coating layer. By normalizing this ratio to the substrate reflectance (R_{sub}), we find a parameter LT that is one if all light entering the coating layer escapes and zero when no light escapes:

$$LT = \frac{R - R_0}{R_{sub}(1 - R_0)} \quad (5.6)$$

where R is the total reflectance (**Figure 69(C)**), and R_0 the front surface reflectance (**Figure 67(A)**). LT for the case of a back surface exhibiting 20% specular reflectivity is depicted in **Figure 69(D)**. LT is on the order of 50% for sufficiently large ARs. In the case of near-normal incident light LT reaches values as low as 37% around AR 0.85. Strong light-trapping is also possible for textures of low aspect ratio at large polar angles. Of source, surface reflectivity is high in this case.

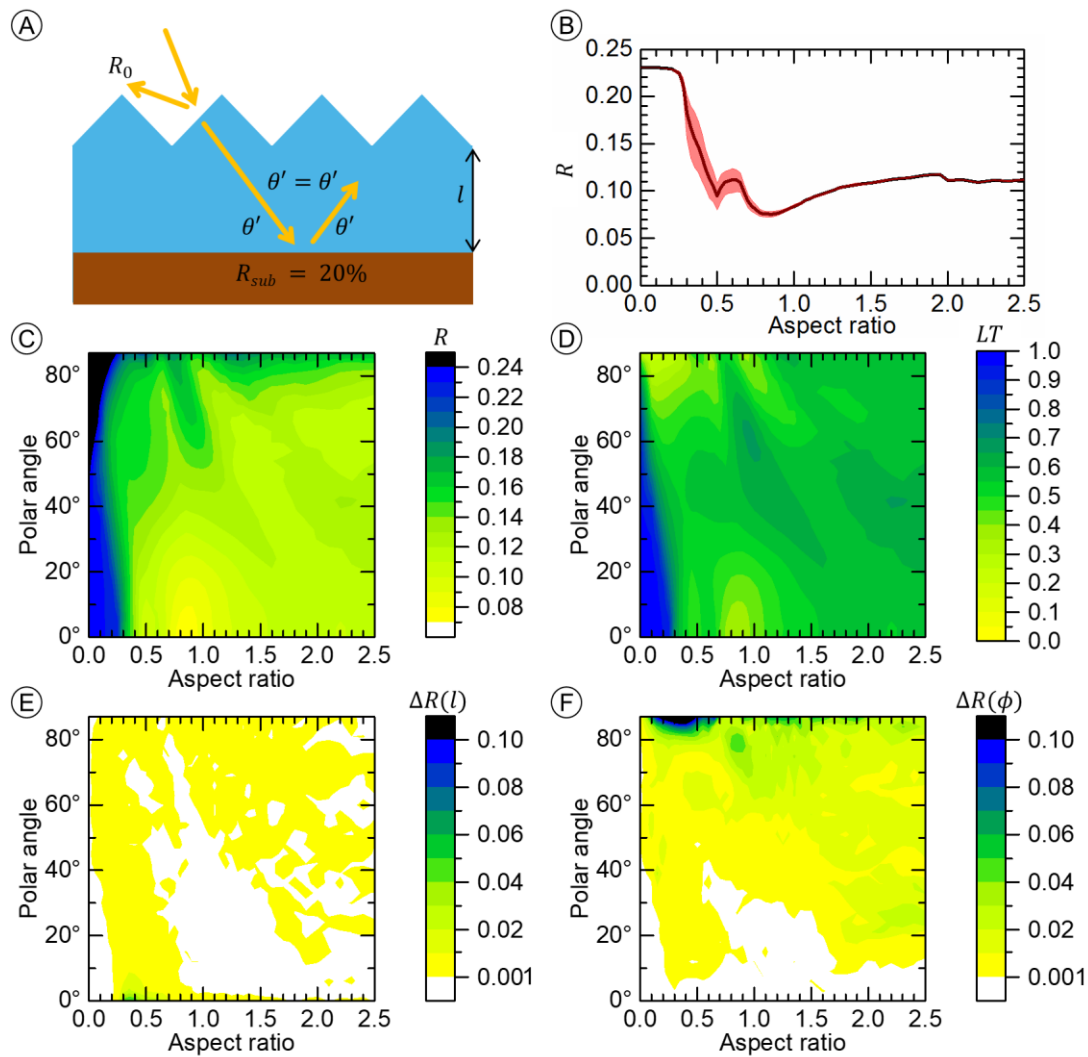


Figure 69. (A) Illustration of the simulation setup for analyzing the light-trapping effect for a specular reflecting substrate. (B) The total reflectance in the case of normal incidence light, including the variation with the layer thickness (l). (C) Total reflectance averaged over l and the azimuth angle (ϕ). (D) Amount of light escaping from the coating layer calculated according to Equation (5.6). (E) Variations in reflectance caused by different thicknesses. (F) Variations in reflectance caused by different azimuth angles.

The second investigated extreme case is **perfect Lambertian reflection**, as illustrated in **Figure 70(A)**. The light-trapping is again investigated for the case of a back surface with a reflectivity of 20%. There are key differences between a back surface exhibiting Lambertian reflection and a back surface exhibiting specular reflection. Firstly, in case of a planar front surface an escape cone is defined. Light scattered in directions outside this escape cone is trapped. Thus, light-trapping is already achieved in case of a planar front surface. Secondly, the coating thickness does not play a role, as light is scattered in all directions. The same consideration apply to different angles of incidence. It follows that the light-trapping does not depend upon the layer thickness and the incidence angle. **Figure 70(B)** shows the total reflectance reaching the far field detector in the case of normal incidence illumination. There is no clear optimum as in the case of specular reflection. All $AR > 0.5$ perform similarly well. The reduction in total reflectance is completely attributed to the reduced interface reflectivity. Taking a look at larger angles of incidence in **Figure 70(C)**, the influence of the reduced interface reflectivity, already known from **Figure 67(A)**, is

clearly visible. Calculating LT according to Equation (5.6) shows that the microcone textures trap light less efficiently than a planar layer (**Figure 70(D)**). Since this is only a very small effect, the reduced interface reflectivity dominates the total reflectance. In summary, the reduced interface reflectivity is the only beneficial effect when employing the microcone texture on a substrate showing perfect Lambertian reflection.

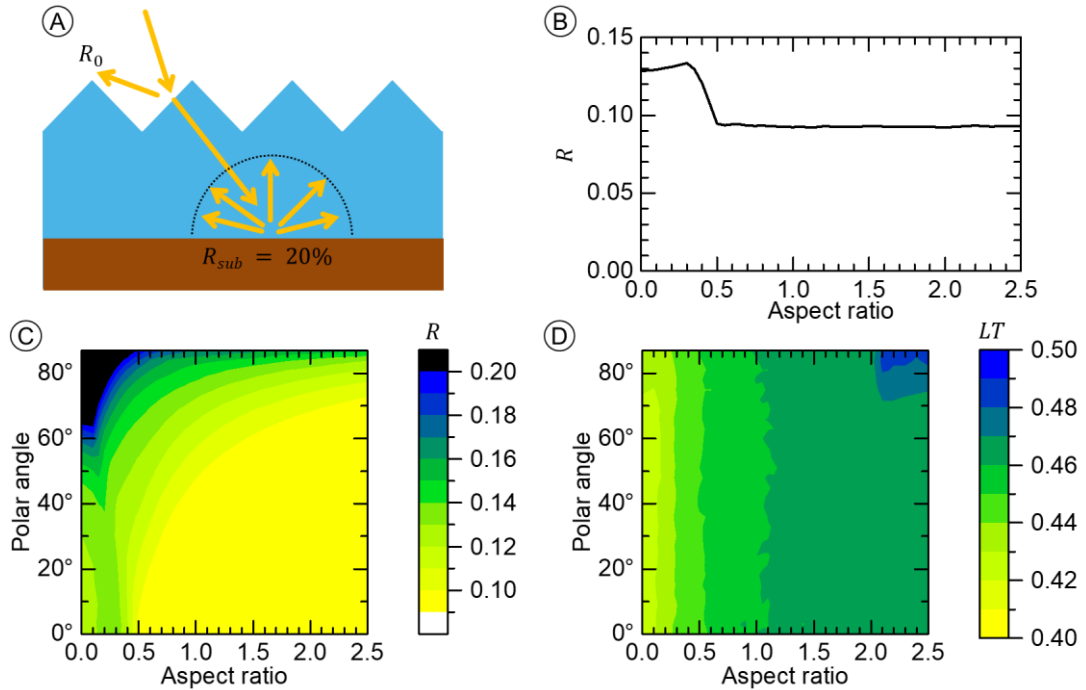


Figure 70. (A) Illustration of the simulation setup for analyzing the light-trapping effect on a substrate showing Lambertian reflection. (B) The total reflectance (R) in the case of normal incidence light. (C) Total reflectance averaged over the azimuth angle. (D) Amount of light escaping from the coating layer calculated according to Equation (5.6).

5.4 Microcone fabrication

5.4.1 DLW prototyping

The microcone textures were fabricated using the Nanoscribe Photonic Professional GT (section 3.1) employing the Photoresist IP-S and the 25 \times objective. IP-S was designed by Nanoscribe to produce smooth surfaces [82]. The microcone textures produced in this work were fabricated on ITO-coated soda lime glass slides. **Figure 71** illustrates the design of a single microcone. Dictated by the galvo-scanning procedure the microcones were exposed plane-by-planar, with each plane separated by the slicing distance h_s . The contour of the microcone textures was designed by defining points on a ring. The galvo system moved from point to point at high speed in line-scanning mode. The interior of the microcones was exposed by spiraling inwards. The individual rings on the spiral were exposed at a hatching distance h_h . At the tip of cone a point exposure was performed.

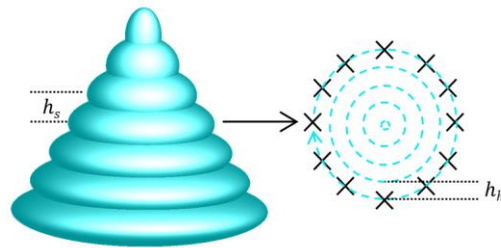


Figure 71. Illustration of the DLW design for an individual microcone. They were fabricated layer-by-layer by moving the voxel continuously to several points on a ring.

The parameters of the DLW exposure procedure were optimized to produce circular cones with straight side walls. It was found that a contour defined with 36 points (**Figure 72(A)**) and exposed at a scan speed 8 mm/s satisfies the requirements. Furthermore, special care had to be taken when choosing h_s . The smaller the AR of the produced microcone the smaller h_s needed to be to prevent steps between slicing planes (compare **Figure 72(C)**). In general $h_s/AR \leq 1$ was a good rule of thumb. The upper limit for h_s was about $0.5 \mu\text{m}$ due to the finite size of the voxel. Shape perfection was not necessary when exposing the interior. A larger scan speed of 40 mm/s was used, along with a hatching distance (h_h) of $0.30 \mu\text{m}$.

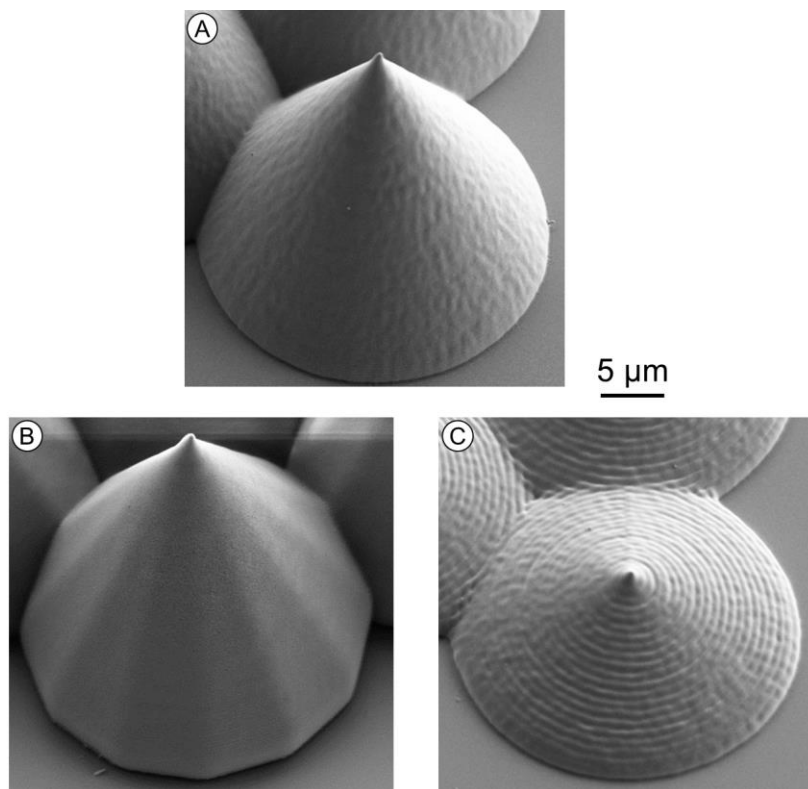


Figure 72. SEM images of fabricated microcones. **(A)** A microcone close to the intended circular design with straight side walls. **(B)** When defining too few contour points a polygonal base appears. **(C)** When choosing the hatching distance too big (in relation to the AR) steps appear.

A lattice constant of $25\ \mu\text{m}$ was chosen for all fabricated textures. To ensure the fabrication of every single microcone, as well as good adhesion to the substrate, the first plane was exposed one micrometer below the detected substrate surface. The ring in the plane of the substrate surface was defined with a diameter of $2/\sqrt{3} \cdot 25\ \mu\text{m}$. In accordance with the targeted hexagonal lattice the microcones were spaced $25\ \mu\text{m}$ apart in y -direction and $\sqrt{3}/2 \cdot 25\ \mu\text{m}$ in x -direction with a shift of $12.5\ \mu\text{m}$. Within the field of view of the $25\times$ object about 100 microcones could be fabricated in this lattice geometry. Several of such fields of microcones were stitched together to cover larger areas. **Figure 73** shows a top view optical image of a fabricated microcone array. The stitching lines are visible in the image. The larger the height of the microcones the more volume had to be exposed leading to longer fabrication times. Depending on the targeted AR the fabrication speeds varied from about $0.6\ \text{mm}^2/\text{h}$ to about $1.4\ \text{mm}^2/\text{h}$. Areas of $5\ \text{mm}$ by $10\ \text{mm}$ were textured, large enough for optical measurements. Microcone textures of various ARs were fabricated by varying the microcone height (and if necessary the slicing distance).

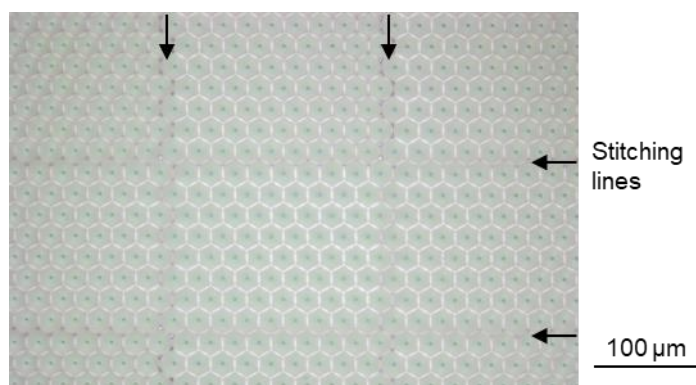


Figure 73. Top view optical image of a fabricated microcone array.

5.4.2 Texture replication

DLW is a rapid prototyping method when talking about design-to-prototype. The drawbacks of the technology are a comparably slow fabrication speed and the use of photoresist materials not necessarily usable for PV applications. Therefore, a scalable process was used to replicate the textures. The replication process has been described for example by Hünig *et al.* [56] and Lin *et al.* [163].

In this replication process the inverse of the DLW fabricated textures was first transferred to polydimethylsiloxan (PDMS). To achieve anti-adhesion and to facilitate the PDMS lift-off process DLW fabricated textures were silanized. As hydroxyl groups (-OH) are necessary for the silanization, the samples were coated with aluminum oxide (Al_2O_3) via atomic layer deposition (ALD, SUNALE R-200 Advanced, Picosun, Dresden, Germany). The silanization was performed by placing the samples together with $200\ \mu\text{l}$ of perfluorooctyl-trichlorosilane (PFOTS, Sigma Aldrich, Darmstadt, Germany) into a desiccator, pumped to $200\ \text{mbar}$, for $30\ \text{min}$. Next, PDMS was prepared by mixing the silicone elastomer base (SYLGARD 184, Dow Corning, Midland MI, USA) and the appropriate silicon elastomer curing agent (SYLGARD 184, Dow Corning) in a $10:1$ ratio. The mixture was rigorously stirred with a glass bar and then placed in a vacuum desiccator. Vacuum was used to extract air bubbles from the mixture. Finally, the PDMS mixture was poured over the samples with the Al_2O_3 coated DLW prototypes and placed on a hot

plate at 60°C for 3 h for the PDMS polymerization. The hardened PDMS stamp was lifted from the DLW fabricated textures. The fabrication of the PDMS stamp is illustrated in **Figure 75(A)-(C)**.

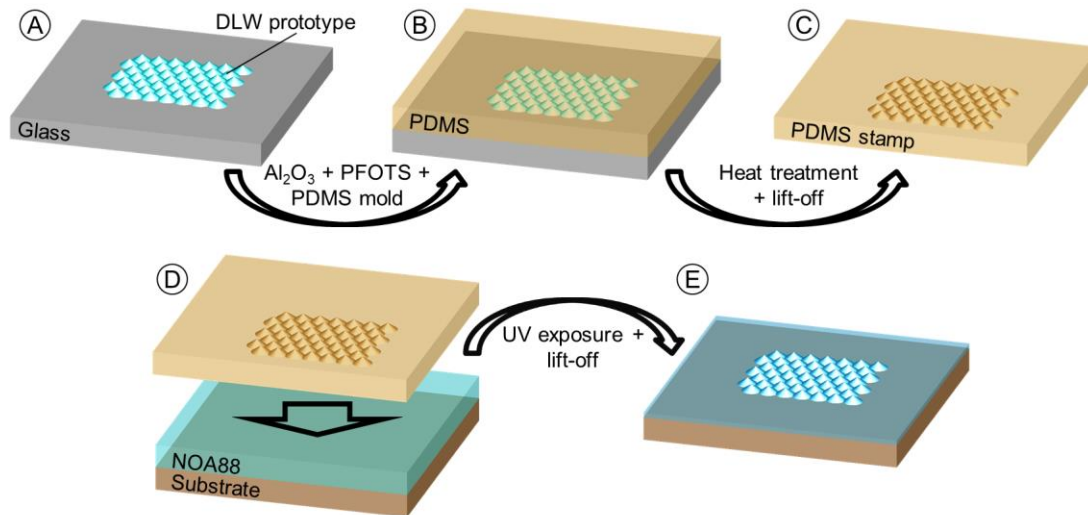


Figure 74. Illustration of the replication processed used for multiplying the DLW fabricated prototypes on to various substrates..

The fabricated PDMS stamps were be used for transferring the microcone textures into a UV curable resin on various substrates. In this work, the textures were transferred into the highly transparent photoresist Norland Optical Adhesive 88¹ (NOA88, Nordland, Cranbury, NJ, USA) [144]. A drop of NOA88 was placed on the desired substrate and the PDMS stamp pressed into it. The NOA88 was then optically cured through the transparent PDMS mold. For curing, the samples were placed in an irradiation chamber (Opsytec Dr. Gröbel GmbH, Ettlingen, Germany) and illuminated with 405 nm LEDs at an intensity of $\sim 75 \text{ mW/cm}^2$ for 5 min. After exposure the PDMS was carefully lifted from the substrate, leaving behind a replica of the original DLW fabricated texture on the surface of a hundredth of micro-meter thick layer of NOA88. The replication process using the PDMS stamp is illustrated in **Figure 74(D)-(E)**.

Microcone textures of six different ARs were prepared using DLW. **Figure 75** shows cross-sectional SEM images of all fabricated microcone textures after replication into the photoresist NOA88. Mainly due to shrinkage of the photoresist IP-S the microcones turn out a bit smaller than programmed. The OAs (compare **Figure 64**) of the final replicas in NOA88 where determined from the SEM images in **Figure 75** with high precision ($\pm 1^\circ$). The AR, the IA and the AOR of the prepared samples were calculated according to Equations (5.1) to (5.3) and are summarized in **Table 3**.

¹The manufacturer specifies a refractive index of 1.56 for cured NOA88.

This value was confirmed using the 2010/M (Metritcon), resulting in a value of 1.5593 at 637 nm.

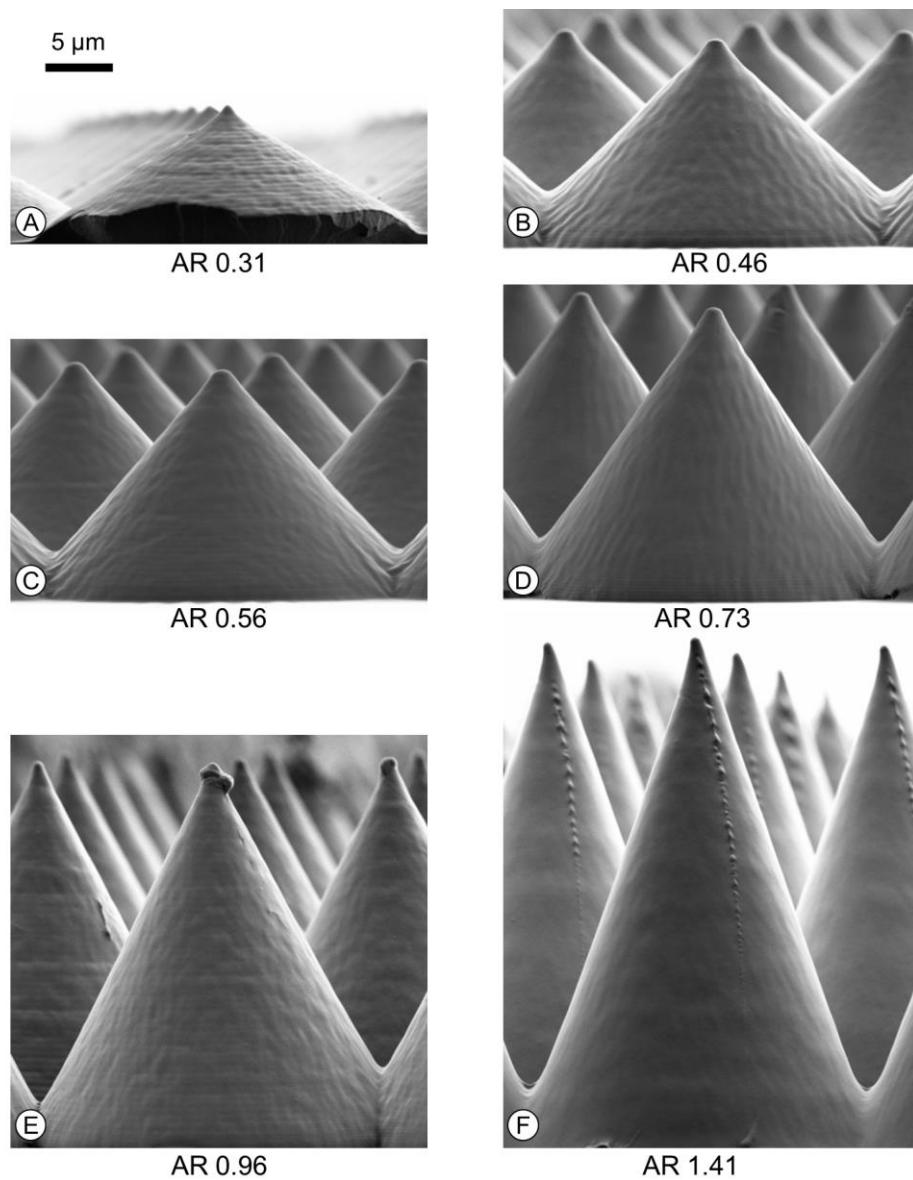


Figure 75. (A)-(F) SEM images in cross-section of individual microcones of varying height in a hexagonal lattice of constant lattice constant 25 μm. The images show microcones replicated into the photoresist NOA88. The aspect ratio (AR) of the replicated microcones was extracted from measuring the opening angle (OA) in these images.

AR	OA	IA	AOR
0.31	118°	31°	12°
0.46	95°	43°	17°
0.56	84°	48°	20°
0.73	69°	56°	24°
0.96	55°	63°	28°
1.41	39°	71°	33°

Table 3. The aspect ratio (AR), the opening angle (OA), the inclination angle (IA), and the angle of refraction (AOR) of the different fabricated microcone textures. Each of these parameters is visualized in **Figure 64**. For calculating the AOR a refractive index of 1.56 was used.

5.5 Optical analysis

Before applying the microcone textures to solar cells their performance was evaluated on different substrates by performing transmittance and reflectance measurements. For each experimental setup matching simulations were designed. The performance of the microcone textures was compared to one another, as well as to the simulation results. Transmittance measurements were performed to evaluate how closely the fabricated textures match their digital twin. Reflectance measurements were performed to investigate the reduced interface reflectivity, as well as the light-trapping effect of the microcone textures of different ARs. The basic working principle of micron-scale textures is wavelength independent. Only the refractive index induces slight differences in reflectance for different wavelengths. On the other hand, the dispersion of the refractive of the employed materials is small in the visible wavelength range. Therefore, it was sufficient to only evaluate the results in terms of the reduced interface reflectivity and the light-trapping effect at a single wavelength.

5.5.1 Photogoniometric analysis

For an initial evaluation of the optical performance of the microcone texture, photogoniometric measurements were performed. The setup for the photogoniometric measurements is described in section 3.2.3. The measurement results were compared to simulation results to determine the optical quality of the microcone textures. In general, experimental results matched simulation results. Most light was detected under the AOR. In simulations using LightTools a layers of refractive index 1.56 with the microcone textures at the front surface was illuminated under normal incidence from air. The microcone textures refract light to oblique angles. The angles the light is transmitted to were analyzed in 1° steps. These simulations were performed by Raphael Schmager. **Figure 76(A), (C), and (E)** show the simulation results for microcone textures of AR 0.31, AR 0.46, and AR 0.73, respectively. Most of the incident light is refracted to a ring after one interaction with a cone-element. The ring is positioned at the AOR indicated in **Table 3**. Further features of lower intensity are visible at larger transmission angles for light having impinged on multiple microcones. In the respective experimental results (**Figure 76(B), (D), and (F)**) the main ring is visible, as well as some of the stronger features at larger transmission angles. In contrast to simulation results a significant amount of light was detected at transmission angles smaller than the AOR. These features are most likely due to surface roughness, also visible in the SEM images in **Figure 75**. Overall, the fabricated textures should perform very similar to their numerical counterparts.

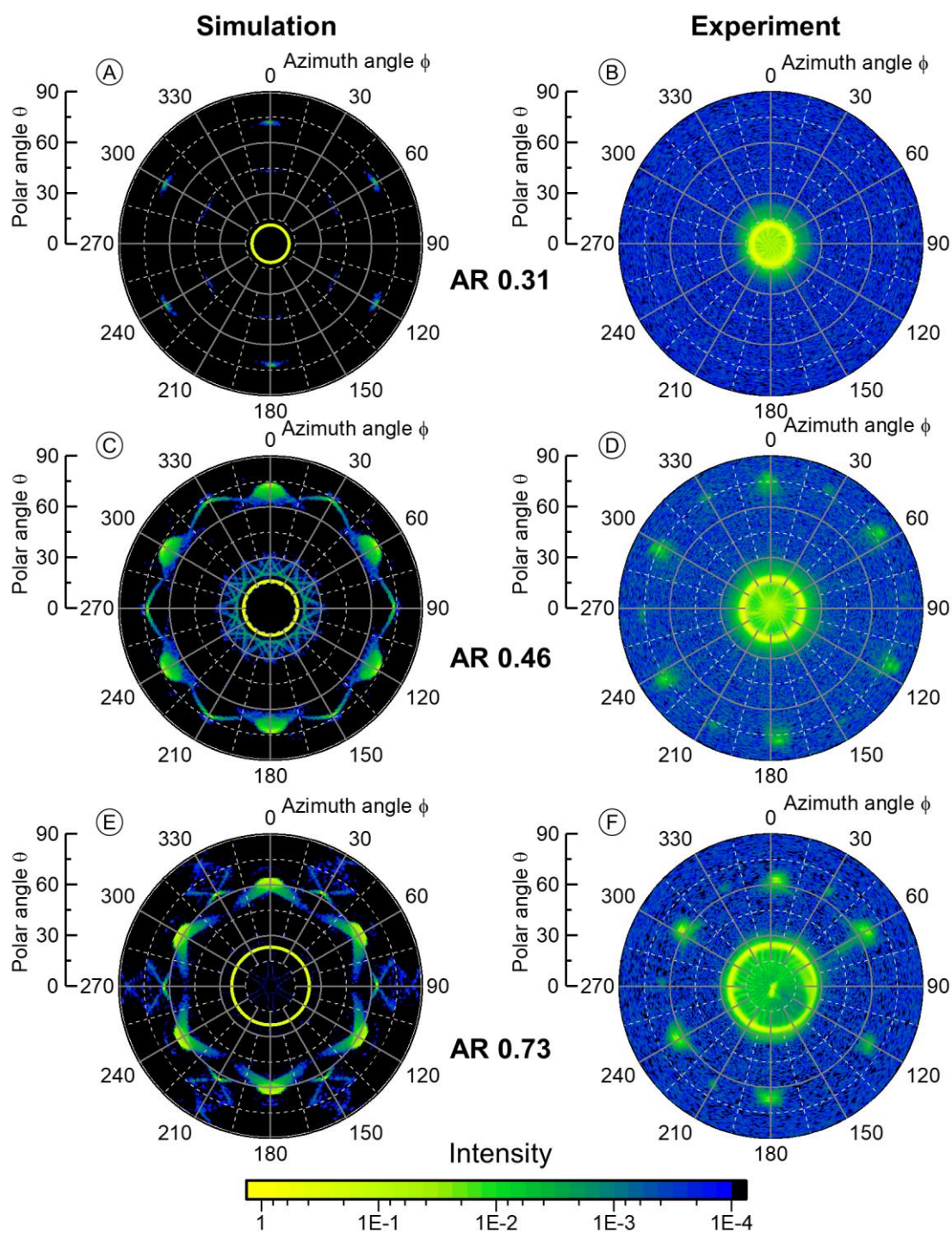


Figure 76. Angle-dependent transmittance for microcone textures of AR 0.31 (A,B), AR 0.46 (C,D), and AR 0.73 (E,F). (A,C,E) simulation results for perfect right, circular cones with straight side walls. (B,D,F) experimental results obtained with a photogoniometric setup for DLW fabricated microcones textures replicated onto soda-lime glass into the photoresist NOA88.

5.5.2 Analyzing the reduced interface reflectivity

The reduced interface reflectivity was analyzed by employing the microcone textures on soda-lime glass substrates and making use of a UV/Vis spectrometer equipped with an integrating sphere (for details see section 3.2.2). To obtain the interface reflectance measurements by employing an absorbing layer at the back surface of the substrate – a procedure identical to the simulation work described in section 5.3.1. Reflectance measurements without the absorber layer did not lead to useful results, as the total reflectance complexly depends upon the transmission angles of the microcones and the reflectance at the rear air-glass interface. It is further to be noted that transmittance measurements were even less useful. Light, refracted by the microcone texture to large angles, was trapped inside the substrate, as illustrated in **Figure 77(A)**, and did not reach the detector. Using reflectance measurements and utilizing the absorber layer no light escaped from the substrate (**Figure 77(B)**) detected light must have been reflected at the front surface. A black adhesive (Leit-Tab, Plano GmbH, Wetzlar, Germany) was used as an absorber layer on the back surface of the glass slide. By comparing the reflectance from the planar soda-lime glass with and without the absorber layer the reflectivity of the glass-absorber interface could be estimated with 1% (**Figure 77(C)**); A value reasonably low for investigating the reduced interface reflectivity of the front surface.

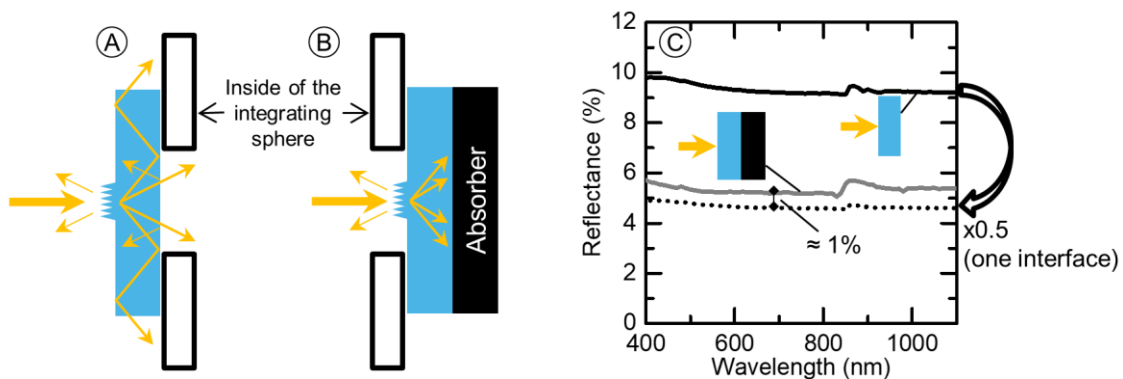


Figure 77. (A) Illustration of a standard setup for measuring the total transmittance. The setup is not suitable for obtaining the desired data in this case. (B) Illustration of a suitable setup for determining the front surface reflectance of a textured sample. (C) Reflectance measurement results for a glass substrate with and without an absorber at the back side. (C) was adapted with permission from [140], © 2019 Wiley.

Figure 78 shows the obtained results when measuring the reflectance of the microcone textures front surface. **Figure 78(A)** again illustrates the setup and **Figure 78(B)** shows a prepared sample (AR 0.73). The rectangular outline of the stamp is visible. The textured area is much darker than the planar area, already proofing the functionality. **Figure 78(C)** shows the measured reflectance of the different microcone textures prepared in this manner. The step and uncertainty around 860 nm arises from a detector and grating switch in the spectrometer. With increasing AR the reflectance decreases for all wavelengths. This is a clear indication that the chosen lattice constant of 25 μm is large enough for the applicability of ray optics.

Simulations for comparing and expanding the experimental results were performed as described in section 5.3. The simulated microcone texture was illuminated from a polar angle of 8° and 1% specular reflectivity was implemented for the back surface. **Figure 78(D)** compares the measurement results at a wavelength of 600 nm to simulation results. Simulation- and experimental- results are in good

agreement, the microcone textures perform as expected. Therefore, the experimental- and the simulation- setup closely match. Around 600 nm the refractive index of NOA88 closely matches the 1.56 implemented in simulations. Furthermore, NOA88 was considered non-absorbing at this wavelength.

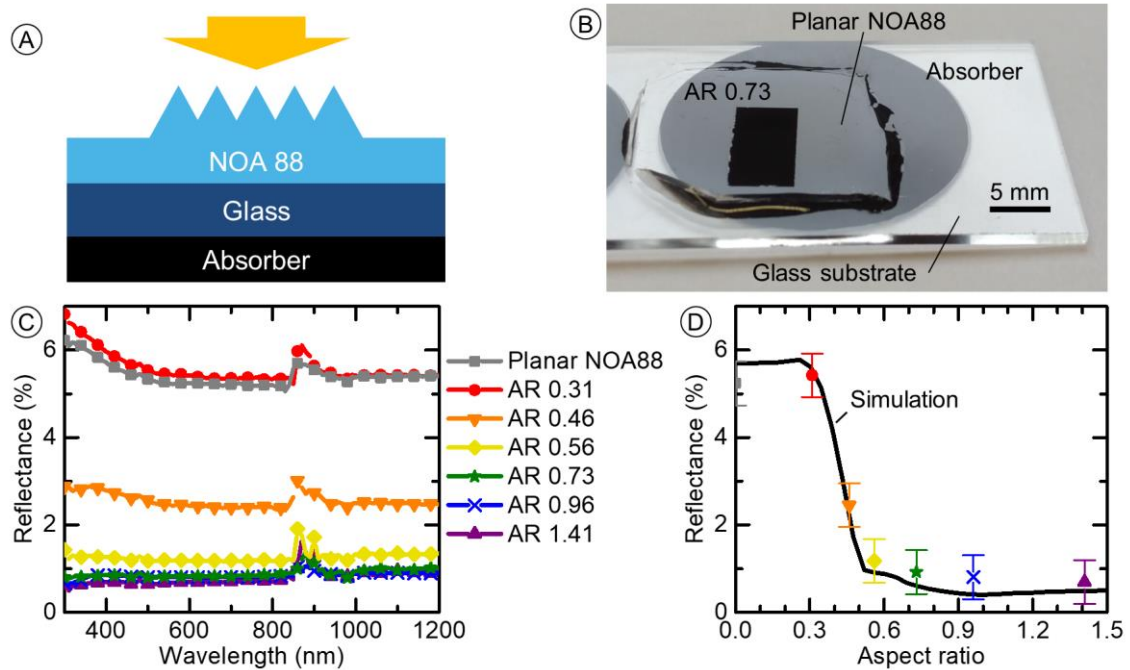


Figure 78. Reflectance measurements on soda-lime glass with an absorber layer glued to the back surface and the microcone textures on the front surface. **(A)** Illustration of the layer stack for analyzing the reduced interface reflectivity. **(B)** Photo of a sample realizing the layer stack. **(C)** Wavelength-dependent reflectance for the different microcone textured samples. **(D)** Simulation and experimental results showing the reduced interface reflectivity. **(C)** and **(D)** were adapted with permission from [140], © 2019 Wiley.

5.5.3 Analyzing the light-trapping

The light-trapping was investigated on a single-side polished silicon wafer and on an alkaline-etched silicon wafer. Polished silicon wafers show large Fresnel-type reflection due to a large refractive index step. Therefore, a polished silicon wafer is a good candidate for visualizing the light-trapping effect. An alkaline etched silicon wafer with a random pyramid textured was used a substrate of known diffuse reflectance. In both cases the microcone textures were directly applied to the wafer using the photoresist NOA88 and a PDMS stamp.

The results for the polished silicon wafer are summarized in **Figure 79**. **Figure 79(A)** illustrates the layer stack and a corresponding photo is shown in **Figure 79(B)**. **Figure 79(C)** shows the measured reflectance with the microcone textures of different AR applied to the polished silicon wafer. Again a uniform reduction in reflectance was visible for all wavelengths when applying the microcone textures. In the range ~ 400 nm to ~ 1050 nm the reflectance solely varied due to the material dispersion. For wavelengths shorter than 400 nm the NOA88 shows absorption, decreasing the sample reflectance. For

wavelengths longer than 1050 nm light was weakly absorbed in the silicon wafer and partially escaped from the wafer adding to the total reflectance.

A simulation setup was designed to closely match the experiment. A substrate of refractive index 3.94 (closely matching the refractive index of silicon at a wavelength of 600 nm) was implemented beneath the coating layer of refractive index 1.56. The angle-dependent reflectivity at the coating to substrate interface (calculated using the Fresnel equations) is given in **Table 4** for unpolarized light. As discussed in section 5.3.2 the thickness of the coating layer influenced the total reflectance in simulations. The simulation result in **Figure 79(D)** shows the mean reflectance, when averaging over different layer thicknesses. Experimental results are likely to match these mean values as the thickness of the NOA88 layer is likely to vary across the wafer. For completeness the variation of simulation results with the layer thickness is indicated by the red area in **Figure 79(D)**. Again simulation and experimental results closely match. The best performing microcone texture of AR 0.73 is close to the optimum found in simulations.

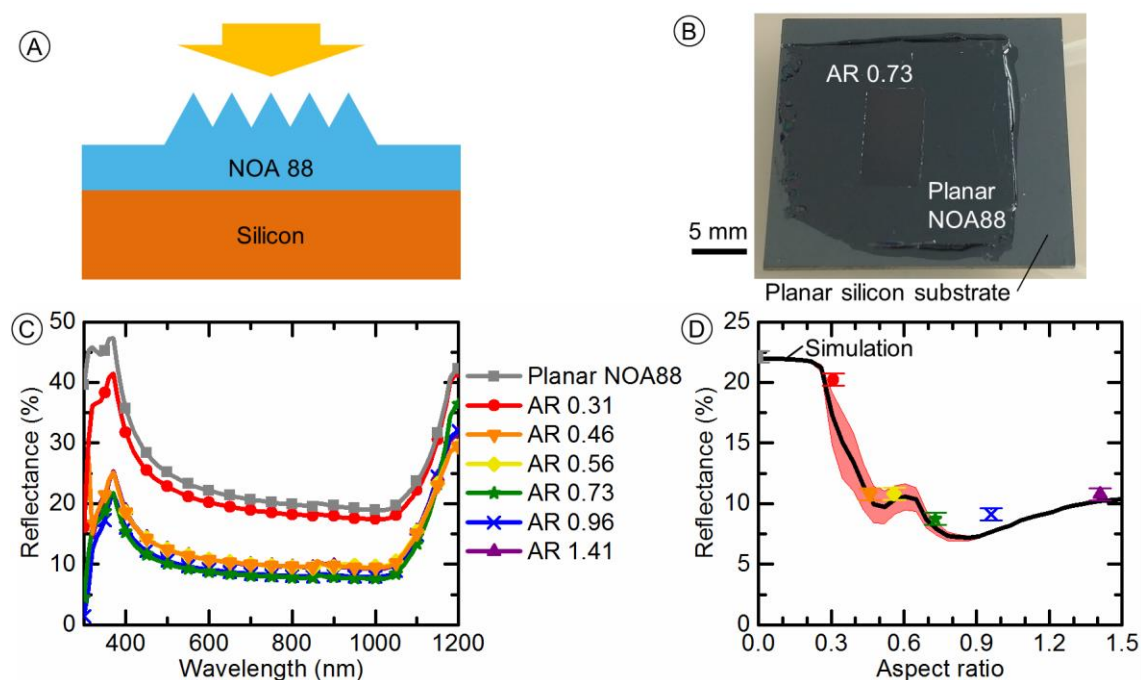


Figure 79. Reflectance measurements on polished silicon wafers coated with the microcone textures. **(A)** Illustration of the layer stack. **(B)** Photo of a piece from a polished silicon with the NOA88 coating. **(C)** Wavelength-dependent reflectance for the different microcone textures on polished silicon wafers. **(D)** Simulation and experimental results corresponding to a wavelength of 600 nm comparing the performance of the different microcone textures. **(C)** and **(D)** were adapted with permission from [140], © 2019 Wiley.

The simulations in the previous section have shown that the light-trapping effect strongly varies with the AR in the case of specular reflection, while it is hardly influenced by the AR in the case of diffuse reflection. An alkaline-etched silicon wafer shows diffuse reflection and was used to experimentally confirm this finding. The results for the alkaline-etched silicon wafer are summarized in **Figure 80**. **Figure 80(A)** illustrates the layer stack and a corresponding photo is shown in **Figure 80(B)**. **Figure 80(C)** shows the measured reflectance with the microcone textures of different AR applied to the alkaline-etched silicon wafer. Again reflectance strongly reduces when applying a microcone texture of sufficiently high

AR. This shows the possibility of using the microcone texture to complement an already textured semiconductor layer.

In simulations, matching the experimental setup, Lambertian reflection of the alkaline-etched silicon substrate was assumed. The incidence angle-dependent reflectivity at the coating layer to silicon interface was determined using an online ray tracer [177]. The calculated angle-dependent reflectance at a wavelength of 600 nm, given in **Table 4**, was used in the LightTools simulations. It was again sufficient to only investigate one wavelength for determining the general light-trapping properties of the microcone textured layer. As discussed in section 5.5.3 the thickness of the coating layer does not play a role for the case of diffuse reflection. **Figure 80(D)** shows the simulation result, as well as the experimental results, at a wavelength of 600 nm. In general, a close match was again achieved. In simulations an optimum was achieved around AR 0.5. The total reflectance increased for larger ARs as a result of the slightly decreased light-trapping (see section 5.3.2) and the increased AOR (leading to stronger interface reflection (see **Table 4**)). This behavior was not observed in experiments. A possible reason is that an alkaline-etched silicon wafer does not show the perfect Lambertian reflection assume in simulations.

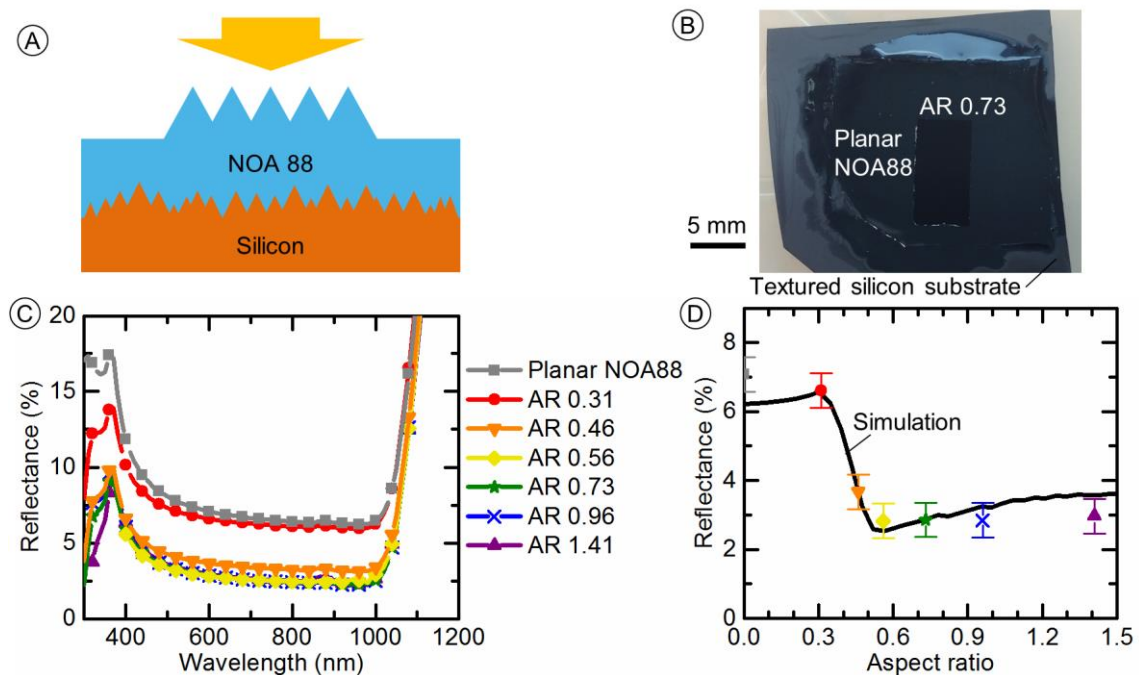


Figure 80. Reflectance measurements on alkaline-etched silicon wafers coated with the microcone textures. **(A)** Illustration of the layer stack. **(B)** Photo of a piece from an alkaline-etched silicon wafer with the NOA88 coating applying the microcone texture. **(C)** Measured wavelength-dependent reflectance for the different microcone textures. **(D)** Simulation and experimental results corresponding to a wavelength of 600 nm comparing the performance of the different microcone textures. **(C)** and **(D)** were adapted with permission from [140], © 2019 Wiley.

Incidence angle	0°	10°	20°	30°	40°	50°	60°	70°	80°	90°
Polished silicon	0.187	0.187	0.188	0.189	0.192	0.201	0.223	0.278	0.434	1
Alkaline-etched silicon	0.037	0.039	0.044	0.072	0.091	0.109	0.131	0.159	0.185	0.203

Table 4. Incidence angle-dependent reflectivity at the coating layer to silicon interface implemented in simulations.

5.6 Applying the microcone textures to solar cells

The microcone textures were applied to three different types of solar cells to demonstrate their enhancement potential in PV applications. First, the microcone textures of different AR were applied to planar silicon solar cells. The used planar silicon solar cells were particularly useful for comparing the performance enhancement of the different microcone textures. Planar silicon solar cells show homogenous performance, enabling a direct comparison. As an additional advantage, a thin-film ARC adapted in thickness to the silicon-air interface had been applied to the here used planar silicon solar cells. Thus, when applying the NOA88 coating of higher refractive index comparably high reflectance was observed. High reflectance aided in the demonstration of the light-trapping effect. The other two typed of used solar cells are highly relevant when it comes to state-of-the-art. The microcone textures were employed on commercial c-Si solar cells with a semiconductor layer textured by alkaline etching. An energy yield analysis was performed for demonstrating the efficiency enhancement the microcone textures bring in an outdoor application. Lastly, the microcone textures were applied to CIGS thin-film solar cells of high efficiency.

5.6.1 Comparing the microcone textures on planar silicon solar cells

With the planar silicon solar cells a detailed study of the performance differences of the microcone textures was performed. It was possible to demonstrate that the optima found in simulations is directly transferrable to PV. Furthermore, the broadband, angle-stable solar cell performance enhancement of the microcone textures was studied in detail.

The planar silicon solar used for comparing the performance of the microcone textures were provided by the Forschungszentrum Jülich (FZJ). The basis for the solar cells was an n-type 280 μm thick silicon wafer passivated with intrinsic amorphous silicon deposited via plasma enhanced chemical vapor deposition (PECVD). N-type nano-crystalline $\text{SiO}_x\text{:H}$ was used as front surface field and p-type nano-crystalline $\text{SiO}_x\text{:H}$ as an emitter, both deposited by PECVD. The back surface of the wafer was fully covered with silver. On the front surface of the wafer areas of 1 cm by 1 cm were coated with 70 nm of indium tin oxide (ITO) and a silver grid, to form small solar cells. More details are available in the work of Richter *et al.* [156]. An image of one of these solar cells is shown in **Figure 81(A)**. For better handling, the 10 cm diameter wafer with the solar cells was cut into quarters. Two 1 cm^2 solar cells were available on every quarter. A drop of NOA88 was placed on every solar cell. The PDMS stamps were used to employ the microcone texture on one half of the solar cell and a planar layer of NOA88 on the other half (see **Figure 81(B)**).

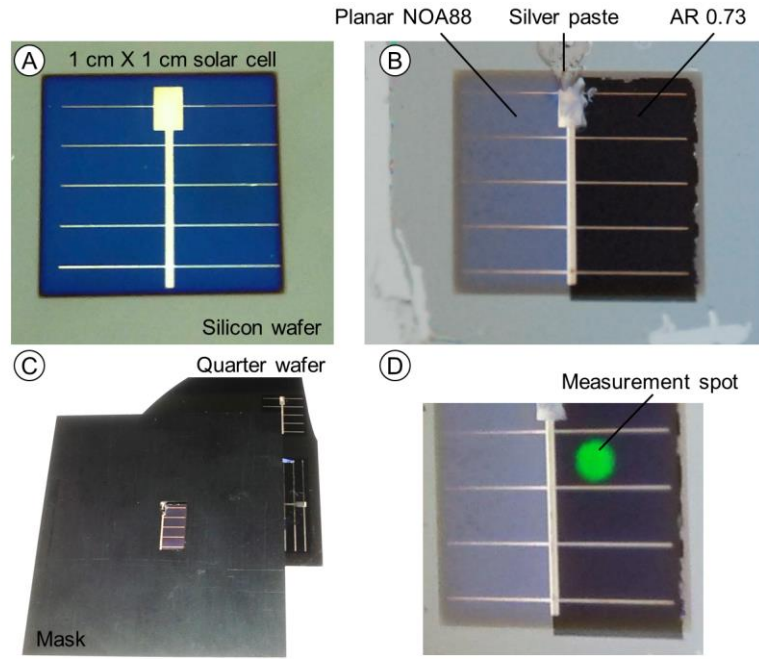


Figure 81. Photographs showing the planar silicon solar cells. **(A)** Bare solar cell as prepared by the FZI. **(B)** Solar cell coated with NOA88 by applying the prepared PDMS stamps. **(C)** Mask on top of solar cell used for IV-measurements. **(D)** Solar cell during EQE measurements.

I-V measurements. The most important solar cell characteristic is the current-voltage ($I-V$) relationship (details in section 2.1.2). $I-V$ measurements of the bare (without a NOA88 coating) silicon solar cells, as well as $I-V$ measurements after coating with the microcone textured NOA88 layer were performed using a solar simulator (section 3.2.5). For obtaining the $I-V$ curve of a desired area masking of the rest of the wafer was necessary, as shown in the photo in **Figure 81(C)** (mask opening size: 1 cm by 0.5 cm). The obtained characteristic solar cell parameters J_{SC} , V_{OC} , FF and PCE are summarized in **Table 5**. From the table it is clear that the microcone textured solar cells outperform the solar cells without a front surface texture. However, for analyzing a clear trend the uncertainty in J_{SC} was too high. The uncertainty in J_{SC} of $\pm 0.5 \text{ mA/cm}^2$ is given in the first line of **Table 5**, where the average of the measured bare solar cells is shown. The large uncertainty arose from the small microcone textured area of 1 cm by 0.5 cm. The exact position of the mask (especially in relation to the contacts) had a large impact on the performance of the solar cells. As a consequence, the detailed discussion of the microcone textures in the following was based on EQE measurements (section 3.2.5). In EQE measurements masking was not necessary.

	$J_{SC} \text{ (mA/cm}^2\text{)}$	$V_{OC} \text{ (mV)}$	FF (%)	PCE (%)
Bare (average)	35.3 ± 0.5	659 ± 5	78 ± 1	18.1 ± 0.3
Planar coating	34.4	651	78	17.5
AR 0.31	36.1	651	79	18.6
AR 0.46	36.4	649	79	18.7
AR 0.56	37.2	653	77	18.7
AR 0.73	37.9	665	79	19.9
AR 0.96	37.5	649	80	19.5
AR 1.41	37.4	656	78	19.1

Table 5. Solar cell characteristics of planar silicon solar cells with and without a microcone texture.

Normal incidence EQE. Using EQE measurements it is possible to calculate the J_{SC} for different incidence spectra. For standard conditions the air-mass 1.5 global tilt spectrum (AM1.5g see section 2.1.3, units: photons/s) is made use of. The J_{SC} is then given by (compare Equation (2.2)):

$$J_{SC} = e \int \text{EQE}(\lambda) \text{AM1.5g}(\lambda) d\lambda \quad (5.7)$$

where λ is the wavelength and e is the elementary charge. EQE measurements were performed between the contact lines of the solar cells. The measurement spot is shown in the photo in **Figure 81(D)**. Measurements on a grid line would have led to a similar problem in positioning as the masking in I - V measurements. From EQE measurements an average J_{SC} of the bare solar cells of 34.7 ± 0.1 mA/cm² was determined. The slight variation to the J_{SC} of 35.3 mA/cm² obtained from I - V measurements is common and a result of the very different utilized methods. Importantly, the variation in J_{SC} obtained from EQE measurements of different solar cells was only ± 0.1 mA/cm² allowing a direct comparison of the different microcone textures.

From the calculated J_{SC} the best performing microcone texture was determined. **Figure 82** shows the same trend already observed in simulations (**Figure 69**) and on the planar silicon substrate (**Figure 79**): All microcone textures perform much better than the planar reference and an optimum is obtained in the range $0.7 < \text{AR} < 1$. The microcone texture with AR 0.73 shows the best performance with a J_{SC} of 37.1 mA/cm². 4.0 mA/cm² more than the solar cell with a planar coating of NOA88, equal to a 12% relative enhancement.

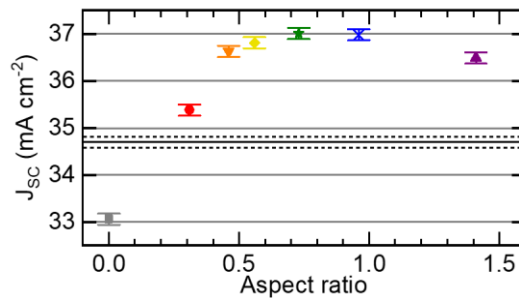


Figure 82. Short circuit current (J_{SC}) obtained from EQE measurements of the planar silicon solar cells with the microcone textured front surface and a planar layer (AR 0) of NOA88. The straight line indicates the average J_{SC} of the bare solar cells and the dashed lines the standard deviation. Adapted with permission from [140], © 2019 Wiley.

Apart from determining the J_{SC} , EQE measurements are an important tool in analyzing the wavelength-dependent response of solar cells. In combination with reflectance measurements, it is possible to precisely analyze optical loss mechanism in the solar cell. **Figure 83(A)** compares the EQE and reflectance, obtained from a bare solar cell, to the spectra of a solar cell with a planar coating of NOA88, and one with a microcone textured front surface of AR 0.73. The EQE is enhanced for all wavelengths. The reflectance is equally low for all wavelengths, clearly showing the broadband improvement the microcone texture brings. To set the obtained 12% relative J_{SC} enhancement into context, the maximum possible increase in J_{SC} was estimated. For this estimation, it was assumed that the internal quantum efficiency (IQE) of the solar cell was unaffected by the NOA88 coating layer. Perfect light-trapping is achieved in case all light reflected by the solar cell with the planar NOA88 is utilized in the device. Thus, the maximum possible J_{SC} increase ($\Delta J_{SC,max}$) of the solar cell with the planar coating of NOA88 was estimated according to:

$$\Delta J_{SC,max} = e \int R(\lambda)IQE(\lambda)AM1.5g(\lambda) d\lambda \quad (5.8)$$

Where, R is the reflectance of the solar cell coated with a planar layer of NOA88. The IQE is given by: $IQE = EQE/(1 - R)$. **Figure 83(B)** compares the factor $R \cdot IQE$ for a solar cell with a planar coating of NOA88 to the achieved enhancement in EQE for a front surface microcone texture of AR 0.73. In the visible range, near ideal utilization of the reflected light was achieved. The approximated maximum enhancement was $\Delta J_{SC,max} = 5.6 \text{ mA/cm}^2$, equal to a maximum possible relative enhancement of 17%. Therefore, 12% is a large portion of the maximum possible enhancement.

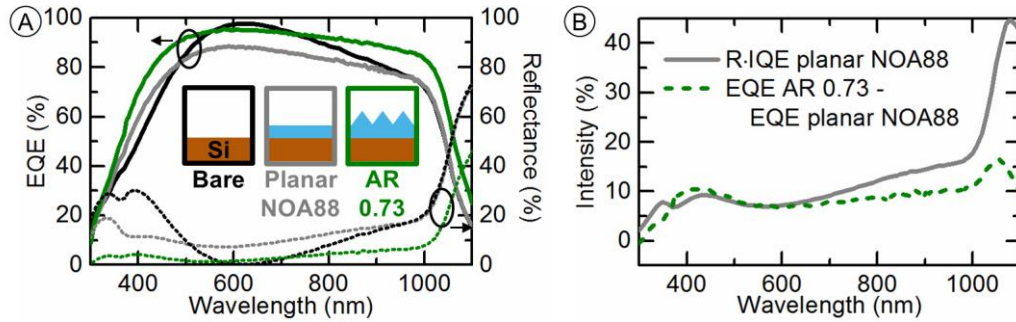


Figure 83. (A) External quantum efficiency (EQE) and reflectance (R) of an uncoated, bare planar silicon solar cell, a solar cell with a planar coating of NOA88, and a solar cell with a microcone texture of AR 0.73. **(B)** Approximation of the maximum possible enhancement of the solar cell coated with planar NOA88 ($R \cdot IQE$), as well as the achieved enhancement in EQE when employing the microcone texture of AR 0.73. **(A)** was adapted with permission from [140], © 2019 Wiley.

Angle-dependent EQE. Angle-dependent EQE measurements confirmed the simulation results (section 5.3). To recall, compared to planar layers the microcone textures performed much better at large polar incidence angles, with microcone textures of large ARs showing the strongest angular stability. The azimuth of the incidence angle did not have a large impact on the reflectance of the microcone textures. Therefore, only the polar angle was varied in experiments, termed the angle of incidence (AOI) in the following. For protocol, with regards to the incidence beam the microcone textures were aligned according to the 0° azimuth angle illustrated in **Figure 65(B)**. The spot size in EQE measurements increased with the AOI. For performing measurement between the contacts the AOI was limited to 75° in case of the planar silicon solar cells.

The calculated J_{SC} of the angle-dependent EQE measurements is plotted in **Figure 84**. All microcone textures perform better than the planar coating layer for all AOIs. For large AOIs ARs > 0.5 are beneficial, with the microcone texture with the largest AR of 1.41 showing the most angle-stable performance – perfectly in-line with simulation results. At large AOIs the light-trapping effect only plays a minor role. The reduced interface reflectivity in the case of large ARs was of much higher importance. In conclusion, the optimum AR does not only depend upon the reflectance of the underlying solar cell, but also on the illumination condition. This topic will be discussed in more detail in the next section, where an energy yield analysis will be performed.

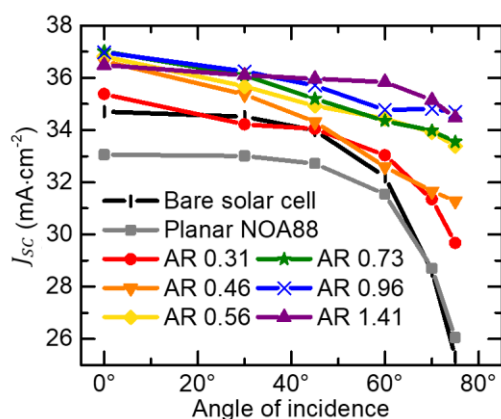


Figure 84. Short circuit current density (J_{sc}) calculated from EQE measurements for various angles of incidence for the planar silicon solar cells with and without the microcone textures of various aspect ratio (AR).

5.6.2 Microcone textures on silicon solar cells with a textured semiconductor layer

While the planar silicon solar cells were highly useful for comparing the microcone textures, silicon solar cells with a textured semiconductor layer are state-of-the-art. Therefore, showing the performance of the microcone textures on these types of solar cells was highly important. It is to be noted, that there is a smaller potential for enhancement using the light-trapping schemes as less light is reflected by the solar cell. In this work, commercial c-Si silicon solar cells with a random pyramid textured semiconductor layer were used. Additionally, a thin-film ARC layer, likely silicon nitrite, was present on top of the textured silicon surface – as is state-of-the-art. The solar cells were produced by the company E-Ton Solar Tech Co. Ltd. (Tainan, Taiwan R.O.C.) A photograph of a solar cell coated with NOA88 by employing PDMS stamps is shown in **Figure 85**.

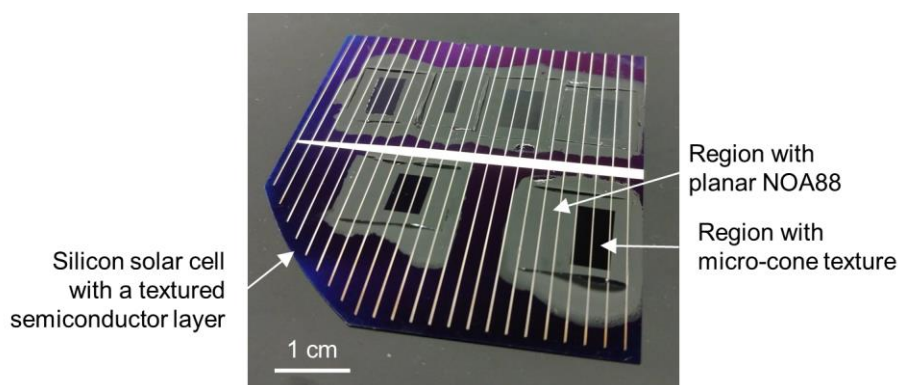


Figure 85. Photograph of a commercial silicon solar cell with an alkaline-etched semiconductor layer. Various regions are visible where NOA88 was employed using PDMS stamps.

I-V measurements. For characterizing the performance of solar cells *I-V* measurements were taken in different bare positions on the solar cell, as well as in regions with the planar NOA88 coating and regions with the microcone textures of various ARs. Again masks (1 mm by 0.5 mm opening) were employed during measurements. The measured characteristic solar cell parameters are shown in **Table 6**. Masking

was again highly problematic as it led to a large uncertainty in the J_{SC} and additionally to a low V_{OC} of about 480 mV. For comparison the V_{OC} of a larger area of 5 cm² was about 560 mV.

	J_{SC} (mA/cm ²)	V_{OC} (mV)	FF (%)	PCE (%)
Bare (average)	37.4± 0.8	476± 5	72± 1	12.8± 0.3
Planar coating	35.2	478	73	12.3
AR 0.31	35.3	476	72	12.1
AR 0.46	36.2	479	73	12.7
AR 0.56	36.7	477	72	12.6
AR 0.73	37.6	478	73	13.1
AR 0.96	36.8	479	73	12.9
AR 1.41	38.4	482	73	13.5

Table 6. Solar cell characteristics of the commercial alkaline-etched silicon solar cells with and without a microcone texture.

EQE measurements. To perform a detailed study again EQE measurements were found to be more reliable. By measuring different positions on the bare solar cell the uncertainty in J_{SC} was determined with ± 0.4 mA/cm² - much larger than in the case of the planar silicon solar cells, but still allowing an analysis of trends. For normal incidence illumination, the microcone texture of AR 0.73 showed the best performance. The EQE measured on the bare solar cell, as well as in a region with the microcone texture of AR 0.73, and in a region with planar coating of NOA88, are shown in **Figure 86(A)**. For all wavelengths, the microcone texture outperformed the planar coated reference, again highlighting the wavelength independent performance enhancement. Encouragingly, the solar cell with the microcone textures coating performed even better than the bare solar cell. It is worth noting again that the microcone texture complemented the textured semiconductor layer and eliminated all the losses arising from adding an additional interface.

The J_{SC} was calculated according to Equation (5.7). With a J_{SC} of 37.2 mA/cm² the microcone texture of AR 0.73 showed a 5.4% increase in J_{SC} , compared to a planar layer of NOA88 ($J_{SC} = 35.3$ mA/cm²). As in the case of the planar silicon solar cells, this relative increase was compared to the estimated ideal increase in J_{SC} . The factor $R \cdot IQE$ for a region with a planar coating of NOA88 is plotted in **Figure 86(B)**. The measured increase in EQE by the microcone texture showed that near perfect enhancement was achieved in the visible. $\Delta J_{SC,max} = 1.9$ mA/cm² was calculated, amounting to an ideal increase in J_{SC} of 5.4%. Therefore, the measured 5.4% J_{SC} enhancement was close to perfection for the case of normal incidence light.

Commercial silicon solar cells with a textured semiconductor layer were used in this study, to show the relevance of the microcone textures on state-of-the-art solar cells. To further set the 5.4% J_{SC} enhancement into context, a comparison to a state-of-the-art front surface ARC was necessary. A thin-film ARC on the front glass surface of a solar module is an industry standard. Typically, a relative enhancement of 3% has been achieved when applying a thin-film ARC to a planar glass surface [178]. Therefore, the micro-textures outperform the state-of-the-art even in case of normal incidence illumination.

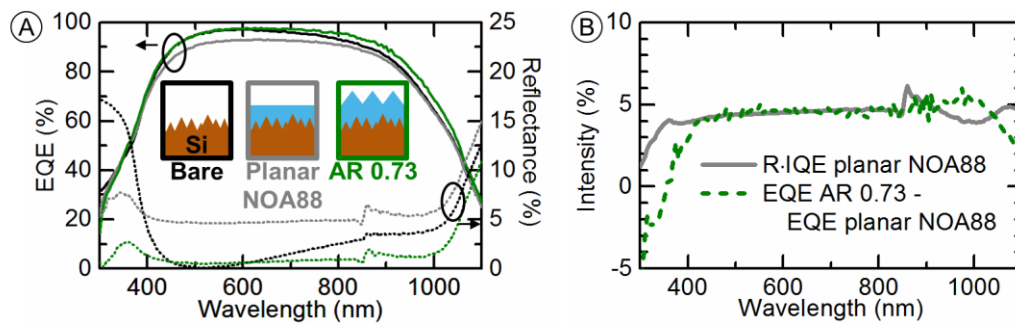


Figure 86. (A) External quantum efficiency (EQE) and reflectance (R) spectra of the bare commercial c-Si silicon solar cell with a textured semiconductor layer, as well as a solar cell with a planar coating of NOA88, and a solar cell with a microcone texture of AR 0.73. (B) Approximation of the maximum possible enhancement of the solar cell coated with planar NOA88 (R -IQE), as well as the achieved enhancement in EQE when employing the microcone texture of AR 0.73. (A) was adapted with permission from [140], © 2019 Wiley.

Angle-dependent EQE measurements were performed, to show the performance enhancement for non-normal incidence illumination and to conduct a calculation of the energy yield in an outdoor application. The J_{SC} , calculated from the EQE measurements, is shown in **Figure 87**. The overall trends matched the findings in simulations and the ones for the planar c-Si solar cells. With the micro-scale textures large gains were possible compared to planar layers at large AOIs. Plus, microcone textures of larger AR performed better for larger AOIs. Thus, the angular distribution of the incidence illumination determines the optimum AR in an application.

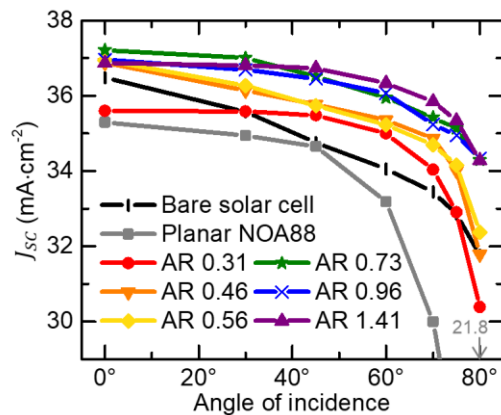


Figure 87. Angle of incidence dependent J_{SC} , calculated from the measured EQE, for an alkaline-etched silicon solar cell with a planar layer of NOA88, and microcone textures of various aspect ratio (AR).

Energy yield modeling. To investigate the performance of the microcone textures in an outdoor application, and determine optimum ARs, energy yield (EY) modeling was performed. Irradiance data for different sites in the US were available from the National Renewable Energy Laboratory (NREL). EY modeling of the used commercial alkaline-etched silicon solar cells was performed based on the obtained EQE data. The EQE data was interpolated linearly in 1° steps from 0° to 80° and extrapolated to 89° linearly in 1°, using the values at 75° AOI and at 80° AOI. NREL irradiance data from Phoenix, AZ, USA was made use of to calculate an hourly resolved J_{SC} over the course of one year (TMY3). The EY software module developed by Malte Langenhorst, Raphael Schmager, and Jonathan Lehr [141,179] was employed. In the software the direct and the diffuse clear sky irradiance was determined by the ‘simple

model of the atmospheric radiative transfer of sunshine' (SMARTS). A fractional model of cloud coverage was applied and the diffuse irradiance distributed Lambertian over the sky. From the irradiance and the EQE data an hourly resolved J_{SC} was calculated. By multiplying with the $FF(J_{SC})$ and the $V_{OC}(J_{SC})$ the hourly resolved EY was determined. The J_{SC} dependent FF and V_{OC} were determined by shifting the J - V curve as illustrated in **Figure 88** to match the J_{SC} calculated in the model. The J - V curve was measured on a solar cell without applying a mask.

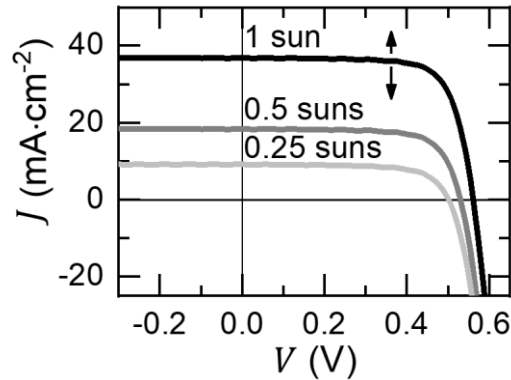


Figure 88. Measured J - V characteristics of the commercial alkaline-etched silicon solar cell obtained from an area of 5 cm^2 . The arrows indicate the shifting of the J - V curve for energy yield modeling. Reprinted with permission from [140], © 2019 Wiley.

In addition to the location of the solar module, its tilt is important for determining the irradiance. Different scenarios are possible. Typically a solar module is mounted on a roof top at a fixed angle, or it is used in solar field, sometimes tracking the sun. In building-integrated PV (BIPV), solar modules are not only mounted to roof tops, but have also been applied to building facades [180]. The EY was calculated for the three very difference scenarios of (A) perfect two-axis sun tracking, (B) stationary panel on a roof top facing south - mounted at the optimized angle of 25° , and (C) stationary panel on a building facade (90° tilt) facing south. **Figure 89** shows the calculated AR-dependent EY in the three cases. In the case of perfect sun tracking, with most light at normal incidence, the microcone textures with $AR > 0.31$ perform very similar. The AR 0.73 microcone texture shows the best performance. In the stationary case a large amount of light is incident from larger AOIs – favoring larger ARs. In the BIPV case light is only incident from large AOIs – the importance of higher ARs is even more pronounced. All three trends are indicated by the arrows in the graphs. In all three cases the microcone textures perform much better than the planar front surface layer (AR 0). The maximum calculated relative EY enhancements are 7%, 9%, and 12% for the three cases (A), (B), and (C), respectively. For comparison, in the case of a conventional thin-film ARC on glass a 4% increase in EY has been measured [181,182].

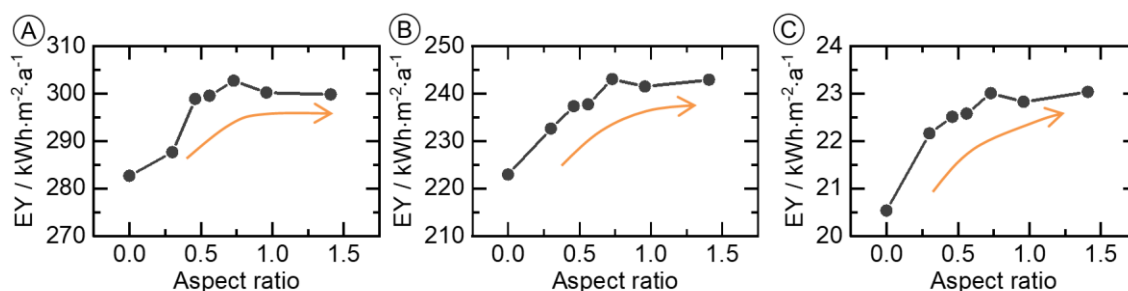


Figure 89. Energy yield (EY) modeling of the commercial alkaline-etched silicon solar cells with microcone front surface textures using irradiance data from Phoenix, AZ, US. **(A)** Perfect 2-axis sun tracking. **(B)** Facing south at an optimized tilt of 25° (roof top). **(C)** Facing south at 90° tilt (building facade). **(A)** and **(B)** were adapted with permission from [140], © 2019 Wiley.

5.6.3 Microcone textures on CIGS thin-film solar cells

The microcone textures were applied to state-of-the-art CIGS thin-film solar cells with a PCE > 20% to show the relevance of these textures on high performing solar cells. On the thin-film solar cells masking was not necessary for I - V measurements, as charge carriers do not travel far. The CIGS thin-film solar cells therefore enabled direct measurements of the PCE improvement introduced by the microcone textures. In contrast to the silicon solar cells above, where only the improvement in J_{SC} was studied in detail. Furthermore, available CIGS solar cells with and without a MgF_2 thin-film ARC enabled a more direct comparison of the microcone textures to a state-of-the-art thin-film ARC. The CIGS thin-film solar cells were provided by the Zentrum für Sonnenenergie- und Wasserstoff-Forschung Baden-Württemberg (ZSW). The thin-film solar cells were produced on soda-lime glass. First, a molybdenum layer (500 nm to 900 nm) was sputtered onto the solar-lime glass. On the molybdenum layer Cu, In, Ga and Se were co-evaporated to grow the CIGS layer (2.5 μm to 3.0 μm). After annealing, a CdS buffer layer (30 nm to 50 nm) was applied in a chemical bath. Finally, ZnO (50 nm to 100 nm) and AZO (150 nm to 200 nm) were sputtered as buffer layer and transparent front contact layer, respectively. As already mentioned, a MgF_2 thin-film ARC was deposited on some of the solar cells. Further details on the fabrication are available in the works of Jackson *et al.* [183,184].

I-*V* measurements. The best performing microcone texture of AR 0.73 were applied to CIGS thin-film solar cells without a MgF_2 thin-film ARC. **Table 7** summarizes the measured characteristic solar cell parameters before and after applying the microcone textures to five different CIGS thin-film solar cells (1) to (5). In the best case, for solar cell (2), the J_{SC} was increased by 2 mA/cm², while a 0.7% absolute increase in PCE was measured. In all five cases the V_{OC} and FF were slightly lower after applying the microcone texture. One possible reason is an increased contact resistance due to NOA88 spilling onto the contact pads in thin layers, although care was taken to avoid this. Another possible reason is the PDMS stamp lift-off causing micro-damage in the layer stack of the solar cell. If the V_{OC} and FF had stayed unaffected the 2 mA/cm² increase in J_{SC} would have led to an absolute increase in PCE of 1%. Similar values have been reported in the best case, when applying a conventional MgF_2 thin-film ARC [183].

	J_{SC} (mA/cm ²)	V_{OC} (mV)	FF (%)	PCE (%)
(1) Uncoated	43.2	655	74.7	21.1
(1) Textured	44.7	648	73.9	21.4
(2) Uncoated	39.2	660	78.0	20.2
(2) Textured	41.2	655	77.5	20.9
(3) Uncoated	39.4	665	77.8	20.4
(3) Textured	40.9	660	77.4	20.9
(4) Uncoated	39.3	666	77.8	20.4
(4) Textured	40.5	663	77.5	20.8
(5) Uncoated	39.3	668	77.8	20.4
(5) Textured	40.9	664	77.3	21.0

Table 7. Solar cell characteristics of five separate CIGS thin-film solar cells before and after applying a microcone texture of AR 0.73.

Comparison to MgF₂ coating. For a further analysis of the enhancement the EQE and reflectance of solar cell (2) are shown in **Figure 90**. For comparison the data from a CIGS solar cell with a MgF₂ ARC from a different batch is also shown. The J_{SC} of the bare, the microcone textured and the MgF₂ coated solar cells were calculated according to Equation (5.7) 37.1 mA/cm², 39.5 mA/cm², and 38.8 mA/cm², respectively. In terms of J_{SC} , it is therefore clearly possible for the microcone textures to outperform a conventional MgF₂ thin-film ARC. From **Figure 90** it is also clear that this is mostly due the microcone textures reducing reflection losses in the wavelength range 800 nm to 1050 nm. The CIGS thin-film solar cell with the microcone texture shows low reflectance of $\approx 1\%$ over almost the complete relevant spectral range. This shows the excellent capabilities of these textures to improve the performance of solar cells of high efficiency. It should be noted, that slight device variations occur in every batch. Therefore, this direct comparison of the microcone textured solar cell and the MgF₂ coated solar cell should be treated with caution. Nevertheless, these device variations mainly influence resistances in the solar cell and should have little influence on the reflectance. The confidence in the presented result is high.

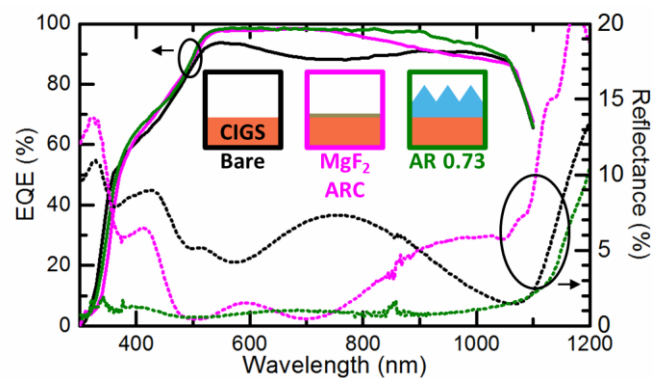


Figure 90. Wavelength-dependent external quantum efficiency (EQE) and reflectance of a bare CIGS thin-film solar cell, a CIGS thin-film solar cell with a MgF₂ ARC, and a CIGS solar cell with the microcone textures of AR 0.73. Adapted with permission from [140], © 2019 Wiley.

The microcone textures excel at larger AOIs. Angle-dependent EQE measurements were performed to directly compare the performance of the microcone texture to a conventional thin-film ARC. **Figure 91** shows the AOI-dependent J_{SC} calculated from these EQE measurements for solar cell (2), as well as the solar cell with a MgF_2 thin-film ARC. Both, the planar bare device and the planar ARC, show a strong decline in J_{SC} for AOIs $>60^\circ$, while the microcone texture maintained much higher values. On top of the excellent performance, the microcone texture already represents the encapsulation and cover glass in a solar module. While additional encapsulation layer on top of the MgF_2 layer are needed.

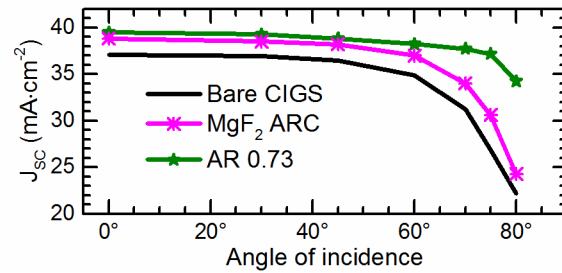


Figure 91. Angle on incidence dependent J_{SC} , calculated from EQE measurements, of a bare CIGS thin-film solar cell, a CIGS thin-film solar cell with a MgF_2 ARC, and a CIGS solar cell with the microcone textures of AR 0.73. Adapted with permission from [140], © 2019 Wiley.

6 Conclusion & Outlook

6.1 Nano-optics for ink infiltrated photonic crystal solar cells

In chapter 4, the use of DLW for fabricating nano-scale textures for increasing the absorptance in PV devices using PhCs was demonstrated. The study focused on the development of a process that enables the rapid prototyping of textures. The textures targeted a coupling of incident light to modes guided in a solar cell. Furthermore, an infiltration process based on a CIS nanocrystal ink was demonstrated, allowing the DLW pattern to be employed in a solar cell without causing additional electrical losses. Another vital part of the study was the measurement of the complex refractive indices of the used DLW polymer (IP-Dip) and of the CIS nanocrystal layer. The complex refractive indices were used in numerical simulations, enabling a detailed understanding of the observed mode coupling, as well as the optimization of design parameters.

The complex refractive index of the CIS nanocrystal layer was determined using spectroscopic ellipsometry, aided by TMM simulations. The best fit to experimental data was obtained for a refractive index on the order of 2.0. The penetration depth of light in the wavelength range 600 nm to 1300 nm was large compared to the targeted layer thicknesses, leaving a lot of room for light-trapping schemes. The refractive index of IP-Dip was determined using a prism coupling technique. A refractive index on the order of 1.53 was determined for DLW exposed IP-Dip. Additionally, it was found that the refractive index of IP-Dip exposed during DLW is genuinely lower than that of UV exposed IP-Dip. Furthermore, slight absorption of visible light was observed in exposed IP-Dip. The small refractive index step between the CIS nanocrystal layer and IP-Dip of $\Delta n \approx 0.47$ was identified as the limiting factor for light-trapping in the investigated material system.

The obtained complex refractive indices were employed in analytical calculations of the coupling condition, as well as FDTD simulations. It was possible to show in detail how to optimize the PhC geometrical parameters to the desired spectral region for light-trapping. For the investigated square lattice it was found that lattice constants around 650 nm and IP-Dip volumetric filling fractions around 20% are highly desirable for the investigated system.

Experimentally, a DLW process was developed for producing nanocone patterns on fused silica, ITO, and gold. Making use of the flexibility of DLW the lattice constant of the produced patterns was precisely adjusted to the numerically found optimum. The infiltration approach was tested and was found to form a layer neatly embedding the nanocone pattern. A close match was achieved between the positions of peaks in the absorptance spectrum found numerically and experimentally. Using the nanocrystal infiltration technique it was clearly possible to achieve mode coupling. Furthermore, using I - V measurements it was possible to show that the infiltration technique is non-disruptive to the device performance. PhC infiltrated devices performed just as well as their planar counterparts. It is to be noted that the layer thickness was slightly higher in the patterned area (due to an observed capillary effect) leading to an overall increase in absorptance. On the other hand, distinct peaks in the EQE, related to mode coupling, were not detected in the devices.

In future studies the flexibility of DLW allows an experimental pattern investigation, in contrast to the commonly employed solely numerical based studies. To make use of the full potential of the combination of DLW fabrication and the novel ink infiltration technique it is in the interest of such a study to obtain a stronger coupling between incident light and guided modes. To a large extent, the current study was limited by the small refractive index difference ($\Delta n \approx 0.47$) between the CIS nanocrystal layer ($n \approx 2.00$) and the IP-Dip PhC texture ($n \approx 1.53$).

Impact of increased refractive index difference. FDTD simulations, along the lines described in section 4.6.2, were performed to demonstrate the impact of an increased refractive index of the CIS nanocrystal layer. In these simulations only the real part of the refractive index of the semiconductor layer was increased. All structural parameters of the setup, as well as the extinction coefficient of the semiconductor layer, were kept constant. **Figure 92(A)** compares the absorptance in a planar 300 nm thick CIS nanocrystal layer on a fused silica substrate to the absorptance in a PhC patterned CIS nanocrystal layer of identical thickness using $a = 600$ nm and $F = 25\%$ (compare section 4.6.2). In this thin layer a single TE mode was present for longer wavelengths and the small peak in absorptance at 850 nm did not compensate the slightly lowered overall absorptance. This led to a reduced weighted average absorptance (Equation (4.17)) of 0.33 in the PhC patterned layer compared to 0.34 in the planar layer. In contrast, when performing the same simulation and increasing the refractive index of CIS nanocrystal by 0.6 (therefore: $\Delta n \approx 1$) the result completely changed (**Figure 92(B)**). More modes were present in the layer and the coupling was stronger. In the case of this increased refractive index difference, the weighted average absorptance of the planar layer was 0.33 and that of the PhC patterned layer was 0.47. A relative increase of more than 40%.

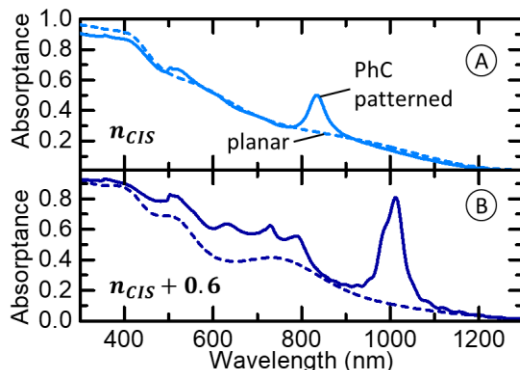


Figure 92. FDTD simulated absorptance in a 300 nm thick CIS nanocrystal layer textured into a PhC using IP-Dip with a volume fraction of 25% and a lattice constant 600 nm. In simulations first **(A)** the measured refractive index of the CIS nanocrystal layer was used and second **(B)** a constant of 0.6 was added to the measured refractive index of the CIS nanocrystal layer.

Routes to increasing the refractive index difference. Bulk CIS layers, produced using conventional thermal evaporation, have shown a refractive index on the order of 3.0 [185], while the here investigated CIS nanocrystal layers only showed a refractive index on the order of 2.0. The difference was most likely a result of the oleylamine ligands attached to the nanocrystals. Therefore, one possibility for increasing the refractive index is a ligand exchange [186], and replacing oleylamine with shorter ligands. Furthermore, the refractive index of the layers should increase when annealing the layers at high temperature. Preliminary tests have shown that the polymeric nanocone in the CIS layer withstand high temperatures of up to 300°C.

A further possibility to increase the refractive index difference, is the use of completely different materials in the described infiltration scheme. One possible material class to replace the CIS nanocrystals are the novel perovskite PV ink depositable materials. For example, ellipsometry measurements on $\text{CH}_3\text{NH}_3\text{PbI}_3$ layers have indicated a refractive index >2.5 [187]. Furthermore, with a value of 1.53 the refractive index of IP-Dip is comparably high for a polymeric material. IP-Dip was made use of in this study due to its availability and high compatibility with the DLW system. In general, while IP-Dip is an appropriate material for rapid prototyping of textures, the direct application of IP-Dip in PV devices should be seen critical due to the absorption of visible light (section 4.4.4). Employing a highly transparent polymeric material of lower refractive index is highly desirable. Especially, fluorinated polymers (with a low refractive index on the order of 1.3 to 1.4) are known to fulfill both properties [188]. While the DLW exposure of fluorinated polymers has been shown [189], the transfer of an IP-Dip pattern into a fluorinated polymer using imprinting, as described in section 5.4.2, is also possible.

Novel PhC patterns. For the process development targeted in this dissertation, a simple square lattice was chosen. Using the developed process, it will be possible to investigate complex 2D PhC patterns experimentally. A few interesting examples of possible patterns from literature are: Superlattices [99] with lattice elements of varying dimensions that add diffraction possibilities. Quasi-random patterns with a tailored disorder [190,191] that allow broadband coupling. And supercells [192] with multiple periods tailored to suppress specific diffraction orders. As a first demonstration, a lattice combining two periods was fabricated. An SEM image of the fabricated lattice combining two lattices of lattice constants 500 nm and 700 nm is shown in **Figure 93**.

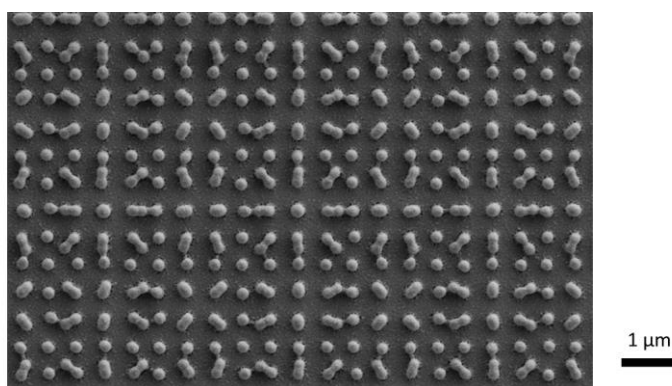


Figure 93. SEM image of IP-Dip nanocones on fused silica arranged in a combination of two lattices of periods 500 nm and 700 nm.

6.2 Micro-optics for the front surface of solar modules

In chapter 5, the use of DLW to prototype micro-textures for the front surface of solar modules was demonstrated. Microcone textures were programmed and fabricated (as designed) using DLW, and then transferred to solar cells using a PDMS based replication process. The microcone shape was chosen based on the textures found on many petals and leaves. The impact of the aspect ratio on enhancing the solar cell performance was investigated in detail numerically and experimentally. While their biomimetic counterparts fulfil a variety of optical purposes, such as the focusing of light, the here produced microcone textures were evaluated for their ability to reduce interface reflectivity and trap light in the PV device they were applied to. The fabricated textures were applied to state-of-the-art silicon based

solar cells, as well as CIGS based solar cells. The superiority of the microcone textures was shown in comparison to conventional planar thin-film ARCs, especially when illuminated from large incidence angles.

Geometrical optics based simulations were performed for a detailed understanding of the interaction of light with the microcone textures, and for comparing simulation to experimental results. Using these simulations, several conclusions about the aspect ratio could be drawn: Firstly, aspect ratios above 0.5 greatly reduced the interface reflectivity. Secondly, the larger the angle of incidence of light the higher the needed aspect ratios for achieving near zero reflectance. Thirdly, for a specular reflecting solar cell surface the best trapping of normal incidence light was achieved with an aspect ratio in the range 0.7 to 1.0, with an optimum around 0.85. Lastly, for a diffusely scattering solar cell surface the textures did not trap more light than a planar front surface.

Partially these conclusions have been drawn for other types of front surface textures found in literature. Just like in the case of the PhC patterns for PV applications discussed in chapter 4 various textures have been investigated numerically, while an experimental prove has not necessarily been possible. In an unprecedented study DLW was used to prepare the numerically investigated textures. A close match between numerical and experimental results was achieved in reflectance and transmittance measurements on various substrates. Furthermore, using silicon solar cell with a planar semiconductor layer, it was shown that the conclusions drawn in numerical studies were directly applicable to the EQE enhancement induced by the microcone textures. Of the fabricated microcone textures the one with an aspect ratio of 0.73 led to the largest improvement in EQE under normal incidence illumination. For incidence angles above 30° the microcone textures with larger aspect ratios led to larger improvements in EQE.

By nature, the light-trapping scheme is most vital when applying the microcone textures to solar cells showing significant reflection losses. Consequently, most front textures found in literature were demonstrated on thin-film solar cells, and especially on organic solar cells. Here, on the contrary, state-of-the-art solar cells showing very little reflectance losses were used to demonstrate the superiority of the microcone textures over conventional thin-film ARCs. Using commercial silicon solar cells, with a textured semiconductor layer, it was possible to show that the microcone texture of aspect ratio 0.73 regained almost all of the light, otherwise lost to reflection. Demonstrating that the front surface textures were a non-invasive complement to an already texture semiconductor layer. Furthermore, using angle-dependent EQE data, the increase in EY was calculated that the microcone textures would generate in an application. For a rooftop mounted solar module a relative increase in EY of up to 9% (compared to a front surface without an ARC) was calculated, while conventional thin-film ARCs are known to only achieve a 4% relative improvement in EY. Additionally, using the EY analysis, it was demonstrated that aspect ratios above one are of interest for BIPV.

A reduction of interface reflectance is of interest for almost any solar cell technology. Making use of high performing CIGS based thin-film solar cells the increase in PCE, provided by the microcone textures, was shown directly. Modern CIGS solar cells are devices of inherently low reflectance. Nevertheless, using the microcone textures of aspect ratio 0.73 a broadband reduction of the reflectance was achieved for the CIGS devices. In the best case leading to an absolute increase of 0.7% in PCE. The PCE increase was directly comparable to that achieved with a conventional thin-film MgF₂ coating. While the thin-film MgF₂ layer had the sole purpose of demonstrating a device with a world record in PCE, the microcone texture already presented the encapsulation needed in a real application and completely outperformed the thin-film ARC for large angles of incidence.

In future work the move from this highly promising proof-of-concept to an applicable product is of interest. Future investigations include: A large-area texturing process, as well as different materials, since the longevity of NOA88 in outdoor conditions is at best unclear. Furthermore, improvements of the texture design might be possible.

Optical design improvements. In numerical studies, the excellent anti-reflection and light-trapping capabilities of tetrahedral textures have been shown [171,193]. A direct comparison between the here produced conical textures and tetrahedral textures would be of high interest. The numerical studies indicated that ideal tetrahedral textures show the best performance of any texture for normal incidence illumination. A benefit of conical textures is their high rotational symmetry making their optical properties robust against perturbations in the design. Furthermore, tetrahedral textures such as the corner cube lead to perfect retroreflection. As a consequence, light reflected by the contacts of a solar cell is trapped in the coating layer by the texture, but does not impinge upon the semiconductor layer. Therefore, in addition to the reflectance of the solar cell and the illumination condition the design of the solar cell should be taken into account when comparing the performance of different texture geometries.

Multiple functionality. In the introduction to chapter 5 the bio-inspiration behind the conical texture design was presented. It was mentioned that natural occurring micron-scale textures show anti-soiling properties. Anti-soiling properties arise from superhydrophobicity. Water drops easily roll off from a textured surface - washing away dust particles. The anti-soiling properties of the microcone textures is affected by their periodicity and their aspect ratio. A detailed investigation of the anti-soiling properties of the microcone textures on different materials will give rise to further optimizations in the design.

Large-area replication. DLW is a rapid prototyping technique in terms of design to prototype. The fabrication of large-area textures using DLW is a time consuming process. Therefore, a process needs to be developed to scale small stamps produced from DLW prototypes to larger areas. The stamp needs to withstand multiple replication cycles. Soft imprinting using PDMS stamps does not fulfill this criteria. Texturing using nickel stamps and employing hot-embossing, on the other hand, might pave the way towards mass fabrication [194].

Materials for PV applications. In the here presented study the microcone textures were transferred to the photoresist NOA88 onto solar cells. For an outdoor PV application a material with a high tolerance against environmental conditions is needed at the front surface. A material to which textures are easily applicable and which shows a high durability is fluorinated ethylene propylene (FEP). FEP has successfully been applied to PV devices. An advantage of FEP is its naturally low surface energy, leading to a large contact angle and a small roll-off angle that are very beneficial for inducing anti-soiling properties [195].

A novel kind of material with a large potential for PV applications is liquid glass [196]. Liquid glass consists of a silica powder in a monomeric mixture. Before sintering it is possible to texture liquid glass like any optically curable resin. After a sintering process at 1300°C degrees the properties of the glass closely resemble those of conventional fused silica. In a first step the optical enhancement of PV devices using textures produced from liquid glass has been shown [197].

Appendix Refractive index data

Measured data

CIS nanocrystals
n, κ: ellipsometry (VASE)

Wavelength (nm)	<i>n</i>	<i>κ</i>
300	1.89757	0.33123
325	1.90685	0.30194
350	1.91599	0.28491
375	1.92614	0.27122
400	1.96932	0.25397
425	2.01137	0.22977
450	2.02148	0.20018
475	2.01209	0.16996
500	2.00094	0.14358
525	1.99193	0.12311
550	1.98555	0.10855
575	1.98146	0.09897
600	1.97916	0.09317
625	1.97816	0.09003
650	1.97806	0.08744
675	1.97853	0.08473
700	1.97935	0.0819
725	1.98038	0.07891
750	1.98148	0.07575
775	1.98261	0.07241
800	1.98373	0.06891
825	1.98481	0.06523
850	1.98587	0.06141
875	1.9869	0.05745
900	1.988	0.05339
925	1.98934	0.04924
950	1.99112	0.04505
975	1.99294	0.04083
1000	1.99311	0.03663
1025	1.99049	0.03247
1050	1.98583	0.0284
1075	1.98092	0.02445
1100	1.97691	0.02065
1125	1.97384	0.01704
1150	1.9714	0.01366
1175	1.96936	0.01055
1200	1.96759	0.00773
1225	1.96601	0.00524
1250	1.96457	0.00312

IP-Dip (UV exposed)
n: mode coupling (Model 2010/M)
κ: absorption measurement (Lambda 950)

Wavelength (nm)	<i>n</i>	<i>κ</i>
426	1.5740	51·10 ⁻⁶
532	1.5574	11·10 ⁻⁶
588	1.5524	4·10 ⁻⁶
637	1.5489	2·10 ⁻⁶
706	1.5450	>1·10 ⁻⁶
780	1.5425	>1·10 ⁻⁶
850	1.5406	>1·10 ⁻⁶
980	1.5380	>1·10 ⁻⁶
1550	1.5331	3·10 ⁻⁶

IP-Dip (DLW exposed)
n: mode coupling (Model 2010/M)

Wavelength (nm)	<i>n</i>	<i>κ</i>
426	1.5615	-
532	1.5480	-
588	1.5437	-
637	1.5410	-
706	1.5365	-
780	1.5343	-
850	1.5327	-
980	1.5301	-
1550	1.5260	-

NOA 88
n: mode coupling (Model 2010/M)

Wavelength (nm)	<i>n</i>	<i>κ</i>
637	1.5593	-
		-
		-
		-
		-
		-
		-
		-
		-
		-
		-
		-

Literature data

Gold (Au)

Source: P. Johnson and R. Christy [198]

Wavelength (nm)	n	κ
300	1.50736	1.81319
350	1.50544	1.8539
400	1.45651	1.95409
450	1.41142	1.95244
500	0.93786	1.87149
550	0.36417	2.41407
600	0.20959	3.04176
650	0.16419	3.57198
700	0.15169	4.04481
750	0.15289	4.48428
800	0.16162	4.90387
850	0.17471	5.31288
900	0.19119	5.71422
950	0.21227	6.10667
1000	0.23504	6.49657
1050	0.26146	6.88101
1100	0.28922	7.26400
1150	0.32108	7.64255
1200	0.35295	8.02110
1250	0.38925	8.39656
1300	0.42757	8.77061

Indium tin oxide (ITO)

Source: Z. Holman et al. [199]

Wavelength (nm)	n	κ
300	2.509	0.2778
350	2.418	0.1193
400	2.318	0.03268
450	2.229	0.00156
500	2.175	0.00126
550	2.140	0.00170
600	2.114	0.00224
650	2.094	0.00287
700	2.076	0.00361
750	2.061	0.00447
800	2.047	0.00545
850	2.034	0.00658
900	2.021	0.00785
950	2.008	0.00928
1000	1.996	0.01087
1050	1.984	0.01265
1100	1.971	0.01461
1150	1.959	0.01678
1200	1.946	0.01915
1250	1.933	0.02176
1300	1.919	0.02461

Zinc oxide (ZnO)

Source: H. ElAnzeery et al. [200]

Wavelength (nm)	n	κ
300	2.073	0.550300
350	2.291	0.242800
400	2.191	0.041570
450	2.060	0.000071
500	2.002	0.003979
550	1.978	0.015660
600	1.963	0.022190
650	1.951	0.025290
700	1.938	0.026510
750	1.923	0.026750
800	1.907	0.026490
850	1.888	0.025990
1300	1.7	0.025000
(extrapolated)		

Cadmium sulfate (CdS)

Source: H. ElAnzeery et al. [200]

Wavelength (nm)	n	κ
300	1.448	0.4334
350	1.454	0.3145
400	1.418	0.2044
450	1.398	0.1811
500	1.427	0.1481
550	1.411	0.1013
600	1.396	0.0818
650	1.387	0.0710
700	1.382	0.0636
750	1.379	0.0580
800	1.377	0.0536
850	1.376	0.0499
900	1.376	0.0500
1300	1.37	0.0500
(extrapolated)		

Fused silica

Source: I. Malitson [201]

Wavelength (nm)	n
300	1.4878
350	1.4769
400	1.4701
450	1.4656
500	1.4623
550	1.4599
600	1.4580
650	1.4565
700	1.4553
750	1.4542
800	1.4533
850	1.4525
900	1.4518
950	1.4511
1000	1.4504
1050	1.4498
1100	1.4492
1150	1.4486
1200	1.4481
1250	1.4475
1300	1.4469

References

- [1] L. M. Fraas. *Low-Cost Solar Electric Power*, Springer, Cham, Switzerland (2014).
- [2] D. M. Chapin, C. S. Fuller, and G. L. Pearson. "A New Silicon p-n Junction Photocell for Converting Solar Radiation into Electrical Power," *J. Appl. Phys.* **25**(5), 676-677 (1954).
- [3] S. Europe. *Global Market Outlook for Solar Power 2018-2022*; (2018).
- [4] M. A. Green, Y. Hishikawa, E. D. Dunlop, D. H. Levi, J. Hohl-Ebinger, M. Yoshita, and A. W. Y. Ho-Baillie. "Solar cell efficiency tables (Version 53)," *Prog. Photovolt.: Res. Appl.* **27**(1), 3-12 (2019).
- [5] L. C. Andreani, A. Bozzola, P. Kowalczewski, M. Liscidini, and L. Redorici. "Silicon solar cells: toward the efficiency limits," *Adv. Phys. X* **4**(1), 1548305 (2019).
- [6] M. J. Kerr, P. Campbell, and A. Cuevas. Lifetime and efficiency limits of crystalline silicon solar cells. *Conference Record of the Twenty-Ninth IEEE Photovoltaic Specialists Conference*, New Orleans, LA, USA (2002).
- [7] M. A. Green. "Thin-film solar cells: review of materials, technologies and commercial status," *J. Mater. Sci.: Mater. Electron. Suppl* **1**(18), S15-S19 (2007).
- [8] National Renewable Energy Laboratory (NREL). *Research Cell Record Efficiency Chart*. <https://www.nrel.gov/pv/assets/pdfs/pv-efficiencies-07-17-2018.pdf>. Accessed Okt 18, 2018.
- [9] J. Peng, L. Lu, and H. Yang. "Review on life cycle assessment of energy payback and greenhouse gas emission of solar photovoltaic systems," *Renew. Sustain. Energy Rev.* **19**, 255-274 (2013).
- [10] J. D. Servaites, M. A. Ratner, and T. J. Marks. "Organic solar cells: A new look at traditional models," *Energy Environ. Sci.* **4**(11), 4410-4422 (2011).
- [11] N. Yeh and P. Yeh. "Organic solar cells: Their developments and potentials," *Renew. Sustain. Energy Rev.* **21**, 421-431 (2013).
- [12] M. A. Green, Y. Hishikawa, E. D. Dunlop, D. H. Levi, J. Hohl-Ebinger, and A. W. Y. Ho-Baillie. "Solar cell efficiency tables (version 52)," *Prog. Photovolt.: Res. Appl.* **26**(7), 427-436 (2018).
- [13] A. Kojima, K. Teshima, Y. Shirai, and T. Miyasaka. "Organometal Halide Perovskites as Visible-Light Sensitizers for Photovoltaic Cells," *J. Am. Chem. Soc.* **131**(17), 6050-6051 (2009).
- [14] S. Yang, W. Fu, Z. Zhang, H. Chen, and C.-Z. Li. "Recent advances in perovskite solar cells: efficiency, stability and lead-free perovskite," *J. Mater. Chem. A* **5**(23), 11462-11482 (2017).
- [15] G. H. Carey, A. L. Abdelhady, Z. Ning, S. M. Thon, O. M. Bakr, and E. H. Sargent. "Colloidal Quantum Dot Solar Cells," *Chem. Rev.* **115**(23), 12732-12763 (2015).
- [16] W. Yoon, E. E. Foos, M. P. Lumb, and J. G. Tischler. Solution processing of CdTe nanocrystals for thin-film solar cells. *38th IEEE Photovoltaic Specialists Conference*, Austin, TX, USA (2012).

References

- [17] H. Azimi, Y. Hou, and C. J. Brabec. "Towards low-cost, environmentally friendly printed chalcopyrite and kesterite solar cells," *Energy Environ. Sci.* **7**(6), 1829-1849 (2014).
- [18] M. Bernechea, N. C. Miller, G. Xercavins, D. So, A. Stavrinadis, and G. Konstantatos. "Solution-processed solar cells based on environmentally friendly AgBiS₂ nanocrystals," *Nat. Photonics* **10**, 521 (2016).
- [19] S. Chattopadhyay, Y. F. Huang, Y. J. Jen, A. Ganguly, K. H. Chen, and L. C. Chen. "Anti-reflecting and photonic nanostructures," *Mater. Sci. Eng. R Rep.* **69**(1), 1-35 (2010).
- [20] W. H. Lowdermilk and D. Milam. "Graded-index surface to limit reflection," *Laser Focus* **12**, 64-70 (1980).
- [21] S. A. Boden and D. M. Bagnall. "Tunable reflection minima of nanostructured antireflective surfaces," *Appl. Phys. Lett.* **93**(13), 133108 (2008).
- [22] S. J. Wilson and M. C. Hutley. "The Optical Properties of 'Moth Eye' Antireflection Surfaces," *Opt. Acta: Inter. J. Opt.* **29**(7), 993-1009 (1982).
- [23] C.-H. Hsu, J.-R. Wu, Y.-T. Lu, D. J. Flood, A. R. Barron, and L.-C. Chen. "Fabrication and characteristics of black silicon for solar cell applications: An overview," *Mater. Sci. Semicond. Process.* **25**, 2-17 (2014).
- [24] X. Liu, P. R. Coxon, M. Peters, B. Hoex, J. M. Cole, and D. J. Fray. "Black silicon: fabrication methods, properties and solar energy applications," *Energy Environ. Sci.* **7**(10), 3223-3263 (2014).
- [25] I. M. Thomas. "Method for the preparation of porous silica antireflection coatings varying in refractive index from 1.22 to 1.44," *Appl. Opt.* **31**(28), 6145-6149 (1992).
- [26] S. Walheim, E. Schäffer, J. Mlynek, and U. Steiner. "Nanophase-Separated Polymer Films as High-Performance Antireflection Coatings," *Science* **283**(5401), 520-522 (1999).
- [27] H. W. Deckman, C. B. Roxlo, and E. Yablonovitch. "Maximum statistical increase of optical absorption in textured semiconductor films," *Opt. Lett.* **8**(9), 491-493 (1983).
- [28] D. Dominé, F.-J. Haug, C. Battaglia, and C. Ballif. "Modeling of light scattering from micro- and nanotextured surfaces," *J. Appl. Phys.* **107**(4), 044504 (2010).
- [29] S. Mokkaḡpati and K. R. Catchpole. "Nanophotonic light trapping in solar cells," *J. Appl. Phys.* **112**(10), 101101 (2012).
- [30] R. B. Wehrspohn and J. Üpping. "3D photonic crystals for photon management in solar cells," *J. Opt.* **14**(2), 024003 (2012).
- [31] H. A. Atwater and A. Polman. "Plasmonics for improved photovoltaic devices," *Nat. Mater.* **9**, 205 (2010).
- [32] S. Mokkaḡpati, F. J. Beck, A. Polman, and K. R. Catchpole. "Designing periodic arrays of metal nanoparticles for light-trapping applications in solar cells," *Appl. Phys. Lett.* **95**(5), 053115 (2009).
- [33] C. Heine and R. H. Morf. "Submicrometer gratings for solar energy applications," *Appl. Opt.* **34**(14), 2476-2482 (1995).

- [34] G. Demésy and S. John. "Solar energy trapping with modulated silicon nanowire photonic crystals," *J. Appl. Phys.* **112**(7), 074326 (2012).
- [35] M. D. Kelzenberg, S. W. Boettcher, J. A. Petykiewicz, D. B. Turner-Evans, M. C. Putnam, E. L. Warren, J. M. Spurgeon, R. M. Briggs, N. S. Lewis, and H. A. Atwater. "Enhanced absorption and carrier collection in Si wire arrays for photovoltaic applications," *Nat. Mater.* **9**, 239 (2010).
- [36] E. Yablonovitch and G. D. Cody. "Intensity enhancement in textured optical sheets for solar cells," *IEEE Trans. Electron Devices* **29**(2), 300-305 (1982).
- [37] W. L. Bailey, M. G. Coleman, C. B. Harris, and I. A. Lesk, inventors. Motorola Solutions Inc, assignee. Texture etching of silicon: method. US patent 4 137 123, January 30 (1979).
- [38] H. Angermann. "Passivation of structured p-type silicon interfaces: Effect of surface morphology and wet-chemical pre-treatment," *Appl. Surf. Sci.* **254**(24), 8067-8074 (2008).
- [39] *Handbook of Nanotechnology*, B. Bhushan (Ed.), Springer, Berlin, Germany (2007).
- [40] M. Madou. *Fundamentals of Microfabrication*, CRC Press LLC, New York, US (1997).
- [41] C. Zechner, G. Hahn, W. Jooss, M. Wibrál, B. Bitnar, S. Keller, M. Spiegel, P. Fath, G. Willeke, and E. Bucher. Systematic study towards high efficiency multicrystalline silicon solar cells with mechanical surface texturization. *Twenty Sixth IEEE Photovoltaic Specialists Conference*, Anaheim, CA, USA (1997).
- [42] H. Taniguchi, H. Sannomiya, K. Kajiwara, K. Nomoto, Y. Yamamoto, K. Hiyoshi, H. Kumada, M. Murakami, and T. Tomita. "Amorphous silicon solar cell on textured tempered glass substrate prepared by sandblast process," *Sol. Energy Mater. Sol. Cells* **49**(1), 101-106 (1997).
- [43] Y.-T. Cheng, J.-J. Ho, S.-Y. Tsai, Z.-Z. Ye, W. Lee, D.-S. Hwang, S.-H. Chang, C.-C. Chang, and K. L. Wang. "Efficiency improved by acid texturization for multi-crystalline silicon solar cells," *Sol. Energy* **85**(1), 87-94 (2011).
- [44] H. Han, Z. Huang, and W. Lee. "Metal-assisted chemical etching of silicon and nanotechnology applications," *Nano Today* **9**(3), 271-304 (2014).
- [45] C. Cardinaud, M.-C. Peignon, and P.-Y. Tessier. "Plasma etching: principles, mechanisms, application to micro- and nano-technologies," *Appl. Surf. Sci.* **164**(1), 72-83 (2000).
- [46] F. L. Gonzalez, L. Chan, A. Berry, D. E. Morse, and M. J. Gordon. "Simple colloidal lithography method to fabricate large-area moth-eye antireflective structures on Si, Ge, and GaAs for IR applications," *J. Vac. Sci. Technol. B* **32**(5), 051213 (2014).
- [47] J. Yoo. "Reactive ion etching (RIE) technique for application in crystalline silicon solar cells," *Sol. Energy* **84**(4), 730-734 (2010).
- [48] W. Lee and S.-J. Park. "Porous Anodic Aluminum Oxide: Anodization and Templated Synthesis of Functional Nanostructures," *Chem. Rev.* **114**(15), 7487-7556 (2014).
- [49] X. Sheng, J. Liu, I. Kozinsky, A. M. Agarwal, J. Michel, and L. C. Kimerling. "Design and Non-Lithographic Fabrication of Light Trapping Structures for Thin Film Silicon Solar Cells," *Adv. Mater.* **23**(7), 843-847 (2011).

References

- [50] M. D. Kelzenberg, D. B. Turner-Evans, M. C. Putnam, S. W. Boettcher, R. M. Briggs, J. Y. Baek, N. S. Lewis, and H. A. Atwater. "High-performance Si microwire photovoltaics," *Energy Environ. Sci.* **4**(3), 866-871 (2011).
- [51] S. Sumaiya, K. Kardel, and A. El-Shahat. "Organic Solar Cell by Inkjet Printing—An Overview," *Technol.* **5**(3), 53 (2017).
- [52] M. Zohar, Z. Fradkin, E. Rimon, H. Efraim, M. Auslender, and M. Roitman. "Solar cell efficiency improvement using dip-pen nanolithography," *J. Photonics Energy* **8**(2), 022503 (2017).
- [53] L. T. Varghese, Y. Xuan, B. Niu, L. Fan, P. Bermel, and M. Qi. "Enhanced Photon Management of Thin-Film Silicon Solar Cells Using Inverse Opal Photonic Crystals with 3D Photonic Bandgaps," *Adv. Opt. Mater.* **1**(10), 692-698 (2013).
- [54] G. Köppel, B. Rech, and C. Becker. "Sinusoidal nanotextures for light management in silicon thin-film solar cells," *Nanoscale* **8**(16), 8722-8728 (2016).
- [55] Y. Yang, K. Mielczarek, A. Zakhidov, and W. Hu. "Efficient Low Bandgap Polymer Solar Cell with Ordered Heterojunction Defined by Nanoimprint Lithography," *ACS Appl. Mater. Interfaces* **6**(21), 19282-19287 (2014).
- [56] R. Hünig, A. Mertens, M. Stephan, A. Schulz, B. Richter, M. Hetterich, M. Powalla, U. Lemmer, A. Colmann, and G. Gomard. "Flower Power: Exploiting Plants' Epidermal Structures for Enhanced Light Harvesting in Thin-Film Solar Cells," *Adv. Opt. Mater.* **4**(10), 1487-1493 (2016).
- [57] M. A. González Lazo, R. Teuscher, Y. Letierrier, J.-A. E. Månson, C. Calderone, A. Hessler-Wyser, P. Couty, Y. Ziegler, and D. Fischer. "UV-nanoimprint lithography and large area roll-to-roll texturization with hyperbranched polymer nanocomposites for light-trapping applications," *Sol. Energy Mater. Sol. Cells* **103**, 147-156 (2012).
- [58] O. Schultz, G. Emanuel, W. Glunz, and G. P. Willeke. Texturing of multicrystalline silicon with acidic wet chemical etching and plasma etching. *3rd World Conference on Photovoltaic Energy Conversion*, Osaka, Japan (2003).
- [59] X. Meng, G. Gomard, O. El Daif, E. Drouard, R. Orobitchouk, A. Kaminski, A. Fave, M. Lemiti, A. Abramov, P. Roca i Cabarrocas, and C. Seassal. "Absorbing photonic crystals for silicon thin-film solar cells: Design, fabrication and experimental investigation," *Sol. Energy Mater. Sol. Cells* **95**, S32-S38 (2011).
- [60] J. C. Ruiz-Morales, A. Tarancón, J. Canales-Vázquez, J. Méndez-Ramos, L. Hernández-Afonso, P. Acosta-Mora, J. R. Marín Rueda, and R. Fernández-González. "Three dimensional printing of components and functional devices for energy and environmental applications," *Energy Environ. Sci.* **10**(4), 846-859 (2017).
- [61] M. F. Schumann, S. Wiesendanger, J. C. Goldschmidt, B. Bläsi, K. Bittkau, U. W. Paetzold, A. Sprafke, R. B. Wehrspohn, C. Rockstuhl, and M. Wegener. "Cloaked contact grids on solar cells by coordinate transformations: designs and prototypes," *Optica* **2**(10), 850-853 (2015).
- [62] A. Goetzberger and V. Hoffmann. *Photovoltaic solar energy generation*, Springer, Berlin, Germany (2005).
- [63] K. Mertens. *Photovoltaik: Lehrbuch zu Grundlagen, Technologie und Praxis*, Carl Hanser Verlag GmbH & Co. KG, Leipzig, Germany (2018).

- [64] T. Fliessbach. *Elektrodynamik*, Spektrum Akademischer Verlag, Heidelberg (2012).
- [65] C. Klingshirn. *Semiconductor optics*, Springer, Heidelberg, Germany (2005).
- [66] B. E. A. Saleh and M. C. Teich. *Fundamentals of Photonics*, Wiley-Interscience, a John Wiley & Sons, Inc., Hoboken, US (2007).
- [67] M. J. Adams. *An Introduction to Optical Waveguides*, John Wiley and Sons Ltd., New York (1981).
- [68] D. Marcuse. *Theory of dielectric optical waveguides*, Academic Press Inc, Boston, US (1991).
- [69] A. McGurn. *Nanophotonics*, Springer, Cham, Switzerland (2018).
- [70] J. D. Joannopoulos, S. G. Johnson, J. N. Winn, and R. D. Meade. *Photonic crystals*, Princeton University Press, Princeton, US (2008).
- [71] A. Angelini. *Photon Management Assisted by Surface Waves on Photonic Crystals*, Springer, Cham, Switzerland (2017).
- [72] O. Stenzel. *The Physics of Thin Film Optical Spectra : An Introduction*, Springer, Cham, Switzerland (2016).
- [73] U. Würfel, A. Cuevas, and P. Würfel. "Charge Carrier Separation in Solar Cells," *EEE J. Photovolt.* **5**(1), 461-469 (2015).
- [74] National Renewable Energy Laboratory (NREL). *ASTM G173-03 Reference Spectra*. <http://rredc.nrel.gov/solar/spectra/am1.5/ASTMG173/ASTMG173.html>. Accessed Okt 2016.
- [75] W. Shockley and H. J. Queisser. "Detailed Balance Limit of Efficiency of p-n Junction Solar Cells," *J. Appl. Phys.* **32**(3), 510-519 (1961).
- [76] C. J. Maxwell. "VIII. A dynamical theory of the electromagnetic field," *Philos. Trans. R. Soc. London* **155**, 459-512 (1865).
- [77] A. Chutinan and S. John. "Light trapping and absorption optimization in certain thin-film photonic crystal architectures," *Phys. Rev. A* **78**(2), 023825 (2008).
- [78] G. de Miguel, G. Vicidomini, B. Harke, and A. Diaspro. Linewidth and Writing Resolution, in: *Three-Dimensional Microfabrication Using Two-Photon Polymerization*, William Andrew Publishing, Oxford (2016).
- [79] Q. Zhan. Focusing Through High-Numerical Aperture Objectives, in: *Three-Dimensional Microfabrication Using Two-Photon Polymerization*, T. Baldacchini (Ed.), Elsevier Inc., (2016).
- [80] S. Maruo, O. Nakamura, and S. Kawata. "Three-dimensional microfabrication with two-photon-absorbed photopolymerization," *Opt. Lett.* **22**(2), 132-134 (1997).
- [81] K.-S. Lee, D.-Y. Yang, S. H. Park, and R. H. Kim. "Recent developments in the use of two-photon polymerization in precise 2D and 3D microfabrications," *Polym. Adv. Technol.* **17**(2), 72-82 (2006).
- [82] Nanoscribe GmbH. *Nanoscribes's IP photoresins*. <https://www.nanoscribe.de/en/products/ip-photoresins/>. Accessed Nov 2017.

References

- [83] S. H. Park, T. W. Lim, D.-Y. Yang, N. C. Cho, and K.-S. Lee. "Fabrication of a bunch of sub-30-nm nanofibers inside microchannels using photopolymerization via a long exposure technique," *Appl. Phys. Lett.* **89**(17), 173133 (2006).
- [84] J. B. Preinfalk, T. Eiselt, T. Wehler, V. Rohnacher, T. Hanemann, G. Gomard, and U. Lemmer. "Large-Area Screen-Printed Internal Extraction Layers for Organic Light-Emitting Diodes," *ACS Photonics* **4**(4), 928-933 (2017).
- [85] H. Fujiwara and R. W. Collins. *Spectroscopic Ellipsometry for Photovoltaics Volume 1: Fundamental Principles and Solar Cell Characterization*, Springer, Cham, Switzerland (2018).
- [86] A. Taflove and S. C. Hagness. *Computational Electrodynamics: The Finite-difference Time-domain Method*, Artech House, (2005).
- [87] K. Ohta and H. Ishida. "Matrix formalism for calculation of electric field intensity of light in stratified multilayered films," *Appl. Opt.* **29**(13), 1952-1959 (1990).
- [88] M. C. Tropicovsky, A. S. Sabau, A. R. Lupini, and Z. Zhang. "Transfer-matrix formalism for the calculation of optical response in multilayer systems: from coherent to incoherent interference," *Opt. Express* **18**(24), 24715-24721 (2010).
- [89] C. C. Katsidis and D. I. Siapkas. "General transfer-matrix method for optical multilayer systems with coherent, partially coherent, and incoherent interference," *Appl. Opt.* **41**(19), 3978-3987 (2002).
- [90] S. Dottermusch, D. Busko, M. Langenhorst, U. W. Paetzold, and B. S. Richards. "Exposure-dependent refractive index of Nanoscribe IP-Dip photoresist layers," *Opt. Lett.* **44**(1), 29-32 (2019).
- [91] S. Dottermusch, A. Quintilla, G. Gomard, A. Roslizar, V. R. Voggu, B. A. Simonsen, J. S. Park, D. R. Pernik, B. A. Korgel, U. W. Paetzold, and B. S. Richards. "Infiltrated photonic crystals for light-trapping in CuInSe₂ nanocrystal-based solar cells," *Opt. Express* **25**(12), A502-A514 (2017).
- [92] M. G. Nature Communications Panthani, V. Akhavan, B. Goodfellow, J. P. Schmidtke, L. Dunn, A. Dodabalapur, P. F. Barbara, and B. A. Korgel. "Synthesis of CuInS₂, CuInSe₂, and Cu(In_xGa_{1-x})Se₂ (CIGS) Nanocrystal "Inks" for Printable Photovoltaics," *J. Am. Chem. Soc.* **130**(49), 16770-16777 (2008).
- [93] V. R. Voggu, J. Sham, S. Pfeffer, J. Pate, L. Phillip, T. B. Harvey, R. M. Brown, and B. A. Korgel. "Flexible CuInSe₂ Nanocrystal Solar Cells on Paper," *ACS Energ. Lett.* **2**(3), 574-581 (2017).
- [94] V. A. Akhavan, M. G. Panthani, B. W. Goodfellow, D. K. Reid, and B. A. Korgel. "Thickness-limited performance of CuInSe₂ nanocrystal photovoltaic devices," *Opt. Express* **18**(19), A411-A420 (2010).
- [95] S. M. McLeod, C. J. Hages, N. J. Carter, and R. Agrawal. "Synthesis and characterization of 15% efficient CIGS solar cells from nanoparticle inks," *Prog. Photovolt.: Res. Appl.* **23**(11), 1550-1556 (2015).
- [96] K. R. Catchpole and M. A. Green. "A conceptual model of light coupling by pillar diffraction gratings," *J. Appl. Phys.* **101**(6), 063105 (2007).
- [97] E. Yablonovitch. "Statistical ray optics," *J. Opt. Soc. Am.* **72**(7), 899-907 (1982).

- [98] P. Sheng, A. N. Bloch, and R. S. Stepleman. "Wavelength-selective absorption enhancement in thin-film solar cells," *Appl. Phys. Lett.* **43**(6), 579-581 (1983).
- [99] Y. Tanaka, Y. Kawamoto, M. Fujita, and S. Noda. "Enhancement of broadband optical absorption in photovoltaic devices by band-edge effect of photonic crystals," *Opt. Express* **21**(17), 20111-20118 (2013).
- [100] K. X. Wang, Z. Yu, V. Liu, A. Raman, Y. Cui, and S. Fan. "Light trapping in photonic crystals," *Energy Environ. Sci.* **7**(8), 2725-2738 (2014).
- [101] Z. Yu, A. Raman, and S. Fan. "Nanophotonic light-trapping theory for solar cells," *Appl. Phys. A* **105**(2), 329-339 (2011).
- [102] A. Bozzola, M. Liscidini, and L. C. Andreani. "Photonic light-trapping versus Lambertian limits in thin film silicon solar cells with 1D and 2D periodic patterns," *Opt. Express* **20**(S2), A224-A244 (2012).
- [103] T. K. Chong, J. Wilson, S. Mokkaapati, and K. R. Catchpole. "Optimal wavelength scale diffraction gratings for light trapping in solar cells," *J. Opt.* **14**(2), 024012 (2012).
- [104] S. Domínguez, I. Cornago, O. García, M. Ezquer, M. J. Rodríguez, A. R. Lagunas, J. Pérez-Conde, and J. Bravo. "Design, optimization and fabrication of 2D photonic crystals for solar cells," *Photonic Nanostruct.* **11**(1), 29-36 (2013).
- [105] S. Eyderman, A. Deinega, and S. John. "Near perfect solar absorption in ultra-thin-film GaAs photonic crystals," *J. Mater. Chem. A* **2**(3), 761-769 (2014).
- [106] K. Ishizaki, M. De Zoysa, Y. Tanaka, S.-W. Jeon, and S. Noda. "Progress in thin-film silicon solar cells based on photonic-crystal structures," *Jpn. J. Appl. Phys.* **57**(6), 060101 (2018).
- [107] W. P. R. Liyanage, J. S. Wilson, E. C. Kinzel, B. K. Durant, and M. Nath. "Fabrication of CdTe nanorod arrays over large area through patterned electrodeposition for efficient solar energy conversion," *Sol. Energy Mater. Sol. Cells* **133**, 260-267 (2015).
- [108] J. Wallentin, N. Anttu, D. Asoli, M. Huffman, I. Åberg, M. H. Magnusson, G. Siefert, P. Fuss-Kailuweit, F. Dimroth, B. Witzigmann, H. Q. Xu, L. Samuelson, K. Deppert, and M. T. Borgström. "InP Nanowire Array Solar Cells Achieving 13.8% Efficiency by Exceeding the Ray Optics Limit," *Science* **339**(6123), 1057-1060 (2013).
- [109] S. Jeong, L. Hu, H. R. Lee, E. Garnett, J. W. Choi, and Y. Cui. "Fast and Scalable Printing of Large Area Monolayer Nanoparticles for Nanotexturing Applications," *Nano Lett.* **10**(8), 2989-2994 (2010).
- [110] J. Escarré, C. Battaglia, K. Söderström, C. Pahud, R. Biron, O. Cubero, F. J. Haug, and C. Ballif. "UV imprinting for thin film solar cell application," *J. Opt.* **14**(2), 024009 (2012).
- [111] K. Wilken, U. W. Paetzold, M. Meier, M. Smeets, N. Prager, M. Fahland, F. Finger, and V. Smirnov. "Light Management in Flexible Thin-Film Solar Cells—The Role of Nanoimprinted Textures and Tilted Surfaces," *EEE J. Photovolt.* **5**(6), 1646-1653 (2015).
- [112] D.-H. Ko, J. R. Tumbleston, A. Gadisa, M. Aryal, Y. Liu, R. Lopez, and E. T. Samulski. "Light-trapping nano-structures in organic photovoltaic cells," *J. Mater. Chem.* **21**(41), 16293-16303 (2011).

References

- [113] A. Mellor, H. Hauser, C. Wellens, J. Benick, J. Eisenlohr, M. Peters, A. Guttowski, I. Tobías, A. Martí, A. Luque, and B. Bläsi. "Nanoimprinted diffraction gratings for crystalline silicon solar cells: implementation, characterization and simulation," *Opt. Express* **21**(S2), A295-A304 (2013).
- [114] M. Niggemann, M. Glatthaar, A. Gombert, A. Hinsch, and V. Wittwer. "Diffraction gratings and buried nano-electrodes—architectures for organic solar cells," *Thin Solid Films* **451-452**, 619-623 (2004).
- [115] V. Depauw, X. Meng, O. E. Daif, G. Gomard, L. Lalouat, E. Drouard, C. Trompoukis, A. Fave, C. Seassal, and I. Gordon. "Micrometer-Thin Crystalline-Silicon Solar Cells Integrating Numerically Optimized 2-D Photonic Crystals," *EEE J. Photovolt.* **4**(1), 215-223 (2014).
- [116] D. Duché, E. Drouard, J. J. Simon, L. Escoubas, P. Torchio, J. Le Rouzo, and S. Vedraïne. "Light harvesting in organic solar cells," *Sol. Energy Mater. Sol. Cells* **95**, S18-S25 (2011).
- [117] D.-H. Ko, J. R. Tumbleston, L. Zhang, S. Williams, J. M. DeSimone, R. Lopez, and E. T. Samulski. "Photonic Crystal Geometry for Organic Solar Cells," *Nano Lett.* **9**(7), 2742-2746 (2009).
- [118] G. Gomard, X. Meng, E. Drouard, K. E. Hajjam, E. Gerelli, R. Peretti, A. Fave, R. Orobtcchouk, M. Lemiti, and C. Seassal. "Light harvesting by planar photonic crystals in solar cells: the case of amorphous silicon," *J. Opt.* **14**(2), 024011 (2012).
- [119] Y. Tanaka, K. Ishizaki, M. De Zoysa, T. Umeda, Y. Kawamoto, S. Fujita, and S. Noda. "Photonic crystal microcrystalline silicon solar cells," *Prog. Photovolt.: Res. Appl.* **23**(11), 1475-1483 (2015).
- [120] E. Garnett and P. Yang. "Light Trapping in Silicon Nanowire Solar Cells," *Nano Lett.* **10**(3), 1082-1087 (2010).
- [121] G. Köppel, D. Amkreutz, P. Sonntag, G. Yang, R. V. Swaaij, O. Isabella, M. Zeman, B. Rech, and C. Becker. "Periodic and Random Substrate Textures for Liquid-Phase Crystallized Silicon Thin-Film Solar Cells," *EEE J. Photovolt.* **7**(1), 85-90 (2017).
- [122] N. D. Gupta, V. Janyani, M. Mathew, M. Kumari, and R. Singh. "Design and fabrication of InGaN/GaN superlattice-based solar cell using photonic crystal structure," *J. Nanophotonics* **12**(4), 043505 (2018).
- [123] Y. Wang, P. Wang, X. Zhou, C. Li, H. Li, X. Hu, F. Li, X. Liu, M. Li, and Y. Song. "Diffraction-Grated Perovskite Induced Highly Efficient Solar Cells through Nanophotonic Light Trapping," *Adv. Energy Mater.* **8**(12), 1702960 (2018).
- [124] C. A. Overvig, S. Shrestha, and N. Yu. "Dimerized high contrast gratings," *Nanophotonics* **7**(6), 1157 (2018).
- [125] H.-B. Sun, T. Tanaka, and S. Kawata. "Three-dimensional focal spots related to two-photon excitation," *Appl. Phys. Lett.* **80**(20), 3673-3675 (2002).
- [126] T. Gissibl, S. Wagner, J. Sykora, M. Schmid, and H. Giessen. "Refractive index measurements of photo-resists for three-dimensional direct laser writing," *Opt. Mater. Express* **7**(7), 2293-2298 (2017).
- [127] A. Erdmann, C. L. Henderson, and C. G. Willson. "Impact of exposure induced refractive index changes of photoresists on the photolithographic process," *J. Appl. Phys.* **89**(12), 8163-8168 (2001).

- [128] A. Žukauskas, I. Matulaitienė, D. Paipulas, G. Niaura, M. Malinauskas, and R. Gadonas. "Tuning the refractive index in 3D direct laser writing lithography: towards GRIN microoptics," *Laser Photonics Rev.* **9**(6), 706-712 (2015).
- [129] J. S. Oakdale, J. Ye, W. L. Smith, and J. Biener. "Post-print UV curing method for improving the mechanical properties of prototypes derived from two-photon lithography," *Opt. Express* **24**(24), 27077-27086 (2016).
- [130] D. B. Fullager, G. D. Boreman, and T. Hofmann. "Infrared dielectric response of nanoscribe IP-dip and IP-L monomers after polymerization from 250 cm⁻¹ to 6000 cm⁻¹," *Opt. Mater. Express* **7**(3), 888-894 (2017).
- [131] M. Mangirdas, Ž. Albertas, P. Vytautas, B. Kastytis, M. Andrej, P. Domas, G. Roaldas, P. Algis, G. Holger, G. Arunė, S. Ioanna, F. Maria, and J. Saulius. "Femtosecond laser polymerization of hybrid/integrated micro-optical elements and their characterization," *J. Opt.* **12**(12), 124010 (2010).
- [132] M. I. Alonso, K. Wakita, J. Pascual, M. Garriga, and N. Yamamoto. "Optical functions and electronic structure of CuInSe₂, CuGaSe₂, CuInS₂, and CuGaS₂," *Phys. Rev. B* **63**(7), 075203 (2001).
- [133] G. E. Jellison(Jr.) and F. A. Modine. "Parameterization of the optical functions of amorphous materials in the interband region," *Appl. Phys. Lett.* **69**(3), 371-373 (1996).
- [134] S. M. Rytov. "Electromagnetic Properties of a Finely Stratified Medium," *Sov. Phys. J. Exp. Theor. Phys.* **2**(3), 466-475 (1954).
- [135] A. Navid and L. Pilon. "Effect of polarization and morphology on the optical properties of absorbing nanoporous thin films," *Thin Solid Films* **516**(12), 4159-4167 (2008).
- [136] C. Zhang, S. Liu, T. Shi, and Z. Tang. "Fitting-determined formulation of effective medium approximation for 3D trench structures in model-based infrared reflectometry," *J. Opt. Soc. Am. A* **28**(2), 263-271 (2011).
- [137] R. Bräuer and O. Bryngdahl. "Design of antireflection gratings with approximate and rigorous methods," *Appl. Opt.* **33**(34), 7875-7882 (1994).
- [138] B. Liang, M. Bai, H. Ma, N. Ou, and J. Miao. "Wideband Analysis of Periodic Structures at Oblique Incidence by Material Independent FDTD Algorithm," *IEEE Trans. Antennas Propag.* **62**(1), 354-360 (2014).
- [139] B. E. McCandless and W. N. Shafarman, inventors. University of Delaware, assignee. Chemical surface deposition of ultra-thin semiconductors (2003).
- [140] S. Dottermusch, R. Schmager, E. Klampaftis, S. Paetel, O. Kiowski, K. Ding, B. S. Richards, and U. W. Paetzold. "Micro-cone textures for improved light in-coupling and retroreflection-inspired light trapping at the front surface of solar modules," *Prog. Photovolt.: Res. Appl.* **27**(7), 593-602 (2019).
- [141] R. Schmager, M. Langenhorst, J. Lehr, U. Lemmer, B. S. Richards, and U. W. Paetzold. "Methodology of energy yield modelling of perovskite-based multi-junction photovoltaics," *Opt. Express* **27**(8), A507-A523 (2019).

References

- [142] A. Gombert, B. Bläsi, C. Bühler, P. Nitz, J. Mick, W. Hoßfeld, and M. Niggemann. "Some application cases and related manufacturing techniques for optically functional microstructures on large areas," *Opt. Eng.* **43**, 2525-2533 (2004).
- [143] P. Campbell and M. A. Green. "Light Trapping Properties of Pyramidally Textured Surfaces," *J. Appl. Phys.* **62**(1), 243-249 (1987).
- [144] D. Redfield. "Multiple-pass thin-film silicon solar cell," *Appl. Phys. Lett.* **25**(11), 647-648 (1974).
- [145] S. C. Baker-Finch and K. R. McIntosh. "Reflection distributions of textured monocrystalline silicon: implications for silicon solar cells," *Prog. Photovolt.: Res. Appl.* **21**(5), 960-971 (2013).
- [146] K. R. McIntosh and L. P. Johnson. "Recombination at textured silicon surfaces passivated with silicon dioxide," *J. Appl. Phys.* **105**(12), 124520 (2009).
- [147] R. S. Bonilla, B. Hoex, P. Hamer, and P. R. Wilshaw. "Dielectric surface passivation for silicon solar cells: A review," *Phys. Status Solidi A* **214**(7), 1700293 (2017).
- [148] H. Savin, P. Repo, G. von Gastrow, P. Ortega, E. Calle, M. Garín, and R. Alcubilla. "Black silicon solar cells with interdigitated back-contacts achieve 22.1% efficiency," *Nature Nanotechnology* **10**, 624 (2015).
- [149] B. L. Sopori. "Reflection characteristics of textured polycrystalline silicon substrates for solar cells," *Sol. Cells* **25**(1), 15-26 (1988).
- [150] H. Hauser, B. Michl, S. Schwarzkopf, V. Kübler, C. Müller, M. Hermle, and B. Bläsi. "Honeycomb Texturing of Silicon Via Nanoimprint Lithography for Solar Cell Applications," *EEE J. Photovolt.* **2**(2), 114-122 (2012).
- [151] B. K. Nayak, V. V. Iyengar, and M. C. Gupta. "Efficient light trapping in silicon solar cells by ultrafast-laser-induced self-assembled micro/nano structures," *Prog. Photovolt.: Res. Appl.* **19**(6), 631-639 (2011).
- [152] P. Nostell, A. Roos, and B. Karlsson. "Optical and mechanical properties of sol-gel antireflective films for solar energy applications," *Thin Solid Films* **351**(1), 170-175 (1999).
- [153] H. Hauser, N. Tucher, K. Tokai, P. Schneider, C. Wellens, A. K. Volk, S. Seitz, J. Benick, S. Barke, F. Dimroth, C. Müller, T. Glinsner, and B. Bläsi. "Development of nanoimprint processes for photovoltaic applications," *J. Micro. Nanolithogr. MEMS MOEMS* **14**(3), 031210 031210 (2015).
- [154] A. Pimpin and W. Srituravanich. "Review on Micro- and Nanolithography Techniques and Their Applications," *Eng. J.* **16**(1), 37-56 (2011).
- [155] M. Tao, W. Zhou, H. Yang, and L. Chen. "Surface texturing by solution deposition for omnidirectional antireflection," *Appl. Phys. Lett.* **91**(8), 081118 081118 (2007).
- [156] A. Richter, F. Lentz, M. Meier, F. Finger, and K. Ding. "Light management in planar silicon heterojunction solar cells via nanocrystalline silicon oxide films and nano-imprint textures," *Phys. Status Solidi A* **213**(7), 1976-1982 (2016).
- [157] R. Schmager, B. Fritz, R. Hünig, K. Ding, U. Lemmer, B. S. Richards, G. Gomard, and U. W. Paetzold. "Texture of the Viola Flower for Light Harvesting in Photovoltaics," *ACS Photonics* **4**(11), 2687-2692 (2017).

- [158] C. Ulbrich, A. Gerber, K. Hermans, A. Lambertz, and U. Rau. "Analysis of short circuit current gains by an anti-reflective textured cover on silicon thin film solar cells," *Prog. Photovolt.: Res. Appl.* **21**(8), 1672-1681 (2013).
- [159] S.-J. Choi and S.-Y. Huh. "Direct Structuring of a Biomimetic Anti-Reflective, Self-Cleaning Surface for Light Harvesting in Organic Solar Cells," *Macromol. Rapid Commun.* **31**(6), 539-544 (2010).
- [160] S. Esiner, T. Bus, M. M. Wienk, K. Hermans, and R. A. J. Janssen. "Quantification and Validation of the Efficiency Enhancement Reached by Application of a Retroreflective Light Trapping Texture on a Polymer Solar Cell," *Adv. Energy Mater.* **3**(8), 1013-1017 (2013).
- [161] J. D. Myers, W. Cao, V. Cassidy, S.-H. Eom, R. Zhou, L. Yang, W. You, and J. Xue. "A universal optical approach to enhancing efficiency of organic-based photovoltaic devices," *Energy Environ. Sci.* **5**(5), 6900-6904 (2012).
- [162] R. Lampande, G. W. Kim, M. J. Park, B. Y. Kang, and J. H. Kwon. "Efficient light harvesting in inverted polymer solar cells using polymeric 2D-microstructures," *Sol. Energy Mater. Sol. Cells* **151**, 162-168 (2016).
- [163] J.-S. Lin, W.-P. Chu, F.-S. Juang, N.-P. Chen, Y.-S. Tsai, C.-C. Chen, C.-M. Chen, and L.-C. Liu. "Manufacture of light-trapping (LT) films by ultraviolet (UV) irradiation and their applications for polymer solar cells (PSCs)," *Mat. Lett.* **67**(1), 42-45 (2012).
- [164] B. Lipovšek, A. Čampa, F. Guo, C. J. Brabec, K. Forberich, J. Krč, and M. Topič. "Detailed optical modelling and light-management of thin-film organic solar cells with consideration of small-area effects," *Opt. Express* **25**(4), A176-A190 (2017).
- [165] S.-Y. Kuo, M.-Y. Hsieh, H.-V. Han, F.-I. Lai, T.-Y. Chuang, P. Yu, C.-C. Lin, and H.-C. Kuo. "Flexible-textured polydimethylsiloxane antireflection structure for enhancing omnidirectional photovoltaic performance of Cu(In,Ga)Se₂ solar cells," *Opt. Express* **22**(3), 2860-2867 (2014).
- [166] M. Jošt, S. Albrecht, L. Kegelmann, C. M. Wolff, F. Lang, B. Lipovšek, J. Krč, L. Korte, D. Neher, B. Rech, and M. Topič. "Efficient Light Management by Textured Nanoimprinted Layers for Perovskite Solar Cells," *ACS Photonics* **4**(5), 1232-1239 (2017).
- [167] D.-L. Wang, H.-J. Cui, G.-J. Hou, Z.-G. Zhu, Q.-B. Yan, and G. Su. "Highly efficient light management for perovskite solar cells," *Sci. Rep.* **6**, 18922 (2016).
- [168] M. Jaysankar, M. Filipic, B. Zielinski, R. Schmager, W. Song, W. Qiu, U. W. Paetzold, T. Aernouts, M. Debucquoy, R. Gehlhaar, and J. Poortmans. "Perovskite-silicon tandem solar modules with optimised light harvesting," *Energy Environ. Sci.* **11**(6), 1489-1498 (2018).
- [169] B. Fritz, R. Hunig, R. Schmager, M. Hetterich, U. Lemmer, and G. Gomard. "Assessing the influence of structural disorder on the plant epidermal cells' optical properties: a numerical analysis," *Bioinspir Biomim* **12**(3), 036011 (2017).
- [170] B. Lipovšek, J. Krč, and M. Topič. "Optimization of Microtextured Light-Management Films for Enhanced Light Trapping in Organic Solar Cells Under Perpendicular and Oblique Illumination Conditions," *EEE J. Photovolt.* **4**(2), 639-646 (2014).
- [171] B. Lipovšek, J. Krč, and M. Topič. "Microtextured Light-Management Foils and Their Optimization for Planar Organic and Perovskite Solar Cells," *EEE J. Photovolt.* **8**(3), 783-792 (2018).

References

- [172] R. J. Martín-Palma and A. Lakhtakia. "Progress on bioinspired, biomimetic, and bioreplication routes to harvest solar energy," *Appl. Phys. Rev.* **4**(2), 021103 (2017).
- [173] D. Gkikas, A. Argiropoulos, and S. Rhizopoulou. "Epidermal focusing of light and modelling of reflectance in floral-petals with conically shaped epidermal cells," *Flora* **212**, 38-45 (2015).
- [174] H. L. Gorton and T. C. Vogelmann. "Effects of Epidermal Cell Shape and Pigmentation on Optical Properties of Antirrhinum Petals at Visible and Ultraviolet Wavelengths," *Plant Physiol.* **112**(3), 879-888 (1996).
- [175] T. Sun, L. Feng, X. Gao, and L. Jiang. "Bioinspired Surfaces with Special Wettability," *Acc. Chem. Res.* **38**(8), 644-652 (2005).
- [176] A. Schulte. *Light-trapping and Superhydrophobic Plant Surfaces – Optimized Multifunctional Biomimetic Surfaces for Solar Cells* [dissertation]. Bonn, Germany: Rheinischen Friedrich-Wilhelms-Universität Bonn (2012).
- [177] PV Lighthouse Pty. Ltd. *PV Lighthouse Wafer Ray Tracer*. <https://www2.pvlighthouse.com.au/calculators/wafer%20ray%20tracer/wafer%20ray%20tracer.html>. Accessed Okt 17, 2017.
- [178] J. Wohlgemuth, D. Cunningham, J. Shaner, A. Nguyen, S. Ransome, and A. Artigao. Crystalline silicon photovoltaic modules with anti-reflective coated glass. *Conference Record of the Thirty-first IEEE Photovoltaic Specialists Conference*, Lake Buena Vista, FL, USA (2005).
- [179] J. Lehr, M. Langenhorst, R. Schmager, S. Kirner, U. Lemmer, B. S. Richards, C. Case, and U. W. Paetzold. "Energy yield modelling of perovskite/silicon two-terminal tandem PV modules with flat and textured interfaces," *Sustainable Energy Fuels* **2**(12), 2754-2761 (2018).
- [180] M. Debbarma, K. Sudhakar, and P. Baredar. "Comparison of BIPV and BIPVT: A review," *Resour.-Effic. Technol.* **3**(3), 263-271 (2017).
- [181] J. H. Wohlgemuth, D. W. Cunningham, A. M. Nguyen, J. Shaner, S. J. Ransome, A. Artigao, and J. M. Fernandez. Increased energy collection using anti-reflective coated glass. *20th European Photovoltaic Solar Energy Conference*, Barcelona, Spain (2005).
- [182] C. Ballif, J. Dicker, D. Borchert, and T. Hofmann. "Solar glass with industrial porous SiO₂ antireflection coating: measurements of photovoltaic module properties improvement and modelling of yearly energy yield gain," *Sol. Energy Mater. Sol. Cells* **82**(3), 331-344 (2004).
- [183] P. Jackson, D. Hariskos, R. Wuerz, W. Wischmann, and M. Powalla. "Compositional investigation of potassium doped Cu(In,Ga)Se₂ solar cells with efficiencies up to 20.8%," *Phys. Status Solidi RRL* **8**(3), 219-222 (2014).
- [184] P. Jackson, R. Wuerz, D. Hariskos, E. Lotter, W. Witte, and M. Powalla. "Effects of heavy alkali elements in Cu(In,Ga)Se₂ solar cells with efficiencies up to 22.6%," *Phys. Status Solidi RRL* **10**(8), 583-586 (2016).
- [185] P. D. Paulson, R. W. Birkmire, and W. N. Shafarman. "Optical characterization of CuIn_{1-x}Ga_xSe₂ alloy thin films by spectroscopic ellipsometry," *J. Appl. Phys.* **94**(2), 879-888 (2003).
- [186] C. J. Stolle, M. G. Panthani, T. B. Harvey, V. A. Akhavan, and B. A. Korgel. "Comparison of the Photovoltaic Response of Oleylamine and Inorganic Ligand-Capped CuInSe₂ Nanocrystals," *ACS Appl. Mater. Interfaces* **4**(5), 2757-2761 (2012).

- [187] P. Löper, M. Stuckelberger, B. Niesen, J. Werner, M. Filipič, S.-J. Moon, J.-H. Yum, M. Topič, S. De Wolf, and C. Ballif. "Complex Refractive Index Spectra of CH₃NH₃PbI₃ Perovskite Thin Films Determined by Spectroscopic Ellipsometry and Spectrophotometry," *J. Phys. Chem. Lett.* **6**(1), 66-71 (2015).
- [188] W. Groh and A. Zimmermann. "What is the lowest refractive index of an organic polymer?," *Macromolecules* **24**(25), 6660-6663 (1991).
- [189] Y. Hanada, K. Sugioka, and K. Midorikawa. "UV waveguides light fabricated in fluoropolymer CYTOP by femtosecond laser direct writing," *Opt. Express* **18**(2), 446-450 (2010).
- [190] M. C. van Lare and A. Polman. "Optimized Scattering Power Spectral Density of Photovoltaic Light-Trapping Patterns," *ACS Photonics* **2**(7), 822-831 (2015).
- [191] E. R. Martins, J. Li, Y. Liu, V. Depauw, Z. Chen, J. Zhou, and T. F. Krauss. "Deterministic quasi-random nanostructures for photon control," *Nat. Commun.* **4**, 2665 (2013).
- [192] E. R. Martins, J. Li, Y. Liu, J. Zhou, and T. F. Krauss. "Engineering gratings for light trapping in photovoltaics: The supercell concept," *Phys. Rev. B* **86**(4), 041404 (2012).
- [193] A. Deinega, I. Valuev, B. Potapkin, and Y. Lozovik. "Minimizing light reflection from dielectric textured surfaces," *J. Opt. Soc. Am. A* **28**(5), 770-777 (2011).
- [194] B. Fritz, M. Guttman, P. C. Soler, A. Roslizar, M. Langenhorst, M. Schneider, U. W. Paetzold, B. S. Richards, U. Lemmer, R. Huenig, and G. Gomard. Towards mass fabrication of hot embossed plant surface texture replicas as photovoltaic cover layers. *SPIE Nanoscience + Engineering*, (2018).
- [195] A. Roslizar, S. Dottermusch, F. Vüllers, M. N. Kavalenka, M. Guttman, M. Schneider, U. W. Paetzold, H. Hölscher, B. S. Richards, and E. Klampaftis. "Self-cleaning performance of superhydrophobic hot-embossed fluoropolymer films for photovoltaic modules," *Sol. Energy Mater. Sol. Cells* **189**, 188-196 (2019).
- [196] F. Kotz, K. Plewa, W. Bauer, N. Schneider, N. Keller, T. Nargang, D. Helmer, K. Sachsenheimer, M. Schäfer, M. Worgull, C. Greiner, C. Richter, and B. E. Rapp. "Liquid Glass: A Facile Soft Replication Method for Structuring Glass," *Adv. Mater.* **28**(23), 4646-4650 (2016).
- [197] M. Langenhorst, D. Ritzer, F. Kotz, P. Risch, I. Hossain, S. Dottermusch, A. Roslizar, R. Schmagel, B. S. Richards, B. E. Rapp, and U. W. Paetzold. Advanced optical microstructures embedded in transparent encapsulation glass for photovoltaics. *SPIE OPTO*, San Francisco, CA, USA (2019).
- [198] P. B. Johnson and R. W. Christy. "Optical Constants of the Noble Metals," *Phys. Rev. B* **6**(12), 4370-4379 (1972).
- [199] Z. C. Holman, M. Filipič, A. Descoedres, S. D. Wolf, F. Smole, M. Topič, and C. Ballif. "Infrared light management in high-efficiency silicon heterojunction and rear-passivated solar cells," *J. Appl. Phys.* **113**(1), 013107 (2013).
- [200] H. ElAnzeery, O. El Daif, M. Buffière, S. Oueslati, K. Ben Messaoud, D. Agten, G. Brammertz, R. Guindi, B. Kniknie, M. Meuris, and J. Poortmans. "Refractive index extraction and thickness optimization of Cu₂ZnSnSe₄ thin film solar cells," *Phys. Status Solidi A* **212**(9), 1984-1990 (2015).
- [201] I. H. Malitson. "Interspecimen Comparison of the Refractive Index of Fused Silica*,†," *J. Opt. Soc. Am.* **55**(10), 1205-1209 (1965).

List of related publications

Journals

S. Dottermusch, A. Quintilla, G. Gomard, A. Roslizar, V. R. Voggu, B. A. Simonsen, J. S. Park, D. R. Pernik, B. A. Korgel, U. W. Paetzold, and B. S. Richards, "Infiltrated photonic crystals for light-trapping in CuInSe₂ nanocrystal-based solar cells," *Opt. Express* **25**(12), A502-A514 (2017).

S. Dottermusch, D. Busko, M. Langenhorst, U. W. Paetzold, and B. S. Richards, "Exposure-dependent refractive index of Nanoscribe IP-Dip photoresist layers," *Opt. Lett.* **44**(1), 29-32 (2019).

S. Dottermusch, R. Schmager, E. Klampaftis, S. Paetel, O. Kiowski, K. Ding, B. S. Richards, and U. W. Paetzold, "Micro-cone textures for improved light in-coupling and retroreflection-inspired light trapping at the front surface of solar modules," *Prog. Photovolt. Res. Appl.*, **27**(7), 593-602 (2019).

Conferences

S. Dottermusch, A. Quintilla, G. Gomard, D. R. Pernik, V. Reddy, B. A. Korgel, U. W. Paetzold, and B. S. Richards, "Direct Laser Written Nanophotonics for Embedded CIS Nanocrystal Solar Cells," OSA Light Energy and the Environment, Leipzig, Germany, Nov 2016, paper PW3B.2.

S. Dottermusch, A. Quintilla, G. Gomard, U. W. Paetzold, and B. S. Richards, "Simulation of Absorption Enhancement and Optical Modes in CIS Nanocrystal Embedded Photonic Crystal Designs," OSA Light Energy and the Environment, Leipzig, Germany, Nov 2016, paper PTu2B.3.

S. Dottermusch, R. Schmager, E. Klampaftis, B. S. Richards, U. W. Paetzold, "Microcone structured encapsulations for light trapping in photovoltaics," SPIE Photonics Europe, Strasbourg, France, April 2018.

Acknowledgments

It is my great pleasure to thank all the wonderful people who were involved in this work and supported me on this journey.

A foremost, I would like to thank my supervisor Prof. Dr. Bryce Richards for giving me the opportunity to work in the exciting field of photovoltaics and giving me a great amount of freedom with my topic. I was very grateful to be one of the first in your group at KIT and could enjoy watching the growth of a very international group thriving under your cheerful character.

I am very grateful to Prof. Dr. Christiane Becker and Prof. Dr. Heinz Kalt for having agreed to be the second reviewers of this dissertation.

A special thanks goes out to all my collaborators for making this work possible. I am very grateful for all the support from Dr. Aina Quintilla when I started in the labs. The same goes for Dr. Guillaume Gomard who help me with the theoretical background and was a great source of ideas. Thank you Dr. Ulrich Paetzold for being inspirational, stepping in as a part-time supervisor of my work, and keeping me on track. It was a pleasure to get to know Dr. Efthymios Klampaftis, his practical approaches taught me a lot. The long discussions with Raphael Schmager were important building blocks in developing this work. It was my pleasure to learn the replication process from Malte Langenhorst and how to work with lasers from Dr. Dmitry Busko. I also want to thank Aiman Roslizar for the help in the lab and the fruitful discussions. I am very thankful for the support from Benjamin Fritz with ray-tracing simulations and Jan Preinfalk with the goniometer setup. Thank you Taby Tom for designing a sample holder for angle-dependent EQE measurements. From my collaborators in the Korgel group I want to first of all thank Vikas Voggu for all the support with the CIS nanocrystals and detailed explanations. I am furthermore very thankful of Prof. Dr. Brian Korgel and Dr. Doug Pernik for fostering this collaboration. I want to thank Dr. Kaining Ding for providing the silicon solar cells used in this work, and Dr. Stefan Paetel, as well as Dr. Oliver Kiowski for providing the CIGS solar cells.

I want to thank everyone in the Nanophotonics for Energy group for designing such a wonderful working environment. I am very grateful for having shared my office with Michael Oldenburg, Ella Marais, Deski Beri, and Vinay Kumar, thank you for all the laughs and shared time. Thank you Dr. Ian Howard for always having an open door and spending advice. A very special thanks goes to Raphael Schmager, Michael Adams, Malte Langenhost, and Micheal Oldenburg for proof reading this dissertation.

My gratitude is also with the IMT staff providing the foundation for making this scientific work possible. Explicitly, I want to thank Stefan Hengsbach and Florian Rupp for support with DLW and for always having an open ear. Further thanks goes to the clean room staff under the supervision of Uwe Köhler for maintaining such a great working environment. Special gratitude also goes to Alexandra Moritz and her mechanical workshop team for aiding in the design and the fabrication of customized parts.

Finally, I would like to thank my family for their support. My parents for enabling me to freely choose my studies. My wonderful and understanding wife Linda for always being on my side. And of course my daughter for making every day more enjoyable.